UNIVERSITY OF CALIFORNIA

Santa Barbara

The Utility and Development of Brønsted Acids for Advanced Functional Material

A dissertation submitted in partial satisfaction of the

requirements for the degree Doctor of Philosophy

in Chemistry

by

Manuel Sanchez Zayas

Committee in charge:

Professor Javier Read de Alaniz, Co-Chair

Professor Rachel A. Segalman, Co-Chair

Professor Christopher M. Bates

Professor Craig J. Hawker

Professor Gabriel Ménard

September 2021

The dissertation of Manuel Sanchez Zayas is approved.

_____

Javier Read de Alaniz, Committee Co-Chair

_____

Rachel A. Seglman, Committee Co-Chair

_____

Christopher M. Bates

_____

Craig J. Hawker

_____

Gabriel Ménard

July 2021

This dissertation is dedicated to the light of my world, my son, Isaac Angel Zayas. Your heart of gold and constant laughter always kept me grounded and gave me the strength to keep pushing through it all. This is for you lil' man!

The Utility and Development of Brønsted Acids for Advanced Functional Material

ACKNOWLEDGEMENTS

First and foremost, I want to thank my advisors, Javier Read de Alaniz and Rachel Segalman. I cannot thank you both enough for the tremendous amount of support and patience throughout the years. Javier, I appreciate how candid our conversations would always be, and the countless times I've come to your office overwhelmed and lost, yet you have an uncanny ability to reinvigorate us all. I would always leave your office feeling like I could take on the world. Rachel, the amount of support you demonstrated when I first announced the pregnancy was unparalleled. My initial thought was this was the end of grad school for me, but your words of encouragement and support through it all is a large part of the reason I decided to stick it through, and for that I cannot thank you enough.

I would like to acknowledge the rest of my committee Chris, Craig, and Gab and thank them for their helpful discussions over the years. You each always found a way to challenge me and push me further than I ever thought possible, and I appreciate your guidance through it all.

I also want to thank my undergraduate advisor, Arsalan Mirjafari. Thank you for showing me that there was another way and there were more options available to me. You encouraged me to pursue a PhD, which up until that point I didn't even really know what that was. Thank you for taking the time to mentor me on such a personal level, for all the constant laughs during our office hours and for being a great friend.

I want to thank all of my collaborators and mentors over the years, I've learned so much and have grown thanks to all of your help and patience. I would be remiss if I do not specifically thank Emre, Andre, Yvonne, Jeff, Neil, Meghan, Andrei, Hui, Nicole, Seamus, Allison, Julie, and Jessica for your guidance and fruitful discussions over the years. I want to also recognize Jesus, Miguel,

Kelsey, and Justin who I've had the privilege to mentor over the years. I've learned so much from you all and I'm excited to see what the future has in hold for each of you.

I want to give a huge shout out to all the friends I've made over the years, you've all made graduate school much more fun, countless bonfires, rooftop parties, sloshball games: Meghan, Andre, Kyle, Jeff, Marco, Fritz, Allison, Angelique, Zongheng, Pat, Josh, Jake, and Kerry. To the Usual Suspects: Kan, Sheng, Dezmond, Dori, Jocelyn, and Pavel, I think the name says it all. My main man Marco Preuss, even though you were only here for a short time, you quickly became one of my best friends, your hysterical sense of humor is something that I still laugh about to this day! We are still doing Oktoberfest one day! My other main man, Jeffrey Self, my oh my have these years been one hell of a rollercoaster. You've been my guy since day one and to have shared a lab with you and worked alongside all these years, it still feels surreal we are on our way. I can't express how proud I am to call you my best friend, and I'm excited to see where life takes you!

And I know I've said this a million times, but I will say it a million more, Courtney and Josh, thank you for all you've done. I know that I wouldn't be here today if it wasn't for the immense generosity you've shown over the years. To open your doors to practically a stranger, really made the difference in helping me continue going through school. I cannot repay what you have done for me and I hope you realize how much, what you've done, means to me.

Nathalie, you've done such an amazing job raising our son, Isaac, and for that I cannot thank you enough. You're the perfect mother for him and you've shown him so much love and so much care I can see it in him. His laughter and his kindness just goes to show how great you have been with him, thank you.

Meghan, these last few years have been an absolute whirlwind, but I couldn't imagine anyone else I'd rather share this experience with. Through the ups and downs of graduate school and life,

you've been my rock and my support. You've helped me through the toughest of times and for that I am eternally grateful. I'm so proud of everything you've accomplished and I'm excited to see what the future has for us.

And finally, to my family. Gracias por todo su apoyo durante todos estos años. No ha sido un viaje fácil, pero ustedes jamás dudaron de mí. Agradezco todos los consejos, todas las veces que me soportaron. He podido lograr todas mis metas gracias a ustedes. Los amos mucho y ya finalmente no hay que ir a mas graduaciones jaja.

EDUCATION

University of California Santa Barbara, Santa Barbara, CA — July 2016 – Present
Doctorate in Philosophy in Material Chemistry

Florida Gulf Coast University, Fort Myers, FL — Aug. 2013 – May 2016
Bachelors of Art Chemistry
GPA: 3.99 (*Summa Cum Laude)*

Edison State College, Fort Myers, FL — Aug. 2008 – Aug. 2013
Bachelors of Applied Sciences in Cardiopulmonary Sciences
GPA: 3.69 (*Cum Laude*)

RESEARCH EXPERIENCE

BASF Leadership Development Program Internship, RTP, NC — Aug. 2020 – Oct. 2020
Assignment Manager: Nikki Cochrane, APR-DS

- Developed new environmentally sustainable seed coating formulations for global clients
- Coordinated with global stakeholders, held regular meetings to share results

Univeristy of California Santa Barbara, Santa Barbara, CA — July 2016 – Current
Ph. D. Candidate
Co-Advisors: Javier Read de Alaniz and Rachel Segalman

- Synthesis and characterization of novel photoresponsive molecules for stimuli responsive materials and catalysis
- Synthesized a dynamic covalently adaptable network with tunable response rates, and performed physical characterization.
- Mentored four undergraduate student researchers through instrument training, synthetic methods development, and characterization techniques and ensured safe execution. (2 current graduate students, 1 industry internship, 1 industry)

Florida Gulf Coast University, Fort Myers, FL — Sept. 2014 – May 2016
Undergraduate Research
Advisor: Arsalan Mirjafari

- Primary undergraduate institution
- Designed and synthesized novel ionic liquids utilizing a number of robust and orthogonal chemistries to incorporate varying functional handles.
- Mentored two junior undergraduate researchers through synthetic methods development and safety.

PROFESSIONAL EXPERIENCE

UCSB Dept. of Chemistry and Biochemistry, Santa Barbara, CA
Teaching Assistant Organic Chemistry Series — Jan. 2019 – March 2019
Teaching Assistant General Chemistry Series — Sept. 2016 – Dec. 2018

FGCU Dept. of Chemistry and Physics, Fort Myers, FL
Undergraduate Research — Aug. 2014 – May 2016
Teaching Assistant General Chemistry II — Aug. 2014 – Dec. 2014

Physicians Regional Medical Center, Naples, FL — Dec. 2011 – June 2016
Cardiovascular Technologist (RCIS)

PUBLICATIONS

"The influence of acid dissociation constant on ionic conductivity in polymeric ionic liquids" **Zayas, M. S.**; Nikolaev, A.; Peterson, J.; Jones, S. D.; Richardson, P.; Rawlings, D. H.; Koutsoukos, K.; Clement, R.; Read de Alaniz, J.; Segalman, R. A., ***Manuscript in preparation***

"Controlled single photochrome multi-mode photoswitching system for complex photoswitching responses." Stricker, F.; Sanchez, D. M.; Raucci, U.; Dolinski, N. D.; **Zayas, M. S.**; Meisner, J.; Hawker, C. J.; Martinez, T. J.; Read de Alaniz, J., ***Manuscript in preparation***

"Light-switchable and self-healing polymer electrolytes based on dynamic diarylethene and metal-ion coordination." Nie, H.; Schauser, N. S.; Self, J. L.; Tabassum, T.; Oh, S.; Geng, Z.; Jones, S. D.; **Zayas, M. S.**; Reynolds, V. G.; Chabinyc, M. L.; Hawker, C. J.; Han, S.; Bates, C. M.; Segalman, R. A.; Read de Alaniz, J., *J. Am. Chem. Soc.*, **2021**, *143*, 1562-1569.

"Polymer stereocomplexation as a scalable platform for nanoparticle assembly." Abdilla, A.; Dolinski, N. D.; de Roos, P.; Ren, J. M.; vad der Woude, E.; Seo, S. E.; **Zayas, M. S.**; Lawrance, J.; Read de Alaniz, J.; Hawker, C. J., *J. Am. Chem. Soc.*, **2020**, *142*, 1667-1672.

"Norbornadienes: Robust and scalable building blocks for cascade 'click' coupling of high molecular weight polymers." St. Amant, A. H.; Discekici, E. H.; Bailey, S. J.; **Zayas, M. S.**; Song, J. A.; Shankel, S. L.; Nguyen, S. N.; Bates, M. W.; Anastasaki, A.; Hawker, C. J.; Read de Alaniz, J., *J. Am. Chem. Soc.*, **2019**, *141*, 13619-13624.

"Tuning merocyanine photoacid structure to enhance solubility and temporal control: Application in ring opening polymerization." **Zayas, M. S.**; Dolinski, N. D.; Self, J. L.; Abdilla, A.; Hawker, C. J.; Bates, C. M.; Read de Alaniz, J., *ChemPhotoChem*, **2019**, *3*, 467-472.

"Brønsted-acid catalyzed exchange in polyester dynamic covalent networks." Self, J. L.; Dolinski, N. D.; **Zayas, M. S**.; Read de Alaniz, J.; Bates, C. M., *ACS Macro Lett.*, **2018**, *7*, 817-821.

"Biomimetic design of protic lipidic ionic liquids with enhanced fluidity." O'brien, R. A.; **Zayas, M. S.**; Nestor, S. T.; Gaitor, J. C.; Paul, L. M.; Edhegard, F. A.; Minkowicz, S.; Sykora, R. E.; Sheng, Y.; Michael, S. F.; Isern, S.; Mirjafari, A., *New Journal of Chemistry*, **2016**, *40*, 7795-7803.

"'Click Synthesis' of mercaptosilyl-functionalized ionic liquids *via* thiol-ene chemistry for use as hydrophobic surface coating agents." **Zayas, M. S.**; Nestor, S.; Gaitor, J.; Reardon, M.; Mirjafari, A., *ECS Trans*. **2016**, *75*, 191-198.

"Bifunctional hydrophobic ionic liquids: Facile synthesis by thiol-ene 'click' chemistry." **Zayas, M. S.**; Gaitor, J. C.; Nestor, S. N.; Mirjafari, A., *Green Chemistry*, **2016**, *18*, 2443-2452.

"Crystal structure of a methimazole-based ionic liquid." Gaitor, J. C.; **Zayas, M. S.**; Myrthil, D. J.; White, F.; Hendrich, J. M.; Sykora, R. E.; O'Brien, R. A.; Reilly, J. T.; Mirjafari, A. *Acta Crystallographica Section E: Crystallographic Communications*, **2015**, *71*, o1008-o1009.

PRESENTATIONS

257th American Chemical Society National Meeting; Orlando, FL — March 2019
"*Expanding the scope of metastable photoacids into material applications*" - Oral Presentation

ACS Scholars Symposium — November 2017
Invited Speaker for ACS Scholars Program

253th American Chemical Society National Meeting; San Fransisco, CA — April 2017
Invited Speaker for ACS Scholars Program

FGCU Whitaker Center's STEM Undergraduate Symposium — Dec. 2015
"*Bifunctional Hydrophobic Ionic Liquids: A Facile Synthesis via Thiol-ene 'Click' Chemistry with Surface Coating Applications*" - Oral Presentation

FGCU Research Day — April 2015
"*Click chemistry-mediated synthesis of novel functionalized ionic liquids containing trialkoxysilane moieties*"
Dean's Award for Outstanding Undergraduate Poster in the Sciences

249th American Chemical Society National Meeting; Denver, CO — March 2015
"*Click chemistry-mediated synthesis of novel functionalized ionic liquids containing trialkoxysilane moieties*"
Sci-Mix Poster Presentation, General Poster Presentation

FGCU Whitaker Center's STEM Undergraduate Symposium — Dec. 2014
"*Click Chemistry Mediated Synthesis of Novel Lipid Inspired Ionic Liquids*"
General Poster Presentation

SELECT LEADERSHIP AND OUTREACH

Graduate Students for Diversity in Science

President — Sept. 2018 – June 2020

- Directed a student led organization to promote diversity and inclusion by hosting and coordinating a visit from leading scientists from across the nation
- Organized and oversaw bi-annual Dow Foundation Distinguished Lecturer series to promote diversity and research excellence at UCSB
- Oversaw the California State Universities visits – promising upper division undergraduate students from underrepresented minorities visited our campus and learned more about graduate school

Scheduling Chair — Sept. 2017 – Sept. 2018

- Coordinated schedules of invited speaker with faculty and student organizations across campus

Gamma Sigma Epsilon, Chemistry Honor Society — May 2015 – May 2016
Inaugural President

SELECT AWARDS

Outstanding Service to the Department Award — May 2019
Sandra Lamb Memorial Fellowship — May 2019
Mellichamp Academic Initiative in Sustainability Fellowship — Summer 2018
Jarrod Davidson Memorial Fellowship — May 2018

National Science Foundation GRFP Honorable Mention	April 2017
South Florida American Chemical Society's Honor Award for *Outstanding Achievement in Chemistry*	April 2016
FGCU College of Arts and Science - Student of the Year Nominee	2014/15 & 2015/16
American Chemical Society Scholar	2015/16
Alice and Karl Sheffield Scholarship *STEM Undergraduate Research*	Summer 2015

ABSTRACT

The Utility and Development of Brønsted Acids for Advanced Functional Material

by

Manuel Sanchez Zayas

Proton driven processes are one of the most ubiquitous chemistries found and are present across many different disciplines. Brønsted acids provides the ability to selectively regulate the extent of proton transfer offering a myriad of possibilities by controlling reaction kinetics, proton gradients, and chemical environment. As such, we can take advantage of one of the most fundamental processes in chemistry to help us better study and develop the emerging class of advanced functional materials. In this dissertation, I will highlight the projects I've led in this area. Beginning with a fundamental study on the effect of acid strength in polymeric protic ionic liquids (polyPILs), I will demonstrate a direct correlation with ionic conductivity as a function of the Brønsted acid's pK_a. Furthermore, the ionic nature of these systems is explored using pulse field gradient NMR demonstrating how the extent of proton transfer directly correlates to the ΔpK_a of the constituent acid-base pair. The density field theory calculated physicochemical values correlate closely with the experimentally obtained data suggesting that pK_a can be used as metric to approximate ion pair strength/lifetime association in polyPILs. Next, I will discuss the development of a new merocyanine-based photoacid, which demonstrates improved solubility in organic media and enhanced switching kinetics that can be used to impart temporal control over

ring opening polymerization. The effect of the structural modification on solubility, thermal relaxation kinetics, and activation energy were evaluated using ^{1}H NMR and pump-probe absorption spectroscopies. Overall, the new merocyanine based photoacid provides access to a wider range of chemical and material applications with improved solvent compatibility and temporal control. Finally, I will discuss how we developed a Brønsted acid catalyzed dynamic covalent chemistry using commodity polymers. Herein, a novel triblock polyester system is prepared from the chain extension of readily available commercial polymers. With a newly developed bis-lactone crosslinker and the merocyanine photoacid previously discussed, a photo-curable resin is demonstrated, highlighting the potential for various applications including photo-patterning and additive manufacturing. Altogether, I hope this dissertation will demonstrate the effective value Brønsted acids have in the development of advanced functional materials.

TABLE OF CONTENTS

1 Introduction 1

1.1 The Expanding Role of Organic Chemistry 1

1.2 Defining Brønsted Acid 2

1.2.1 Conjugate Acid-Base Pairs 3

1.2.2 Acid Strength and the Acid Dissociation Constant, K_a and pK_a[7] 4

1.3 The role of Brønsted Acids in Organic Chemistry 8

1.3.1 Defining Polymeric Ionic Liquids 11

1.3.2 Overview of Photoacid Generators and Reversible Photoacids 12

1.3.3 Brønsted Acids in Polymerization Reactions and Vitrimer Exchange 14

1.4 Outline 20

1.5 References – Chapter 1 21

2 The influence of pK_a on proton transfer and ionic conductivity in pyridinium based methacrylic polymeric protic ionic liquids 26

2.1 Abstract 26

2.2 Introduction 27

2.3 Results and Discussion 30

2.4 Conclusion 45

2.5 Materials and Methods 46

2.5.1 Experimental Details 46

2.5.1.1 Materials 46
2.5.1.2 Instrumentation 46
2.5.1.3 Synthesis 48
2.5.2 Characterization 56
2.5.2.1 NMR 56
2.5.2.2 Size Exclusion Chromatography 66
2.5.2.3 Differential Scanning Calorimetry 67
2.5.2.4 Ionic Conductivity 69
2.5.2.5 Pulse Field Gradient Nuclear Magnetic Resonance Spectroscopy 75
2.5.3 Density Functional Theory Calculations 78
2.6 References – Chapter 2 81
3 Tuning merocyanine photoacid structure to enhance solubility and temporal control: application in ring opening polymerization 85
3.1 Abstract 85
3.2 Introduction 85
3.3 Results and Discussion 88
3.4 Conclusion 97
3.5 Materials and Methods 97
3.5.1 Experimental Details 97
3.5.1.1 Materials 97

3.5.1.2 Instrumentation 98
3.5.1.3 Synthesis 99
3.5.1.4 Temporal photo-ring opening polymerization 101
3.5.2 Characterization 102
3.5.2.1 NMR 102
3.5.2.2 UV-Vis 106
3.5.2.3 Solubility tests 115
3.5.2.4 Kinetics 116
3.5.2.5 Photo-ring opening polymerization GPCs 132
3.6 References – Chapter 3 140
4 Triblock polyester vitrimers from commercial polymers 142
4.1 Abstract 142
4.2 Introduction 142
4.3 Results and Discussion 144
4.4 Conclusion 151
4.5 Future Work 151
4.6 Experimental Details 153
4.7 References – Chapter 4 159

LIST OF FIGURES

Figure 1.1 Visual examples demonstrating the vast applications of stimuli responsive materials. 17

Figure 1.2 Methanesulfonic acid catalyzed polyester networks are recyclable as expected for dynamic networks that undergo associative exchange. (Reprinted with permission from ACS Macro Lett. 2018, 7 (Reference 15) Copyright 2018 American Chemical Society.) 18

Figure 1.3 a) Schematic describing the ROP synthesis of low-T_g polyester vitrimers. b) Brønsted acid catalysts used to promote ROP and subsequent exchange reactions via transesterification. pK_a values are referenced in H_2O. c) Oscillatory rheology step-strain stress relaxation experiments on low-T_g polyester vitrimer formulations containing Brønsted acid catalysts at 55 °C. d) Activation energy (E_a filled symbols) and Arrhenius prefactor (τ_0, open symbols) are strongly correlated with Brønsted acid pK_a. (Adapted with permission from ACS Macro Lett. 2018, 7 (Reference 15) Copyright 2018 American Chemical Society.) 19

Figure 2.1 a) Compiled conductivities measured by EIS plotted in a T_g normalized manner. b) Conductivity comparison of the bis(sulfonimides). 35

Figure 2.2 T_g normalized conductivities as a function of aqueous pK_a values at a specified T/T_g. Black dashed arrow added to suggest the correlation of pKa and conductivity. 37

Figure 2.3 Comparison of conductivities of protic and aprotic a) TfO derivatives and b) TFA derivatives. For the TfO derivatives, the two samples demonstrate the same conductivity, where the aprotic TFA has an increase of about 3-5 times as compared to the protic version. 38

Figure 2.4 Conductivity measurements comparing PFG-NMR calculated conductivities to EIS measured values for the pPy-TFSI polyPIL 41

Figure 2.5 Conductivity measurements comparing PFG-NMR calculated conductivities to EIS measured values for the pPy-DFA polyPIL. PFG Total denotes the summation of the PFG Acidic Proton and PFG Anion values. The PFG Anion is an average of the ^{1}H and ^{19}F signals assigned to the anion, with error bars included. 43

Figure 2.6. Conductivity measurements comparing PFG-NMR calculated conductivities to EIS measured values for the pPy-MFA polyPIL. PFG Total denotes the summation of the PFG Acidic Proton and PFG Anion values. The PFG Anion is an average of the ^{1}H and ^{19}F signals assigned to the anion, with error bars included. 44

Figure 2.7 ^{1}H NMR (600 MHz, $CDCl_3$) **RAFT-pPyMA**. Insert shows chain end present, which was utilized to calculate M_n(NMR). The degree of polymerization for this polymer was estimated by the analysis of the methylene peaks at the chain end α to the trithiocarbonate group (b) to the methylene polymer peaks α to the ester of the methacrylate repeat unit (a). 56

Figure 2.8 ^{1}H NMR (600 MHz, $CDCl_3$) **pPyMA**. Insert demonstrates absence of chain end, indicating successful cleavage of terminal functional group. 57

Figure 2.9 ^{1}H NMR (600 MHz, DMSO-*d*6) **pPy-TFSI** 57

Figure 2.10 ^{19}F NMR (100 MHz, DMSO-*d*6**) pPy-TFSI** 58

Figure 2.11 ^{1}H NMR (600 MHz, DMSO-*d*6) **pPy-NMes2** 58

Figure 2.12 ^{1}H NMR (600 MHz, DMSO-*d*6) **pPy-TfO** 59

Figure 2.13 ^{19}F NMR (100 MHz, DMSO-*d*6) **pPy-TfO** 59

Figure 2.14 ^{1}H NMR (600 MHz, DMSO-*d*6) **pPy-MS** 60

Figure 2.15 ^{1}H NMR (600 MHz, DMSO-*d*6) **pPy-TFA** 60

Figure 2.16 ^{19}F NMR (100 MHz, DMSO-*d*6) **pPy-TFA** 61

Figure 2.17 ^{1}H NMR (600 MHz, DMSO-*d*6) **pPy-DFA** 61

Figure 2.18 ^{19}F NMR (100 MHz, DMSO-*d*6**) pPy-DFA** 62

Figure 2.19 ^{1}H NMR (600 MHz, DMSO-*d*6) **pPy-MFA** 62

Figure 2.20 ^{19}F NMR (100 MHz, DMSO-*d*6**) pPy-MFA** 63

Figure 2.21 ^{1}H NMR (600 MHz, DMSO-*d*6) **aPy-TfO** 63

Figure 2.22 ^{19}F NMR (100 MHz, DMSO-*d*6) **aPy-TfO**..... 64

Figure 2.23 ^{1}H NMR (600 MHz, DMSO-*d*6) **aPy-MSA** 64

Figure 2.24 ^{1}H NMR (600 MHz, DMSO-*d*6) **aPy-TFA** 65

Figure 2.25 ^{19}F NMR (100 MHz, DMSO-*d*6) **aPy-TFA**. By ^{19}F NMR integration ~97% anion exchange to the TFA counterion. 65

Figure 2.26 Size exclusion chromatography (DMF, 0.01% LiBr) tracing comparing **pPyMA**, the polymer sample before any acid addition, and **pPy-TfO**, with the addition of TfOH, one of the stronger acids utilized in this study. No noticable differnce in the tracing or molecular weight of the polymer sample suggests no degradation upon addition of acid to the polymer. Molecular weight and dispersity based on polystyrene standards: 66

Figure 2.27 Differential scanning calorimetry curves for the protic polymeric ionic liquids examined in this study. Midpoint analysis of the T_g feature of the second heating curve gives the following glass transition temperatures: 67

Figure 2.28 Differential scanning calorimetry curves for the aprotic control samples tested. Protic analogues are plotted along for comparison. Midpoint analysis of the T_g feature of the second heating curve gives the following glass transition temperatures: 68

Figure 2.29 Conductivities measured by EIS of the polyPILs in this study plotted in an Arrhenius fashion, unnormalized by T_g. 69

Figure 2.30 Condutivities of polyPILs with sulfonate Brønsted acids. A greater difference, over 1 order of magnitude, is noted at lower temperatures, but when temperature is increased, the overall conductivities begin to converge. This is thought to be as a result of overcoming the H-bonding forces, facilitating anion motion. 70

Figure 2.31 Conductivities of the polyPILS containing fluorinated acetate Brønsted acids. Overall conductivities increase as function of acid strength. 71

Figure 2.32 Arrhenius Tg normalized plot of conductivities of measured samples. 72

Figure 2.33 Normalized conductivity comparing the protic MSA (**pPy-MS**) and the aprotic MSA (**aPy-MS**) polymer samples. 73

Figure 2.34 Normalized condictivities of aprotic analogues studied. Above T_g all poly aprotic ionic liquids collapse onto a single line, suggesting that H-bonding is the dominant interionic interaction in the polyPILs. 74

Figure 2.35 Optimized structure for triflate (TfO) with pyridine-H^+; X-H bond = 1.75 Å; N-H bond = 1.04 Å 79

Figure 2.36 Optimized structure for fluoroacetate, CFH_2COO^-, ($[MFA]^-$) with pyridine-H^+; X-H bond = 1.05 Å; N-H bond = 1.53 Å 79

Figure 2.37 T_g normalized conductivities as a function of ΔE values calculated from DFT in acetone at a specified T/T_g. Black dashed arrow added to suggest the correlation of ΔE and conductivity. Compared to **Figure 2.2**, an almost identical trend is noted, showcasing the utility of DFT as a means to help predict the performance of polyIL structures. 80

Figure 3.1 Differences in solubility between a) PAH-1 and b) PAH-2. Each sample was prepared targeting a 2.6 mM of the respective mPAH in DCM. (Reprinted with permission from ChemPhotoChem., 2019, 3. Copyright 2019 John Wiley and Sons.)..... 89

Figure 3.2 Pump–probe absorption spectroscopy of PAH-2 at room temperature, irradiating with 470 nm LED. (a) Detailed cycle showing photoresponse (<60 s) followed by thermal equilibration over 6.7 h in methanol. Time axis break accentuates the first 6 minutes of the cycle to highlight rapid rate of photocyclization. (b) Detailed cycles showing rapid photoresponse (<60 s) followed by fast thermal equilibration (≈4 min) in methylene chloride. (Reprinted with permission from ChemPhotoChem., 2019, 3. Copyright 2019 John Wiley and Sons.) 90

Figure 3.3 a) Schematic of thermal relaxation from the SP to MCH^+ isomer. b) The ratio of MCH^+ over time for **PAH-2** in methanol-d_4 at varying temperatures. Inset plots the rate constants in an Arrhenius fashion. c) Comparison of activation energies for the ring closing reaction (MCH^+ to SP, left bar) and the ring opening reaction (SP to MCH^+, middle bar) as well as the ring opening rate constant (right bar) for each given condition. (Reprinted with permission from ChemPhotoChem., 2019, 3. Copyright 2019 John Wiley and Sons.)..... 93

Figure 3.4 a) Reaction scheme used to temporally control the ring-opening polymerization of ε-caprolactone with an mPAH photocatalyst. b) **PAH-1** (orange squares) exerts poor temporal control over polymerization. Once the reaction is initiated, polymerization continues almost unaffected by light being cycled on or off. In contrast, **PAH-2** (blue circles) exhibits a marked improvement in the speed of the polymerization during irradiation, which almost completely halts during off periods. c) Similar results are observed in DCM with lower catalyst loading (10 mol%). **PAH-1** induces poor temporal control and sluggish kinetics, unlike **PAH-2**. (Reprinted with permission from ChemPhotoChem., 2019, 3. Copyright 2019 John Wiley and Sons.) 95

Figure 3.5 ^{1}H NMR (500 MHz, DMSO-d_6) **PAH-2.** Red boxes indicate the peaks that correspond to the **SP** isomer of **PAH-2** (See **Figure 3.6**). 102

Figure 3.6 ^{1}H NMR (500 MHz, DMSO-d_6) Photoproduct of **PAH-2 (SP isomer)** after irradiation with 470 nm light for 30 min. 103

Figure 3.7 ^{13}C NMR (100 MHz, Methanol-d_4) **PAH-2** 104

Figure 3.8 NMR spectra of **PAH-2** (9 mM in **DMSO-*d*$_6$**) during thermal relaxation (only aromatic region shown for clarity). Herein, only two species are observed, **MCH$^+$** (shown by green solid box) and the **SP** isomer (shown by red dotted box). The doublet peaks at 8.62 and 7.81 have *J* constants of 16.1 and 16.0, respectively, consistent with a *trans* alkene for the **MCH$^+$** isomer. Whereas the peaks at 7.00 and 5.78 have *J* constants of 10.2 consistent with a *cis* alkene, coupled with the absence of the hydroxy group (not shown in this NMR, see Figure 3.6) suggests that the **SP** isomer is present. Although it is understood that mechanistically, a *cis-trans* isomerization is necessary for the photoacid to switch between states, these findings where only two species are observed is consistent with previous literature of this class of mPAHs.[21] 105

Figure 3.9 Determination of the molar extinction coefficient in **DCM**. Samples ranging from 2.0 x 10^{-5} to 5.0 x 10^{-5} M were freshly prepared and measured. The **λ_{max}** was determined to be at **λ = 453 nm**. 106

Figure 3.10 The absorbance of the samples from **Figure 3.9** was plotted versus concentration and the molar extinction coefficient was determined to be ≈**20400 L mol^{-1} cm^{-1}.** 107

Figure 3.11 Comparison of **PAH-1** and **PAH-2** in **DCM** demonstrating that the structural modifications do not result in a significant shift in the λ_{max}. The solution for **PAH-1** was prepared by mixing a supersaturated solution, irradiating the sample with 470 nm light, and

allowing to relax thermally. The dispersion was allowed to settle and a sample of the supernatant was taken and measured via UV-Vis. **PAH-2** was prepared at **5.0 x 10^{-5} M** in **DCM**. 108

Figure 3.12 Comparison of **PAH-1** and **PAH-2** in **methanol** demonstrating that the structural modifications do not result in a significant shift in the λ_{max}. The solution for **PAH-1** was prepared at **5.0 x 10^{-5} M** in **methanol**. **PAH-2** was prepared at **1.0 x 10^{-4} M** in **methanol**. 109

Figure 3.13 UV-Vis spectra of **PAH-2** in **DCM (5.0 x 10^{-5} M)**. The sample was prepared and allowed to equilibrate for 2 h before UV-Vis spectra was collected. The trace labeled 'dark' is from the sample taken at equilibrium, while the 'irradiated' sample was collected after irradiating with 470 nm light for 4 min and the photostationary state achieved at ~46% (**Figure 3.20**). 110

Figure 3.14 UV-Vis spectra of **PAH-2** in ***p*-xylene (saturated)**. The supersaturated sample was prepared and allowed then irradiated for 30 min using 470 nm light. The sample was then allowed to equilibrate for 3 h and a sample of the supernatant was collected, and passed through a 0.45 micron filter before UV-Vis spectra was collected. The trace labeled 'dark' is from the sample taken at equilibrium, while the 'irradiated' sample was collected after irradiating with 470 nm light for 3 min and the photostationary state achieved. 111

Figure 3.15 UV-Vis spectra of **PAH-2** in **MeCN (1.5 x 10^{-4} M)**. The sample was prepared and allowed to equilibrate for 3 h before UV-Vis spectra was collected. The trace labeled 'dark' is from the sample taken at equilibrium, while the 'irradiated' sample was collected after irradiating with 470 nm light for 3 min and the photostationary state achieved. 112

Figure 3.16 UV-Vis spectra of **PAH-2** in **THF (2.0 x 10^{-4} M)**. The sample was prepared and irradiated with 470 nm for 15 min and then allowed to equilibrate for 2 h before UV-Vis spectra

was collected. The trace labeled ‘dark’ is from the sample taken at equilibrium, while the ‘irradiated’ sample was collected after irradiating with 470 nm light for 3 min and the photostationary state achieved. 113

Figure 3.17 UV-Vis spectra of **PAH-2** in **methanol (1.0 x 10^{-4} M)**. The sample was prepared and allowed to equilibrate for 16 h before UV-Vis spectra was collected. The trace labeled ‘dark’ is from the sample taken at equilibrium, while the ‘irradiated’ sample was collected after irradiating with 470 nm light for 3 min and the photostationary state achieved. 114

Figure 3.18 A) 3.5 x 10^{-4} M solution of **PAH-1** (left) and **PAH-2** (right) in **THF**. B) 5.2 x 10^{-4} M solution of **PAH-1** (left) and **PAH-2** (right) in **acetone**. C) 5.2 x 10^{-4} M solution of **PAH-1** (left) and **PAH-2** (right) in **acetonitrile**. D) 5.2 x 10^{-4} M solution of **PAH-1** (left) and **PAH-2** (right) in ***p*-xylene**. 115

Figure 3.19 Home built UV-Vis pump probe setup. 117

Figure 3.20 PAH-2 in **DCM (5.0 x 10^{-5} M, λ_{max} = 453)** initial 2 min in dark to establish equilibrium state, followed by 4 min of irradiation with 470 nm light with a scan taken every 4 s. The sample was then monitored in the dark with a scan taken every 4 s for 5 min before being irradiated again for 4 min. The final dark recovery cycle was monitored for 10 min. The photoirradiation is denoted by the gray boxes. 118

Figure 3.21 PAH-2 in ***p*-xylene (2.2 x 10^{-4} M, λ_{max} = 441)** initial 3 min in dark to establish equilibrium state, followed by 2 min of irradiation with 470 nm light with a scan taken every 4 s. The sample was then monitored in the dark with a scan taken every 4 s for 10 min before being irradiated again for 2 min. This cycle was repeated three times. The final dark recovery cycle was monitored for an additional 10 min. The photoirradiation is denoted by the gray boxes. 119

Figure 3.22 PAH-2 in **MeCN (8.0 x 10^{-5} M, λ_{max} = 419)** initial 3 min in dark to establish equilibrium state, followed by 6 min of irradiation with 470 nm light with a scan taken every 4 s. The sample was then monitored in the dark with a scan taken every 12 s. Zoom in on first 15 min of sample (insert) to highlight the initial equilibrated state and photoirradiation (gray box). 120

Figure 3.23 PAH-2 in **THF (3.9 x 10^{-4} M, λ_{max} = 440)** initial 3 min in dark to establish equilibrium state, followed by 8 min of irradiation with 470 nm light with a scan taken every 6 s. The sample was then monitored in the dark with a scan taken every 12 s. Zoom in on first 15 min of sample (insert) to highlight the initial equilibrated state and photoirradiation (gray box). 121

Figure 3.24 PAH-2 in **MeOH (1.0 x 10^{-4} M, λ_{max} = 439)** initial 3 min in dark to establish equilibrium state, followed by 3 min of irradiation with 470 nm light with a scan taken every 6 s. The sample was then monitored in the dark with a scan taken every 60 s. Zoom in on first 15 min of sample (insert) to highlight the initial equilibrated state and photoirradiation (gray box). 122

Figure 3.25 Correlating half-life of the dark recovery of **PAH-2** with the Taft-Kamlet β values of different solvents. The blue circles correspond to the half-lives interpolated from the model fitted to the data collected *via* UV-Vis spectroscopy presented above. The orange squares correspond to half-lives extrapolated to 22 °C from NMR data presented in the next section. 123

Figure 3.26 PAH-2 in **50 wt% ε-caprolactone/DCM (1.5 x 10^{-4} M, λ_{max} = 442)** initial 3 min in dark to establish equilibrium state, followed by 3 min of irradiation with 470 nm light with a scan taken every 6 s. The sample was then monitored in the dark with a scan taken every 60 s.

Zoom in on first 15 min of sample (insert) to highlight the initial equilibrated state and photoirradiation (gray box). The equilibrium state after irradiation lies at 75% of the MCH^+ isomer..... 124

Figure 3.27 Stack of ^{1}H-NMR spectra showing various stages of switching from the open to the closed form of **PAH-1** in **DMSO** at 45 °C. Peaks labeled **MCH$^+$** and **SP**, respectively, were used for calculations according to **Equation 3.2**..... 126

Figure 3.28 Stack of ^{1}H-NMR spectra showing various stages of switching from the open to the closed form of **PAH-2** in **DMSO** at 30 °C. Peaks labeled **MCH$^+$** and **SP**, respectively, were used for calculations according to **Equation 3.2**..... 127

Figure 3.29 9mM solutions of **PAH-1** in **DMSO-d_6** monitoring the recovery of the MCH^+ isomer over time at varying temperatures in the NMR. The red dotted line is the model fit using the dynamic equilibrium model **Equation 3.1**. 128

Figure 3.30 Arrhenius plot of the rate constants of **PAH-1** in **DMSO-d_6**. The square data points are the $k_{forward}$ values and the circle data points are the $k_{reverse}$ values..... 129

Figure 3.31 9mM solutions of **PAH-2** in **DMSO-d_6** monitoring the recovery of the MCH+ isomer over time at varying temperatures in the NMR. The red dotted line is the model fit using the dynamic equilibrium model (**Equation 3.1**)..... 130

Figure 3.32 Arrhenius plot of the rate constants of **PAH-2** in **DMSO-d_6**. The square data points are the $k_{forward}$ values and the circle data points are the $k_{reverse}$ values..... 131

Figure 3.33 Control experiment demonstrating that photoirradiation is necessary for polymerization to occur. Each sample was prepared according to the procedure described on page S5. An NMR was taken immediately after sample was prepared and then 24 h later with the sample kept in the dark. No NMR changes can be observed in any of the samples. A) PAH-

1 in propylene carbonate, B) PAH-2 in propylene carbonate, C) PAH-1 in DCM, D) PAH-2 in DCM. 132

Figure 3.34 UV-Vis sample of **PAH-2** in polymer mixture of 50 wt% ε-caprolactone in DCM. First sample (black tracing) was irradiated for 3 minutes and then monitored as the sample thermally equilibrated at room temperature. An equivalent sample was irradiated for 8 hours (gray tracing) and similarly monitored as it thermally equilibrated at room temperature as well. As observed here, both sample equilibrate to the same state regardless of irradiation time suggesting there is no photodegradation to the mPAH in solution during the long irradiative periods. 133

Figure 3.35 GPC tracings (in THF) of polycaprolactone over time of ROP using **PAH-2** in **DCM** under constant irradiation. 134

Figure 3.36 Plot of molecular weight and dispersity (by GPC in THF) versus time of ROP of caprolactone using **PAH-2** in **DCM** under constant irradiation. 134

Figure 3.37 GPC tracings (in THF) of polycaprolactone over time of ROP using **PAH-1** in **propylene carbonate** under cycles of irradiation and dark 8 h periods..... 135

Figure 3.38 Plot of molecular weight and dispersity (by GPC in THF) versus time of ROP of caprolactone using **PAH-1** in **propylene carbonate** under 8 h cycles of irradiation and dark periods. Condition: [BnOH]:[PAH]:[ε-CL] = 1:0.25:50. 135

Figure 3.39 GPC tracings (in THF) of polycaprolactone over time of ROP using **PAH-2** in **propylene carbonate** under cycles of irradiation and dark 8 h periods. Condition: [BnOH]:[PAH]:[ε-CL] = 1:0.25:50. 136

Figure 3.40 Plot of molecular weight and dispersity (by GPC in THF) versus time of ROP of caprolactone using **PAH-2** in **propylene carbonate** under 8 h cycles of irradiation and dark periods. Condition: [BnOH]:[PAH]:[ε-CL] = 1:0.25:50. 136

Figure 3.41 GPC tracings (in THF) of polycaprolactone over time of ROP using **PAH-1** in **DCM** under cycles of irradiation and dark 8 h periods. Condition: [BnOH]:[PAH]:[ε-CL] = 1:0.1:100. 137

Figure 3.42 Plot of molecular weight and dispersity (by GPC in THF) versus time of ROP of caprolactone using **PAH-1** in **DCM** under 8 h cycles of irradiation and dark periods. Condition: [BnOH]:[PAH]:[ε-CL] = 1:0.1:100. [a]Molecular weight of 8 and 12 h conversion were undeterminable by GPC, given molecular weight is estimated by NMR conversion, 8% and 11% respectively (denoted by green squares)..... 138

Figure 3.43 GPC tracings (in THF) of polycaprolactone over time of ROP using **PAH-2** in **DCM** under cycles of irradiation and dark 8 h periods. Condition: [BnOH]:[PAH]:[ε-CL] = 1:0.1:100. 139

Figure 3.44 Plot of molecular weight and dispersity (by GPC in THF) versus time of ROP of caprolactone using **PAH-2** in **DCM** under 8 h cycles of irradiation and dark periods. Condition: [BnOH]:[PAH]:[ε-CL] = 1:0.1:100. 139

Figure 4.1 Polymerization kinetics study of Krasol-initiated ring-opening polymerized, catalyzed by camphorsulfonic acid. (a) Monomer conversion is monitored via NMR and (b) SEC traces highlight the formation of the triblock by a monotonic increase in Mn. 146

Figure 4.2 CSA initiated chain extenstion. a) DOSY NMR spectra showing great agreement in diffusivity between a characteristic p4mCL peak and a characteristic Krasol peak. b) Intensity

normalized gradient-strength resolved decay of both signals demonstrating the agreement in diffusion. 147

Figure 4.3 a) Reaction scheme depicting the crosslinking of the preformed tri-block with varying amounts of crosslinker. b) Freestanding, elastic solids of the crosslinked triblock with increasing amounts of the bis-lactone crosslinker. 149

Figure 4.4 a) HTPB, caprolactone monomer, and di-lactone crosslinker (1:12:2.5 molar equivalents respectively) mixture containing mPAH (1wt%) as catalyst under 470 nm irradiation at 50 °C. b) Post irradiation; un-irradiated sections are not crosslinked and are able to flow readily, leaving behind fully crosslinked photopatterned section. c) Freestanding photopatterned sample. 150

Figure 4.5 Preliminary experiments demonstrating the ability of the network to reform after being damaged via simple molding at elevated temperatures. a) Sample was cut into pieces using a razor blade post crosslinking and drying. b) Using a Carver Press, sample was annealed for 1 h at 100 °C and 4 metric tons of pressure. c) After being reprocessed, sample is a homogenous, free standing sample with no noticeable macroscopic defects. 152

Figure 4.6 Superimposed size-exclusion chromatography (SEC) traces of commercially available HTPB and Krasol. 153

Figure 4.7 Stacked NMR spectra corresponding to a) homopolymer Krasol, b) homopolymer p4mCL, and c) a reaction between Krasol and 4mCL monomer. The two peaks used for independent calculation of diffusivities, Krasol in orange and 4mCL in blue, (via DOSY NMR) and highlighted above in **Figure 4.2**. Insets on (a) and (c) demonstrate the hydrogen peaks alpha to the hydroxy end groups that allow for facile characterization. 154

Figure 4.8 DOSY NMR spectra showing peak signals for p4MCL and HTBP corresponding to different diffusivities with an inset highlighting the gradient-strength resolved decay of signal from two peaks (corresponding to p4MCL and HTPB) showing distinctly different diffusivities. 155

Figure 4.9 TBD initiated chain extenstion. a) DOSY NMR spectra showing great agreement in diffusivity between a characteristic p4mCL peak and a characteristic Krasol peak. b) Intensity normalized gradient-strength resolved decay of both signals demonstrating the agreement in diffusion. 156

Figure 4.10 ^{1}H-NMR of newly designed bis-lactone crosslinker with corresponding structure. 157

Figure 4.11 ^{13}C-NMR of newly designed bis-lactone crosslinker with corresponding structure. 158

LIST OF TABLES

Table 2.1. Physical and chemical properties of poly(Ils) studied in this chapter. [a]ΔE values are depicted as the forward reaction being the dissociation of the ion-ion interactions as described in the short discussion of **Scheme 2.2**, where the stronger the interaction the larger the value and the weaker the interaction the smaller (more negative) the value. [b] For reference, the N-H bond length calculated with no counterion present. [c]Values given in parentheses are adapted from reference 46. 32

Table 2.2 Raw data collected from fitting the PFG-NMR diffusion spectra for **aPy-TFSI**. Conductivity calculated using Nernst-Einstein equation (**Equation 2.1**). 75

Table 2.3 Raw data collected from fitting the PFG-NMR diffusion spectra for **aPy-DFA**..... 76

Table 2.4 Conductivity for pPy-DFA calculated using data from **Table 2.3** and Nernst-Einstein equation (**Equation 2.1**). 76

Table 2.5 Raw data collected from fitting the PFG-NMR diffusion spectra for **aPy-MFA**..... 77

Table 2.6 Conductivity for pPy-MFA calculated using data from **Table 2.5** and Nernst-Einstein equation (**Equation 2.1**) 77

Table 4.1 Sol-gel results for crosslinked tri-block solids referred to in **Figure 4.3**..... 149

LIST OF SCHEMES

Scheme 1.1 Reaction scheme between hydrochloric acid and ammonia demonstrating the concept of conjugate acid-base pairs. 3

Scheme 1.2 Depiction of resonance structure contributions of the conjugate base of a) a carboxylate anion and b) a sulfonate anion. 7

Scheme 1.3 Schematic depicting the effect on induction on the acidity of a series of acetic acids and halogenated acetic acids. a) The pK_a drastically decreases over 4.5 orders of magnitude when fluorine (the strongest electronegative atom) is exchanged in place of hydrogens. b) The induction pattern demonstrating the pull of the electron density away from the oxygen into the fluorines. c) Series of increasing electronegativity from left to right and its effect from substituting one atom. 8

Scheme 1.4 Generic nucleophilic acyl substitution scheme. (Picture adapted from Wikipedia.com) 9

Scheme 1.5 Examples of common ionic liquid a) cations, and b) anions. c) Distinguishing feature between a protic vs aprotic ionic liquid is the presence of the labile proton on the cation. ... 12

Scheme 1.6 Examples of each type of pH altering photoswitch. a) triphenylsulfonium triflate, a photoacid generator, b) pyranine, a photoacid, c) merocyanine photoacid, a meta-stable photoacid. 13

Scheme 1.7 Initiation step of a cationic polymerization of a carbon-carbon double bond (olefin). 14

Scheme 1.8 Activated monomer cationic ring-opening polymerization propagation step, where the hydroxyl end group of the propagating polymer attacks the electrophilic, Brønsted acid activated monomer. 15

Scheme 2.1. a) Synthetic scheme of the parent polymer used in this study. b) Range of acids used in this study arranged by subclass..... 30

Scheme 2.2 Depiction of ion association utilized in DFT calculations to determine the energy of free vs ion-paired ionic liquid motifs. On the left side of the reaction scheme, depicted is the direction interaction between the protic cation and the anion. For the protic series, the lowest energy confirmation, was the anion participating in a hydrogen bond to the cation. On the right side of the equation depicts if the hydrogen bond is broken and the summation of the energy of both species is taken as the total engery for the system. The ΔE for the reaction, defined as the sum of energy of the products (right side of equation) minus the energy of the products (left side of equation), was then calculated. As written, for any ΔE value < 0, the right side of the equation is favored, i.e. free ions, whereas a ΔE value > 0 favors the ion-paired species.78

Scheme 3.1 a) Reaction scheme depicting facile synthesis from commercially available benzaldehyde derivatives. b) T-type photoswitch, forward reaction driven by photoirradiation, whereas the reverse reaction is thermally driven. (Reprinted with permission from ChemPhotoChem., 2019, 3. Copyright 2019 John Wiley and Sons.)..... 88

Scheme 4.1 Reaction scheme for the single-step synthesis of a triblock copolymer from commercially available Krasol polymer precursor. 145

Scheme 4.2 Synthetic route to novel bis-lactone crosslinker 148

LIST OF EQUATIONS

Equation 1.1 $K = [Products][Reactants]$ 4

Equation 1.2 $K = [H3O+][A-]H2O[HA]$ 4

Equation 1.3 $Ka = K[H2O] = [H3O+][A-][HA]$ 5

Equation 1.4 $Ka = [H+][A-][HA]$ 6

Equation 1.5 $[H+] = Ka[HA][A-]$ 6

Equation 1.6 $-log[H+] = -logKa - \log(HA[A-])$ 6

Equation 1.7 $pH = pKa + \log[A-]HA$ 6

Equation 1.8 $Keq = 10\Delta pKa$ 7

Equation 2.1 40

Equation 3.1 92

Equation 3.2 125

1 Introduction

1.1 The Expanding Role of Organic Chemistry

Historically, organic chemistry referred only to the study of compounds derived from living organisms. This originated from the idea of vitalism, the belief that compounds associated with living organisms could only be produced by a "vital force"[1] and could not be reproduced in a laboratory setting by a chemist. During the eighteenth and early nineteenth centuries, the carbon-based compounds isolated and studied had been extracted from plants and animals.[1] However, in the early nineteenth century, the work of two German chemists, Justus von Liebig and Friedrich Wöhler, paved the way for the emergence of organic chemistry. Liebig developed new analytical methods that allowed the precise measurement of organic compounds' compositions, that lead to the discovery of a plethora of new organic compounds.[2] Some historians dispute that vitalism really came into question when in 1828 Wöhler documented for the first time the synthesis of an organic compound, urea, from an inorganic precursor, ammonium cyanate, in a laboratory setting.[3] Later in 1845, Herman Kolbe was able to synthesize acetic acid from carbon disulfide and chlorine, definitively proving that organic compounds could be synthesized in a laboratory.[4] These discoveries are believed to have led to the birth of the field of organic chemistry as we know it today.

More recently, the American Chemical Society has expanded the definition of organic chemistry to include "the study of the structure, properties, composition, reactions, and preparation of carbon-containing compound."[5] That includes studying complex natural products and their synthetic variations, to non-natural (not obtained from biological species) man-made compounds, including polymers and plastics.[5] In addition to the discovery and cost-effective synthesis of hard

to obtain natural products and novel drug discovery in pharmaceuticals, many organic chemists now find themselves at the forefront in fields like polymer chemistry and materials science. With the expeditious advancement of technology, the need to develop new advanced functional materials and compounds with precisely engineered properties is ever-growing. The expansion of organic chemistry into these fields, allows for the preparation of new organic materials, that were previously unobtainable, to address the challenges in resource, health, and energy.

Given this brief introduction, we will now focus on the major topic of this dissertation which is the use and development of Brønsted acids in advancement of functional materials.

1.2 Defining Brønsted Acid

In 1884, the Swedish chemist Svante Arrhenius proposed two specific classifications of compounds, termed acids and bases.[6] When dissolved in an aqueous solution, certain ions were released into the solution, as defined by Arrhenius, acid-base reactions are characterized by acids, which dissociate in aqueous solution to form hydrogen ions (H^+) and bases, which form hydroxide (OH^-) ions.[6]

$$HNO_3\ (aq) + H_2O\ (l) \rightleftharpoons H_3O^+\ (aq) + NO_3^-\ (aq)$$

In the reaction presented above, nitric acid (HNO_3) disassociates into hydrogen (H^+) and nitrate (NO_3^-) ions when dissolved in water. The water molecule behaves as a proton acceptor and thus becomes a hydronium ion (H_3O^+).

$$LiOH\ (s) + H_2O\ (l) \rightleftharpoons Li^+\ (aq) + OH^-\ (aq)$$

In this reaction, lithium hydroxide (LiOH) dissociates into lithium (Li^+) and hydroxide (OH^-) ions in water. But, since not all acid-base reactions occur in water, the definition presented by Arrhenius of acids and bases is quite limited. As research into these compounds continued, new and less limited definitions arose.

In 1923, chemists Johannes Nicolaus Brønsted and Thomas Martin Lowry independently, and simultaneously, developed definitions of acids and bases based on a compound's ability to either donate or accept protons (H^+ ions).[6] Here, an acid is defined as a molecule capable of donating a proton in the form of hydrogen ions; whereas a base is defined by its ability to accept a proton. This took the Arrhenius definition one step further as water is no longer required to participate in the reaction for acid and base reactions to occur. Consider, for example, the reaction of hydrochloric acid (HCl) and ammonia (NH_3).

$$HCl\,(aq) + NH_3\,(aq) \rightleftharpoons NH_4^+\,(aq) + Cl^-\,(aq)$$

In this instance, ammonia is determined to be the base as it accepts a proton to form ammonium; meanwhile, HCl is the acid due to it donating a proton and forming a chloride ion.

1.2.1 Conjugate Acid-Base Pairs

In aqueous solutions, acids and bases can be defined in terms of the transfer of a proton, thus, for every acidic species in an aqueous solution, there exists a species derived from the acid by the loss of a proton (**Scheme 1.1)**. An acid and a base that differ by only the presence or absence of a proton are called a conjugate acid–base pair.[6] Considering again the reaction between hydrochloric

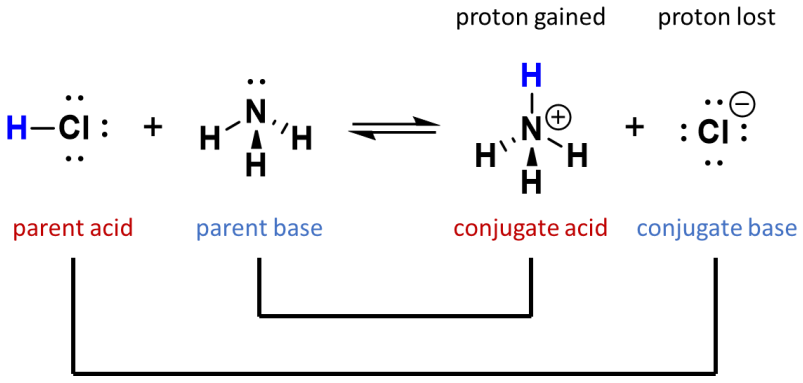

Scheme 1.1 Reaction scheme between hydrochloric acid and ammonia demonstrating the concept of conjugate acid-base pairs.

acid and ammonia, the parent acid, HCl, donates a proton to the parent base, ammonia, thereby forming Cl^-. Therefore, HCl and Cl^- constitute a conjugate acid–base pair. In the reverse reaction, the Cl^- in solution can act as a base to accept a proton from NH_4^+, forming NH_3 and HCl once again. In this case, NH_4^+ and NH_3 constitute a second conjugate acid–base pair. In general, any acid–base reaction must contain two conjugate acid–base pairs, i.e. HCl/Cl^- and NH_4^+/NH_3.

1.2.2 Acid Strength and the Acid Dissociation Constant, K_a and pK_a[7]

One of the most defining characteristics of an acid is its ability to donate protons. By definition, the stronger the acid, the better its ability to donate a proton.[6] For example, for the reaction between a generic acid (HA) and water:

$$HA\ (aq) + H_2O\ (l) \rightleftharpoons H_3O^+\ (aq) + A^-\ (aq)$$

the magnitude of the equilibrium constant can be assessed to determine the relative strength of the acid or base in the reaction. In general, the equilibrium constant for this type of dissociation is defined as:

Equation 1.1

$$K = \frac{[Products]}{[Reactants]}$$

where K is the equilibrium constant that is measured by the ratio of the concentration of the products over the concentration of the reactants.[6] For the given reaction of a generic acid and water, the equilibrium constant is written as:[6]

Equation 1.2

$$K = \frac{[H_3O^+][A^-]}{[H_2O][HA]}$$

In aqueous solutions, the concentration of water is constant so $[H_2O]$ can be incorporated into a new quantity, the acid ionization constant (K_a), also called the acid dissociation constant.[6]

Equation 1.3 $$K_a = K[H_2O] = \frac{[H_3O^+][A^-]}{[HA]}$$

Given that the K_a is the ratio of the concentration of products over reactants, for a strong acid, the ratio can become increasingly larger proportional to the strength of the acid, as the numerator increases due to the formation of the dissociated product and the denominator approaches zero as the acid dissociates. For example, in the case of HCl and water:

$$HCl\ (aq) + H_2O\ (aq) \rightleftharpoons H_3O^+\ (aq) + Cl^-\ (aq)$$

HCl is observed to dissociate 100% in water.[6] The K_a value is large, $K_a = \sim 10^7$, indicating the equilibrium position lies far to the right favoring the formation of products.[6] Since all acids with $K_a > 1$ are considered to be strong acids, HCl is therefore, by definition, considered to be a strong acid.[6] Meanwhile, weak acids, or acids that do not dissociate completely in water, have a $K_a < 1$ and exhibit a greater extent of equilibrium between the products and the reactants.[6] For example, when acetic acid, CH_3COOH, is added to water, only a small fraction will dissociate.

$$CH_3COOH\ (aq) + H_2O\ (aq) \rightleftharpoons H_3O^+\ (aq) + CH_3COO^-\ (aq)$$

This strong vs. weak distinction is of great importance as is it the basis of creating a buffer solution, which is a cornerstone of the mechanism in which biological systems control physiological acid-base equilibria essential for survival.[8] The importance of acid-base chemistry in physiological conditions will be discussed in more detail in Section 1.3.

A simple way of denoting the strength of an acid, and therefore the proton concentration, is by rearranging the acid dissociation constant expression, K_a, and taking the negative logarithm of both sides of the equation, **Equation 1.6**. For simplicity, H_3O^+ can be written as H^+, although it is important to keep in mind that free H^+ does not exist in aqueous solutions and that a proton is transferred to H_2O in all acid ionization reactions to form hydronium ions, H_3O^+.

Equation 1.4 $$K_a = \frac{[H^+][A^-]}{[HA]}$$

Equation 1.5 $$[H^+] = \frac{K_a[HA]}{[A^-]}$$

Equation 1.6 $$-log[H^+] = -logK_a - \log\left(\frac{[HA]}{[A^-]}\right)$$

Equation 1.7 $$pH = pK_a + \log\left(\frac{[A^-]}{[HA]}\right)$$

By the newly derived equation, the relationship between the pH of the solution and the pK_a of the constituent acid is obtained. These are important parameters to understand as they are closely intertwined and can tell us a lot about the system in question. pH is a measure of the concentration of H^+, hydrogen ions, in a solution and as described from **Equation 1.6** to **Equation 1.7** the higher the concentration of H^+ the lower the pH value measured. pH is also dependent on the concentration of the solution. This is an important distinction because it indicates that a concentrated solution of a weak acid could have a lower pH than a diluted strong acid solution. For example, concentrated acetic acid, a weak acid, could have a lower pH than a dilute solution of hydrochloric acid, a strong acid. On the other hand, pK_a is an inherent property of the molecule itself and is unaffected by concentration. Furthermore, it is important to understand that the terms "acids" and "bases" are relative terms and only refer to a molecules ability to donate or accept protons, respectively, in a given environment. For example, even a compound normally considered an acid, like acetic acid, will not be able to dissociate to donate protons if the pH of the environment is low, for example ~2, but once the pH goes above the pK_a value of said acid, for acetic acid ~4.5, then the acid will be able to dissociate. And similarly, if you have a generic base, Y, with a pK_a of 13, at pH levels < 13 it will accept protons and form HY^+, but when the pH exceeds 13, HY^+ will be deprotonated and become Y.

Additionally, pK_a values are a helpful way of comparing the Brønsted acidities of different compounds and predict in which direction, and to what extent protons will be transferred in a given reaction.[6] In other words, pK_a can be used to calculate the equilibrium constant (K_{eq}) for a reaction between any acid-base pair (**Equation 1.8**)

Equation 1.8 $$K_{eq} = 10^{\Delta pK_a}$$

where ΔpK_a is the pK_a of the product acid minus the pK_a of the reactant acid.[6]

Finally, we will cover a few key factors that affect a compound's acidity and pK_a value. Up until now, we have discussed what pK_a means, and how we can use this important parameter to help up understand reaction equilibriums, but now we will explore how the chemical structure affects a compound's ability to donate a proton. Two major factors that we will discuss here are resonance and induction effects. Resonance refers to the ability of a molecule to distribute a charge across multiple atoms in its structure.[6] This distribution helps stabilize the conjugate base, therefore facilitating proton dissociation of the parent acid.[6] The more atoms the charge is able to be distributed to, the greater the stabilization and the more acidic the compound tends to be.[6] For example, in **Scheme 1.2**, we are comparing the contributing resonance structures of the conjugate base for a) acetic acid and b) methanesulfonic acid. Acetic acid, pK_a ~4.5, is able to distribute the negative charge over its two oxygen atoms, helping stabilize the counterion. Methanesulfonic acid,

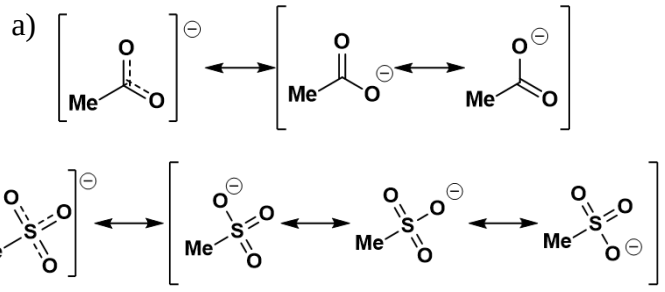

Scheme 1.2 Depiction of resonance structure contributions of the conjugate base of a) a carboxylate anion and b) a sulfonate anion.

pK_a ~−1.9, is able to distribute the charge over the three oxygen molecules, and as such demonstrates a higher acidity. Understandably, this is not a one-to-one comparison since the molecules in **Scheme 1.2** bare different functional groups, but the premise holds true throughout. The other major contributing factor is the induction effect. A compound becomes more acidic when an electronegative atom, an atom with a high affinity towards electrons, is adjacent to an acidic functional group.[6] This is because the electron density on the functional group is pulled away into the electronegative atoms thus making the compound more acidic (**Scheme 1.3**).[6] All in all, anything which helps stabilize the conjugate base will increase the acidity, lower pK_a,of a compound.

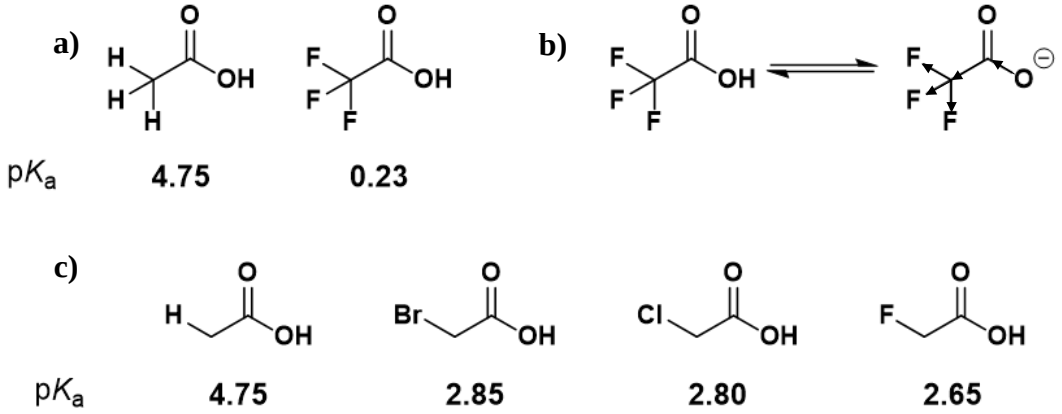

Scheme 1.3 Schematic depicting the effect on induction on the acidity of a series of acetic acids and halogenated acetic acids. a) The pK_a drastically decreases over 4.5 orders of magnitude when fluorine (the strongest electronegative atom) is exchanged in place of hydrogens. b) The induction pattern demonstrating the pull of the electron density away from the oxygen into the fluorines. c) Series of increasing electronegativity from left to right and its effect from substituting one atom.

1.3 The role of Brønsted Acids in Organic Chemistry

Acid-base reactions are one of the most fundamental processes known to humankind. These reactions are ubiquitous across many different disciplines and areas of our daily lives including a

variety of biological applications, such as buffer systems[8] and pharmaceutical drug delivery[9], as well as in nascent technologies throughout material science[10], such as solid-state electrolytes in proton-exchange fuel membrane cells[11]. Although we could cover a wide range of applications of Brønsted acids in many fields, the introduction to this dissertation will mainly focus on the use of Brønsted acids used in polymeric ionic liquids[12], photoacids[13], and polymerization[14] and vitrimer catalysis[15]. Before discussing these, we will briefly describe some fundamental concepts of Brønsted acids in these contexts.

One of the main uses of Brønsted acids in organic chemistry is as an activating agent for substitution reactions.[6] Generally, a substitution reaction occurs between a nucleophile, or electron donator, and an electrophile, an electron acceptor, to form a new covalent bond.[6] Brønsted acids can catalyze these reactions by increasing the electron affinity of the electrophile.[6] This allows for a more efficient attack by the nucleophilic species by pulling even more of the electron density away from the electrophilic center. To highlight this point, one can consider a nucleophilic acyl substitution (**Scheme 1.4**). The reaction begins by the addition of the Brønsted acid into the reaction mixture, creating an acidic environment that activates the electrophile (Step 1). The carbonyl oxygen is protonated by the donated H^+ ion. This positively charged oxygen pulls the electron density away from the electrophilic carbonyl lowering the energy barrier necessary to allow for nucleophilic attack. A nucleophile, denoted as H-Z in **Scheme 1.4**, is then able to donate a pair of electrons (Step 2), forming a new covalent bond. Through a series of proton transfers, the

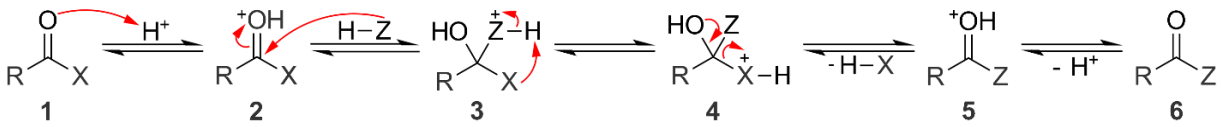

Scheme 1.4 Generic nucleophilic acyl substitution scheme. (Picture adapted from Wikipedia.com)

initial functional group, X, at the acyl site is eliminated (Step 4), and the carbonyl bond is reformed (Step 5). The acidic proton is then removed giving rise to a new acyl compound (Step 6). The strength of the acid, as determined by the acid's pK_a, dictates how efficiently it can catalyze reactions.[6] Some functional groups are harder to protonate, such as carboxylic acids or ketones[6], so having stronger acids, promotes higher H^+ ion concentrations creating a more acidic environment helping catalyze such transformations.

As alluded to previously, not only are acid-base reactions relevant in a chemistry classroom context, but the principles of acid-base equilibria are pertinent in living organisms. One example of this is the ability to control the pH of one's blood which is critical for survival.[8] On average, the pH of human blood is ~7.4.[8] A shift in the pH level by ± 0.2 units is enough to cause severe illness, and a shift of ± 0.4 is often fatal.[8] The human body is able to regulate any drastic shifts by employing a buffer system in the blood serum.[8] A buffer system is the balance between a weak acid and its conjugate base, where both species are present in appreciable amounts. As such, any buildup of either acidic or alkalotic (basic) species are able to be neutralized by the blood preventing large shifts in the body's pH.[8] Additionally, research in emerging pharmaceutical therapies focuses on targeted drug delivery/release.[9] One of the major limitations in some current therapies, such as cancer treatment, is the widespread distribution of the chemical throughout the entire body.[16] Although effective, many undesired side effects are due to this uncontrolled release. It has been found that many tumors and masses caused by some cancers actually have a lower pH environment, higher acid concentration, than the normal physiological pH.[17] So, much effort is focused on trying to take advantage of this feature and designing drugs that will remain intact at normal human body pH, but once they enter the area where these tumors or masses are active with

lower pH, a selective drug release will ensue.[17] This will hopefully increase efficiency of such treatments while mitigating many of the undesirable side effects.

1.3.1 Defining Polymeric Ionic Liquids

Ionic liquids (ILs) are a class of compounds composed entirely of ion pairs, with a melting point below 100 °C.[18] They are highly coveted due to their advantageous set of physicochemical properties including having negligible vapor pressure, wide liquid range, low flammability, high ionic and thermal conductivity, wide electrochemical potential window, and excellent thermal and chemical stability.[19] Through careful selection of the constituent cation and anion pairs, the distinctive properties can be tailored for a wide variety of different applications. ILs are able to melt at relatively low temperatures (< 100 °C) as opposed to conventional ionic species, (i.e., sodium chloride, NaCl, m.p. ~ 800 °C) due to the nature of the ions involved.[20] ILs are typically large and bulky, and have diffuse charges associated with each ion.[18] The diffuse nature of the charges, either by aromaticity or resonance, helps reduce the interionic forces between the cation and anion.[12] The bulkiness of the constituent ions helps furthermore disrupt the crystal lattice packing of the ions, thus significantly suppressing the melting temperatures.[21] ILs can be categorized into two major classes: protic and aprotic. Aprotic ILs (AILs) are distinguished by the lack of a labile and chemically active proton on the cationic structure and are generally quaternized by some alkylating species (**Scheme 1.5c**).[22] Protic ILs (PILs), on the other hand, are characterized by the presence of a protic hydrogen, and are readily synthesized by the neutralization reaction between a Brønsted acid and Brønsted base.[12] The inclusion of a chemically active proton in the PIL subclass imbues them with notably different chemical properties as compared to conventional AILs. The utility of PILs have been demonstrated in a wide-range of applications such as catalysis,[23] CO_2 capture,[24] pharmaceutical applications,[25] fuel processing,[26] as capacitor

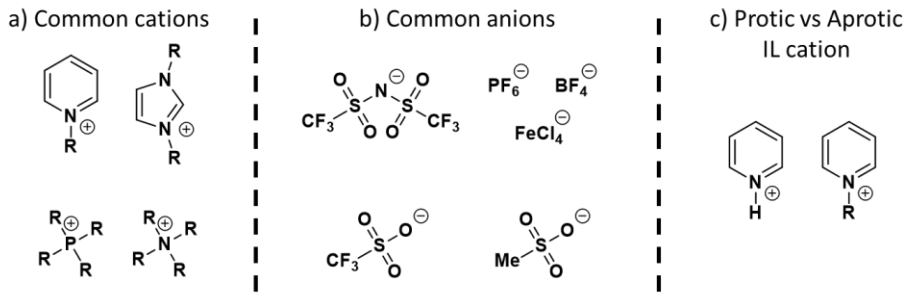

Scheme 1.5 Examples of common ionic liquid a) cations, and b) anions. c) Distinguishing feature between a protic vs aprotic ionic liquid is the presence of the labile proton on the cation.

electrolytes,[27] and, most notably, due to the presence of labile protons in their cationic structure as proton exchange membranes in fuel cells.[20,28–33] However, molecular ionic liquids are often difficult to process, and can often suffer from leakage which deteriorates the performance of the material and potentially lead to combustion.[34]

To circumvent these limitations, ILs were then placed onto polymers, creating polymeric ionic liquids (polyILs). PolyILs, are a class of materials that combine the beneficial properties of ILs with the processability, mechanical strength, and architectural variability of polymers.[22] Polymeric ionic liquids are nonflammable and therefore offer a safer, more robust alternative to ILs without compromising the physical and chemical properties of ILs.[22] The coupling of these two fields together has helped expand the utility of ionic liquids even further.

1.3.2 Overview of Photoacid Generators and Reversible Photoacids

Molecular photoswitches is a class of molecules that upon electromagnetic irradiation, undergoes a change in its geometrical confirmation that leads to drastic changes in the molecule's physicochemical properties.[35] Utilizing light as an external stimulus, allows for benign and remote activation, with high degree of spatial resolution, and control over initiation and propagation. The ability to control acid-driven processes with a high degree of both spatial and temporal control has

a) 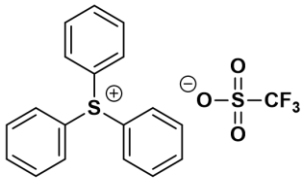 b) 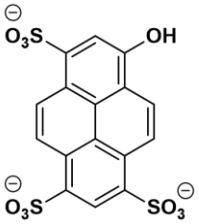 c) 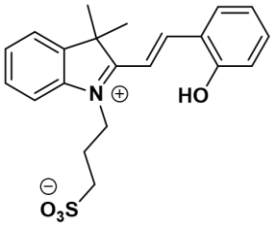

Scheme 1.6 Examples of each type of pH altering photoswitch. a) triphenylsulfonium triflate, a photoacid generator, b) pyranine, a photoacid, c) merocyanine photoacid, a meta-stable photoacid.

enabled breakthrough advances in material science,[36,37] photo-responsive systems,[38,39] and biological systems.[40–42] Photoacid generators (PAGs) are a class of molecules that undergo an irreversible, photo-induced chemical transformation that produces a strong acid, such as triflic or sulfonic acids, *in-situ* in either the solid state or in solution.[43] This class of molecules has been studied for over a century and have primarily found their utility as photo initiators for cationic polymerizations and applied in photolithography and microelectronics.[13,43] Although, not inherently a limitation of this class of materials, but as more advanced materials and applications become the goal, having a reversible pathway to turn on and off the acidic environment is highly desirable to attain complete control over the acid-driven processes.

An excited-state photoacid (PAHs), commonly referred to as simply photoacid, are molecules who have low acidity at their ground state but upon stimulation with UV irradiation, achieve a high-acidity excited state, large change in the pK_a.[13,44] The advantage these molecules possess is that this is a reversible process, since relaxation back to the ground state decreases the acidity to its original state.[45] This class of photoacids have been studied since the 1970's and have been primarily utilized to study molecular proton transfers such as in protein folding and aggregations.[2] This is possible due to the quick disassociation timescales. However, the relaxation time to the non-acidic state is also rapid, therefore it is difficult to achieve a large enough proton

concentration to provide any practical pH change.[46] For this reason, their utility in material applications has been vastly limited.

More recently, in 2011, Liao introduced another class of reversible photoacids which he coined with the term meta-stable photoacids (mPAHs)[46]. These molecules are protonated merocyanine derivatives that under visible light irradiation, reversibly produce a highly acidic state. These mPAHs are long lived and are able to produce large proton concentrations with high efficiency and reversibility. These types of photoswitches are classified as T-type[44], meaning the reverse reaction is thermally driven once the light stimulation has been removed. Since the introduction of this class of photoswitches, there have been a number of examples highlighting their utility in different applications. Liao demonstrated their ability to catalyze transesterification reactions as well as their use in a pH sensitive volume changing hydrogel.[46] Furthermore, Aprahamian showcased their use in reversibly actuating a molecular motor by the protonation/deprotonation of a hydrazone switch.[47] There are limited examples in the literature of these types of photoacids and they have primarily been designed for biological applications and aqueous media.[47–50] Missing from the literature are reversible photoacids developed for material chemistry and sciences.

1.3.3 Brønsted Acids in Polymerization Reactions and Vitrimer Exchange

In addition to the chemical transformations briefly discussed on molecular species, Brønsted acids are also useful for a handful of polymerization reactions. First, is the use of Brønsted acids in cationic polymerization of olefin compounds (**Scheme 1.7**).[51] These protic acids initiate cationic

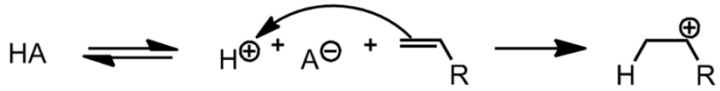

Scheme 1.7 Initiation step of a cationic polymerization of a carbon-carbon double bond (olefin).

polymerization by protonating the olefin, resulting in a secondary carbocation as the propagating species. The strength of the acid again is critical to ensure a reasonable concentration of protonated species exist to allow for efficient polymerization.[51] Additionally, it is critical that the anion (A^-) be non-nucleophilic, otherwise immediate termination would ensue inhibiting any polymerization growth.[51] Strong acids with weak nucleophilic counterions, such as perchloric, sulfuric, phosphoric, methanesulfonic, and triflic acids are all suitable options to initiate this type of reaction.[51] Monomers such as styrene, isobutylene, vinyl ethers, and butadiene are all able to be polymerized using this method.[51] The major limitation of this polymerization type is that only polymers with low molecular weights are formed with these initiators.[51] A second type of polymerization that will be relevant for this dissertation, is the cationic ring-opening polymerization. Ring-opening polymerization (ROP) is the polymerization of cyclic monomers such as cyclic ethers, acetals, lactams (cyclic amides), lactones (cyclic esters), and siloxanes.[51] Most cationic ring-opening polymerizations involve the initiation and propagation of oxonium ion centers, which involves the nucleophilic attack from the monomer onto the propagating oxonium ion on the polymer chain end.[51] On the other hand, some cationic ROPs, and specifically the one we are most interested in throughout this dissertation, proceed by a route called activated monomer polymerization (**Scheme 1.8**). In this variation, the monomer is protonated by the Brønsted acid catalyst, and the activated monomer (electrophile) is then attacked by the neutral functional chain

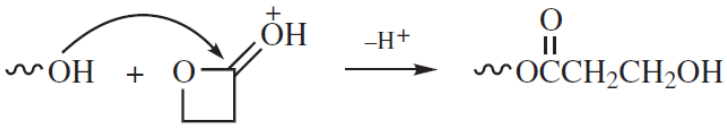

Scheme 1.8 Activated monomer cationic ring-opening polymerization propagation step, where the hydroxyl end group of the propagating polymer attacks the electrophilic, Brønsted acid activated monomer.

end of the propagating polymer.[51] More specifically, when cyclic esters, lactones, are initiated by a primary alcohol unit, the polymerization proceeds via an activated monomer mechanism, where the propagating hydroxy chain end undergoes a nucleophilic attack on a protonated monomer. This type of polymerization is advantageous since it offers the potential to suppress side reactions, is considered a living polymerizations, and can produce polymers with high molecular weights and good dispersity.[51]

Furthermore, Brønsted acid catalysis is not only useful for the initial polymerization reaction, but also are efficient catalysts for stimuli responsive materials.[50] As the name suggests, stimuli responsive materials are an ever-growing class of materials that upon the input of an external stimuli, undergo a predetermined physicochemical transformation in response.[52] The most common stimuli employed include temperature,[53] light,[54] pH,[42] mechanical,[55] electrical,[56] enzyme,[57] and redox,[58] to name a few.[52] **Figure 1.1** highlights a few examples of stimuli responsive materials that respond to physiological,[57] pH,[46], and temperature,[59] stimuli. Covalent adaptable networks (CANs) are an important subclass of stimuli responsive materials. CANs are polymer networks with covalent cross-links with the ability of adapting to an external stimulus.[60] CANs can be further subdivided into two major classes reliant on the inherent exchange mechanism, dissociative and associative cross-link exchanges.[60,61] Dissociative exchanges are characterized by the breaking of chemical bonds, which are then reformed again at another reactive site.[62] This type of exchange mechanism proceeds through a temporary loss of network integrity. On the other hand, associative networks have a fixed cross-link density throughout the covalent bond exchange since the original cross-link is only broken once a new bond at another site is formed.[63] Vitrimers are a special type of associative CAN. The distinguishing characteristic of vitrimers is the gradual viscosity decrease upon heating, a distinctive feature of vitreous silica, hence the name vitrimers.[64]

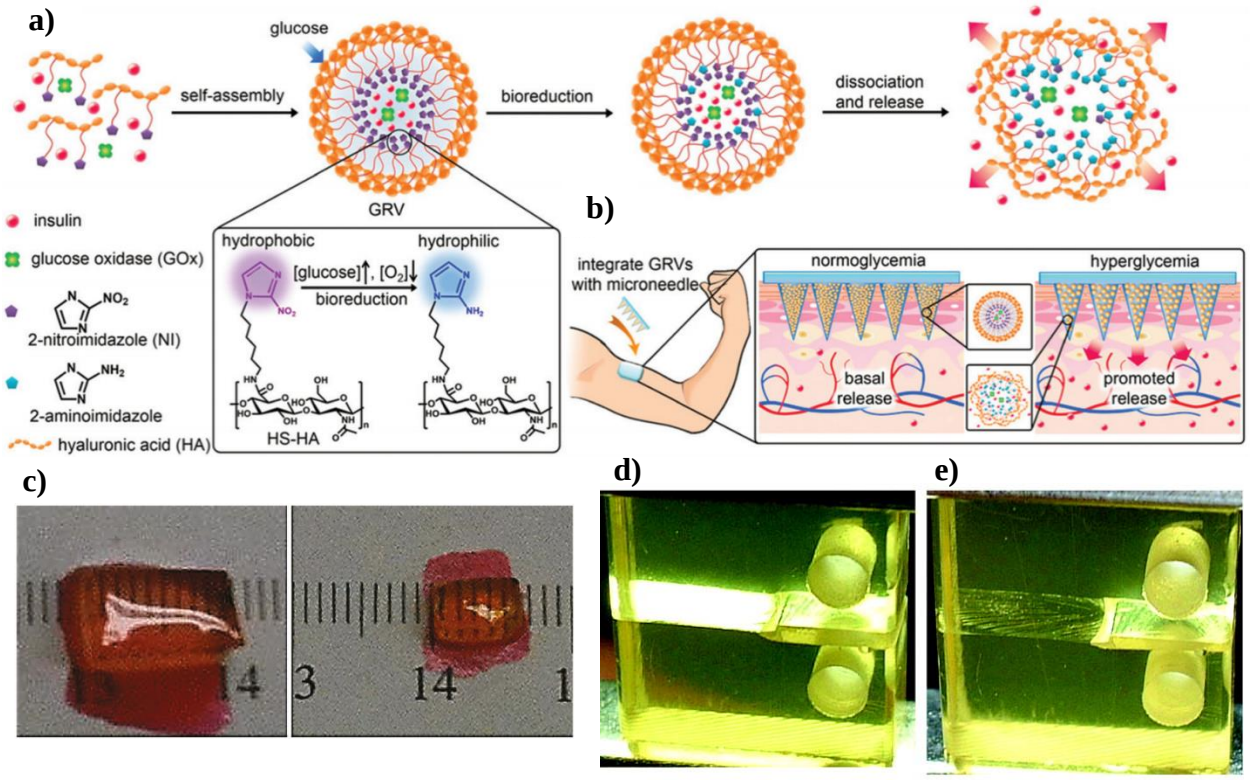

Figure 1.1 Visual examples demonstrating the vast applications of stimuli responsive materials. a) Schematic depiction of the glucose-responsive insulin delivery system using hypoxia-sensitive vesicle-loading microneedle-array patches. Formation and mechanism of glucose responsive vesicles composed of hypoxia-sensitive hyaluronic acid. b) Schematic of the glucose responsive vessicle-containing microneedle-array patch (smart insulin patch) for in vivo insulin delivery (Reprinted with permission from PNAS, 2015, 112 (Reference 57) Copyright 2018 National Academy of Sciences). c) pH sensitive hydrogel before (left) and after (right) being irradiated in a solution of a merocyanine photoacid. (The cuboid was taken out of the solution and measured on a ruler.) (Reprinted with permission from J. Am. Chem. Soc. 2011, 133 (Reference 46) Copyright 2011 American Chemical Society). d) Depiction of a thermally self-healing material, image of a broken specimen before thermal treatment. e) Image of the specimen after thermal treatment (From Science, 2002, 295 (Reference 59) Reprinted with permission from AAAS.)

At high temperatures, the viscosity is controlled by the kinetics of the chemical exchange reactions, giving an Arrhenius dependance on the thermal viscosity decrease.[63,64] Macroscopically, this manifests in the ability to self-heal and reshape the material that is controlled on a molecular level (**Figure 1.2**). Recently, the C. Bates and Read de Alaniz group demonstrated the utility of Brønsted acids in vitrimers, as not only polymerization catalysts, but also the effect of catalyst strength on polyester−alcohol dynamic covalent exchange (**Figure 1.3**).[15] Relaxation times, and activation energies are correlated with pK_a. Strong protic acids induce facile network relaxation at 25 °C on the order of 10^4−10^5 s, significantly faster than Lewis acid alternatives that function only above 100 °C.[15]

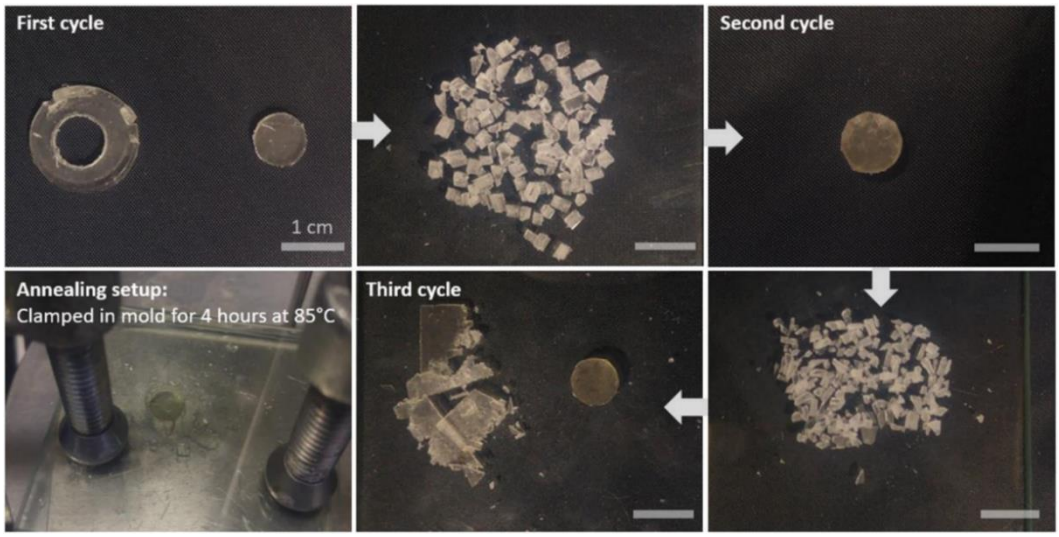

Figure 1.2 Methanesulfonic acid catalyzed polyester networks are recyclable as expected for dynamic networks that undergo associative exchange. (Reprinted with permission from ACS Macro Lett. 2018, 7 (Reference 15) Copyright 2018 American Chemical Society.)

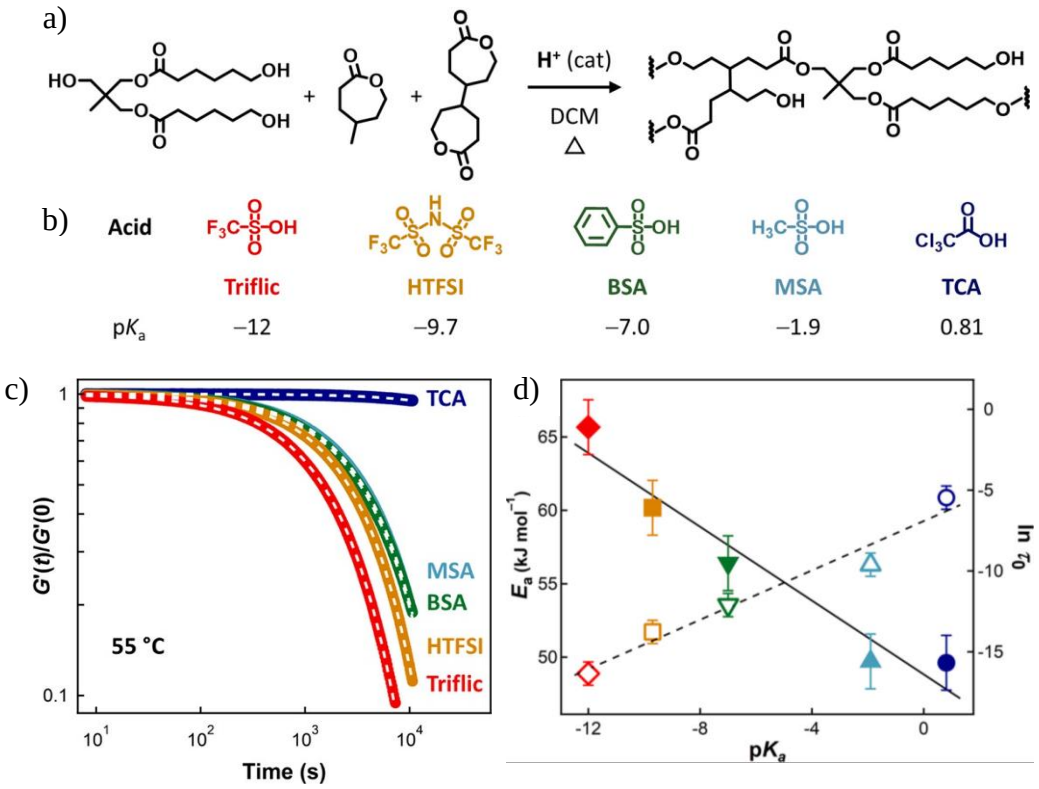

Figure 1.3 a) Schematic describing the ROP synthesis of low-T_g polyester vitrimers. b) Brønsted acid catalysts used to promote ROP and subsequent exchange reactions via transesterification. pK_a values are referenced in H_2O. c) Oscillatory rheology step-strain stress relaxation experiments on low-T_g polyester vitrimer formulations containing Brønsted acid catalysts at 55 °C. d) Activation energy (E_a filled symbols) and Arrhenius prefactor (τ_0, open symbols) are strongly correlated with Brønsted acid pK_a. (Adapted with permission from ACS Macro Lett. 2018, 7 (Reference 15) Copyright 2018 American Chemical Society.)

1.4 Outline

This dissertation will explore the utilization of Brønsted acids in studying ion pair associations and catalysis, as well as developing improved ways to control acidity in advanced materials. In Chapter 2, we begin by conducting a fundamental study on the effect of acid strength on ion conductivity in polymeric protic ionic liquids. By better understanding the physicochemical parameters that govern ion transport in these types of systems, we envision that combined with other studies, these findings will help guide the design principles associated with ion conducting membranes. In Chapter 3, we will introduce a new merocyanine based photoacid with improved organic solubility and better temporal control over the pH regulating ability. In this discussion, we characterize the photoswithes kinetics and ability to catalyze ring opening polymerizations high degree of temporal control. And finally, in Chapter 4, we explore the use of Brønsted acid catalysis to develop a platform to 3D print vitrimer composites using a commercially available macroinitiator. We cover the synthesis and characterization of this platform, and present some preliminary work of some photopatterned materials using the photoacid developed in Chapter 3.

1.5 References – Chapter 1

(1) Bechtel, Wi.; Richardson, R. C. In *Routledge Encyclopedia of Philosophy*; Taylor and Francis, Ed.; Routledge: London, 1998.

(2) Priesner, C. "Liebig, Justus Freiherr von" in: Neue Deutsche Biographie 14 (1985), pp. 497-501 [online version] https://www.deutsche-biographie.de/pnd118572741.html#ndbcontent.

(3) Wöhler, F. *Ann. der Phys. und Chemie* **1828**, *88*, 253–256.

(4) Kolbe, H. *Justus Liebigs Ann. Chem.* **1845**, *54*, 145–188.

(5) American Chemical Society. Organic Chemistry https://www.acs.org/content/acs/en/careers/chemical-sciences/areas/organic-chemistry.html.

(6) Carey, F. A.; Giuliano, R. M. *Organic Chemistry*, 8th ed.; McGraw-Hill: New York, New York, 2011.

(7) Po, H. N.; Senozan, N. M. *J. Chem. Educ.* **2001**, *78*, 1499–1503.

(8) Nelson, D. L.; Cox, M. M.; Leninger, A. L. *Lehninger Principles of Biochemistry*, 5th ed.; W.H. Freeman: New York, New York, 2008.

(9) Jazani, A. M.; Oh, J. K. *Polym. Chem.* **2020**, *11*, 2934–2954.

(10) Callister Jr, R. In *Materials Science and Engineering – An Introduction*; John Wiley & Sons, Inc., 2009; pp 5–6.

(11) Susan, M. A. B. H.; Noda, A.; Mitsushima, S.; Watanabe, M. *Chem. Commun.* **2003**, *3*, 938–939.

(12) Greaves, T. L.; Drummond, C. J. *Chem. Rev.* **2008**, *108*, 206–237.

(13) Liao, Y. *Acc. Chem. Res.* **2017**, *50*, 1956–1964.

(14) Susperregui, N.; Delcroix, D.; Martin-Vaca, B.; Bourissou, D.; Maron, L. *J. Org. Chem.*

2010, *75*, 6581–6587.

(15) Self, J. L.; Dolinski, N. D.; Zayas, M. S.; Read De Alaniz, J.; Bates, C. M. *ACS Macro Lett.* **2018**, *7*, 817–821.

(16) Nathan, D. G. *Trans. Am. Clin. Climatol. Assoc.* **2007**, *118*, 317–323.

(17) Gisbert-Garzaran, M.; Lozano, D.; Vallet-Regí, M.; Manzano, M. *RSC Adv.* **2017**, *7*, 132–136.

(18) Welton, T. *Biophys. Rev.* **2018**, *10*, 691–706.

(19) Wasserscheid, P.; Welton, T. *Ionic Liquids in Synthesis*; Wasserscheid, P., Welton, T., Eds.; Wiley-VCH: Weinheim, 2003.

(20) Smiglak, M.; Pringle, J. M.; Lu, X.; Han, L.; Zhang, S.; Gao, H.; MacFarlane, D. R.; Rogers, R. D. *Chem. Commun.* **2014**, *50*, 9228–9250.

(21) Marcus, Y. *J. Mol. Liq.* **2015**, *209*, 289–293.

(22) Singh, S. K.; Savoy, A. W. *J. Mol. Liq.* **2020**, *297*, 112038.

(23) Zhang, Q.; Yuan, H. Y.; Fukaya, N.; Yasuda, H.; Choi, J. C. *Green Chem.* **2017**, *19*, 5614–5624.

(24) Mumford, K. A.; Pas, S. J.; Linseisen, T.; Statham, T. M.; Johann Nicholas, N.; Lee, A.; Kezia, K.; Vijayraghavan, R.; MacFarlane, D. R.; Stevens, G. W. *Int. J. Greenh. Gas Control* **2015**, *32*, 129–134.

(25) Stoimenovski, J.; Dean, P. M.; Izgorodina, E. I.; MacFarlane, D. R. *Faraday Discuss.* **2012**, *154*, 335–352.

(26) Li, Z.; Xu, J.; Li, D.; Li, C. *RSC Adv.* **2015**, *5*, 15892–15897.

(27) Mayrand-Provencher, L.; Lin, S.; Lazzerini, D.; Rochefort, D. *J. Power Sources* **2010**, *195*, 5114–5121.

(28) Lee, S. Y.; Ogawa, A.; Kanno, M.; Nakamoto, H.; Yasuda, T.; Watanabe, M. *J. Am. Chem. Soc.* **2010**, *132*, 9764–9773.

(29) Snyder, J.; Fujita, T.; Chen, M. W.; Erlebacher, J. *Nat. Mater.* **2010**, *9*, 904–907.

(30) Watanabe, M.; Thomas, M. L.; Zhang, S.; Ueno, K.; Yasuda, T.; Dokko, K. *Chem. Rev.* **2017**, *117*, 7190–7239.

(31) Noda, A.; Hasan Susan, M. A. Bin; Kudo, K.; Mitsushima, S.; Hayamizu, K.; Watanabe, M. *J. Phys. Chem. B* **2003**, *107*, 4024–4033.

(32) Macfarlane, D. R.; Tachikawa, N.; Forsyth, M.; Pringle, J. M.; Howlett, P. C.; Elliott, G. D.; Davis, J. H.; Watanabe, M.; Simon, P.; Angell, C. A. *Energy Environ. Sci.* **2014**, *7*, 232–250.

(33) Khan, A.; Gunawan, C. A.; Zhao, C. *ACS Sustain. Chem. Eng.* **2017**, *5*, 3698–3715.

(34) Nie, H.; Schauser, N. S.; Dolinski, N. D.; Hu, J.; Hawker, C. J.; Segalman, R. A.; Alaniz, J. R. De. *Angew. Chemie - Int. Ed.* **2020**, *59*, 5123–5128.

(35) Pianowski, Z. L. *Chem. – A Eur. J.* **2019**, *25*, 5128–5144.

(36) Kocak, G.; Tuncer, C.; Bütün, V. *Polym. Chem.* **2017**, *8*, 144–176.

(37) Bruns, C. J.; Stoddart, J. F. *Acc. Chem. Res.* **2014**, *47*, 2186–2199.

(38) Vallet, J.; Micheau, J. C.; Coudret, C. *Dye. Pigment.* **2016**, *125*, 179–184.

(39) Kusumoto, S.; Nakagawa, T.; Yokoyama, Y. *Adv. Opt. Mater.* **2016**, *4*, 1350–1353.

(40) Balamuralidhara, V.; Pramodkumar, T. M.; Srujana, N.; Venkatesh, M. P.; Gupta, N. V.; Krishna, K. L.; Gangadharappa, H. V. *Am. J. Drug Discov. Dev.* **2011**, *1*, 24–48.

(41) Neumann, K.; Lilienkampf, A.; Bradley, M. *Polym. Int.* **2017**, *66*, 1756–1764.

(42) Zhu, Y. J.; Chen, F. *Chem. - An Asian J.* **2015**, *10*, 284–305.

(43) Martin, C. J.; Rapenne, G.; Nakashima, T.; Kawai, T. *J. Photochem. Photobiol. C*

Photochem. Rev. **2018**, *34*, 41–51.

(44) Bléger, D.; Hecht, S. *Angew. Chemie - Int. Ed.* **2015**, *54*, 11338–11349.

(45) Tolbert, L. M.; Solntsev, K. M. *Acc. Chem. Res.* **2002**, *35*, 19–27.

(46) Shi, Z.; Peng, P.; Strohecker, D.; Liao, Y. *J. Am. Chem. Soc.* **2011**, *133*, 14699–14703.

(47) Tatum, L. A.; Foy, J. T.; Aprahamian, I. *J. Am. Chem. Soc.* **2014**, *136*, 17438–17441.

(48) Abeyrathna, N.; Liao, Y. *J. Am. Chem. Soc.* **2015**, *137*, 11282–11284.

(49) Abeyrathna, N.; Liao, Y. *J. Phys. Org. Chem.* **2017**, *30*, 1–5.

(50) Wang, Z.; Liao, Y. *Nanoscale* **2016**, *8*, 14070–14073.

(51) Odian, G. *Principles of Polymerization*, 4th ed.; John Wiley & Sons, Inc.: Hoboken, NJ, USA, 2004.

(52) Wei, M.; Gao, Y.; Li, X.; Serpe, M. J. *Polym. Chem.* **2017**, *8*, 127–143.

(53) Self, J. L.; Sample, C. S.; Levi, A. E.; Li, K.; Xie, R.; de Alaniz, J. R.; Bates, C. M. *J. Am. Chem. Soc.* **2020**, *142*, 7567–7573.

(54) Kundu, P. K.; Samanta, D.; Leizrowice, R.; Margulis, B.; Zhao, H.; Börner, M.; Udayabhaskararao, T.; Manna, D.; Klajn, R. *Nat. Chem.* **2015**, *7*, 646–652.

(55) Gossweiler, G. R.; Hewage, G. B.; Soriano, G.; Wang, Q.; Welshofer, G. W.; Zhao, X.; Craig, S. L. *ACS Macro Lett.* **2014**, *3*, 216–219.

(56) Wang, H.; Yang, Y.; Zhang, M.; Wang, Q.; Xia, K.; Yin, Z.; Wei, Y.; Ji, Y.; Zhang, Y. *ACS Appl. Mater. Interfaces* **2020**, *12*, 14315–14322.

(57) Yu, J.; Zhang, Y.; Ye, Y.; DiSanto, R.; Sun, W.; Ranson, D.; Ligler, F. S.; Buse, J. B.; Gu, Z.; Ho, D. *Proc. Natl. Acad. Sci. U. S. A.* **2015**, *112*, 8260–8265.

(58) Karlsson, C.; Strietzel, C.; Huang, H.; Sjödin, M.; Jannasch, P. *ACS Appl. Energy Mater.* **2018**, *1*, 6451–6462.

(59) Chen, X.; Dam, M. A.; Ono, K.; Mal, A.; Shen, H.; Steven, R.; Sheran, K.; Wudl, F.; Science, S.; Series, N.; Mar, N.; Nutt, S. R.; Sheran, K.; Wudl, F. *Science* **2002**, *295*, 1698–1702.

(60) Kloxin, C. J.; Scott, T. F.; Adzima, B. J.; Bowman, C. N. *Macromolecules* **2010**, *43*, 2643–2653.

(61) Kloxin, C. J.; Bowman, C. N. *Chem. Soc. Rev.* **2013**, *42*, 7161–7173.

(62) Chen, X.; Wudl, F.; Mal, A. K.; Shen, H.; Nutt, S. R. *Macromolecules* **2003**, *36*, 1802–1807.

(63) Denissen, W.; Winne, J. M.; Du Prez, F. E. *Chem. Sci.* **2016**, *7*, 30–38.

(64) Montarnal, D.; Capelot, M.; Tournilhac, F.; Leibler, L. *Science* **2011**, *334*, 965–968.

2 The influence of pK_a on proton transfer and ionic conductivity in pyridinium based methacrylic polymeric protic ionic liquids

2.1 Abstract

Polymeric ionic liquids (polyILs) are an emerging class of ion-conducting polymers. The non-volatile macromolecular structure of PILs renders them as a safer alternative to the traditional ionic liquids that generally suffer from leakage and eventual system failure. Previous studies have shown that polymer segmental dynamics (approximated by T_g), polymer architecture, counterion size, ionic aggregation, and dielectric constant directly influence the ion transport of PILs. However, the effect of acid dissociation constant (pK_a) on the ion transport in polymeric protic ionic liquids (polyPILs) remains largely unexplored. En-route to better understand the factors effecting ion transport and conductivity of polyPILs we analyzed a pyridine-based methacrylate polymer with a series of Brønsted acids with a pK_a ranging from approximately −10 to 2.5. We demonstrate that when normalized for T_g effects, polyPILs synthesized with Brønsted acids with lower pK_a show higher ionic conductivity as compared to the higher pK_a analogues due to weaker ion-ion interactions. Furthermore, the ionicity of these systems are explored using pulse field gradient NMR (PFG-NMR) demonstrating the extent of proton transfer directly correlates to the ΔpK_a of the constituent acid-base pair. The measurements compared with the density field theory (DFT)-calculated ΔE values for free versus ion-paired anions correlate closely with the experimentally obtained data suggesting that pK_a can be used as metric to approximate ion pair strength/lifetime association in polyPILs.

2.2 Introduction

Ionic liquids (ILs) are a unique class of compounds comprised entirely of ions with a melting point below 100 °C.[1–4] They have garnered a considerable amount of interest due to their unique set of physicochemical properties including high ionic conductivity, negligible vapor pressure, low flammability, and high thermal and chemical stability.[5–7] Typically, ILs can be broken down into two major classes:[2,4] aprotic ILs, which do not have chemically active protons,[2,8–10] and protic ILs, which are achieved through a simple proton-transfer between Brønsted acid/base pairs.[7,11–15] Protic ILs have been utilized in a wide-range of applications such as catalysis,[16] CO_2 capture,[17] pharmaceutical applications,[18] fuel processing,[19] as capacitor electrolytes,[20] and, most notably, as proton exchange membranes in fuel cells[11,21–26] due to the presence of labile protons in their cationic structure. Covalently tethering ionic liquid species onto macromolecules, forming polymeric ionic liquids (polyILs), further improves the attractive properties and utility of ILs with increased mechanical strength, processability, and architectural variability of polymeric materials.[27–31] On the other hand, covalently linking the IL structure onto the polymer backbone has been shown to decrease the conductivity by 2-3 orders of magnitude when compared to their pure IL analogues.[32] For this reason, much research in polyILs have focused on better understanding the underlying mechanisms that govern charge transport and ionic conductivity in these systems.

Given their inherent ability to conduct ions, polyILs have been extensively studied to better understand the physicochemical properties which govern ion transport in these systems. For instance, numerous studies have demonstrated a strong correlation between the polymer segmental relaxation times (T_g) and ionic conductivity.[29] The effect of T_g on conductivity is evident in the work by Choi et. al.[33] where variations of the counterion size and side chain length lead to changes

in glass transition temperature (T_g), ionic aggregation, and dielectric constant, which directly influenced ion transport. They observed that within a set of imidazolium-based ionomers, those with larger counterions and longer side chains have lower T_g's, resulting in higher ionic conductivity and mobility. Another major contributing factor to ion mobility is its size. Iacob et. al.[34] found that decreasing the counterion volume results in T_g-independent ionic conductivities increasing over a span of ~3 orders of magnitude.

In addition to counter ion volume and T_g of the polymer, ion-pair interaction plays an integral role in ionic conductivity of PILs. Recently, our group synthesized photoresponsive aprotic polyIL materials based on diarylethene (DAE) units which were designed to undergo light-mediated conductivity changes.[35] By tuning the cationic character of the imidazolium bridging unit upon photoswitching of the DAE unit, the cation-anion interaction strength could be modulated, and thus the ionic conductivity could be controlled utilizing light irradiation. Additionally, a few studies using atomistic molecular dynamic (MD) simulations demonstrated that ion motion is seen to be correlated to the average ion-association lifetimes which quantify the dynamics of breaking and formation of ion-associations.[36–38] Chen and coworkers[39] observed enhancements in ionic conductivity in a PIL when the tetrafluoroborate (BF_4^-) anion was exchanged with the bis(trifluoromethanesulfonyl) imide ($TFSI^-$) anion. This was the result of a significant reduction in the glass transition temperature of the polymer, which facilitated higher segmental motion of the polymer and therefore higher anion mobility. Anton and co-workers[40] aptly describe the role of hydrogen bonding (H-bonding) plays on the macroscopic conductivity. In this study, they discuss how the charge transport mechanism, which is governed by thermally activated molecular fluctuations, whereas hydrogen bonding hinders fluctuations and thus reduces the DC-

conductivity. However, a specific experimental comparison evaluating the effect of pK_a association in polymeric protic ionic liquids (polyPILs) has yet to be undertaken.

Chapter 2 describes our effort to better understand the degree to which pK_a/ion association energy influences ionic conductivity in polyPILs. We propose that the pK_a, which is a well-studied metric of proton association, of the constituent acid can be used to approximate the cation-anion association lifetime/energy strength which is then directly related to the ionic conductivity. Therefore, the conjugate bases of Brønsted acids with lower pK_a's will be able to dissociate more readily and have weaker H-bonding due to their diffuse nature as compared to the conjugate base of acids with a higher pK_a. We postulate that in polyPILs the effect of this interaction and its contribution to conductivity can be explored by systematically varying a series of polyPILS doped with a series of Brønsted acids spanning a wide range of pK_a values. To test this hypothesis, we synthesized a pyridine-based methacrylate polymer (**Scheme 2.1a**) which was then mixed with 7 different Brønsted acids (**Scheme 2.1b**) spanning a pK_a range from approximately −10 to 2.5. The selected Brønsted acids can be further divided into three distinct classes: bis(sulfonimides), sulfonates, and fluorinated acetates. In this fashion, we try to account for the effect of functional group and anion size. We experimentally measure the total ionic conductivity using electrochemical impedance spectroscopy (EIS) and subsequently normalize for polymer segmental dynamics to isolate the ionic interaction. This will allow us to directly compare the effect of ionic dissociation/movement as a function of the Bronsted acid's pK_a. Additionally, pulse field gradient nuclear magnetic resonance (PFG-NMR) is utilized to track ion and molecular diffusion. Our results are further corroborated using DFT calculations by investigating the change in free energy between the free versus ion-paired anions.

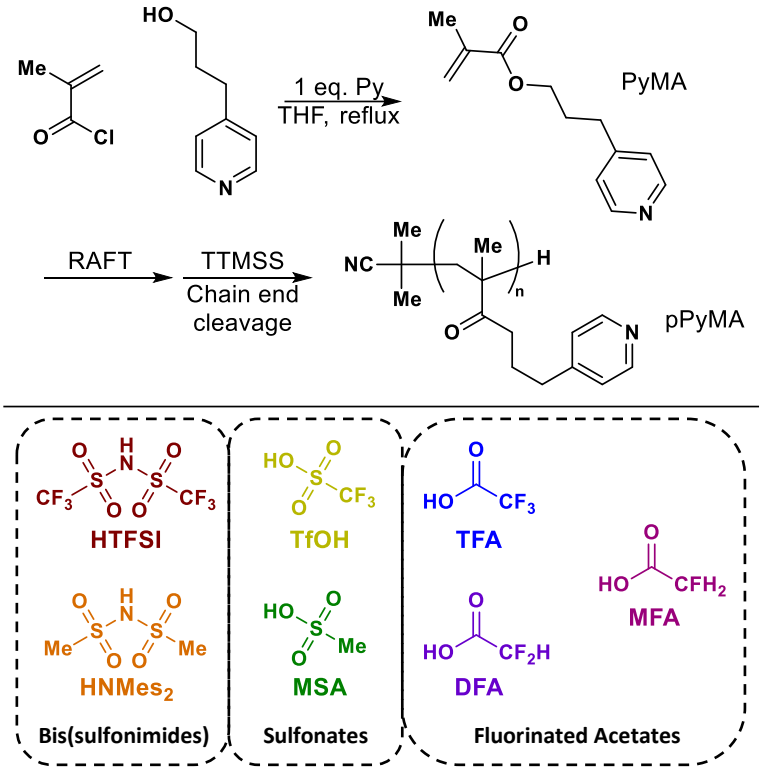

Scheme 2.1. a) Synthetic scheme of the parent polymer used in this study. b) Range of acids used in this study arranged by subclass.

2.3 Results and Discussion

The pyridine propyl methacrylate polymer was specifically chosen to help maximize the IL character of the system and minimize any potential polymer backbone-ion interactions that may interfere with intended study. To begin, we employed reversible addition-fragmentation chain transfer (RAFT) polymerization of the propyl pyridine methacrylate (PyMA) (**Figure 2.7**). Although previous studies have demonstrated good polymerization control utilizing copper mediated atom transfer radical polymerization (Cu-ATRP),[41] complete removal of the copper catalyst is not always trivial,[42] and the presence of residual metal ions could severely interfere with the intended study. Additionally, the trithiocarbonate chain end was removed to avoid any potential complications from nucleophilic elimination, due to the presence of a large excess of pyridine

units, and subsequent di-sulfide formation.[42] This was accomplished (**Scheme 2.1a**, **Figure 2.8)** through a photo-driven reduction utilizing tris(trimethylsilyl)silane (TTMSS) as the radical hydrogen source and 365 nm light irradtion.[43] The ionic conductivity, as previously discussed, is highly dependent on the segmental dynamics (measured by T_g), so choosing a polymer with moderate T_g (34 °C) was essential to allow effective measurements of ionic conductivity. Incorporating the propyl side chain was beneficial in helping decrease the T_g of the polymer to a manageable level (**Table 2.1, Figure 2.27**).[45] Since this study will focus on protic ionic liquids, which are capable of undergoing H-bonding,[46] avoiding the use of acrylamides was also critical. The amide unit is known to participate in strong H-bonding and not only does this dramatically increase the T_g of the polymer, previous studies have shown the amide functionality has a drastic effect on ionic conductivity.[44] Each polyPIL sample was prepared (see Chapter 2, section 2.5) through a simple addition of a stoichiometric equivalent of the corresponding Brønsted acid respective to the monomer repeat unit, and subsequent solvent removal. Successful incorporation of the acid was confirmed by ^{1}H and ^{19}F NMR measurements (**Figure 2.9 – Figure 2.25**). Furthermore, the stability of the polymer backbone was demonstrated by size exclusion chromatography, in where the addition of triflic acid (TfOH), one of the strongest acids utilized in this study, does not change the molecular weight nor dispersity of the polymer backbone (**Figure 2.26**).

Brønsted Acid used in PIL	T_g (°C)	T_g (aprotic) (°C)	pK_a acid	ΔE[a] (kcal/mol)	ΔE[a] (aprotic) (kcal/mol)	N-H bond Length (Å)	X-H bond Length (Å)	Anion Volume[c] (nm^3)
None	34	—	—	—	—	1.02[b]	—	—
HTFSI	31	—	−9.7[45]	−2.2	—	1.04	1.84	0.224 (0.230)
$HNMes_2$	54	—	—	4.8	—	1.07	1.65	0.184
TfOH	69	69	−9.0[45]	−0.2	−3.4	1.04	1.75	0.124 (0.126)
MSA	67	76	−1.9	4.3	−2.6	1.07	1.58	0.106 (0.099)
TFA	44	59	0.23	7.3	—	1.09	1.52	(0.103)
DFA	7	—	1.24	7.8	−2.1	1.45	1.09	0.100
MFA	−4	—	2.59	11.3	−2.6	1.53	1.05	0.099

Table 2.1. Physical and chemical properties of poly(Ils) studied in this chapter. [a]ΔE values are depicted as the forward reaction being the dissociation of the ion-ion interactions as described in the short discussion of **Scheme 2.2**, where the stronger the interaction the larger the value and the weaker the interaction the smaller (more negative) the value. [b] For reference, the N-H bond length calculated with no counterion present. [c]Values given in parentheses are adapted from reference 46.

The thermal properties were characterized using differential scanning calorimetry (DSC). The polyPILs presented glass transitions, with all, except pPy-DFA and pPy-MFA, demonstrating a melting point during the first heating cycle. No cold crystallization peaks were observed during the cooling cycles at a rate of 10 °C/min, and as such, only the glass transitions were observed for all samples on the subsequent heating runs (**Figure 2.27**). The T_g values of the studied pPILs range from −4 to 69 °C (**Table 2.1**). The general increase in T_g of the polyPILs as compared to the parent polymer can be attributed to the introduction of Coulombic interactions and H-bonding due to the formation of ionic bonds,[46] but there are a few notable exceptions to this trend. First is the use of HTFSI as the Brønsted acid. It is extensively documented in the literature that HTFSI produces molecular IL with low viscosities[47] and polyILs with lower T_g's.[51] This is due largely to the conformational flexibility of the $TFSI^-$ anion, and the rotational motion of the bulky CF_3 group leads to the creation of free volume.[48] Hunt, *et. al.*, go on to further explain that the $HNMes_2$ analogue does not demonstrate the same conformational flexibility[48] and thus can explain why the pPy-$NMes_2$ does not exhibit a similar T_g depression. The other two pPILs that significantly deviate from the observed trend are pPy-DFA and pPy-MFA. This deviation cannot be explained by conformational flexibility nor anion volume but rather the extent of proton transfer between the acid and base units. Literature precedence has proposed that in molecular ILs with low ΔpK_a values,[12,49–51] the degree of proton transfer sometimes does not proceed to the extent that is expected from ΔpK_a^{aq} data from aqueous solutions.

To probe this concept a bit further, aprotic derivatives of a select few polyIL samples were synthesized as a base for comparison. These aprotic derivatives consist entirely of ions, where the protic versions exhibit dynamic acid-base equilibria. In the case of comparing the low pK_a versions, the TfO^- derivative was utilized. Both the protic and aprotic versions demonstrated the

same T_g value of 69 °C, **Figure 2.27** and **Figure 2.28**, respectively. This can be understood that when the ΔpK_a is sufficiently large, the extent of proton transfer is to unity, and as such can be approximated to consist entirely of ions comparable to that of the aprotic derivatives.[51] On the other end of the spectrum, when ΔpK_a is small, a larger extent of equilibrium exists between the ion and neutral species, and these neutral species have a large effect on the macroscopic properties of the final material.[47] Unfortunately the aprotic DFA and MFA derivatives proved difficult to synthesize, and thus unavailable in this study for direct comparison, but the TFA and MSA versions were used to help understand the behavior at low ΔpK_a values. The protic and aprotic TFA T_g's were recorded to be 44 °C and 59 °C, respectively, and the protic and aprotic MSA T_g's were recorded to be 67 °C and 76 °C, respectively. The ΔT_g are 15 °C for TFA and 9 °C for the MSA samples. Even at these moderate ΔpK_a values, the presence of neutral species is evident, which behave as plasticizers and lower the T_g values for the protic systems. It is reasonable to believe this trend to hold true at even lower ΔpK_a values, and an even further depression of T_g values, which helps explain the drastic deviation of the pPy-DFA and pPy-MFA samples in the T_g trend. In this case, a larger extent of equilibrium exists increasing the fraction neutral species present which plasticize the system further. The extent of proton transfer as dictated by the difference in pK_a values of the constituent acid-base pair greatly influences the thermal properties of the polyPIL.

The ionic conductivities were measured using electrochemical impedance spectroscopy (EIS) under anhydrous conditions and an inert atmosphere. The conductivity measurements collected were then normalized by T_g (**Figure 2.1a**). The conductivities measured across the spectrum of polyPILs ranges from 10^{-10} to 10^{-4} S/cm in the temperature range of 25 to ca. 115 °C. To isolate the effect of pK_a on conductivity, analysis of the Brønsted acids is broken down into three classes:

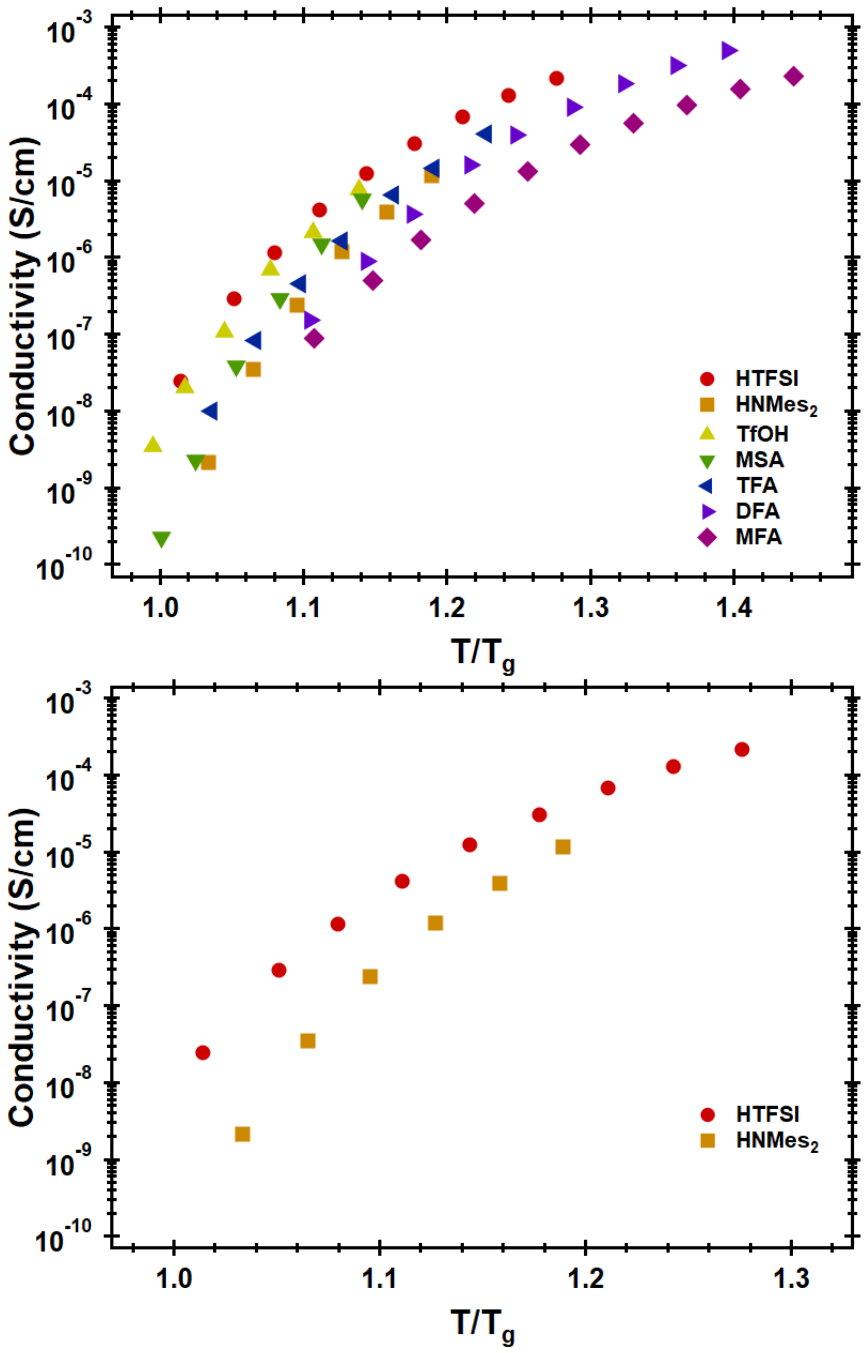

Figure 2.1 a) Compiled conductivities measured by EIS plotted in a T_g normalized manner. b) Conductivity comparison of the bis(sulfonimides).

bis(sulfonimides), sulfonates, and fluorinated acetates, where the functional acidic groups are kept consistent, while attempting to minimize any variations in anion volume and structure. Looking at the first class of acids, the bis(sulfonimides), pPy-TFSI and pPy-$NMes_2$, where there is a large difference in pK_a's (approximated through difference in calculated ΔE values) but keeping the anion confirmation and volume as similar as possible, there is an appreciable difference in ionic conductivity throughout the entire measured temperature range. The pPy-TFSI sample ($pK_a \sim -10$) has an upwards of 2 order of magnitude improvement in T_g normalized conductivity as opposed to the pPy-$NMes_2$ polyPIL (**Figure 2.1b**). At higher temperatures, the conductivities begin to converge, diminishing the enhancement to about 3 times increase. The diminished difference at higher temperatures is thought to be attributed to the overcoming of intermolecular interactions, namely H-bonding, due to the increased thermal energy input into the system. The increased energy can break hydrogen bonds that tie the cation and anion together which will then facilitate the anion movement independent of the ΔpK_a of the system. An almost identical trend is also noted when comparing the sulfonates, pPy-TfO and pPy-MS, where at lower temperatures, over an order of magnitude difference in noted, which then converges to an almost similar conductivity at elevated temperatures (**Figure 2.30**). Interestingly, this method is even able to record differences when the difference in pK_a of the acid utilized is small. This is evident in the fluorinated acetate series of this study where the change in pK_a from the strongest of this set, TFA, to the weakest, MFA, only differs by ~2 pK_a units. **Figure 2.31** demonstrates an approximate 1 order of magnitude increase in conductivity across the temperature spectrum recorded. Considering the entire set of acids tested in this study, when normalized at a specified T/T_g, a very apparent trend is observed when comparing the conductivities of the polyPILs as a function of the aqueous pK_a of the

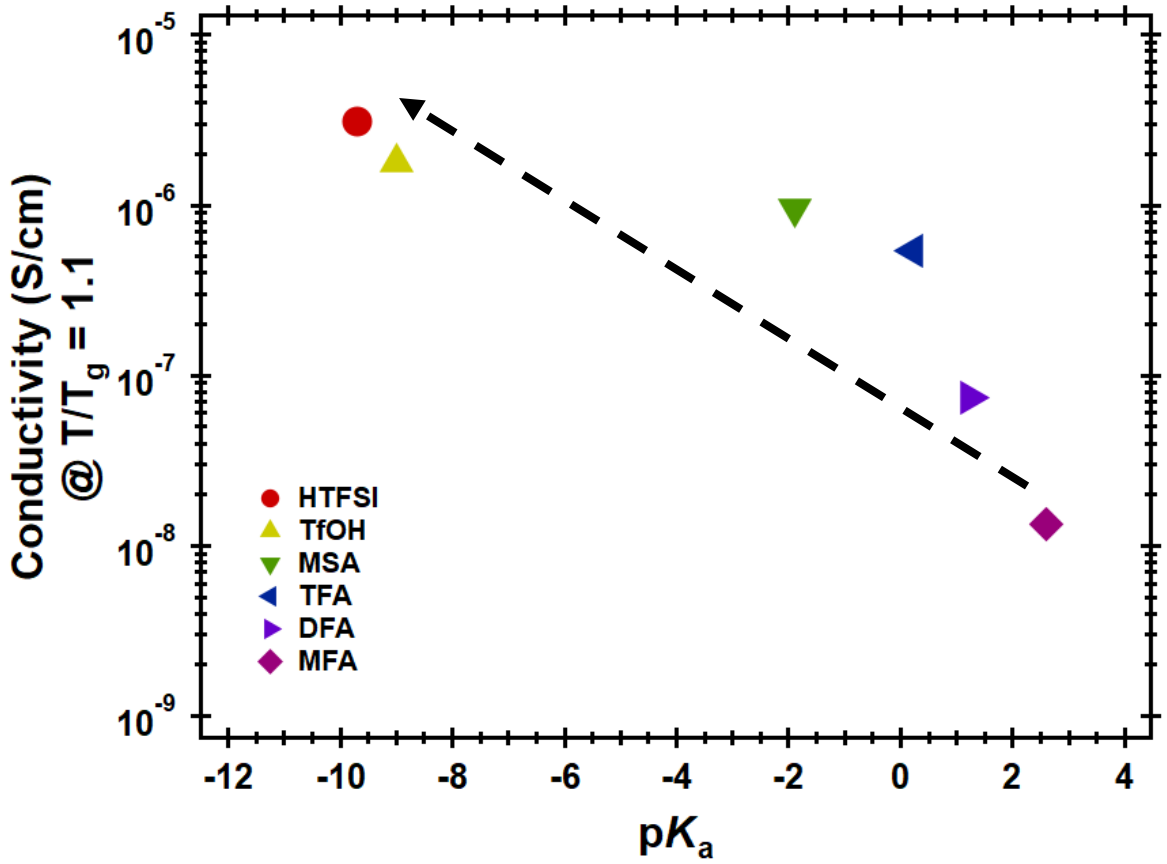

Figure 2.2 T_g normalized conductivities as a function of aqueous pK_a values at a specified T/T_g. Black dashed arrow added to suggest the correlation of pKa and conductivity.

Brønsted acid (**Figure 2.2**). An increase of over 200 times the conductivity is observed that correlates directly to the strength of the acid.

However as previously discussed, we understand that these findings are not only because of the interionic interactions, but also as a result of the extent of proton transfer and acid-base equilibria. To probe the effect of the extent of proton transfer on the ionic conductivity, we tested a set of aprotic derivatives and compared them to their protic analogues. In the case of the stronger acids with low pK_a values, pPy-Tfo vs aPy-TfO, the measured conductivities through EIS

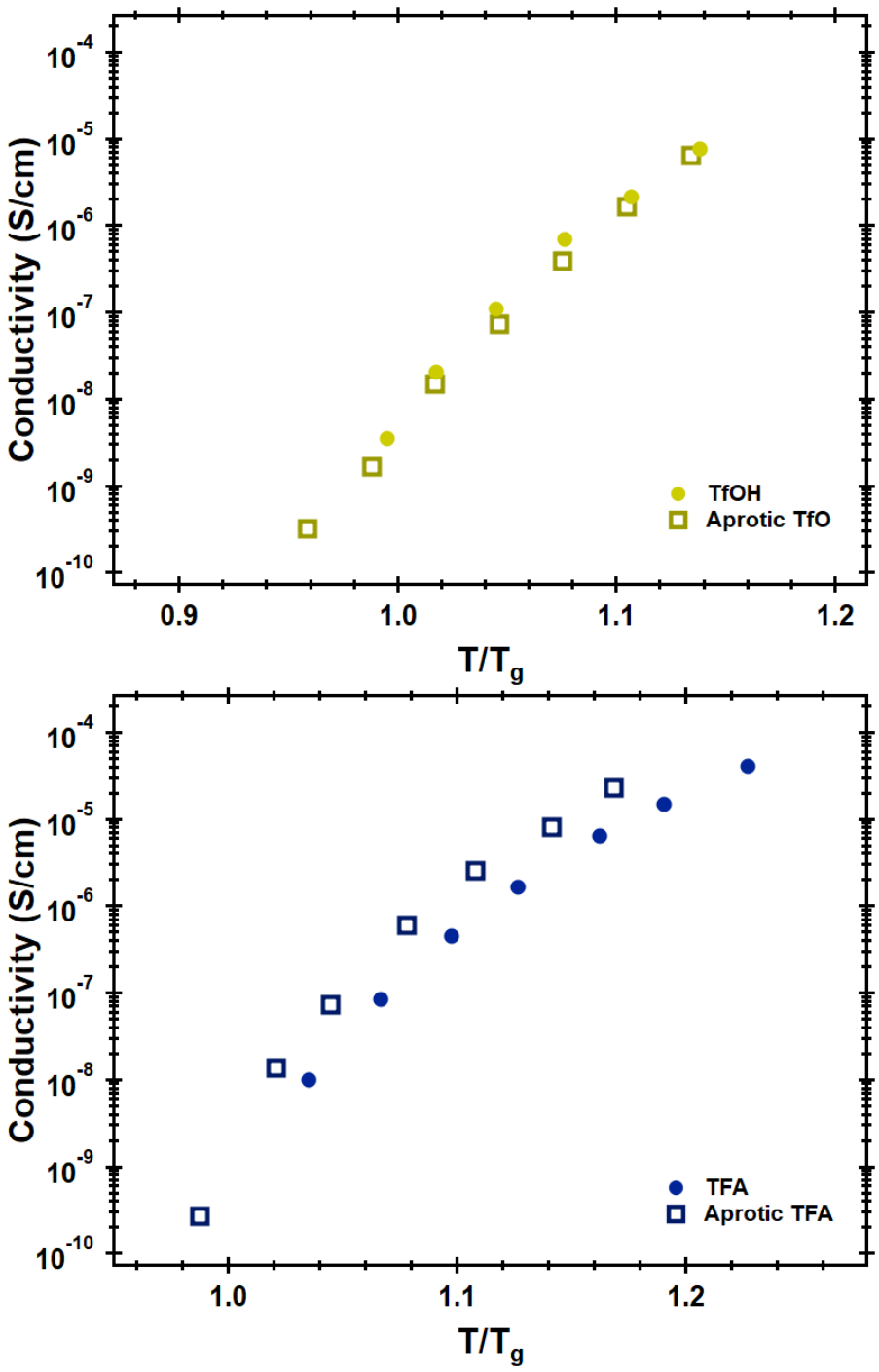

Figure 2.3 Comparison of conductivities of protic and aprotic a) TfO derivatives and b) TFA derivatives. For the TfO derivatives, the two samples demonstrate the same conductivity, where the aprotic TFA has an increase of about 3-5 times as compared to the protic version.

measurements are essentially identical (**Figure 2.3a**). This result suggests a couple of key points: 1) the extent of proton transfer is sufficiently large that a polyPIL with a large ΔpK_a consists entirely of ions, owing that EIS measurements are only sensitive to ionic species; 2) the H-bonding strength is substantially weak allowing for efficient anion dissociation and subsequent diffusion. The latter is further supported by the ΔE values calculated (**Table 2.1**) suggesting that even for protic versions, the ion-ion interaction is sufficiently labile for low pK_a acids. On the other hand, when utilizing acids with high pK_a's, there is a larger extent of equilibrium noted between the ionic and neutral species. In the T_g normalized EIS of the protic and aprotic derivatives of the TFA polyILs, there is an appreciable difference between the two samples (**Figure 2.3b**). The aprotic analogue, aPy-TFA, demonstrates a higher conductivity by a factor of 3 to 5 times as compared to the protic version, pPy-TFA. We hypothesize that this result is of consequence of two major characteristics: 1) an incomplete proton transfer between the higher pK_a acid and the pyridine base, and the presence of neutral species decreases the total number of ionic carriers contributing to the conductivity; 2) an increase in the H-bonding strength between the cation and anion. Again, the latter conclusion is further supported by the ΔE value calculated by DFT (**Table 2.1**), suggesting a stronger interaction between the cation and anion. One could potentially argue that this result is only because of the H-bonding strength increasing but coupled with the results previously discussed in the T_g characterization, the authors believe a combination of both effects is a more complete assessment. If it were due to only the increase in H-bonding, one could reasonably predict an increase in the T_g of the material, and not the T_g suppression as observed experimentally. Similarly, the protic and aprotic derivatives of the methanesulfonate polyILs were compared in this fashion. **Figure 2.33** demonstrates a difference of only 1.5 to 3 times increase in conductivity. Noting the decrease in difference of conductivity between the protic and aprotic polyILs with an

increase in ΔpK_a, we can begin to appreciate that the transition from *pseudo*-IL[51,52] to polyIL is not a specifically defined ΔpK_a, but rather a continuous spectrum for polyPILs.

The role of ion mobility on conductivity was probed using pulsed field gradient NMR (PFG-NMR) to measure the self-diffusion coefficients of NMR-active nuclei. The PFG NMR experiments were analyzed in the context of dilute solution theory. Within this theory, an ionic conductivity can be calculated from the measured diffusion coefficients using the Nernst− Einstein equation

$$\sigma = \frac{F^2}{RT}(z_+^2 c_+ D_+ + z_-^2 c_- D_-)$$

Equation 2.1

where F is Faraday's constant, R is the ideal gas constant, T is the absolute temperature, and $z_\pm$, $c_\pm$, and $D_\pm$ are the valency, concentration, and diffusion coefficient of the cation/anion, respectively, with the assumption of full acid dissociation (i.e., complete acid-base neutralization). This technique does not distinguish between molecular or ionic species unless their chemical shifts or diffusion coefficients are distinguishable over the experimental time scale. As such, we are probing to see if we can measure anion and acidic proton diffusion in these polyPILs. Due to the relatively high T_g of most of the polyPILs in this study and temperature limitations of the instrument, only a few samples were measured using this technique. Both ^{1}H and ^{19}F NMR diffusion coefficients were measured for each sample. The conductivities measured through EIS were then compared to the calculated conductivity values. pPy-TFSI was chosen to study the case of polyPILs with a large ΔpK_a difference. In the case of pPy-TFSI, the conductivity calculated using ^{19}F diffusion agrees relatively well to the measured conductivities (**Figure 2.4**). Interestingly enough, no ^{1}H diffusion was detected even at 83 °C for this sample. Since the polyPILS are made using a stoichiometric

amount of acid and the energetic barrier for the proton to move back onto the TFSI anion is so unfavorable (**Table 2.1**), there are no available proton accepting sites for the acidic proton to move throughout the system. Karlsson et. al. have investigated the effects of nonstoichiometric acid-base mixtures in polyPILs.[53] For the case of polyPILs with small ΔpK_a differences, both pPy-DFA and

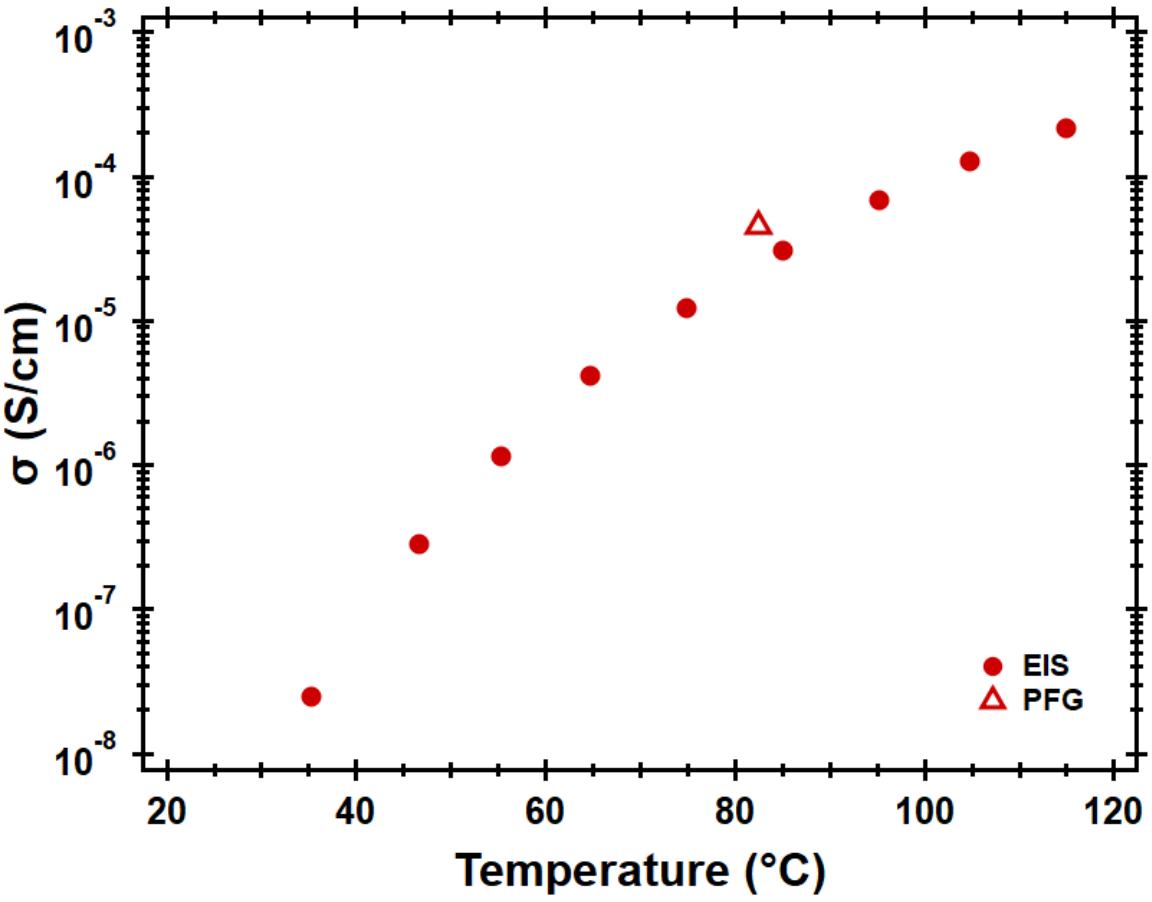

Figure 2.4 Conductivity measurements comparing PFG-NMR calculated conductivities to EIS measured values for the pPy-TFSI polyPIL.

pPy-MFA were measured. Both ^{1}H and ^{19}F diffusion signals were detected. As for pPy-TFSI, the ^{19}F signal understandably originates from the anion movement. For ^{1}H, two signals were detected, one coming from the proton(s) adjacent to the fluorine on the anion, and the other being the acidic proton. The signals were assigned accordingly since one of the diffusion coefficients agreed very closely to the ^{19}F signal (**Table 2.3**). The calculated conductivities were plotted in comparison to the EIS results for pPy-DFA and pPy-MFA samples, **Figure 2.5** and **Figure 2.6**, respectively. The inverse Haven ratio, $H^{-1} = \sigma_{NE}/\sigma_{EIS}$, where σ_{NE} is the conductivity calculated from diffusion measurements (PFG-Total) and σ_{EIS} is the conductivity directly measured (EIS), were calculated to be 0.09 and 0.08 for the pPy-DFA and pPy-MFA samples, respectively. For comparison, the H^{-1} for the pPy-TFSI sample is 0.68. These results allude to the notion that in the polyPILs with small ΔpK_a's the ion-ion correlations are not negligible and strongly affect ion conductivity.

Finally, DFT was utilized to calculate ΔE (in acetone) values for free versus ion-paired anions for the protic polyILs as well as a subset of the aprotic derivatives (**Table 2.1**). The order of ΔE values calculated agrees very closely to the pK_a values of the Brønsted acids: HTFSI < TfOH < MSA < $HNMes_2$ < TFA < DFA < MFA. Additionally, the N-H bond and anion-H bond distances were calculated. The N-H bond length follows a similar order based on the acid: HTFSI ~ TfOH < MSA ~ $HNMes_2$ < TFA << DFA < MFA. A clear shift in the acid-base equilibria can be observed as demonstrated by the jump in N-H bond lengths between TfO and DFA, and as depicted in **Figure 2.35** and **Figure 2.36**, as a function of pK_a (ΔE). When plotting the normalized conductivity as previously done in **Figure 2.2** but exchanging the x-axis for the calculated ΔE values (**Figure 2.37**) an almost identical plot is generated. Another interesting finding of these

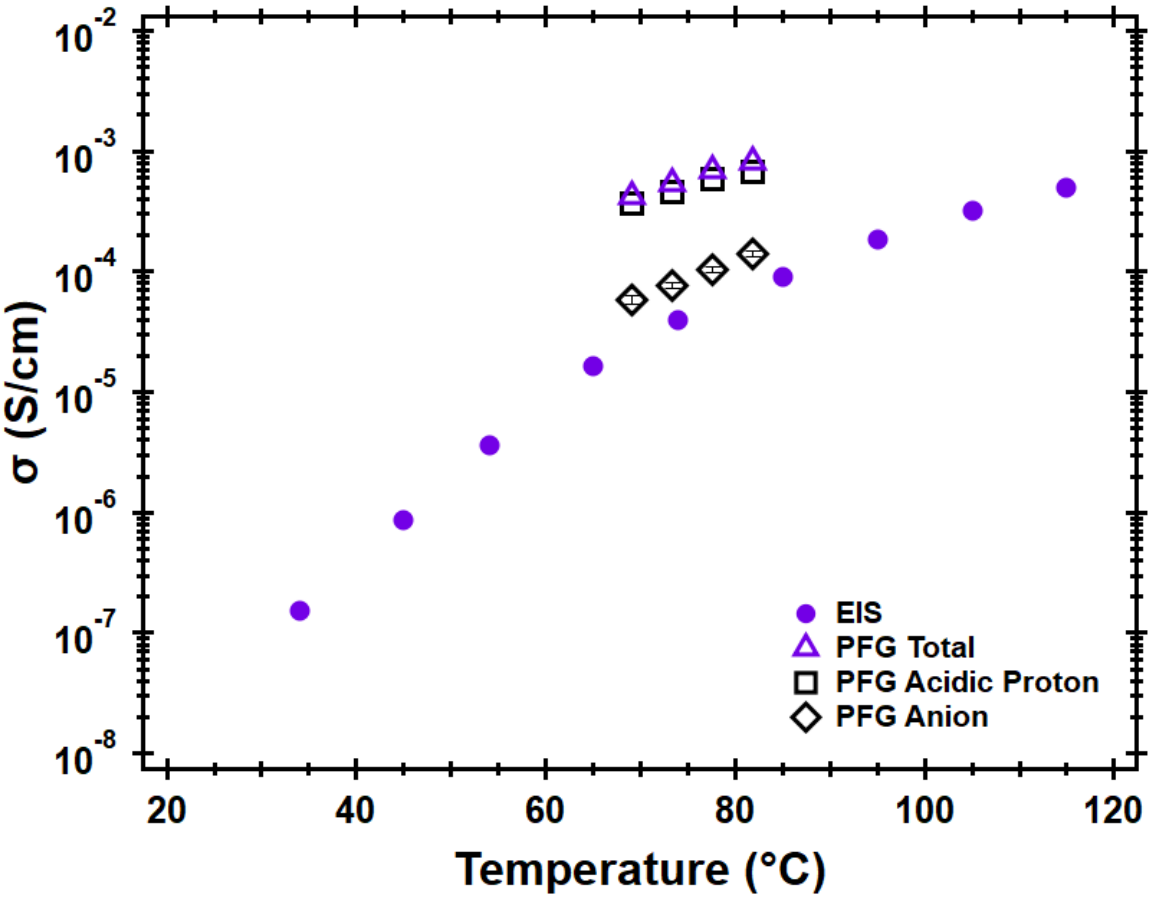

Figure 2.5 Conductivity measurements comparing PFG-NMR calculated conductivities to EIS measured values for the pPy-DFA polyPIL. PFG Total denotes the summation of the PFG Acidic Proton and PFG Anion values. The PFG Anion is an average of the ^{1}H and ^{19}F signals assigned to the anion, with error bars included.

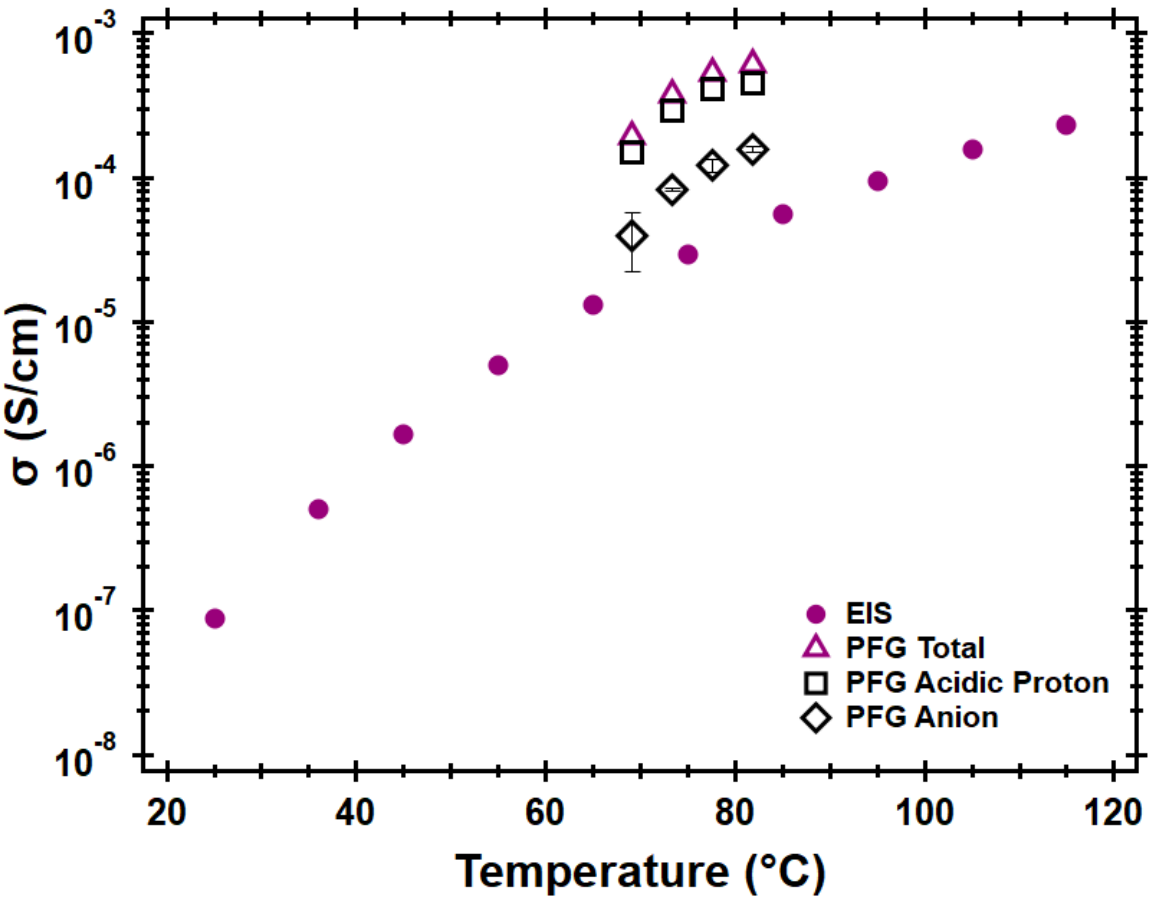

Figure 2.6. Conductivity measurements comparing PFG-NMR calculated conductivities to EIS measured values for the pPy-MFA polyPIL. PFG Total denotes the summation of the PFG Acidic Proton and PFG Anion values. The PFG Anion is an average of the ^{1}H and ^{19}F signals assigned to the anion, with error bars included.

calculations is the trend noted in the ΔE of the aprotic derivatives. Unlike the protic versions where a large difference in both ΔE and conductivity is seen across the pKa range, for the aprotic versions only a very small difference is noted, <1 kcal/mol. This result suggests that the H-bonding is the predominant interion interaction in polyPILs. This idea was tested experimentally, where the aprotic derivatives measured (aPy-TfO, aPy-MSA, and aPy-TFA) were compared directly. As shown in **Figure 2.34**, at values above T_g, the conductivities collapse onto a single trend suggesting similar Coulombic interactions across this broad range, that was suggested by the DFT derived values. These findings showcase the ability to use straightforward DFT calculations to help design high performance polyPILs a priori.

2.4 Conclusion

The difference in pK_a between the cation and anion in polyPILs has a noticeable effect on the overall macroscopic properties including ionic conductivity and thermal properties. When normalized for T_g, there is an increase of conductivity over 200 times and this increase correlates to the Brønsted acid pK_a. Stronger acids tend to have a complete proton transfer, weak hydrogen bonding interactions, and conductivities that are dominated by anionic diffusion. On the other end of the spectrum, weaker acids demonstrate an equilibrium between ion-pairs and neutral species and have strong H-bonding, and as a result facilitate proton movement with poor anion diffusion. This work highlights the importance of understanding the effect ionic interactions in ion transport and conductivity in polyPILS. Using the findings described here in conjunction with other reports, one can envision using pK_a, and related properties, as a potential guiding principle towards the design of high-performance polymeric ionic liquids.

2.5 Materials and Methods

2.5.1 Experimental Details

2.5.1.1 Materials

All materials were purchased from *Sigma Aldrich, Acros Organics*, or *Combi-Blocks* and used as received unless otherwise stated. All solvents were purchased from *Fisher Scientific* and used as received. Flash column chromatography was performed using normal phase silica gel (60 Å, 0.040 – 0.063 mm, Geduran).

2.5.1.2 Instrumentation

The ^{1}H NMR spectra were recorded on an Agilent Technologies 400-MR DD2 400 MHz, or a Varian Unity Inova AS600 600MHz spectrometer with a regulated temperature of 25 °C, unless noted otherwise. The ^{1}H NMR chemical shifts were calibrated to the resonances of chloroform-*d* at $\delta = 7.26$, or dimethylsulfoxide-d_6 $\delta = 2.50$. Data for ^{1}H NMR spectra are reported as follows: chemical shift (δ ppm), multiplicity, coupling constant (Hz) and integration. The ^{19}F NMR spectra were recorded on an Agilent Technologies 400-MR DD2 100 MHz.

Size exclusion chromatography (SEC) for molecular weight analysis, relative to linear polystyrene standards, was performed on a Waters Alliance HPLC system with a 2695 separation module equipped with Waters 2414 refractive index and 2998 photodiode array detectors using DMF with 0.01% LiBr as eluent at a flow rate of 0.3 mL/min.

Differential scanning calorimetry (DSC) measurements were performed on TA Instruments Discovery DSC 2500. Around 5-8 mg of each polymer sample was weighed and loaded into aluminum hermetically sealed pans inside a nitrogen glovebox. Glass transition measurements were recorded on the second heating cycle at a ramp rate of 10 °C/min. The glass transition temperature was analyzed via the midpoint analysis method.

Electrical impedance spectroscopy (EIS) measurements were performed on polymer samples between indium tin oxide (ITO) blocking electrodes. The thickness of the ITO electrodes on glass slides was measured via a micrometer prior to cleaning. ITO electrodes were cleaned via subsequent 5 min sonication in detergent water, deionized water, acetone, and isopropanol followed by UV/ozone treatment. Double-sided Kapton tape with a hole defining the electrode area was adhered to the ITO side of one electrode. EIS measurements were performed using a Biologic SP-200 potentiostat in a nitrogen glovebox. Sinusoidal voltage with a magnitude of 100 mV was applied to the electrodes over a frequency range from 1 to 10 mHz at temperatures ranging from 25 to 115 °C. The conductivity was calculated from the real component of conductivity at the maximum in tan (δ) or an apparent plateau in the real conductivity at low temperatures where a maximum in tan (δ) could not be resolved.

2.5.1.3 Synthesis

3-(pyridin-4-yl)propyl methacrylate (PyMA):

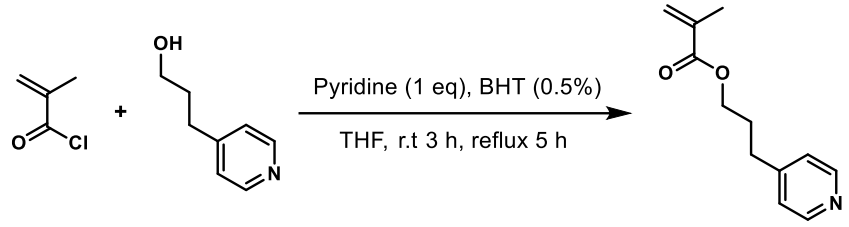

1 **2** **PyMA**

The synthesis 3-(pyridin-4-yl)propyl methacrylate (**PyMA**) was prepared according to previously reported protocols. Spectra agrees with reported literature.[41] **PyMA:** ^{1}H NMR (400 MHz, $CDCl_3$) δ 8.50 (d, *J* = 4.8 Hz, 2H), 7.12 (d, *J* = 4.8 Hz, 2H), 6.07 (s, 1H), 5.56 (s, 1H), 4.17 (t, *J* = 6.5 Hz, 2H), 2.72 (t, *J* = 7.9 Hz, 2H), 2.03 (m, *J* = 7.0 Hz, 2H), 1.94 (s, 3H).

Bis(methanesulfonyl)amine (HNMes$_2$):

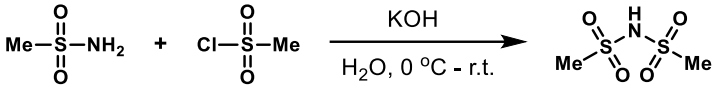

3 **4** **HNMes$_2$**

The synthesis bis(methanesulfonyl)amine **(HNMes$_2$)** was prepared according to previously reported protocols. Spectra agrees with reported literature.[54] **HNMes$_2$:** ^{1}H NMR (600 MHz, D_2O) δ 3.05 (s, 6H). HRMS (TOF MS ES−) Exact mass calcd. for $C_2H_6NO_4S_2^-$ $[M-H]^-$: 171.9738, found: 171.9742.

Fluoroacetic acid (MFA):

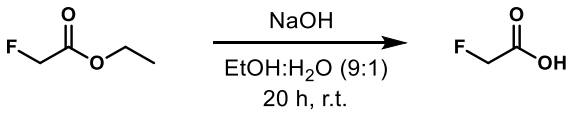

5 **MFA**

The synthesis of fluoroacetic acid **(MFA)** was prepared according to previously reported protocols. Spectra agrees with reported literature.[55] **MFA:** ^{1}H NMR (400 MHz, $CDCl_3$) δ 9.67 (s, 1H), 4.92 (d, *J* = 46.9 Hz, 2H).

Synthesis of RAFT-pPyMA:

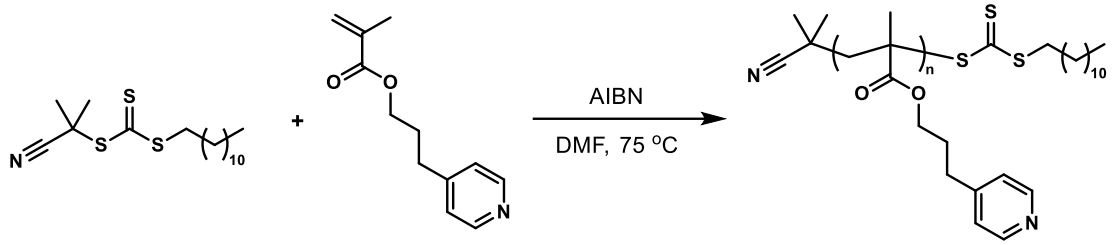

6 **PyMA** **RAFT-pPyMA**

To a 40 mL scintillation vial equipped with a magnetic stir bar and septum cap, **PyMA** (9.8 g, 47.7 mmol, 100 eq.) was added and dissolved in 10 mL of dry DMF. Following this, AIBN (7.7 mg, 0.05 mmol, 0.1 eq.) and the chain transfer agent **6** (2-cyano-2-propyl dodecyl trithiocarbonate) (165 mg, 0.48 mmol, 1 eq.) were added and the resulting reaction mixture was degassed by argon bubbling for 15 minutes. The polymerization was left to react at 75 °C for 8 hours. Monomer conversion was estimated by ^{1}H NMR in deuterated chloroform and determined to be 89%. The solution was concentrated *in vacuo* and then precipitated into diethyl ether. The solid was collected via vacuum filtration and redissolved into a minimal amount of DCM and the precipitation process was repeated for a total of 3 times. The product was obtained as a yellow solid and was used as is in the next step. Conversion 89%, M_n(theoretical) = 18200 g/mol, M_n(NMR) = 17400 g/mol.

Synthesis of pPyMA:

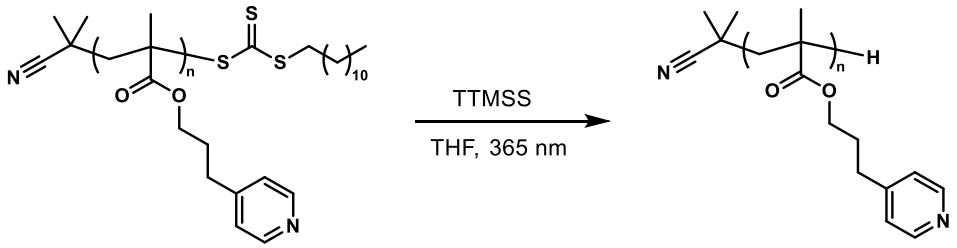

RAFT-pPyMA **pPyMA**

To a 250 mL round bottom flask vial equipped with a magnetic stir bar and septum, **RAFT-pPyMA** (4.0 g, 1 eq.) was added and dissolved in 100 mL of dry THF. Following this, tris(trimethylsilyl)silane (TTMSS) (617 μL, 5 eq.) was added and the resulting reaction mixture

was degassed by argon bubbling for 15 minutes. The reaction was set under continuous irradiation using 365 nm light for 16 hours while stirring. Chain end cleavage was monitored by ^{1}H NMR in deuterated chloroform. After complete chain end removal, the solvent was then evaporated, the resulting crude product was redissolved into a minimal amount of DCM, and then precipitated into room temperature diethyl ether. The solid was collected via vacuum filtration, redissolved into DCM, and the precipitation process was repeated for a total of 3 times. The solid was collected and dried under vacuum overnight. The final product was obtained as an off-white solid. M_n(SEC) =19500 g/mol, $Đ$ = 1.37.

General procedure for synthesis of protic polymeric ionic liquids:

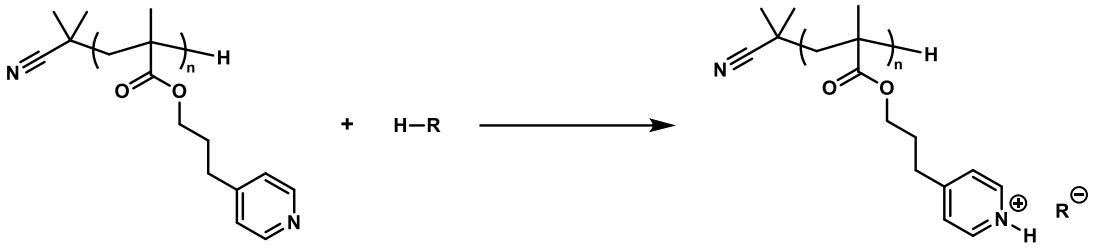

pPyMA **pPy-"R"**

To a 4 mL scintillation vial, 100 mg of **pPyMA** was added and then dissolved into 1 mL of dry methanol. To this mixture 1 eq. (per repeat unit) of the specified Brønsted acid was added, then the vial was capped, and the resulting solution was mixed on a vortexer for 5 minutes. After, the solvent was removed by rotary evaporation and then set to dry under vacuum at 100 mTorr and room temperature for 16 h, followed by further drying under vacuum at 2.8 x 10^{-8} Torr at 25-50 °C for an additional 16 - 48 h. The vial was backfilled with nitrogen and then immediately transferred into and stored in a nitrogen glovebox.

Synthesis of pPy-TFSI:

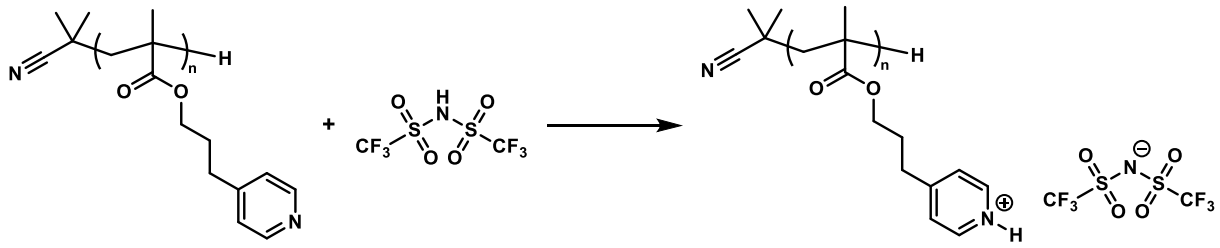

pPyMA **HTFSI** **pPy-TFSI**

Followed general procedure for synthesis of protic polymeric ionic liquids using 100 mg of **pPyMA** and 137 mg of **HTFSI**.

Synthesis of pPy-NMes2:

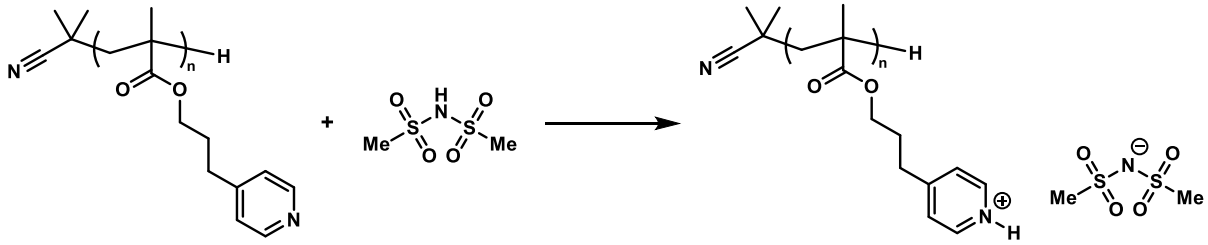

pPyMA **HNMes$_2$** **pPy-NMes$_2$**

Followed general procedure for synthesis of protic polymeric ionic liquids using 100 mg of **pPyMA** and 85 mg of **HNMes$_2$**.

Synthesis of pPy-TfO:

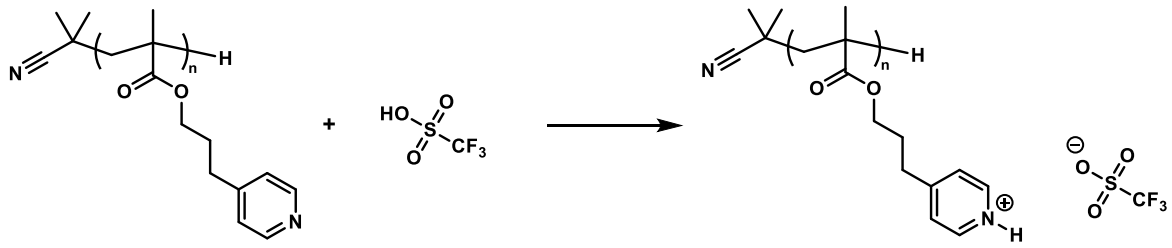

pPyMA **TfOH** **pPy-TfO**

Followed general procedure for synthesis of protic polymeric ionic liquids using 100 mg of **pPyMA** and 73 mg of **TfOH**.

Synthesis of pPy-MS:

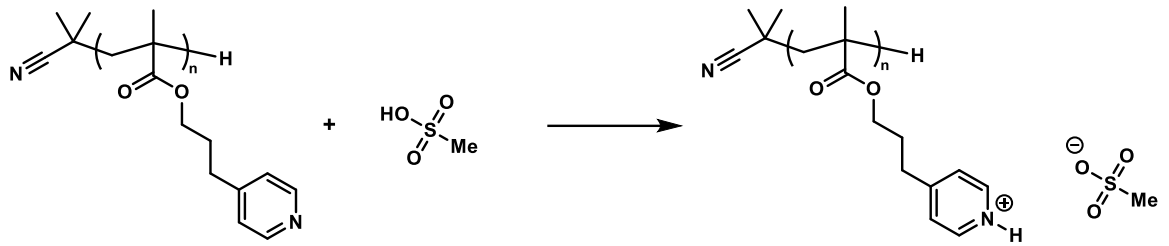

pPyM **MSA** **pPy-MS**

Followed general procedure for synthesis of protic polymeric ionic liquids using 100 mg of **pPyMA** and 47 mg of **MSA**.

Synthesis of pPy-TFA:

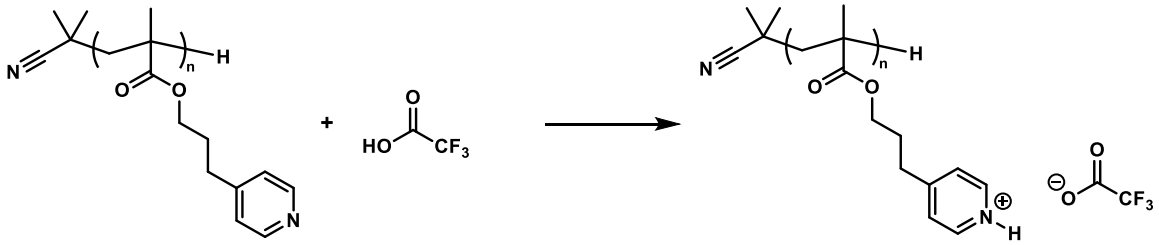

pPyMA **TFA** **pPy-TFA**

Followed general procedure for synthesis of protic polymeric ionic liquids using 100 mg of **pPyMA** and 56 mg of **TFA**.

Synthesis of pPy-DFA:

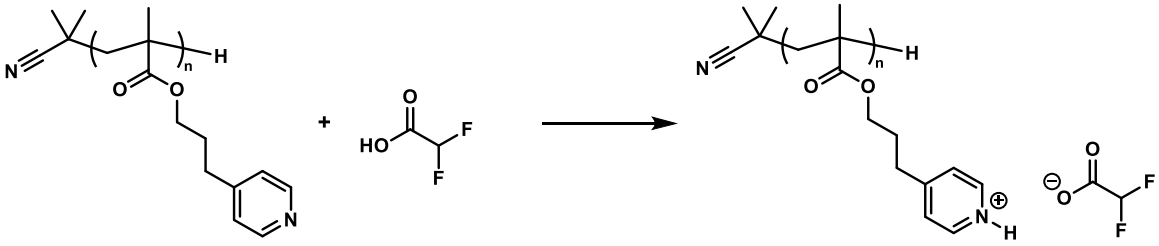

pPyMA **DFA** **pPy-DFA**

Followed general procedure for synthesis of protic polymeric ionic liquids using 100 mg of **pPyMA** and 47 mg of **DFA**. Elevated temperatures were avoided in preparation with longer drying periods.

Synthesis of pPy-MFA:

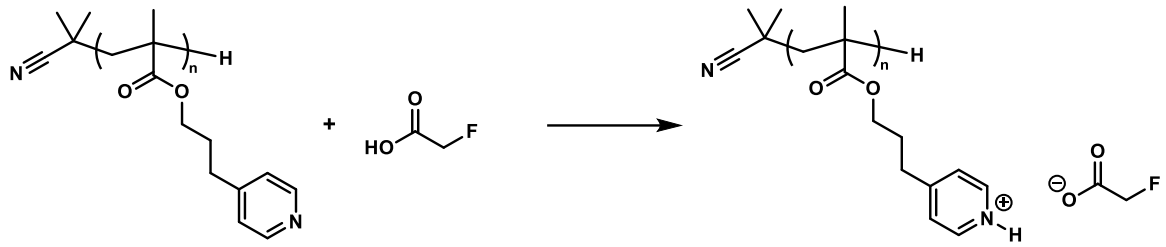

pPyMA **MFA** **pPy-MFA**

Followed general procedure for synthesis of protic polymeric ionic liquids using 100 mg of **pPyMA** and 38 mg of **MFA**. Elevated temperatures were avoided in preparation with longer drying periods.

Synthesis of aPy-TfO:

pPyMA **7** **aPy-TfO**

In a 4 mL scintillation vial, 100 mg of **pPyMA** is weighed out and dissolved into 1 mL of dry DCM. To this solution, 80 mg (1 eq. per repeat unit) of **7** (methyl trifluoromethanesulfonate) is added. This was set to mix on a mechanical stirrer for 15 minutes at room temperature. The solvent was then removed by rotary evaporation and then set to dry under vacuum at 100 mTorr and room temperature for 16 h, followed by further drying under vacuum at 2.8 x 10^{-8} Torr at 50 °C for an additional 16 h. The vial was backfilled with nitrogen and then immediately transferred into and stored in a nitrogen glovebox.

Synthesis of aPy-MS:

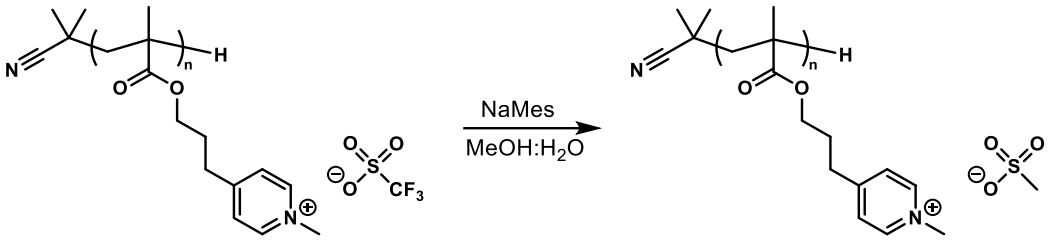

aPy-TfO **aPy-MS**

In a 20 mL scintillation vial, 100 mg of **aPy-TfO** dissolved into 15 mL of a 4:1 mixture of methanol to water along with 20 eq (per repeat unit) of sodium methansulfonate (NaMes). This solution was placed inside a 3.5 kDa dialysis tubing and dialyzed using methanol for 5 days, exchanging the solvent every 12 hours. The extent of anion exchange was estimated using ^{19}F and ^{1}H NMR. The solvent was then removed by rotary evaporation and then set to dry under vacuum at 100 mTorr and room temperature for 16 h, followed by further drying under vacuum at 2.8 x 10^{-8} Torr at 50 °C for an additional 24 h. The vial was backfilled with nitrogen and then immediately transferred into and stored in a nitrogen glovebox. The removal of sodium was also probed by ^{23}Na NMR and no peak was detected.

Synthesis of aPy-TFA:

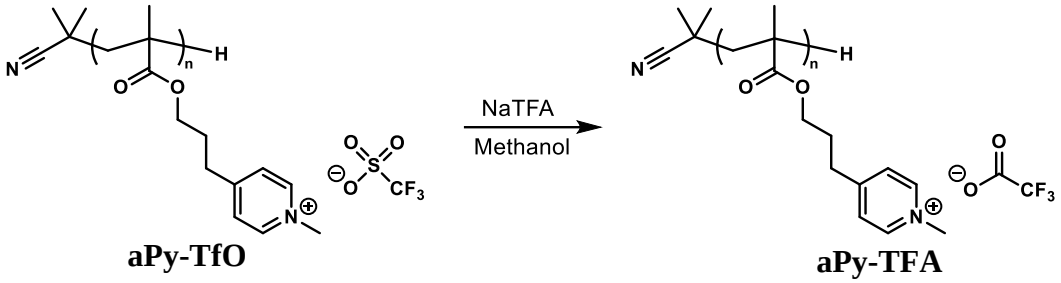

aPy-TfO **aPy-TFA**

In a 20 mL scintillation vial, 100 mg of **aPy-TfO** dissolved into 10 mL of methanol along with 20 eq (per repeat unit) of sodium trifluoroacetate (NaTFA). This solution was placed inside a 3.5 kDa dialysis tubing and dialyzed using methanol for 5 days, exchanging the solvent every 12 hours. The extent of anion exchange was estimated using ^{19}F and ^{1}H NMR. The solvent was then removed by rotary evaporation and then set to dry under vacuum at 100 mTorr and room temperature for 16 h, followed by further drying under vacuum at 2.8 x 10^{-8} Torr at 50 °C for an additional 24 h. The vial was backfilled with nitrogen and then immediately transferred into and stored in a nitrogen glovebox. The removal of sodium was also probed by ^{23}Na NMR and no peak was detected.

2.5.2 Characterization

2.5.2.1 NMR

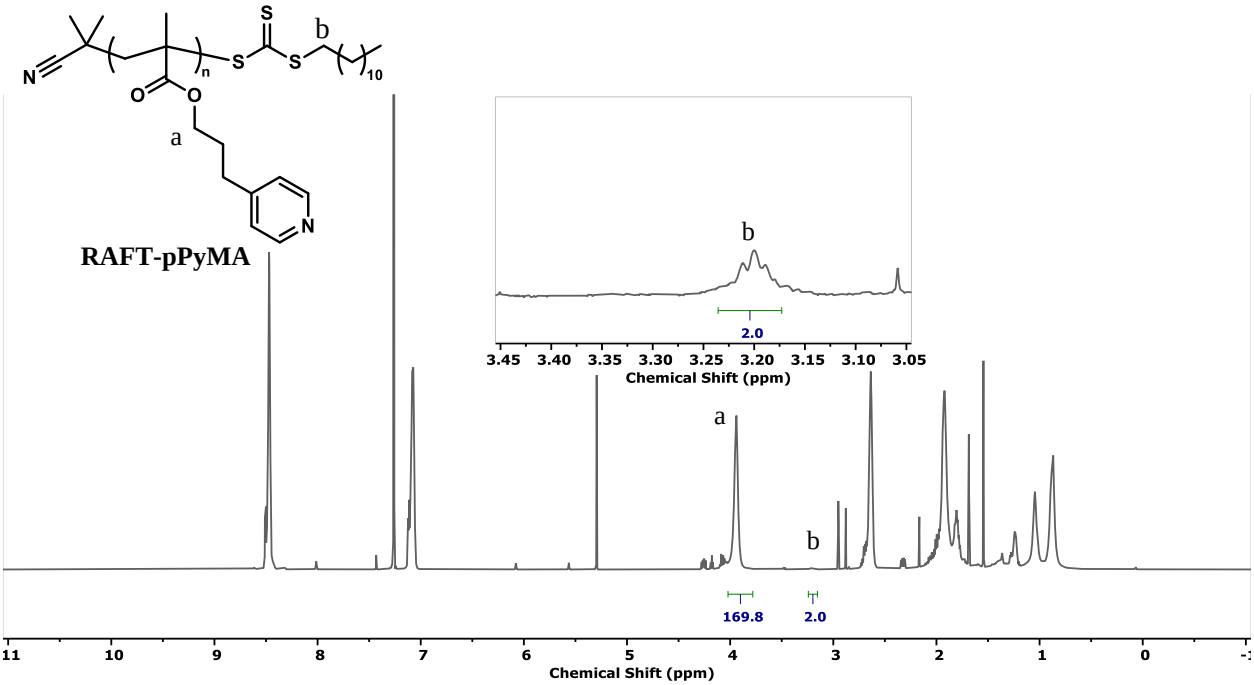

Figure 2.7 ^{1}H NMR (600 MHz, $CDCl_3$) **RAFT-pPyMA**. Insert shows chain end present, which was utilized to calculate M_n(NMR). The degree of polymerization for this polymer was estimated by the analysis of the methylene peaks at the chain end α to the trithiocarbonate group (b) to the methylene polymer peaks α to the ester of the methacrylate repeat unit (a).

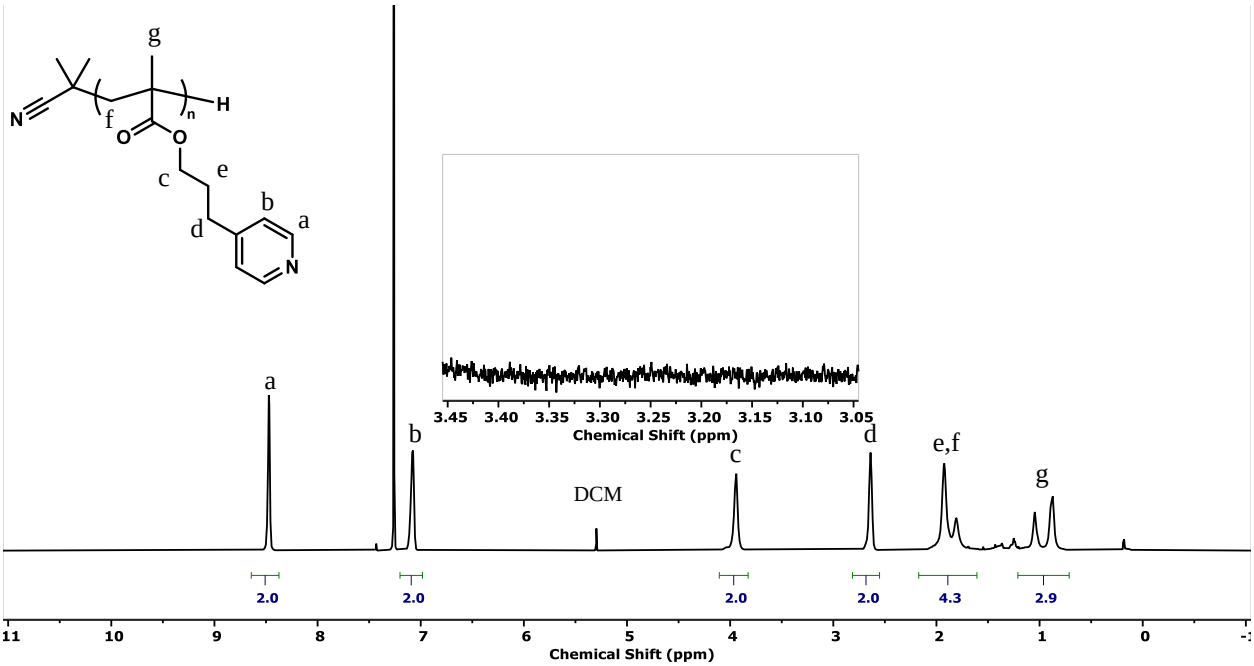

Figure 2.8 ^{1}H NMR (600 MHz, $CDCl_3$) **pPyMA**. Insert demonstrates absence of chain end, indicating successful cleavage of terminal functional group.

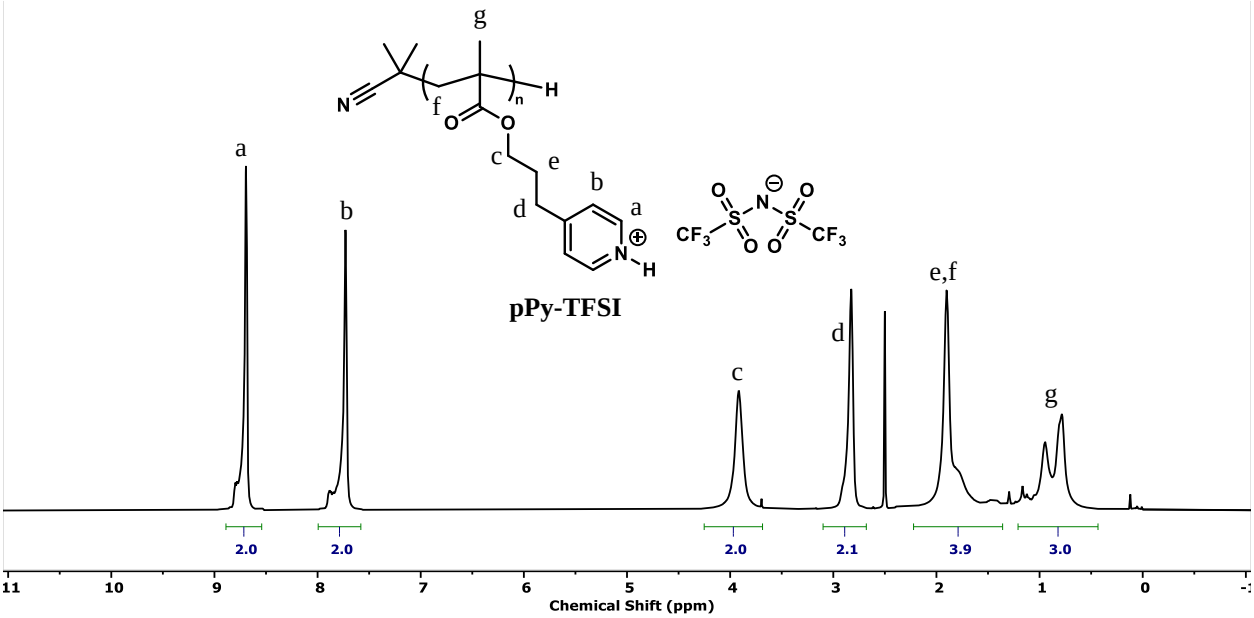

Figure 2.9 ^{1}H NMR (600 MHz, DMSO-*d*6) **pPy-TFSI**

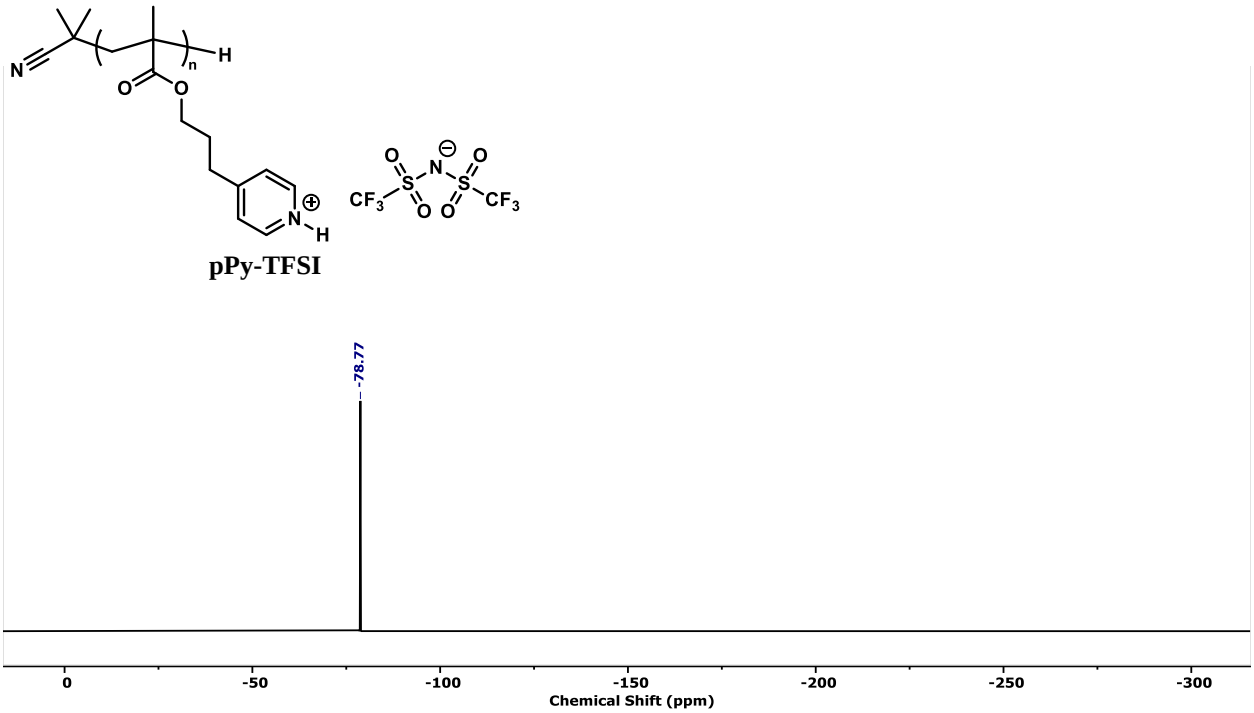

Figure 2.10 ^{19}F NMR (100 MHz, DMSO-*d*6**) pPy-TFSI**

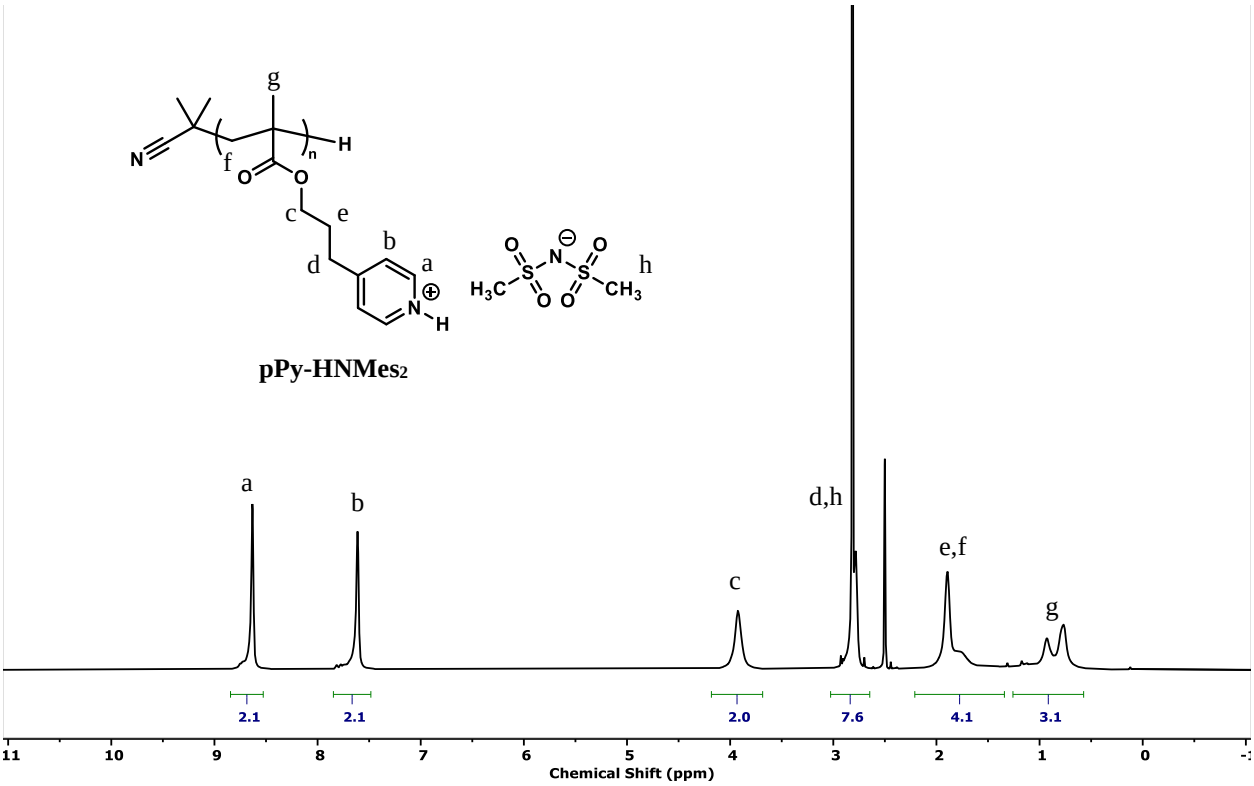

Figure 2.11 ^{1}H NMR (600 MHz, DMSO-*d*6) **pPy-NMes2**

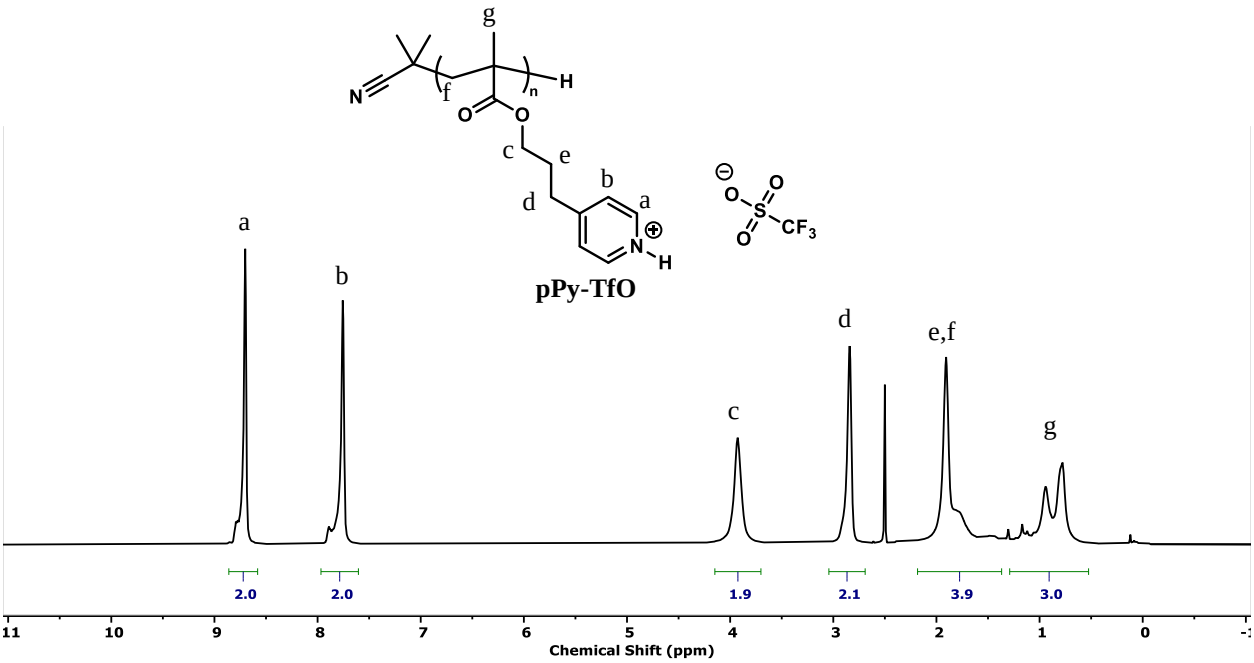

Figure 2.12 ^{1}H NMR (600 MHz, DMSO-*d*6) **pPy-TfO**

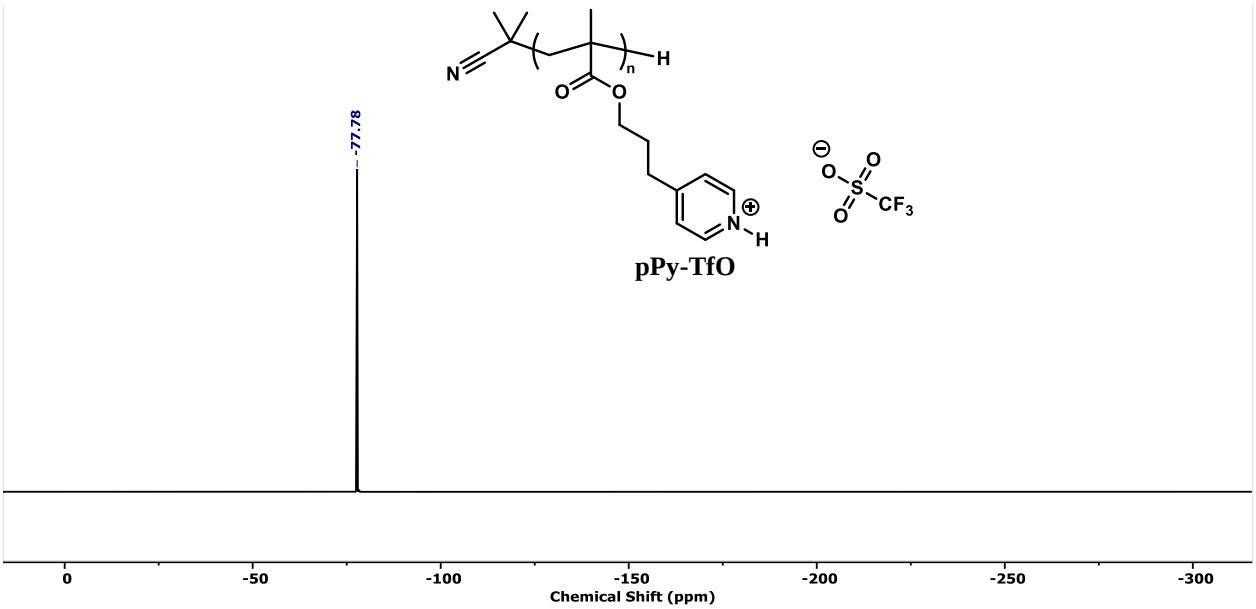

Figure 2.13 ^{19}F NMR (100 MHz, DMSO-*d*6) **pPy-TfO**

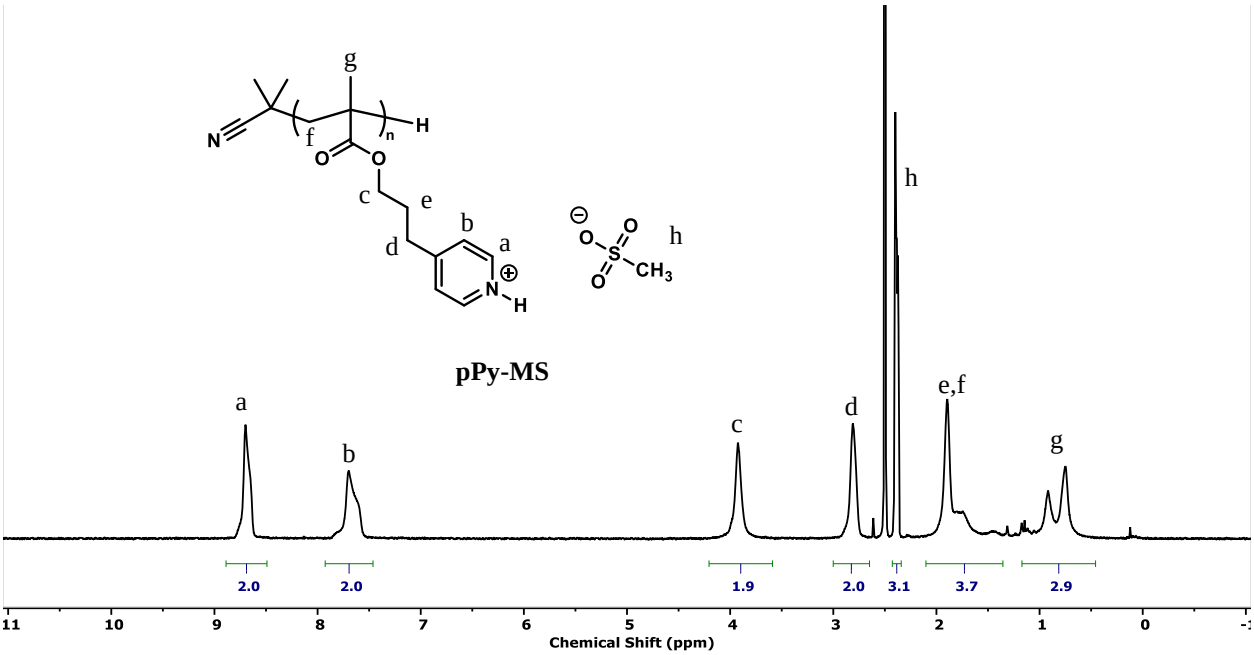

Figure 2.14 ^{1}H NMR (600 MHz, DMSO-*d*6) **pPy-MS**

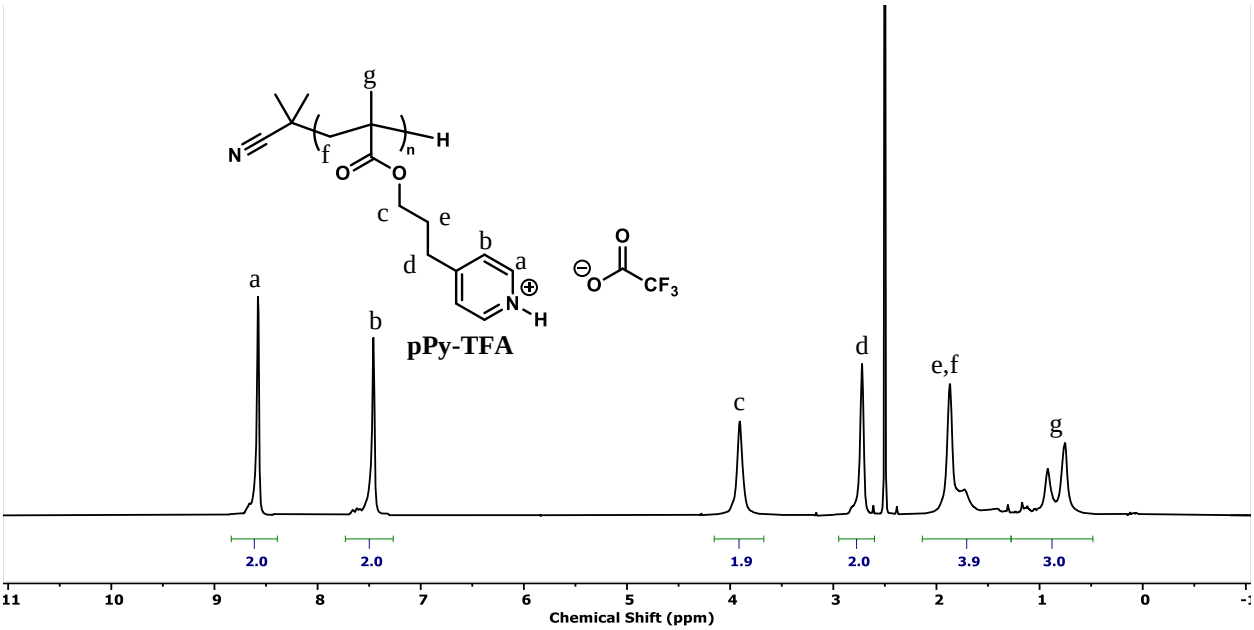

Figure 2.15 ^{1}H NMR (600 MHz, DMSO-*d*6) **pPy-TFA**

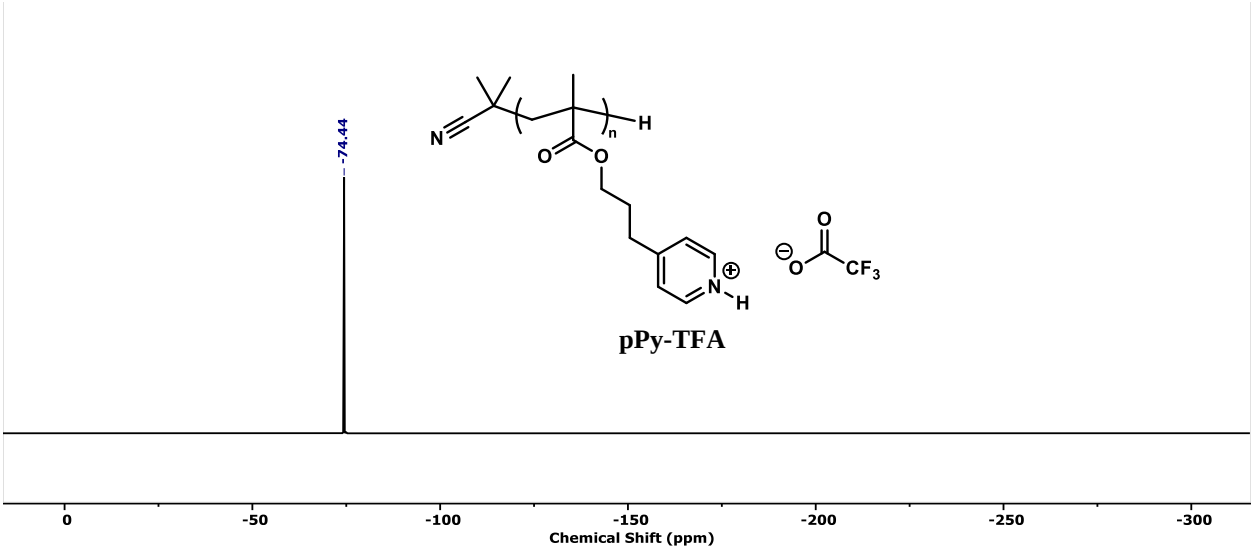

Figure 2.16 ^{19}F NMR (100 MHz, DMSO-*d*6) **pPy-TFA**

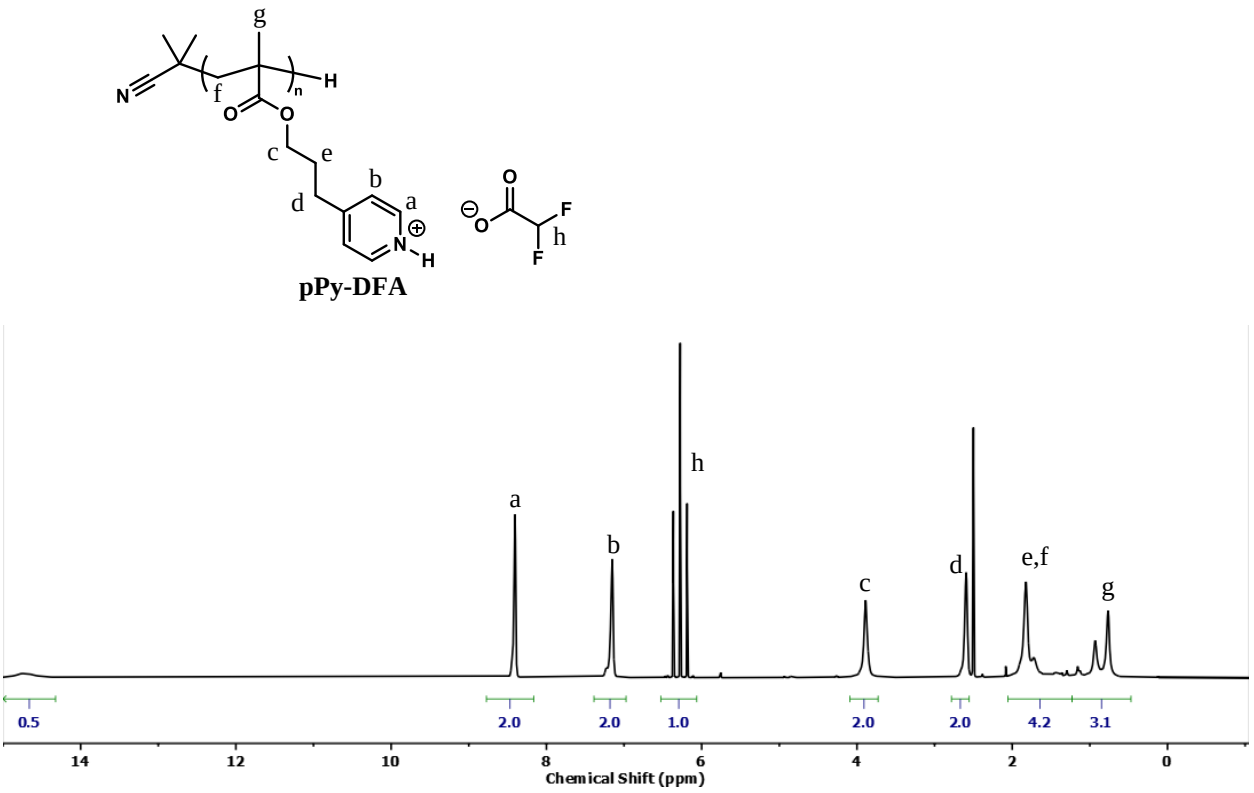

Figure 2.17 ^{1}H NMR (600 MHz, DMSO-*d*6) **pPy-DFA**

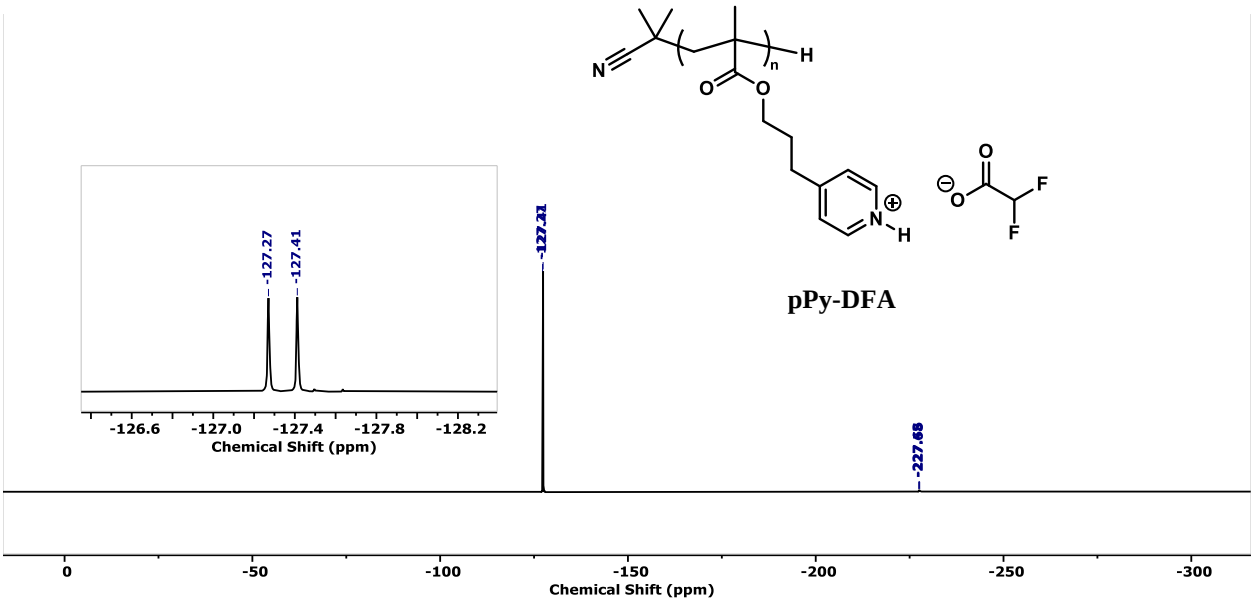

Figure 2.18 ^{19}F NMR (100 MHz, DMSO-*d*6**) pPy-DFA**

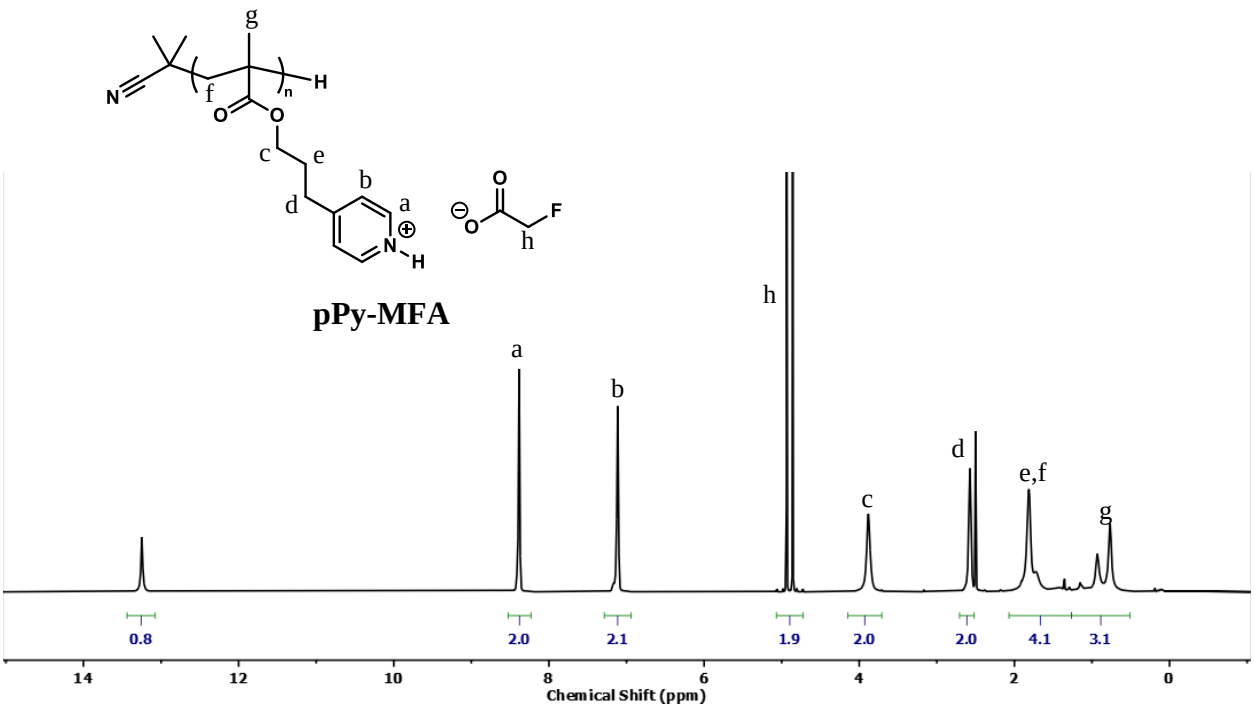

Figure 2.19 ^{1}H NMR (600 MHz, DMSO-*d*6) **pPy-MFA**

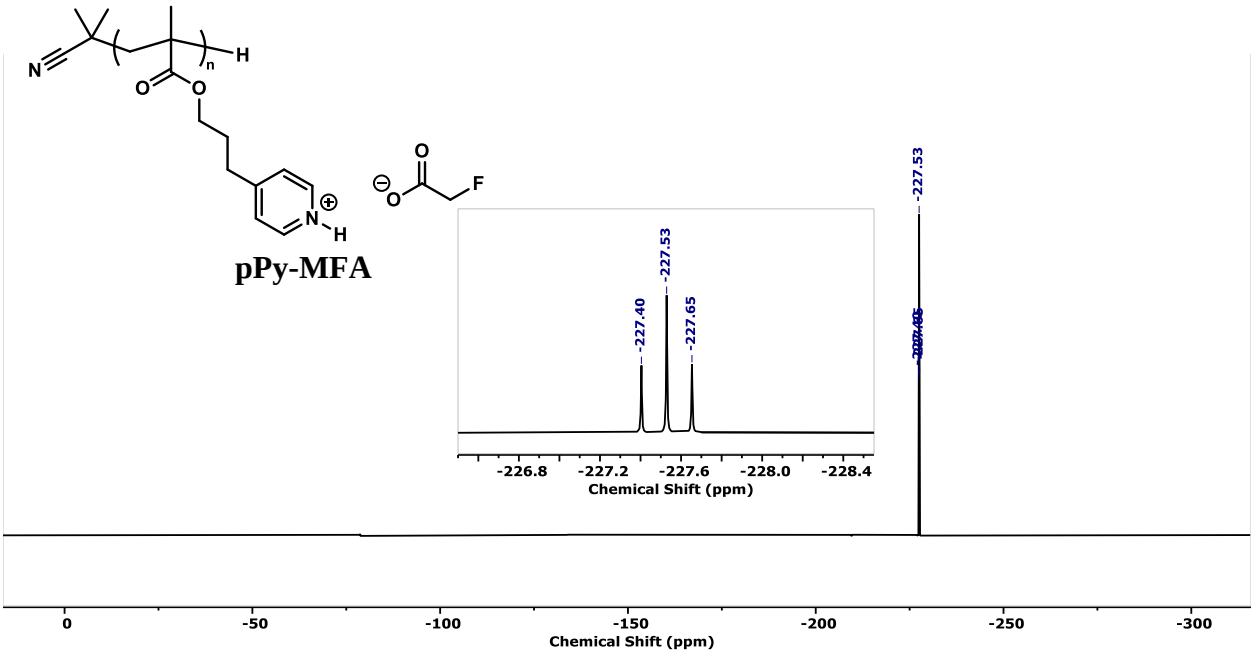

Figure 2.20 ^{19}F NMR (100 MHz, DMSO-*d*6**) pPy-MFA**

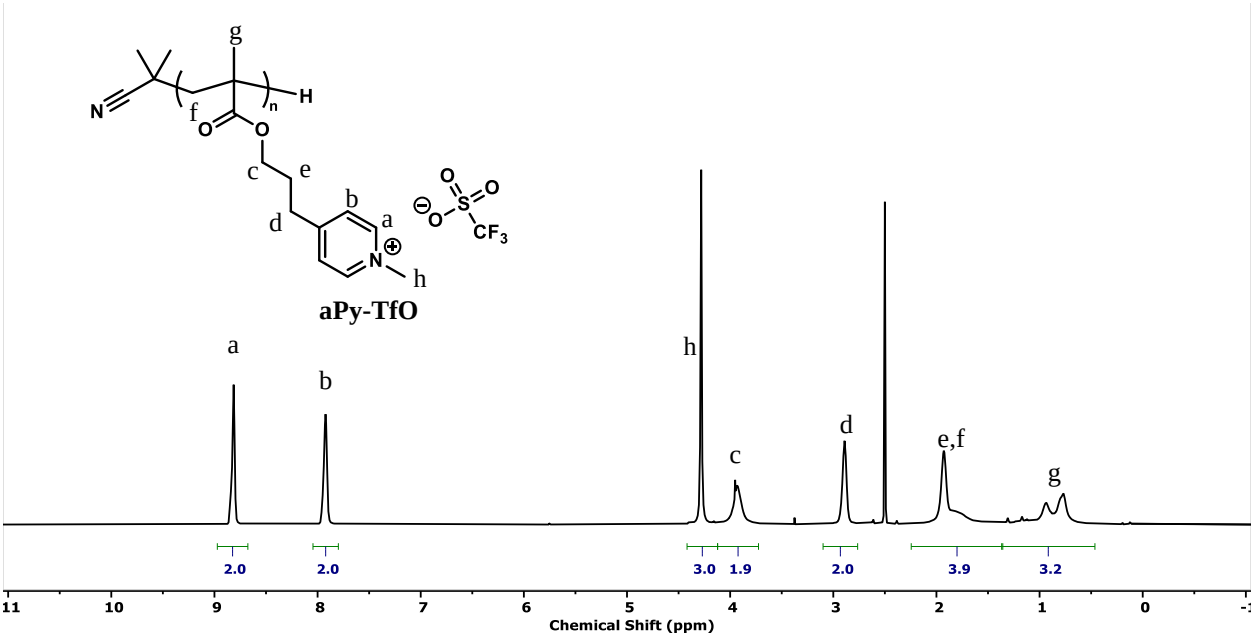

Figure 2.21 ^{1}H NMR (600 MHz, DMSO-*d*6) **aPy-TfO**

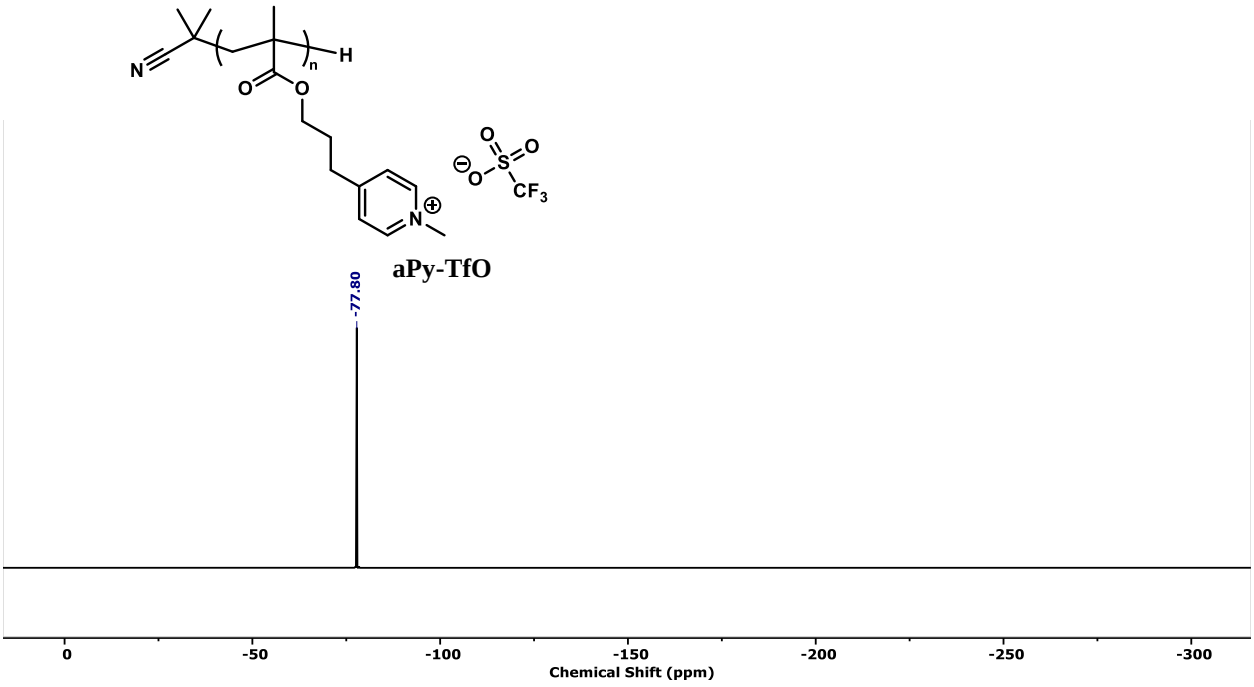

Figure 2.22 ^{19}F NMR (100 MHz, DMSO-*d*6) **aPy-TfO**

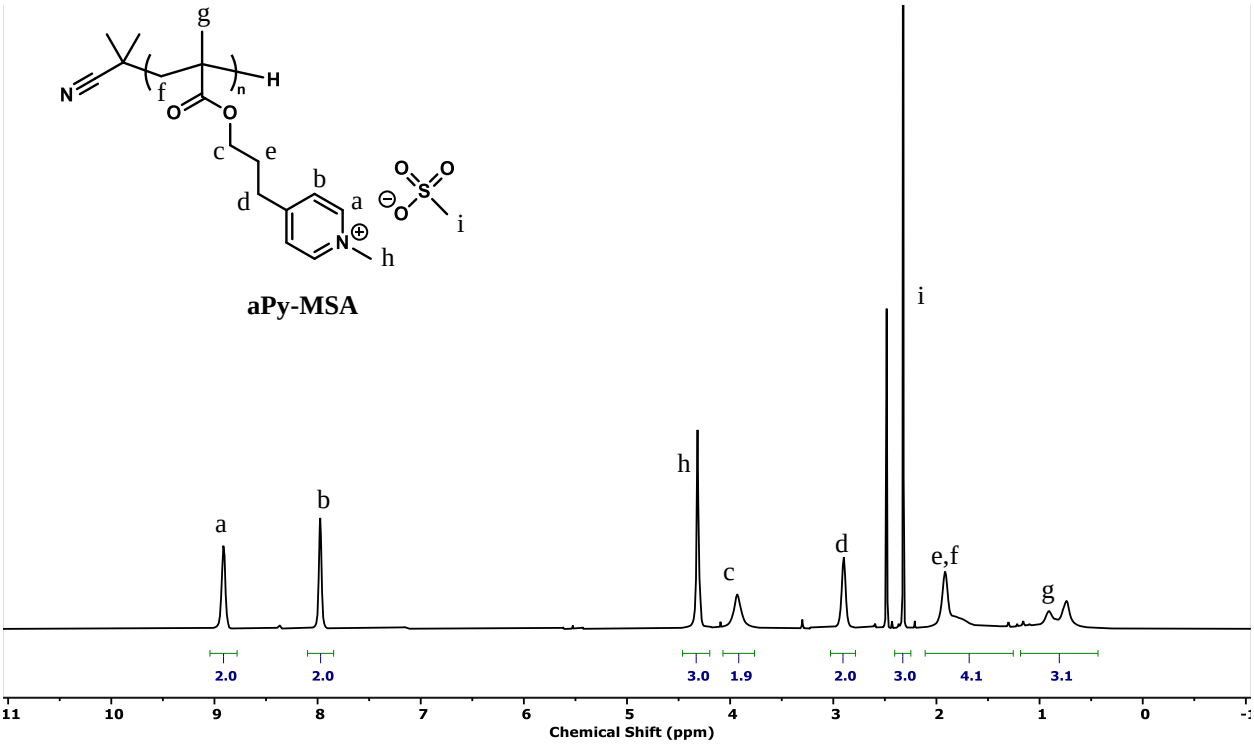

Figure 2.23 ^{1}H NMR (600 MHz, DMSO-*d*6) **aPy-MSA**

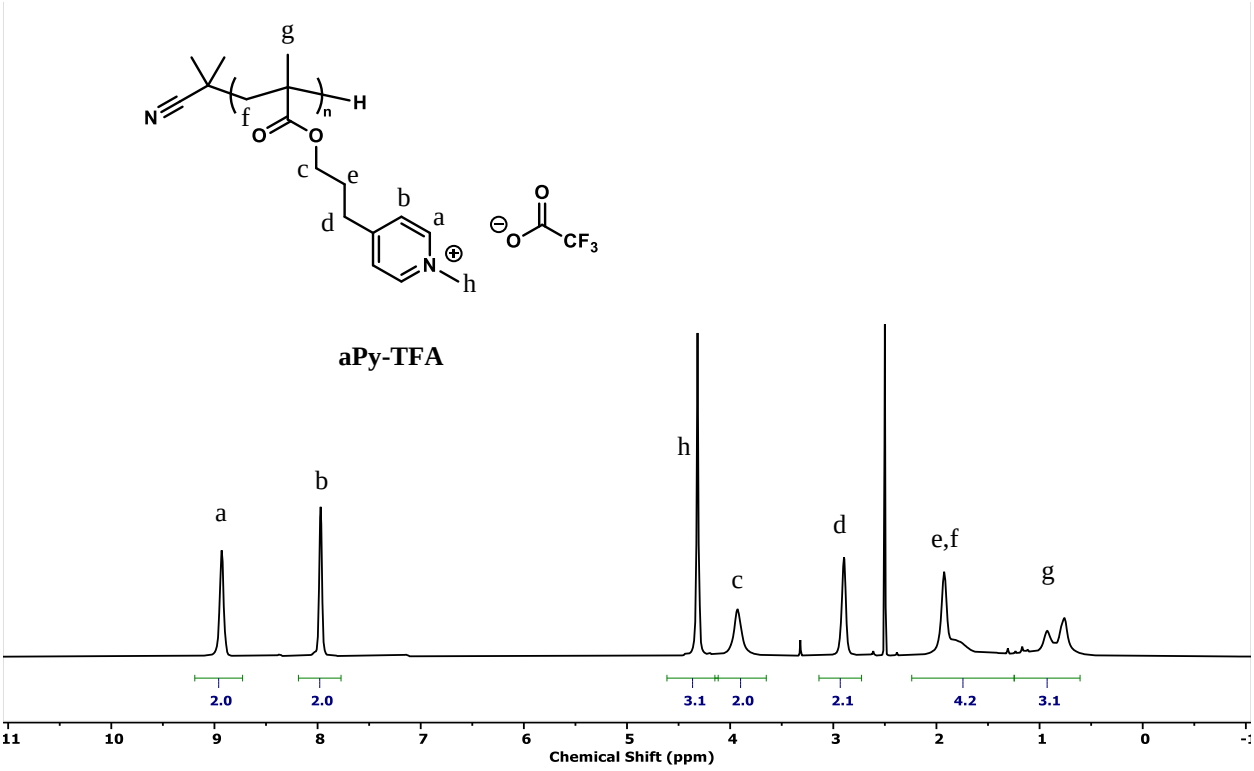

Figure 2.24 ^{1}H NMR (600 MHz, DMSO-*d*6) **aPy-TFA**

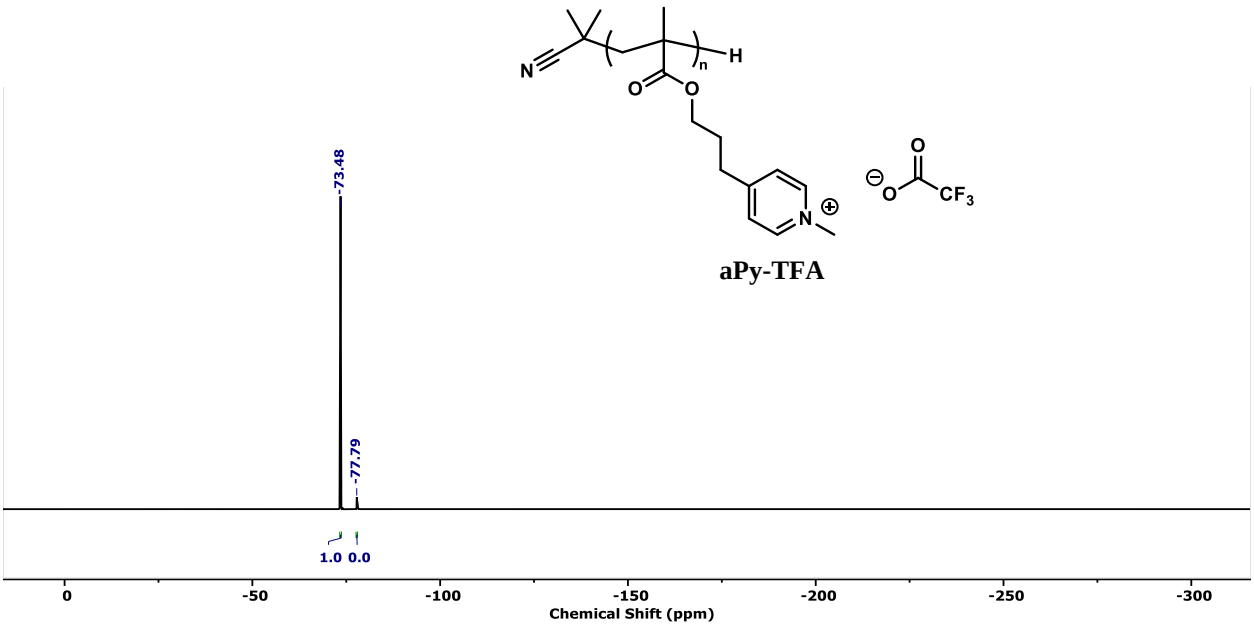

Figure 2.25 ^{19}F NMR (100 MHz, DMSO-*d*6) **aPy-TFA**. By ^{19}F NMR integration ~97% anion exchange to the TFA counterion.

2.5.2.2 Size Exclusion Chromatography

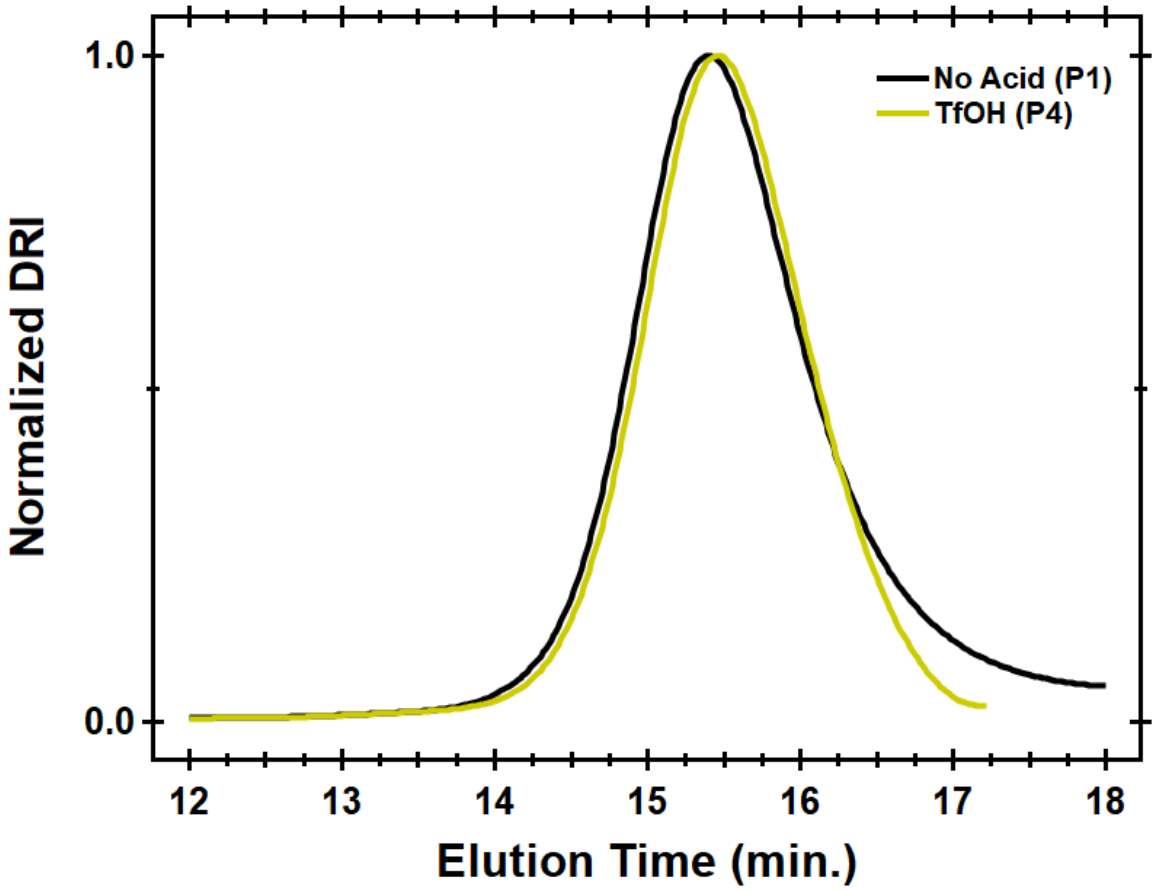

Figure 2.26 Size exclusion chromatography (DMF, 0.01% LiBr) tracing comparing **pPyMA**, the polymer sample before any acid addition, and **pPy-TfO**, with the addition of TfOH, one of the stronger acids utilized in this study. No noticable differnce in the tracing or molecular weight of the polymer sample suggests no degradation upon addition of acid to the polymer. Molecular weight and dispersity based on polystyrene standards:

Sample	M_n	$Đ$
No acid (**pPyMA**)	19500	1.37
TfOH (**pPy-TfO)**	20300	1.30

2.5.2.3 Differential Scanning Calorimetry

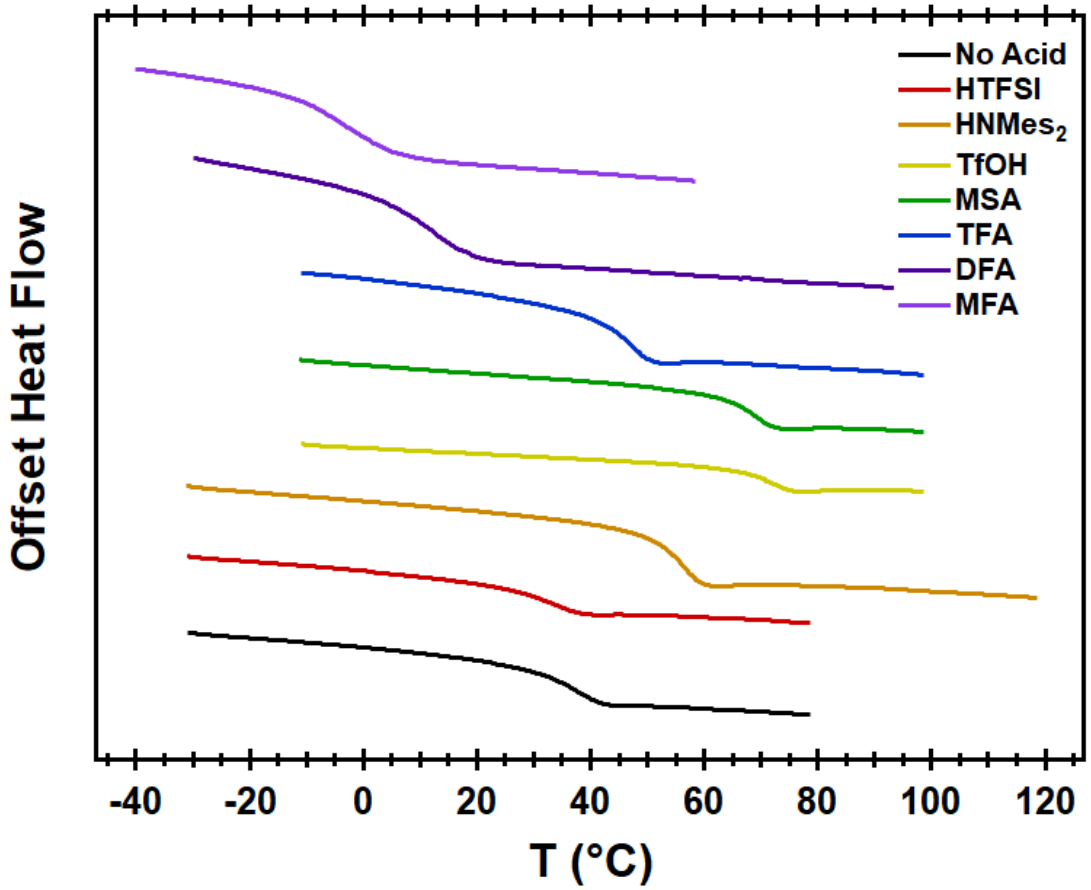

Figure 2.27 Differential scanning calorimetry curves for the protic polymeric ionic liquids examined in this study. Midpoint analysis of the T_g feature of the second heating curve gives the following glass transition temperatures:

Protic PIL sample	T_g (°C)
No acid	34
HTFSI	31
$HNMes_2$	54
TfOH	69
MSA	67
TFA	44
DFA	7
MFA	− 4

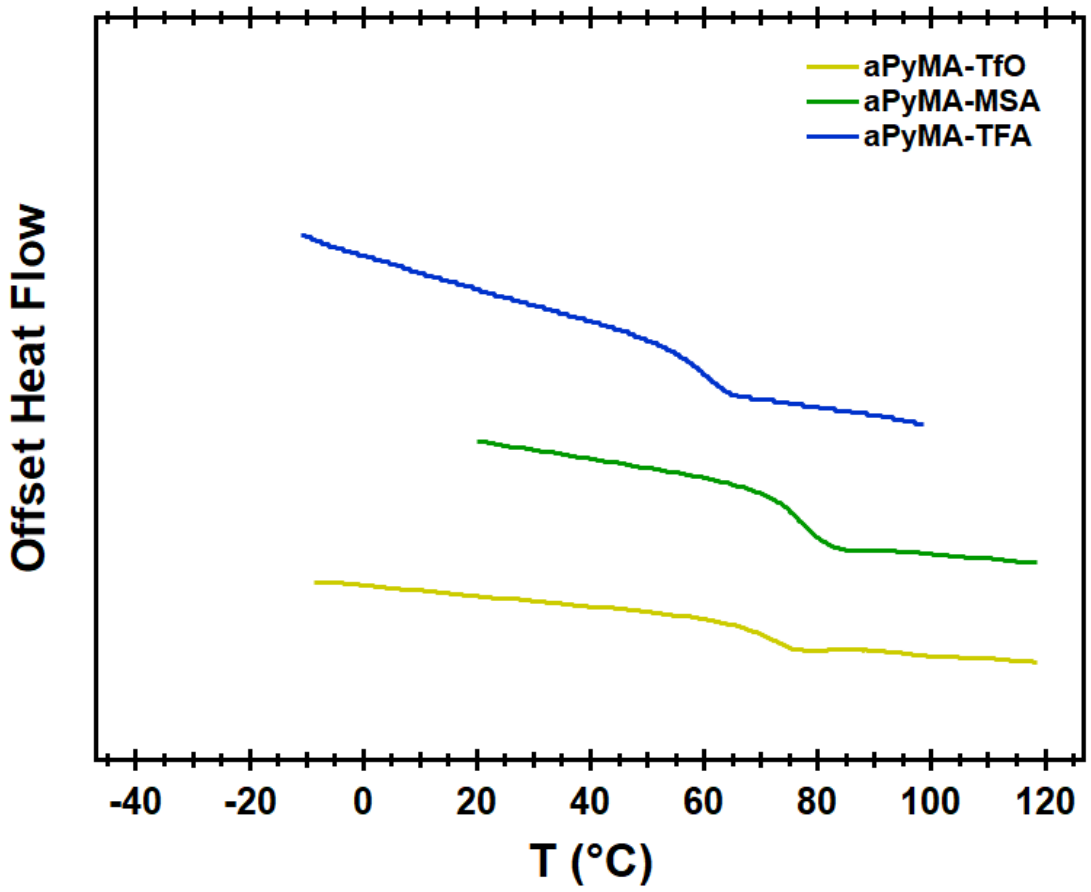

Figure 2.28 Differential scanning calorimetry curves for the aprotic control samples tested. Protic analogues are plotted along for comparison. Midpoint analysis of the T_g feature of the second heating curve gives the following glass transition temperatures:

PIL sample	**T_g (°C)**
Aprotic TfO (**aPy-TfO**)	69
Aprotic MSA (**aPy-MSA**)	76
Aprotic TFA (**aPy-TFA**)	59

2.5.2.4 Ionic Conductivity

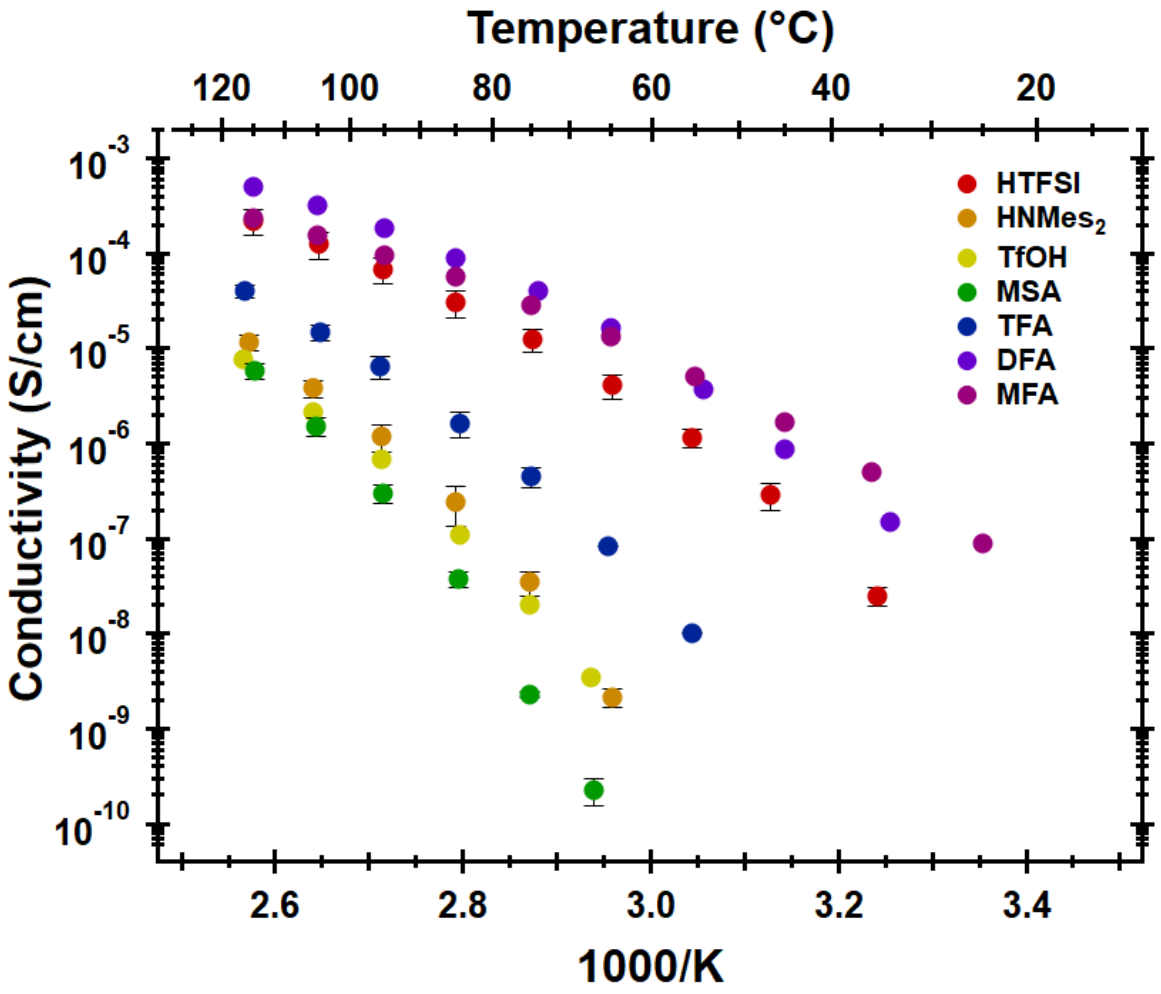

Figure 2.29 Conductivities measured by EIS of the polyPILs in this study plotted in an Arrhenius fashion, unnormalized by T_g.

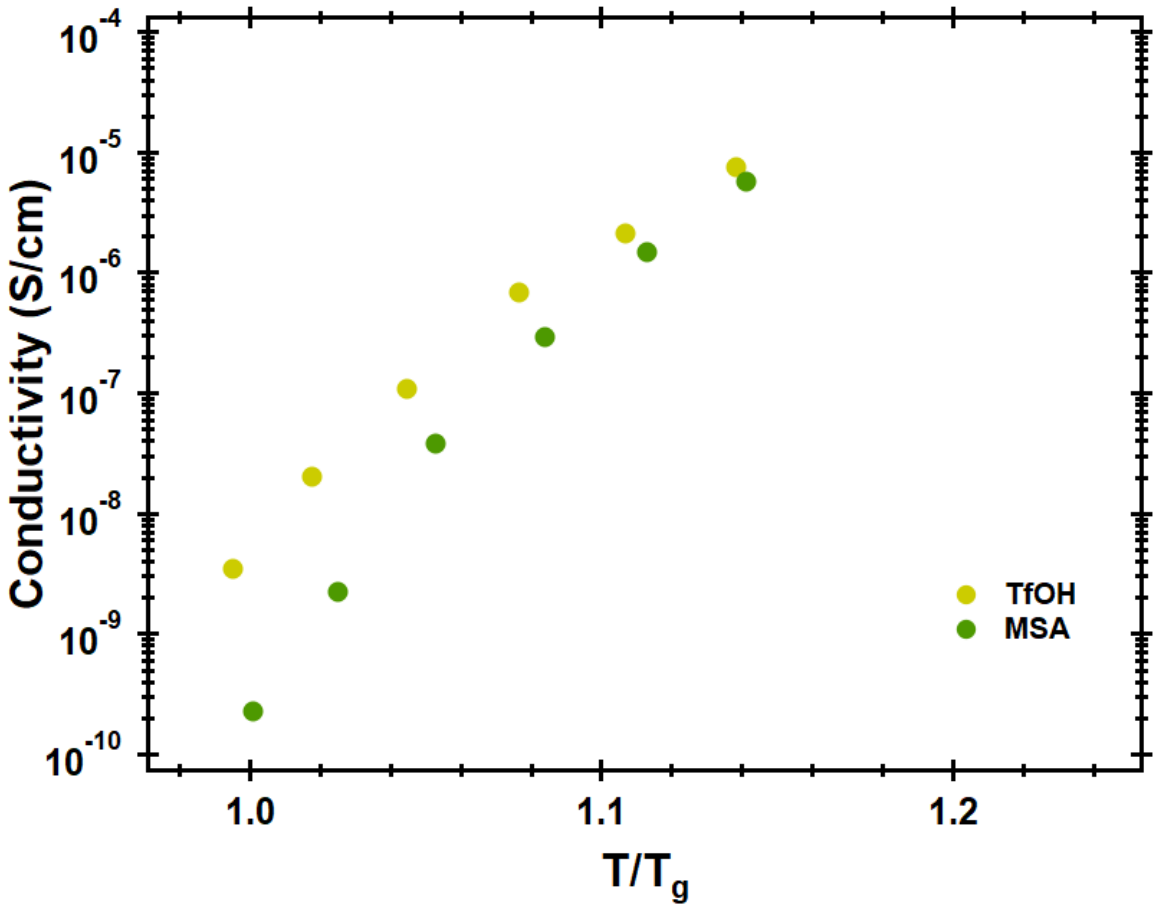

Figure 2.30 Condutivities of polyPILs with sulfonate Brønsted acids. A greater difference, over 1 order of magnitude, is noted at lower temperatures, but when temperature is increased, the overall conductivities begin to converge. This is thought to be as a result of overcoming the H-bonding forces, facilitating anion motion.

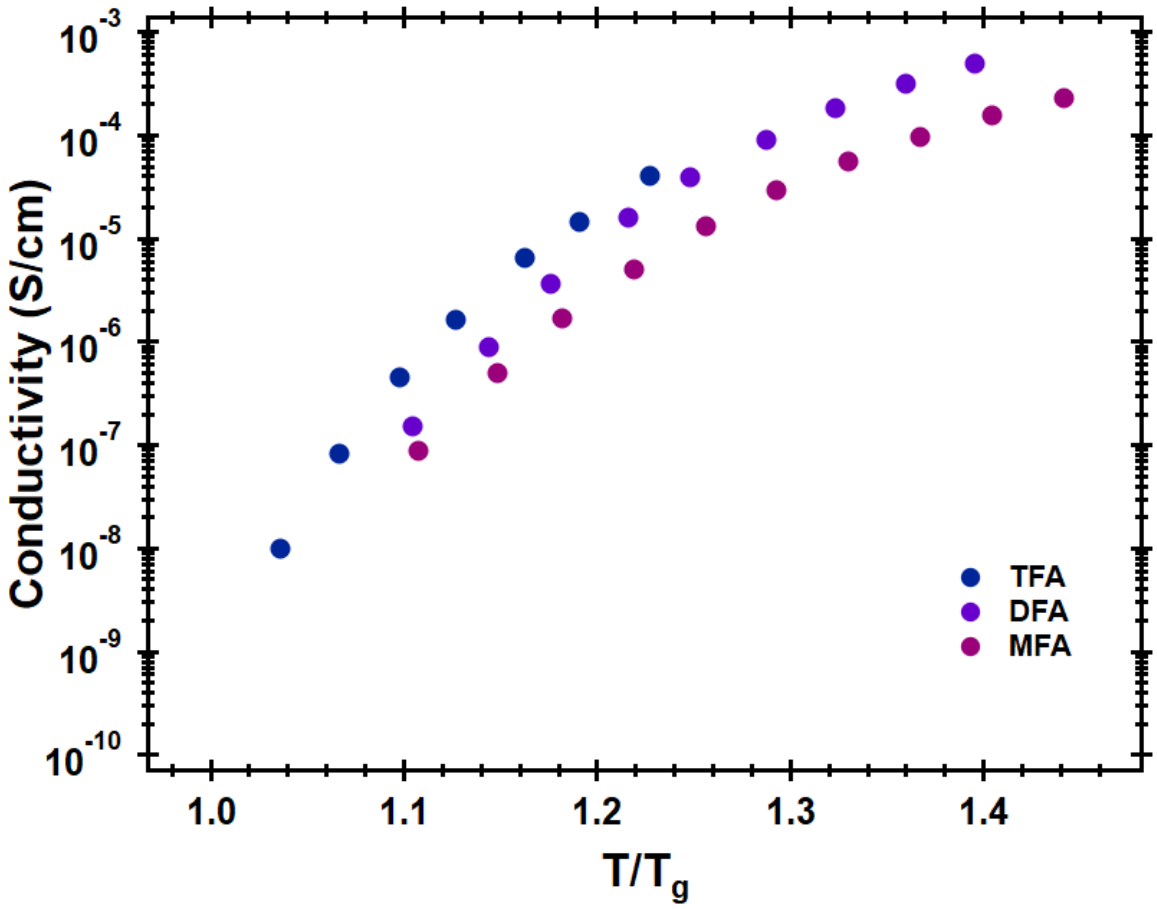

Figure 2.31 Conductivities of the polyPILS containing fluorinated acetate Brønsted acids. Overall conductivities increase as function of acid strength.

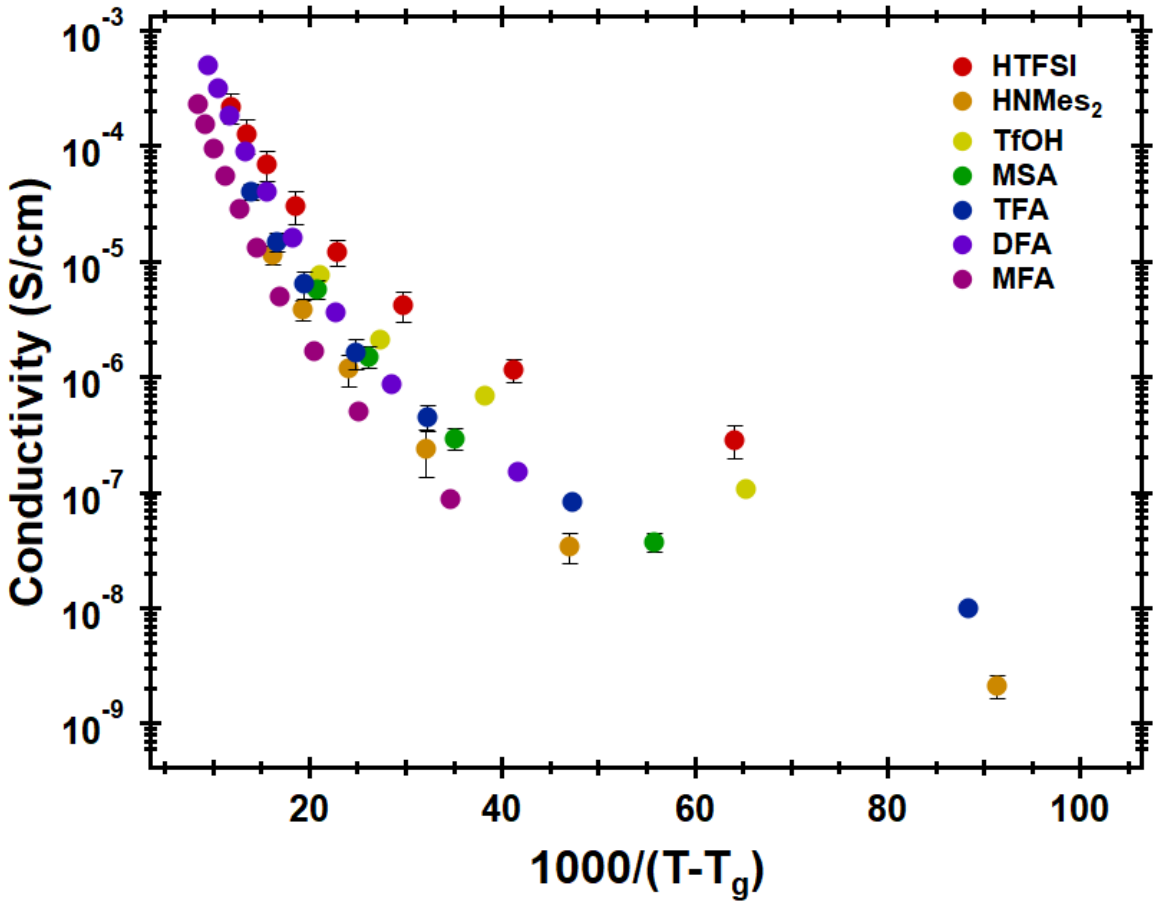

Figure 2.32 Arrhenius Tg normalized plot of conductivities of measured samples.

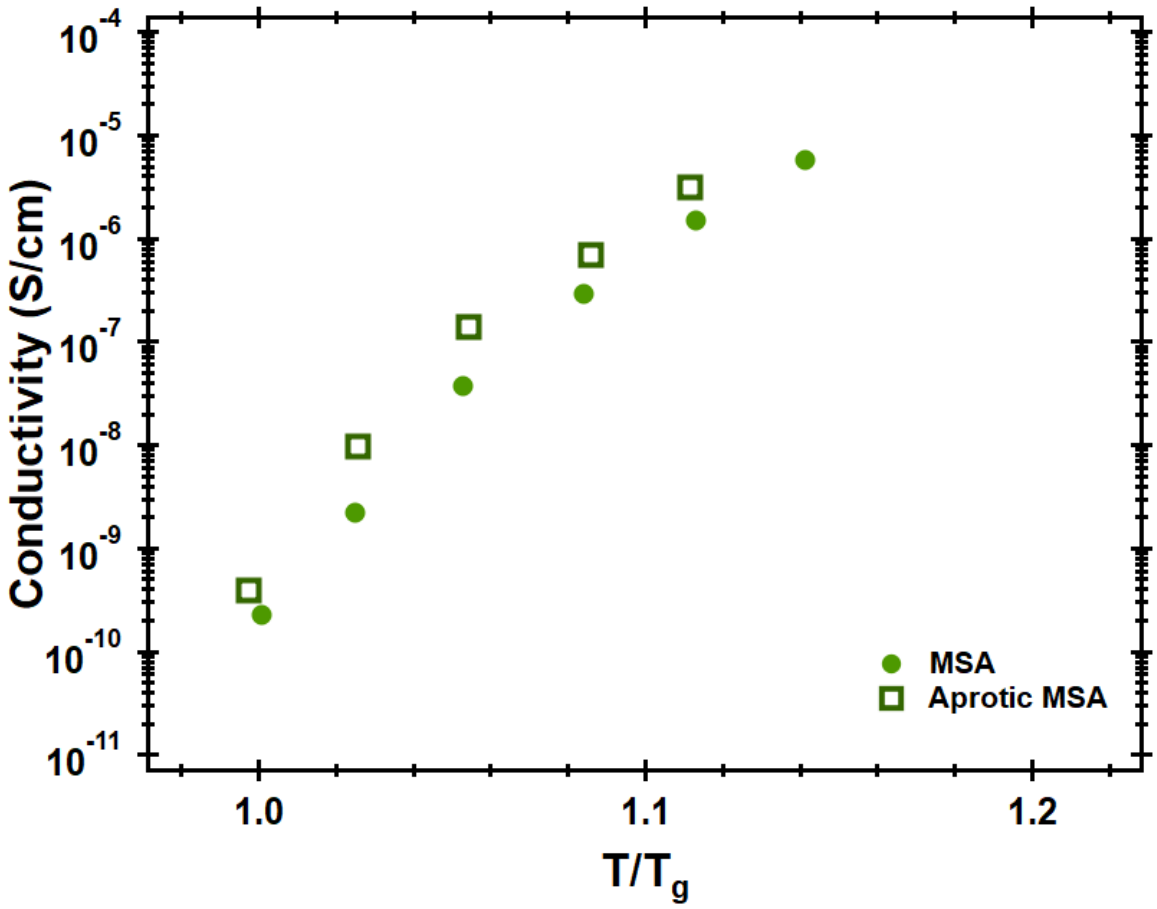

Figure 2.33 Normalized conductivity comparing the protic MSA (**pPy-MS**) and the aprotic MSA (**aPy-MS**) polymer samples.

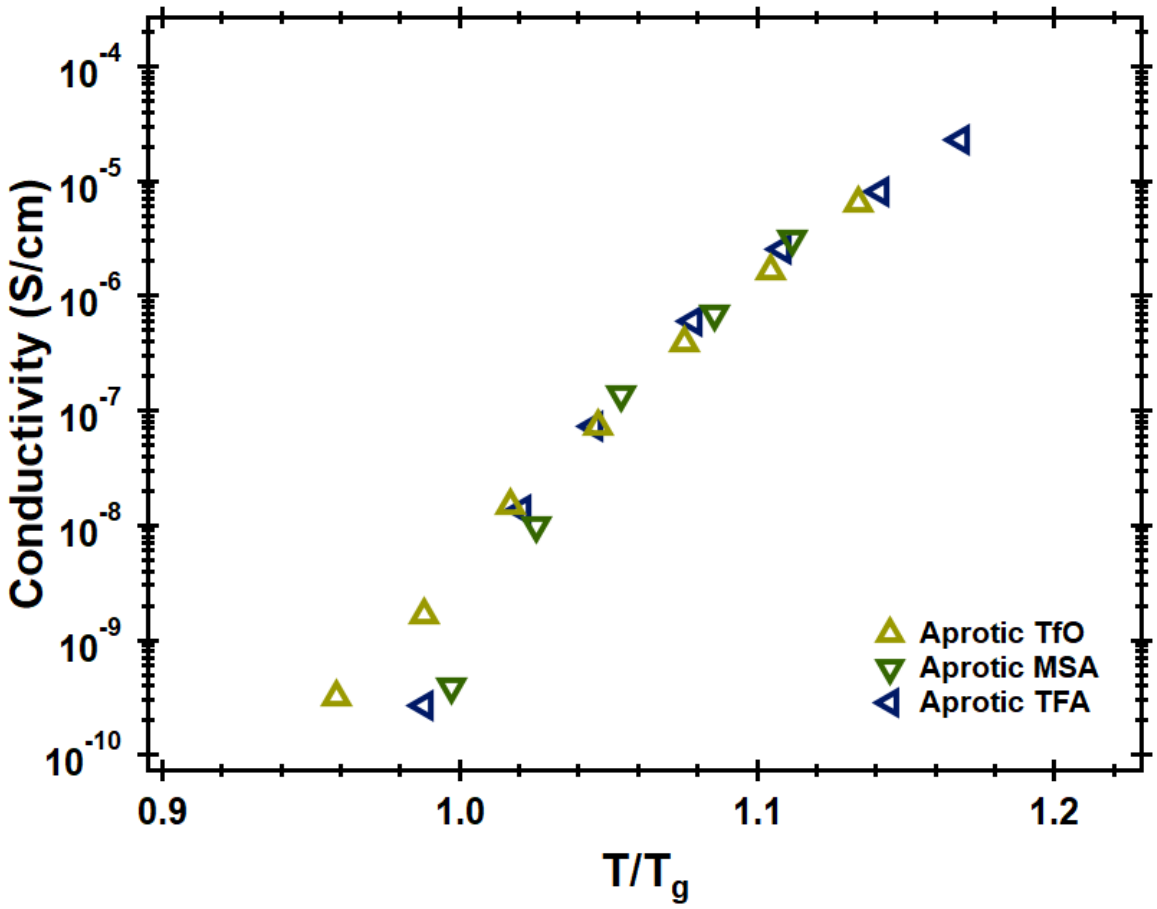

Figure 2.34 Normalized condictivities of aprotic analogues studied. Above T_g all poly aprotic ionic liquids collapse onto a single line, suggesting that H-bonding is the dominant interionic interaction in the polyPILs.

2.5.2.5 Pulse Field Gradient Nuclear Magnetic Resonance Spectroscopy

HTFSI	**^{19}F NMR**			**Calculated**
Set Temp (°C)	Actual Temp (°C)	Temp K	D (m^2s^{-1})	σ (Scm^{-1})
90	82.5	355.6	1.121E-13	4.489E-05

Table 2.2 Raw data collected from fitting the PFG-NMR diffusion spectra for **aPy-TFSI**. Conductivity calculated using Nernst-Einstein equation (**Equation 2.1**).

DFA	19F NMR			1H NMR						
Set Temp	Act Temp	Temp K	D (m^2s^{-1})	Act Temp	Temp K	I1	D1 (m^2s^{-1})	I2	D2 (m^2s^{-1})	^1H Transport
75C	69.3	342.4	3.847E-13	69.1	342.2	0.2708	4.475E-13	0.301	2.609E-12	0.87
80C	73.7	346.8	5.32E-13	73.3	346.5	0.6654	5.804E-13	0.1769	3.336E-12	0.86
85C	78.1	351.2	7.167E-13	77.6	350.7	0.8703	7.996E-13	0.08571	4.327E-12	0.86
90C	82.5	355.6	9.769E-13	81.9	355.0	0.9166	1.075E-12	0.05461	5.048E-12	0.84
									Average t+	0.86
									error	0.01

Table 2.3 Raw data collected from fitting the PFG-NMR diffusion spectra for **aPy-DFA**.

σ (Scm^{-1})						
DFA	19F NMR	1H NMR				
H Temp	Anion	Anion	Protic	Anion Avg	Anion Std Dev	Total
69.1	5.399E-05	6.284E-05	3.664E-04	5.842E-05	4.42642E-06	0.000425
73.3	7.372E-05	8.050E-05	4.627E-04	7.71091E-05	3.3938E-06	0.00054
77.6	9.806E-05	1.096E-04	5.929E-04	0.00010381	5.74717E-06	0.000697
81.9	1.320E-04	1.455E-04	6.833E-04	0.000138766	6.7554E-06	0.000822

Table 2.4 Conductivity for pPy-DFA calculated using data from **Table 2.3** and Nernst-Einstein equation (**Equation 2.1**).

MFA	19F NMR			1H NMR						
Set Temp	Act Temp	Temp K	D (m^2s^{-1})	Act Temp	Temp K	I1	D1 (m^2s^{-1})	I2	D2 (m^2s^{-1})	^1H Transport
75C	69.3	342.4	4.055E-13	69.1	342.2	0.5388	1.613E-13	0.4566	1.074E-12	0.73
80C	73.7	346.8	5.773E-13	73.3	346.5	0.4492	6.147E-13	0.5435	2.11E-12	0.79
85C	78.1	351.2	7.94E-13	77.6	350.7	0.596	9.832E-13	0.401	3.009E-12	0.79
90C	82.5	355.6	1.103E-12	81.9	355.0	0.5121	1.194E-12	0.4905	3.294E-12	0.75
									Average t+	0.76
									error	0.02

Table 2.5 Raw data collected from fitting the PFG-NMR diffusion spectra for **aPy-MFA**.

σ (Scm^{-1})						
MFA	19F NMR	1H NMR				
H Temp	Anion	Anion	Protic	Anion Avg	Anion Std Dev	Total
69.1	5.691E-05	2.265E-05	1.508E-04	3.97807E-05	1.7129E-05	0.000191
73.3	7.999E-05	8.526E-05	2.927E-04	8.26263E-05	2.6341E-06	0.000375
77.6	1.086E-04	1.347E-04	4.123E-04	0.000121676	1.30368E-05	0.000534
81.9	1.491E-04	1.616E-04	4.459E-04	0.00015534	6.28976E-06	0.000601

Table 2.6 Conductivity for pPy-MFA calculated using data from **Table 2.5** and Nernst-Einstein equation (**Equation 2.1**)

2.5.3 Density Functional Theory Calculations

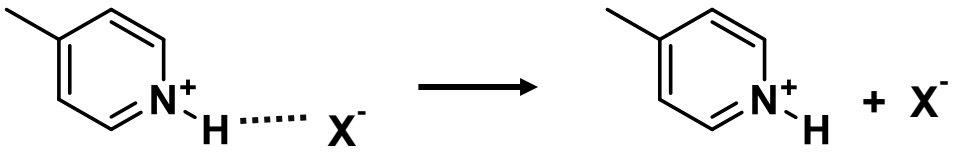

Scheme 2.2 Depiction of ion association utilized in DFT calculations to determine the energy of free vs ion-paired ionic liquid motifs. On the left side of the reaction scheme, depicted is the direction interaction between the protic cation and the anion. For the protic series, the lowest energy confirmation, was the anion participating in a hydrogen bond to the cation. On the right side of the equation depicts if the hydrogen bond is broken and the summation of the energy of both species is taken as the total engery for the system. The ΔE for the reaction, defined as the sum of energy of the products (right side of equation) minus the energy of the products (left side of equation), was then calculated. As written, for any ΔE value < 0, the right side of the equation is favored, i.e. free ions, whereas a ΔE value > 0 favors the ion-paired species.

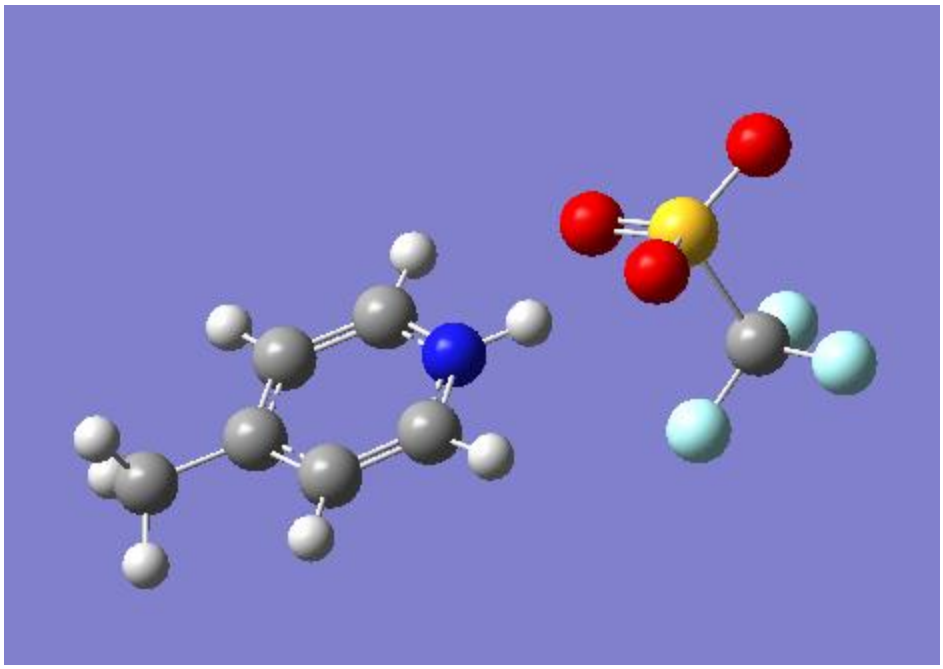

Figure 2.35 Optimized structure for triflate (TfO) with pyridine-H^+; X-H bond = 1.75 Å; N-H bond = 1.04 Å

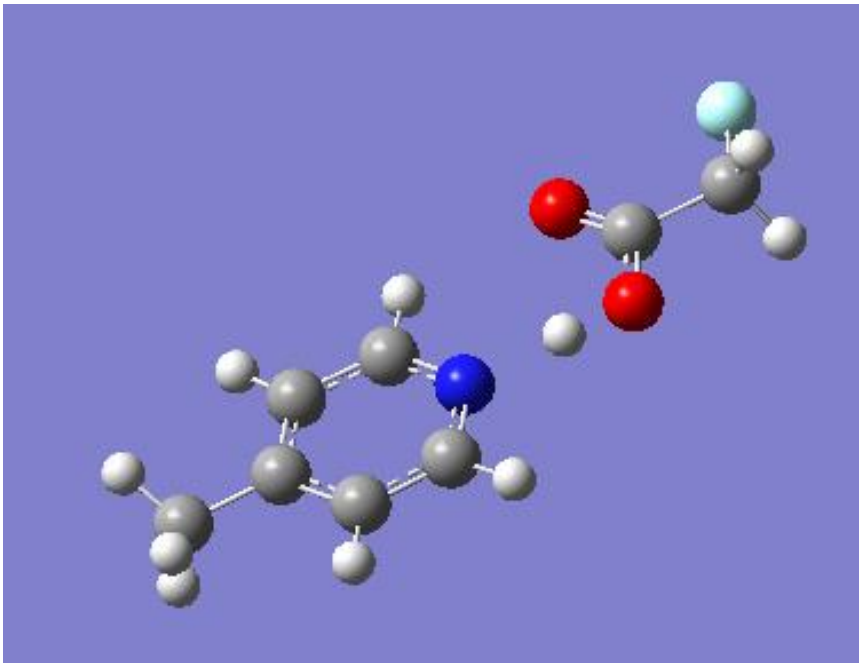

Figure 2.36 Optimized structure for fluoroacetate, CFH_2COO^-, ($[MFA]^-$) with pyridine-H^+; X-H bond = 1.05 Å; N-H bond = 1.53 Å

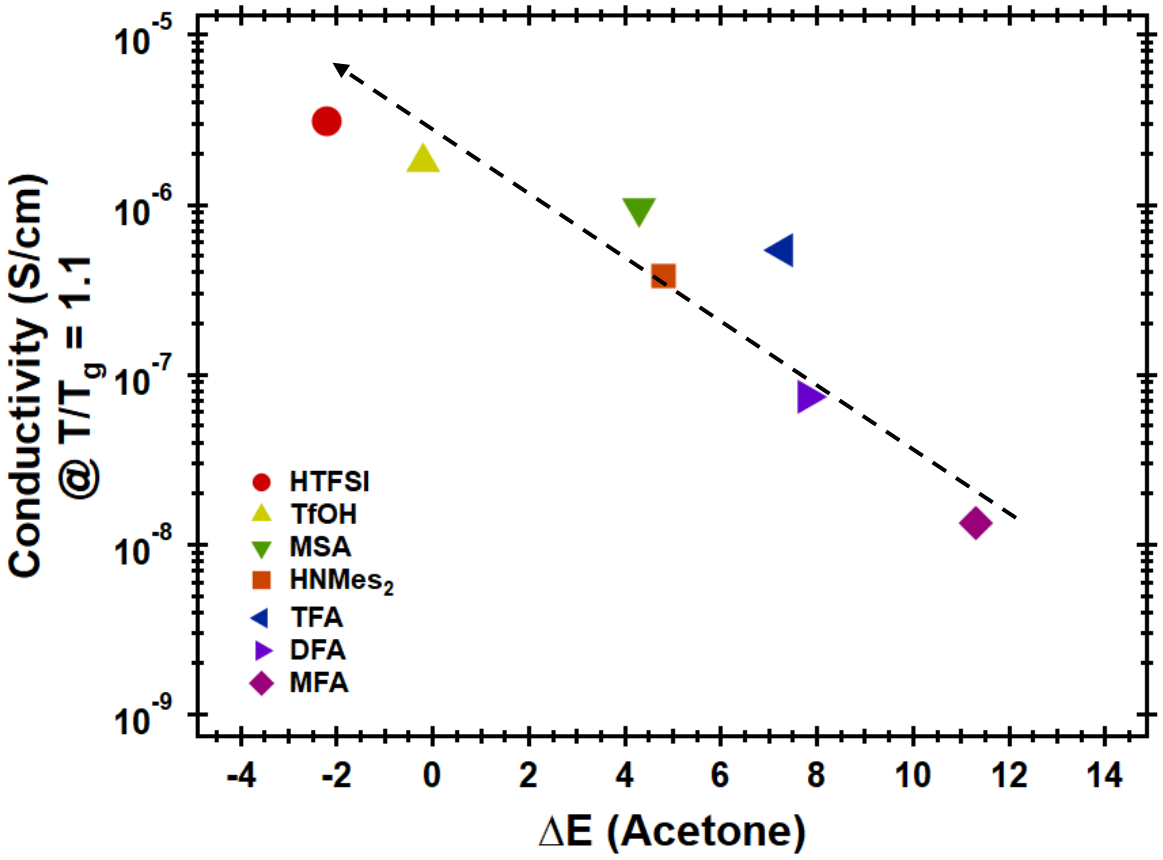

Figure 2.37 T_g normalized conductivities as a function of ΔE values calculated from DFT in acetone at a specified T/T_g. Black dashed arrow added to suggest the correlation of ΔE and conductivity. Compared to **Figure 2.2**, an almost identical trend is noted, showcasing the utility of DFT as a means to help predict the performance of polyIL structures.

2.6 References – Chapter 2

(1) Walden, P. *Bull. l'Academie Imp. des Sci. St.-petersbg.* **1914**, *8*, 405–422.

(2) Angell, C. A.; Byrne, N.; Belieres, J. *Acc. Chem. Res.* **2007**, *40*, 1228–1236.

(3) Belieres, J. P.; Angell, C. A. *J. Phys. Chem. B* **2007**, *111*, 4926–4937.

(4) Hayes, R.; Warr, G. G.; Atkin, R. *Chem. Rev.* **2015**, *115*, 6357–6426.

(5) Hallett, J. P.; Welton, T. *Chem. Rev.* **2011**, *111*, 3508–3576.

(6) Wasserscheid, P.; Welton, T. *Ionic Liquids in Synthesis*; Wasserscheid, P., Welton, T., Eds.; Wiley-VCH: Weinheim, 2003.

(7) Greaves, T. L.; Drummond, C. J. *Chem. Rev.* **2008**, *108*, 206–237.

(8) Zayas, M. S.; Gaitor, J. C.; Nestor, S. T.; Minkowicz, S.; Sheng, Y.; Mirjafari, A. *Green Chem.* **2016**, *18*, 2443–2452.

(9) Vekariya, R. L. *J. Mol. Liq.* **2017**, *227*, 44.

(10) Kulkarni, P. S.; Branco, L. C.; Crespo, J. G.; Nunes, M. C.; Raymundo, A.; Afonso, C. A. M. *Chem. - A Eur. J.* **2007**, *13*, 8478–8488.

(11) Noda, A.; Hasan Susan, M. A. Bin; Kudo, K.; Mitsushima, S.; Hayamizu, K.; Watanabe, M. *J. Phys. Chem. B* **2003**, *107*, 4024–4033.

(12) Miran, M. S.; Kinoshita, H.; Yasuda, T.; Susan, M. A. B. H.; Watanabe, M. *Phys. Chem. Chem. Phys.* **2012**, *14*, 5178–5186.

(13) O'Brien, R. A.; Zayas, M. S.; Nestor, S. T.; Gaitor, J. C.; Paul, L. M.; Edhegard, F. A.; Minkowicz, S.; Sykora, R. E.; Sheng, Y.; Michael, S. F.; Isern, S.; Mirjafari, A. *New J. Chem.* **2016**, *40*, 7795–7803.

(14) Greaves, T. L.; Drummond, C. J. *Chem. Rev.* **2015**, *115*, 11379–11448.

(15) Hirao, M.; Sugimoto, H.; Ohno, H. *J. Electrochem. Soc.* **2000**, *147*, 4168.

(16) Zhang, Q.; Yuan, H. Y.; Fukaya, N.; Yasuda, H.; Choi, J. C. *Green Chem.* **2017**, *19*, 5614–5624.

(17) Mumford, K. A.; Pas, S. J.; Linseisen, T.; Statham, T. M.; Johann Nicholas, N.; Lee, A.; Kezia, K.; Vijayraghavan, R.; MacFarlane, D. R.; Stevens, G. W. *Int. J. Greenh. Gas Control* **2015**, *32*, 129–134.

(18) Stoimenovski, J.; Dean, P. M.; Izgorodina, E. I.; MacFarlane, D. R. *Faraday Discuss.* **2012**, *154*, 335–352.

(19) Li, Z.; Xu, J.; Li, D.; Li, C. *RSC Adv.* **2015**, *5*, 15892–15897.

(20) Mayrand-Provencher, L.; Lin, S.; Lazzerini, D.; Rochefort, D. *J. Power Sources* **2010**, *195*, 5114–5121.

(21) Smiglak, M.; Pringle, J. M.; Lu, X.; Han, L.; Zhang, S.; Gao, H.; MacFarlane, D. R.; Rogers, R. D. *Chem. Commun.* **2014**, *50*, 9228–9250.

(22) Lee, S. Y.; Ogawa, A.; Kanno, M.; Nakamoto, H.; Yasuda, T.; Watanabe, M. *J. Am. Chem. Soc.* **2010**, *132*, 9764–9773.

(23) Snyder, J.; Fujita, T.; Chen, M. W.; Erlebacher, J. *Nat. Mater.* **2010**, *9*, 904–907.

(24) Watanabe, M.; Thomas, M. L.; Zhang, S.; Ueno, K.; Yasuda, T.; Dokko, K. *Chem. Rev.* **2017**, *117*, 7190–7239.

(25) Macfarlane, D. R.; Tachikawa, N.; Forsyth, M.; Pringle, J. M.; Howlett, P. C.; Elliott, G. D.; Davis, J. H.; Watanabe, M.; Simon, P.; Angell, C. A. *Energy Environ. Sci.* **2014**, *7*, 232–250.

(26) Khan, A.; Gunawan, C. A.; Zhao, C. *ACS Sustain. Chem. Eng.* **2017**, *5*, 3698–3715.

(27) Shaplov, A. S.; Marcilla, R.; Mecerreyes, D. *Electrochim. Acta* **2015**, *175*, 18–34.

(28) Nishimura, N.; Ohno, H. *Polymer* **2014**, *55*, 3289–3297.

(29) Qian, W.; Texter, J.; Yan, F. *Chem. Soc. Rev.* **2017**, *46*, 1124–1159.

(30) Mecerreyes, D. *Prog. Polym. Sci.* **2011**, *36*, 1629–1648.

(31) Yuan, J.; Antonietti, M. *Polymer* **2011**, *52*, 1469–1482.

(32) Ohno, H.; Ito, K. *Chemistry Letters*. 1998, pp 751–752.

(33) Choi, U. H.; Ye, Y.; Salas De La Cruz, D.; Liu, W.; Winey, K. I.; Elabd, Y. A.; Runt, J.; Colby, R. H. *Macromolecules* **2014**, *47*, 777–790.

(34) Iacob, C.; Matsumoto, A.; Brennan, M.; Liu, H.; Paddison, S. J.; Urakawa, O.; Inoue, T.; Sangoro, J.; Runt, J. *ACS Macro Lett.* **2017**, *6*, 941–946.

(35) Nie, H.; Schauser, N. S.; Dolinski, N. D.; Hu, J.; Hawker, C. J.; Segalman, R. A.; Alaniz, J. R. De. *Angew. Chemie - Int. Ed.* **2020**, *59*, 5123–5128.

(36) Zhang, Y.; Maginn, E. J. *J. Phys. Chem. Lett.* **2015**, *6*, 700–705.

(37) Mogurampelly, S.; Keith, J. R.; Ganesan, V. *J. Am. Chem. Soc.* **2017**, *139*, 9511–9514.

(38) Keith, J. R.; Rebello, N. J.; Cowen, B. J.; Ganesan, V. *ACS Macro Lett.* **2019**, *8*, 387–392.

(39) Chen, H.; Choi, J. H.; Cruz, D. S. D. La; Winey, K. I.; Elabd, Y. A. *Macromolecules* **2009**, *42*, 4809–4816.

(40) Anton, A. M.; Frenzel, F. **2020**, 6091–6101.

(41) Cui, L.; Lattermann, G. *Macromol. Chem. Phys.* **2002**, *203*, 2432–2437.

(42) Borman, S. *Chem. Eng. News Arch.* **2006**, *84*, 40–41.

(43) Willcock, H.; O'Reilly, R. K. *Polym. Chem.* **2010**, *1*, 149–157.

(44) Fultz, B. A.; Beery, D.; Coia, B. M.; Hanson, K.; Kennemur, J. G. *Polym. Chem.* **2020**, *11*, 5962–5968.

(45) Otsuka, H.; Hagiwara, T.; Yamamoto, S. *J. Nanosci. Nanotechnol.* **2014**, *14*, 6764–6773.

(46) Yoshizawa, M.; Xu, W.; Angell, C. A. *J. Am. Chem. Soc.* **2003**, *125*, 15411–15419.

(47) Schauser, N. S.; Nikolaev, A.; Richardson, P. M.; Xie, S.; Johnson, K.; Susca, E. M.; Wang, H.; Seshadri, R.; Clément, R. J.; Read De Alaniz, J.; Segalman, R. A. *ACS Macro Lett.* **2021**, 104–109.

(48) Paenurk, E.; Kaupmees, K.; Himmel, D.; Kütt, A.; Kaljurand, I.; Koppel, I. A.; Krossing, I.; Leito, I. *Chem. Sci.* **2017**, *8*, 6964–6973.

(49) Marcus, Y. *J. Mol. Liq.* **2015**, *209*, 289–293.

(50) Miran, M. S.; Kinoshita, H.; Yasuda, T.; Susan, M. A. B. H.; Watanabe, M. *Chem. Commun.* **2011**, *47*, 12676–12678.

(51) Ye, Y.; Elabd, Y. A. *Polymer* **2011**, *52*, 1309–1317.

(52) Philippi, F.; Pugh, D.; Rauber, D.; Welton, T.; Hunt, P. A. *Chem. Sci.* **2020**, *11*, 6405–6422.

(53) Stoimenovski, J.; Izgorodina, E. I.; MacFarlane, D. R. *Phys. Chem. Chem. Phys.* **2010**, *12*, 10341–10347.

(54) Miran, M. S.; Hoque, M.; Yasuda, T.; Tsuzuki, S.; Ueno, K.; Watanabe, M. *Phys. Chem. Chem. Phys.* **2019**, *21*, 418–426.

(55) Doi, H.; Song, X.; Minofar, B.; Kanzaki, R.; Takamuku, T.; Umebayashi, Y. *Chem. - A Eur. J.* **2013**, *19*, 11522–11526.

(56) Karlsson, C.; Jannasch, P. *ACS Appl. Energy Mater.* **2019**, *2*, 6841–6850.

(57) Pringle, J. M.; Golding, J.; Baranyai, K.; Forsyth, C. M.; Deacon, G. B.; Scott, J. L.; MacFarlane, D. R. *New J. Chem.* **2003**, *27*, 1504–1510.

(58) Albler, C.; Schmid, W. *European J. Org. Chem.* **2014**, *2014*, 2451–2459.

3 Tuning merocyanine photoacid structure to enhance solubility and temporal control: application in ring opening polymerization

3.1 Abstract

The development of a merocyanine-based photoacid is reported, which demonstrates improved solubility in organic media and enhanced switching kinetics that can be used to impart temporal control over ring opening polymerization. The effect of the structural modification on solubility, thermal relaxation kinetics and activation energy were evaluated using ^{1}H NMR and pump-probe absorption spectroscopies. Overall, the new merocyanine based photoacid provides access to a wider range of chemical and material applications with improved solvent compatibility and temporal control.

3.2 Introduction

The ability to control acid-driven processes with a high degree of both spatial and temporal control has enabled breakthrough advances in material science,[1,2] photo-responsive systems,[3,4] and biological systems.[5–7] Central to these advances has been the development of metastable photoacids (mPAHs) that enable the concentration of protons to be reversibly increased and decreased using visible light as a non-invasive and mild stimulus.[8] Since the report of the first merocyanine-type mPAH in 2011 by Liao and co-workers,[9] a range of structural derivatives have been developed to improve their photoacidity,[4] reduce dark acidity, and increase quantum yield.[10] Although notable advances have been made, optimization of the properties of this emerging class of photoswitch is far from complete.

Challenges that prevent the widespread adoption of merocyanine-type photoacids include poor solubility in aprotic organic media and slow thermal reversion from the spiropyran (SP) photoproduct to the protonated merocyanine (MCH^+).[11] Merocyanine-type mPAHs contain an SO_3^- anion that stabilizes the planar conjugated, open-ring indolinium cation isomer. However, this zwitterionic and planar conjugated structure also results in the poor solubility of these molecules in organic media. The utility of merocyanine-type photoacids has thus largely been limited to polar protic media, most often aqueous and methanol solutions.[8,10,12,13] Limited solubility and aggregate formation are also observed when the merocyanine isomer is generated under irradiation in organic media from the corresponding spiropyran photoswitch.[14] In addition to solubility challenges, the slow thermal reversion limits the spatial and temporal control permitted in pH-driven processes with the remaining acidic SP form continuing to mediate acid-catalyzed reactions. This undesired reactivity was observed when Xu and Boyer employed mPAH for the photoacid-mediated ring-opening polymerization (ROP) of lactones, wherein 15% conversion occurred in the dark after light exposure.[15] Such behavior has been observed in other photo ROP systems[16] and highlights the need to cleanly turn off catalysis after ceasing light irradiation.

One strategy to address these shortcomings is tuning the architecture of mPAHs. Thermal reversion rates from the SP form to the open MCH^+ form and their solubility correlate closely with chemical structure. Liao has published reports of increasing the reversion reaction rate of mPAH in H_2O:acetone solutions[11] and thin films[17] by introducing an electron rich methoxy group on the phenolic moiety. For this system, the reversion rate is ~50-times higher than the derivative lacking the methoxy group. Similar trends have been observed independently by Sumaru[18] and Thomas[19]. Additionally, substitution of an electron-donating methoxy group on the phenolic moiety increased

the conversion rate from SP to MCH^+, whereas the substitution of an electron-withdrawing nitro group decreased the rate. In these examples, the studies were performed in media previously optimized for mPAH and thus exclusively focused on aqueous polar solutions and thin films with highly hydrophilic polymer matrices (i.e., hydroxyethyl methacrylate).[20] Yokoyama has also reported a derivative bearing a *t*-Bu alkyl group on the phenol moiety that improved the solubility of mPAHs in organic solvent.[4] This structurally modified mPAH was successfully solubilized in a chloroform solution, however it was still limited to sub-mM concentrations and no thermal reversion studies were conducted. Since these modifications demonstrate that both the reversion rates and solubility can be tuned, it seems reasonable to anticipate that designing an mPAH that is compatible with organic solvents is feasible.

Guided by the lessons learned from previous work described above, we developed an mPAH that has both enhanced solubility in organic solvents and increased reversion rates. Our initial work focused on incorporating sterically hindered *tert*-butyl groups to increase solubility and to prevent aggregate formation (**Scheme 3.1**). In addition, because the rate limiting step in the reverse reaction is protonation of the phenolic oxygen atom in the SP photoproduct,[21–23] increasing electron density by the addition of electron donating groups should also accelerate the reverse reaction rate.[19,24] With these considerations in mind, we prepared gram scale quantities of mPAH **PAH-2** in 2 steps and 72% overall yield from commercially available 3,5-di-*tert*-butyl-2-hydroxy-benzaldehyde using simple, scalable synthetic strategies. The new derivative is readily solubilized in a wide range of solvents at higher concentrations than previously demonstrated. Furthermore, these simple structural modifications not only retain excellent photoswitching properties but also significantly improve thermal recovery kinetics in aprotic organic solvents. We highlight such advantages by using PAH-2 to mediate photo-ROP of a lactone with on/off temporal control.

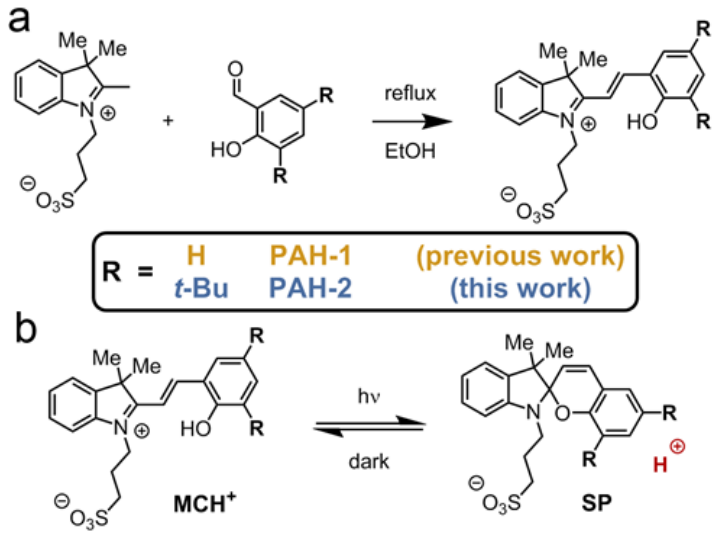

Scheme 3.1 a) Reaction scheme depicting facile synthesis from commercially available benzaldehyde derivatives. b) T-type photoswitch, forward reaction driven by photoirradiation, whereas the reverse reaction is thermally driven. (Reprinted with permission from ChemPhotoChem., 2019, 3. Copyright 2019 John Wiley and Sons.)

3.3 Results and Discussion

To initially establish the increased solubility of this new mPAH derivative in organic solvents, solutions (2.6 x 10^{-3} M) of **PAH-1** and **PAH-2** were prepared in dichloromethane (DCM) (**Figure 3.1**). In the vial containing **PAH-1**, (**Figure 3.1a**) the turbid suspension indicates an inhomogeneous solution. In direct contrast, the transparent solution containing **PAH-2** (**Figure 3.1b**) reveals significantly increased solubility which was also observed in acetonitrile, acetone, *p*-xylene and tetrahydrofuran solvents (**Figure 3.18**). Additionally, the optical properties were characterized by UV-Vis spectroscopy in these solvents and are discussed in detail in the Materials and Methods section (**Figure 3.9 – Figure 3.17**). Combined these studies showcase the utility of this derivative in a wide range of organic media.

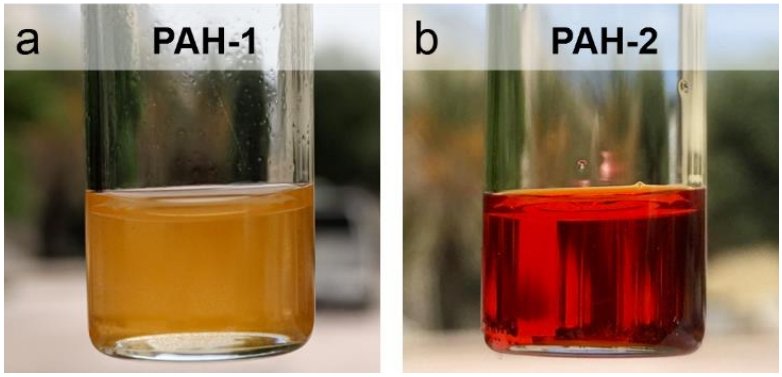

Figure 3.1 Differences in solubility between a) PAH-1 and b) PAH-2. Each sample was prepared targeting a 2.6 mM of the respective mPAH in DCM. (Reprinted with permission from ChemPhotoChem., 2019, 3. Copyright 2019 John Wiley and Sons.)

The photoswitching and thermal relaxation properties of the photoacid were then characterized in various environments. Previous studies of **PAH-1** showed that solvents with a large hydrogen bond donor (HBD) acidity (Taft–Kamlet α scale)[21]{FormattingCitation} increased the rate of reversion from SP to MCH^+. In these cases, the solvents studied (DMSO, ethanol and water) are of two types: hydrogen bond acceptors (HBA), such as DMSO and solvents capable of acting as both HBA's and hydrogen bond donors (HBD's), such as ethanol and water. Although these solvents demonstrate a trend with the α scale, the correlation is better described with the hydrogen bond acceptor (HBA) basicity (Taft–Kamlet β scale) of the solvent.[25] For comparison, the behavior of **PAH-2** was studied in a similar fashion, monitoring the switching rates under light irradiation and subsequent thermal relaxation *via* UV–Vis spectroscopy. To further expand the study, non-hydrogen bonding solvents, such as DCM (**Figure 3.2b**) and *p*-xylene (**Figure 3.21)**, as well as hydrogen bond accepting solvents, acetonitrile (MeCN) (**Figure 3.22**) and tetrahydrofuran (THF) (**Figure 3.23**), were added to the study. Interestingly, as described below, we find the β scale is in better agreement with this data set that compares solvents of all three

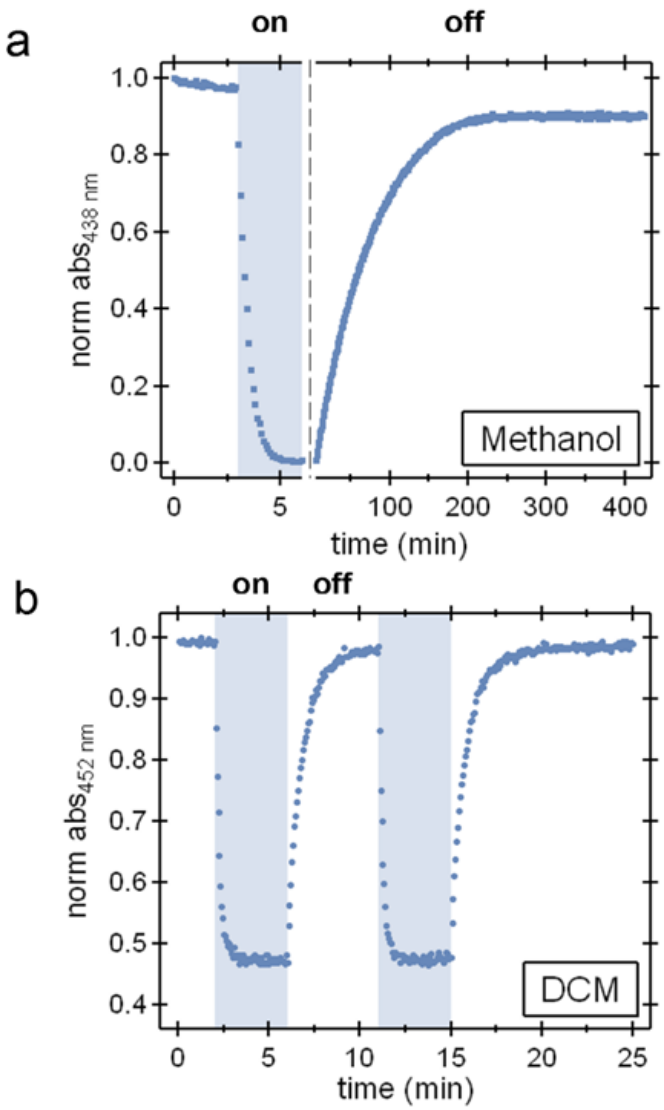

Figure 3.2 Pump–probe absorption spectroscopy of PAH-2 at room temperature, irradiating with 470 nm LED. (a) Detailed cycle showing photoresponse (<60 s) followed by thermal equilibration over 6.7 h in methanol. Time axis break accentuates the first 6 minutes of the cycle to highlight rapid rate of photocyclization. (b) Detailed cycles showing rapid photoresponse (<60 s) followed by fast thermal equilibration (≈4 min) in methylene chloride. (Reprinted with permission from ChemPhotoChem., 2019, 3. Copyright 2019 John Wiley and Sons.)

types: DCM and *p*-xylene (non-hydrogen bonding); DMSO, THF, and MeCN (HBA); and MeOH (HBD and HBA) (**Figure 3.25)**. For these studies, a **PAH-2** solution was left in the dark until equilibrium was reached and then placed into a UV−Vis spectrophotometer (see SI for full details). A 470 nm LED source was used to irradiate the samples orthogonally to the detector for 2–8 minutes, after which the solution was monitored in the dark until the photoswitch returned to equilibrium state. **Figure 3.2** illustrates the results for MeOH and DCM representing the slowest and fastest photoswitching systems, respectively. The half-life recovery time of MeOH, THF, MeCN, *p*-xylene and DCM solutions are 63, 8, 17, 0.97 and 0.64 min with this trend being consistent with HBA basicity (Taft−Kamlet β scale). The β scale values of MeOH, THF, MeCN, *p*-xylene and DCM are 0.66, 0.55, 0.40, 0.12 and 0.10 based on calculations by Marcus.[26] To better understand the effects of a more complex system on the photoswitching behavior, the relaxation kinetics were also studied in a chemical environment that could typically be used for a ring-opening polymerization (**Figure 3.26**). In this sample of 50 wt% ε-caprolactone in DCM, the half-life was found to be 15 min. This helps illustrate the utility of this photoacid in actual reaction conditions, not simply studied in an isolated fashion. The kinetics in methanol and DMSO were also studied using ^{1}H NMR. The half-life recovery times *via* ^{1}H NMR for methanol and DMSO solutions are 14 min and 282 min respectively, which is also consistent with the β-scale. Although further studies are necessary to completely understand solvent effects, the faster kinetics observed in non-hydrogen bonding, polar aprotic solvents imbues the photoswitch with a higher degree of temporal control than previously demonstrated.

The rate of the thermal reversion reaction is also related to the structure of MCH^{+} isomer. To further investigate the impact of the structural modifications (i.e., adding the two *t*-Bu groups to

the phenolic moiety) on the rate of relaxation to the MCH^+ isomer, non-invasive NMR monitoring, and kinetic modeling (**Equation 3.1**)

$$\frac{[B]_t}{[A]_0} = 1 - \left(\frac{k_{\text{close}} + k_{\text{open}} e^{-(k_{\text{close}} + k_{\text{open}})t}}{k_{\text{close}} + k_{\text{open}}} \right)$$

Equation 3.1

were used to directly measure this transformation *in situ.* In this study, a 9 mM solution of the mPAH was prepared in 0.75 mL of deuterated DMSO. The vial containing the solution was then wrapped in aluminum foil and the solution was stirred under irradiation with a 470 nm fiber optic coupled light (see SI) for 30 minutes. Samples were equilibrated to set temperatures in the NMR spectrometer and the appearance of the open MCH^+ isomer was monitored over time with respect to the overall concentration As expected, in a similar chemical environment, **PAH-2** shows much faster relaxation kinetics than does **PAH-1** (**Figure 3.31** and **Figure 3.29**, respectively). This is consistent with previous studies,[11] where increasing the electron density on the phenolic moiety increases the rate of conversion between the SP and MCH^+ isomers. From these rates, kinetic rate constants and activation energies (E_a) (**Figure 3.3b, c**) can be determined by fitting to a dynamic equilibrium model (**Equation 3.1**). This dynamic equilibrium model assumes that both forward and reverse reactions follow first-order kinetics, allowing for the determination of the forward and reverse rates simultaneously. Our group has previously used this model to successfully describe photoswitch equilibration.[27,28] In DMSO, the activation energies are similar for both PAHs (**Figure 3.3c**). However, it should be noted that the equilibrium state of **PAH-2** in DMSO is 59% in the MCH^+ isomer, whereas for **PAH-1** the equilibrium state is 98% in the MCH^+ isomer. This lower equilibrium presents a limitation in the utility of **PAH-2** in this solvent because it can result in undesired catalysis in the dark. To address this limitation, we also explored the relaxation kinetics

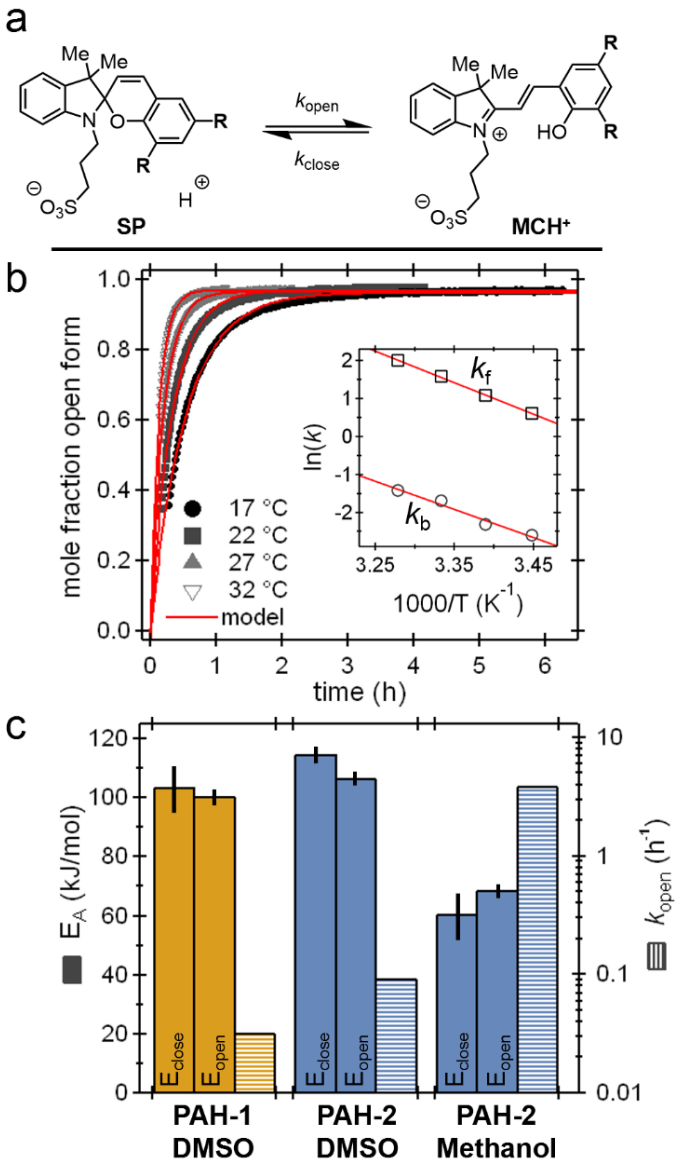

Figure 3.3 a) Schematic of thermal relaxation from the SP to MCH^+ isomer. b) The ratio of MCH^+ over time for **PAH-2** in methanol-d_4 at varying temperatures. Inset plots the rate constants in an Arrhenius fashion. c) Comparison of activation energies for the ring closing reaction (MCH^+ to SP, left bar) and the ring opening reaction (SP to MCH^+, middle bar) as well as the ring opening rate constant (right bar) for each given condition. (Reprinted with permission from ChemPhotoChem., 2019, 3. Copyright 2019 John Wiley and Sons.)

of **PAH-2** in deuterated methanol (**Figure 3.3b**). Here, compared with the DMSO data for **PAH-2**, the methanol solution is able to recover much faster at lower temperatures and the activation energies are significantly lower. Importantly, the equilibrium ratio state of the MCH^+ in deuterated methanol is 98%. This results in a higher degree of control over the photoswitching states, which improves relaxation to the nonacidic state and mitigates the issue of unwanted dark acidity. Attempts were made to study **PAH-1** in methanol but peak broadening of the closed form, likely due to aggregation, was observed that distorted the data and made fitting difficult/unphysical. In addition, attempts were made to study the thermal kinetics of **PAH-2** in deuterated DCM, unfortunately, the sampling rate of the NMR was too slow (~1 scan/30 seconds) to capture the rapid equilibration with enough range for accurate fitting of the reverse reaction rate. Overall, the addition of the sterically bulky, electron donating, alkyl groups on the phenolic side of the mPAH not only increased the solubility into a wider range of organic solvents, but also dramatically improved the rate of relaxation to the MCH^+ isomer.

With this noted increase in temporal control of the on/off photoinduced acidity, the utility of this photoacid was examined via use as a photocatalyst for cationic ROP of lactones. To allow for comparison with previous work, initial studies were conducted in propylene carbonate. Note that in the original study[15]propylene carbonate was chosen as a solvent due to the generally poor solubility of **PAH-1**. A solution of benzyl alcohol (1 eq., 10.8 mg) as the initiator, ε-caprolactone (50 eq., 570 mg), and **PAH-2** (0.25 eq., 12.4 mg) were mixed in 1 mL of propylene carbonate and irradiated with a 470 nm fiber optic coupled LED. This solution was treated with successive 8 h periods of turning the light on and off for a total of 40 h. As observed in **Figure 3.4b**, **PAH-2** (blue circles) demonstrated a large degree of temporal control over the polymerization. During the first 8 h irradiation period, monomer conversion was observed to be 21% by ^1H NMR with further

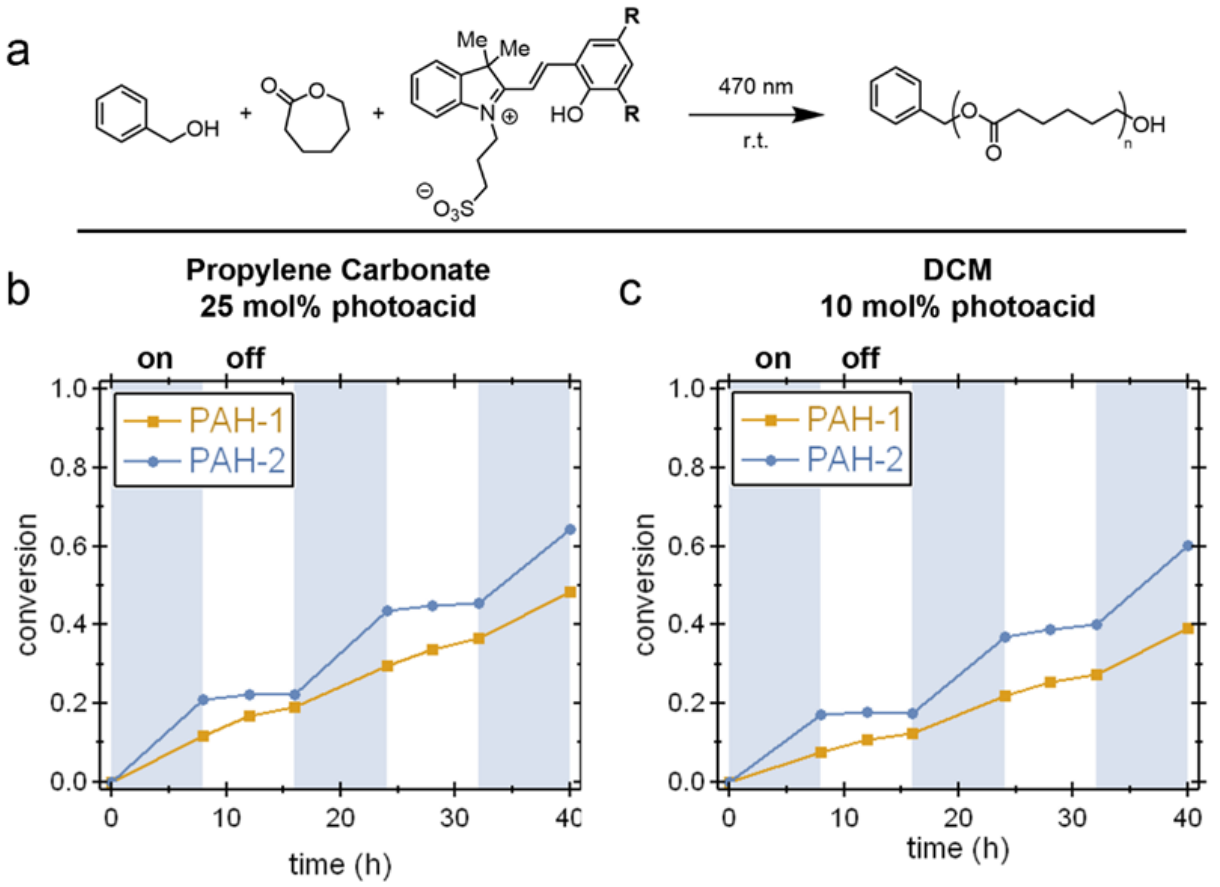

Figure 3.4 a) Reaction scheme used to temporally control the ring-opening polymerization of ε-caprolactone with an mPAH photocatalyst. b) **PAH-1** (orange squares) exerts poor temporal control over polymerization. Once the reaction is initiated, polymerization continues almost unaffected by light being cycled on or off. In contrast, **PAH-2** (blue circles) exhibits a marked improvement in the speed of the polymerization during irradiation, which almost completely halts during off periods. c) Similar results are observed in DCM with lower catalyst loading (10 mol%). **PAH-1** induces poor temporal control and sluggish kinetics, unlike **PAH-2**. (Reprinted with permission from ChemPhotoChem., 2019, 3. Copyright 2019 John Wiley and Sons.)

analysis during the subsequent 8 h dark period showing only 2% conversion. Repetitive cycles of on/off exposure demonstrated the ability to impart a high degree of temporal control. For comparison, the same experimental conditions were used to evaluate the efficiency of **PAH-1** to temporally control the polymerization of caprolactone. As demonstrated in **Figure 3.4b**, the behavior of **PAH-1** (orange squares) follows closely with previously described behavior and results in poor on/off switching. In addition, an unexpected difference with **PAH-1** versus **PAH-2** is a marked decrease in the rate of polymerization with higher conversion being observed when **PAH-2** was used. Motivated by these results and the demonstrated increase in solubility and improved reversion kinetics for **PAH-2** in aprotic organic solvents, the ring opening of ε-caprolactone was studied in DCM (**Figure 3.4c**). In addition to changing solvent, the catalyst loading was decreased to 10 mol%. Under these conditions, **PAH-2** once again demonstrated good temporal control with 17% conversion being observed during the first irradiation period and only 1% conversion during the subsequent 8 h dark period with cycling leading to high conversions. It should be noted that this increased conversion is obtained using DCM despite the catalytic loading being decreased from 25 (propylene carbonate) to 10 mol% (DCM). When **PAH-1** is employed under identical conditions, poor temporal control and inefficient polymerization (approximately 8% conversion during each irradiation period) is attributed to the aforementioned poor solubility of **PAH-1**. To ensure that irradiation is essential for polymerization, the reactions were mixed and then placed in the dark for 24 h in both propylene carbonate and DCM. Under these conditions no change in the NMR spectra was observed supporting that no reaction occurs in the absence of light (**Figure 3.33**). Additionally, due to the long irradiative periods, a control experiment was performed to test for photochemical degradation of the mPAH. In this experiment UV-Vis samples of **PAH-2** in the polymerization conditions of 50 wt% ε-caprolactone in DCM were prepared and

tested. The first sample was irradiated for 8 hours and the second sample irradiated for only 3 minutes. The two samples were then monitored by UV-Vis at room temperature for 4 h and 3 h, respectively. During these studies, both samples recovered to the same absorbance (**Figure 3.34)**, which suggests that photochemical degradation of the mPAH is not significant, despite the long irradiative periods.

3.4 Conclusion

This report describes the development of a merocyanine photoacid derivative that exhibits marked improvements in both organic solvent solubility and reversion kinetics to the non-acidic MCH^+ isomer upon cessation of light exposure. The straightforward structural modifications accessed using commercially available starting materials provide this class of photoswitches an enhanced ability to temporally and reversibly control the delivery of a proton. We envision that these benefits, herein demonstrated in the context of visible-light-mediated ring-opening polymerization, will find broader utility across chemical and materials applications that exploit stimuli-responsive catalysts.

3.5 Materials and Methods

3.5.1 Experimental Details

3.5.1.1 Materials

All materials were purchased from *Sigma Aldrich*, *Acros Organics*, or *Combi-Blocks* and used as received unless otherwise stated. ε-caprolactone was distilled and stored over 3 Å molecular sieves. All solvents were purchased from *Fisher Scientific* and used as received. The optical fiber (FT1000UMT; End A flat cleave; End B SMA adapter; Furcation Tubing-FT038), the T-cube LED driver (LEDD1B), and the fiber-coupled LED, 470 nm (M470F3) were purchased from Thorlabs.

The probe source DH-MINI – Deuterium Halogen light source was purchased from Ocean Optics. A 1 mm hole was drilled into a standard septa cap using an 18-gauge needle to guide the fiber.

3.5.1.2 Instrumentation

The ^{1}H NMR spectra were recorded on an Agilent Technologies 400-MR DD2 400 MHz, Varian Unity Inova 500 MHz, or a Varian Unity Inova AS600 600MHz spectrometer with a regulated temperature of 25 °C, unless noted otherwise. The ^{1}H NMR chemical shifts were calibrated to the resonances of chloroform-*d* at δ = 7.26, dichloromethane-d_2 at δ = 5.32, or dimethylsulfoxide-d_6 δ = 2.50.

FTIR spectra were recorded on a Perkin Elmer Spectrum 100 FT-IR Spectrometer.

UV-Vis spectra were recorded on an Agilent UV-Vis Spectrometer or a home-built setup (see below and **Figure 3.19**).

Size exclusion chromatography (SEC) for molecular weight analysis, relative to linear polystyrene standards, was performed on a Waters e2695 separation module equipped with Waters 2414 refractive index and 2996 photodiode array detectors using THF as eluent at a flow rate of 0.3 mL/min.

For photochemical transformations the LED was coupled into a multimode optical fiber terminated with a flat cleave and the intensity and on/off cycles were controlled through a digital-to-analog converter (National Instruments USB-6009) using LabVIEW, which was connected to a T-cube LED driver (LEDD1B) from Thorlabs. The photoinduced optical absorption kinetics were measured on a home-built pump-probe setup (**Figure 3.19**). The probe beam was generated by a UV-Vis light source (Ocean Optics DH-MINI deuterium halogen light source) coupled into a multimode optical fiber terminated with an output collimator. The pump beam was generated using a fiber-coupled blue LED, 470 nm (Thorlabs M470F3). The LED intensity was controlled

either manually or through a digital-to-analog converter (National Instruments USB-6009) using LabVIEW. The sample holder held 10x10 mm^2 rectangular spectrophotometer cells within. Further details can be found in previous literature.[29]

3.5.1.3 Synthesis

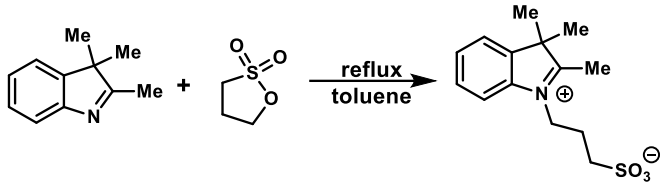

1 2 S1

3-(2,3,3-trimethyl-3*H*-indol-1-ium-1-yl)propane-1-sulfonate (S1):

The synthesis of 3-(2,3,3-trimethyl-3*H*-indol-1-ium-1-yl)propane-1-sulfonate (**S1**) was prepared according to previously reported protocols. Spectra agrees with reported literature.[9] **S1:** ^{1}H NMR (400 MHz, DMSO-d_6) δ 8.05 (d, J = 8.6 Hz, 1H), 7.82 (d, J = 8.7 Hz, 1H), 7.62 (t, J = 3.9 Hz, 2H), 4.70 – 4.61 (m, 1H), 2.83 (s, 3H), 2.62 (t, J = 6.6 Hz, 2H), 2.21 – 2.09 (m, 2H), 1.53 (s, 6H).

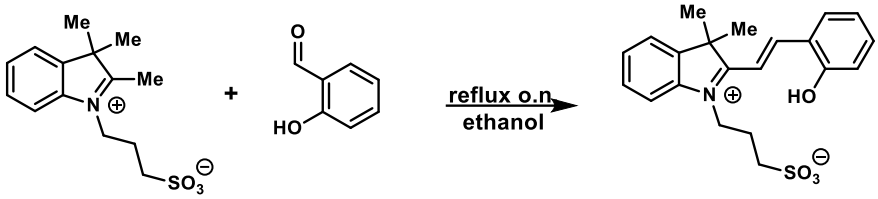

S1 3 PAH-1

(E)-3-(2-(2-hydroxystyryl)-3,3-dimethyl-3*H*-indol-1-ium-1-yl)propane-1-sulfonate (PAH-1):

The synthesis of (E)-3-(2-(2-hydroxystyryl)-3,3-dimethyl-3*H*-indol-1-ium-1-yl)propane-1-sulfonate **(PAH-1)** was prepared according to previously reported protocols. Spectra agrees with reported literature.[9] **PAH-1:** ^{1}H NMR (400 MHz, DMSO-d_6) δ 11.04 (s, 1H), 8.60 (d, *J* = 16.4 Hz, 1H), 8.28 (d, *J* = 8.0, 1H), 8.02 (d, *J* = 7.1 Hz, 1H), 7.93 – 7.84 (m, 2H), 7.62 (tt, *J* = 7.4, 6.1 Hz, 2H), 7.48 (t, *J* = 8.6 Hz, 1H), 7.07 – 6.95 (m, 2H), 4.80 (t, *J* = 8.0 Hz, 2H), 2.65 (t, *J* = 6.5 Hz, 2H), 2.17 (m, 2H), 1.77 (s, 6H).

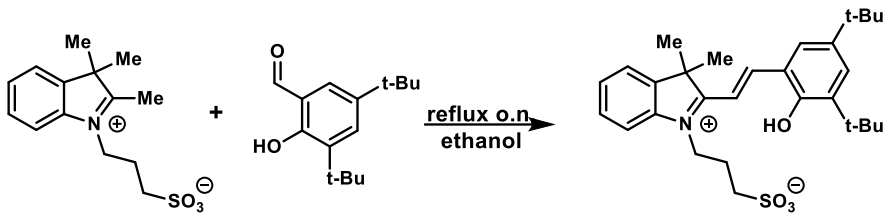

S1 4 PAH-2
72%

(*E*)-3-(2-(3,5-di-*tert*-butyl-2-hydroxystyryl)-3,3-dimethyl-3*H*-indol-1-ium-1-yl)propane-1-sulfonate (PAH-2):

To a solution of 3-(2,3,3-trimethyl-3*H*-indol-1-ium-1-yl)propane-1-sulfonate (**S1**) (3.05 g, 10.8 mmol, 1 eq) in absolute ethanol (30 mL) in a 100 mL round bottom flask charged with a stir bar was added 3,5-di-*tert*-butyl-2-hydroxybenzaldehyde (**4**) (5.51 g, 23.5 mmol, 2.2 eq). The reaction was fitted with a condenser and stirred under reflux for 16 hr. The reaction mixture was cooled in a freezer set to – 21 °C, and then the product was collected over vacuum filtration. The collected powder was washed with excess hexanes and dried *in vacuo*. The collected product was then dried further in a vacuum oven set to 120 °C for 72 hr. **PAH-2** was collected (3.89 g, 72%) as a bright orange powder.

PAH-2: ^{1}H NMR (500 MHz, DMSO-d_6) δ 9.74 (s, 1H), 8.62 (d, J = 16.1 Hz, 1H), 8.06 (d, J = 2.3 Hz, 1H), 8.01 – 7.98 (m, 1H), 7.88 – 7.84 (m, 1H), 7.81 (d, J = 16.0 Hz, 1H), 7.66 – 7.58 (m, 2H), 7.50 (d, J = 2.3 Hz, 1H), 4.89 (t, J = 7.8 Hz, 2H), 2.68 – 2.57 (t, 2H), 2.26 – 2.12 (m, 2H), 1.81 (s, 6H), 1.42 (s, 9H), 1.36 (s, 9H) ppm; ^{13}C NMR (100 MHz, Methanol-d_4) δ 182.7, 155.3, 152.0, 144.6, 143.5, 140.7, 140.4, 130.9, 129.2, 129.2, 125.4, 122.8, 122.6, 114.5, 110.7, 52.4, 45.0, 34.7, 34.3, 30.5, 28.9, 25.7, 24.0 ppm; IR (ATR) 2939, 2864, 1587, 1520, 1467, 1324, 1243, 1141, 1020, 975, 871, 748, 668 cm^{-1}; HRMS (ES+) Exact mass calcd. for $C_{29}H_{39}NO_4SNa^+$ $[M+Na]^+$: 520.2498, found: 520.2481.

SP isomer of PAH-2: ^{1}H NMR (500 MHz, DMSO-d_6) δ 7.12 – 7.02 (m, 4H), 7.01 (d, *J* = 10.2 Hz, 1H), 6.74 (t, *J* = 7.4, 0.9 Hz, 1H), 6.58 (d, J = 7.6 Hz, 1H), 5.78 (d, *J* = 10.2 Hz, 1H), 3.07 (m, 1H), 2.96 (m, 1H), 2.50 – 2.43 (m, 1H), 2.43 – 2.33 (m, 1H), 1.89 – 1.76 (m, 2H), 1.27 – 1.18 (m, 12H), 1.14 (s, 3H), 1.03 (s, 9H).

3.5.1.4 Temporal photo-ring opening polymerization

Polymerizations in propylene carbonate:

Benzyl alcohol (10.8 mg, 0.10 mmol, 1 eq), ε-caprolactone (0.570 g, 5.0 mmol, 50 eq), photoacid (9.6 mg **PAH-1** or 12.4 mg **PAH-2**, 0.025 mmol, 0.25 eq) and propylene carbonate (1.0 mL) were placed in a 4 mL glass vial. From this solution, 1.0 mL was transferred to another 4 mL glass vial charged with stir bar. The solution was then irradiated under 470 nm blue light (on) for 8 h followed by removal of blue light (off) for 8 h. The on/off process was repeated for a total of three cycles. Aliquots were withdrawn at predetermined time interval for NMR analysis in $CDCl_3$. The NMR samples were then quenched with triethylamine and then analyzed by GPC.

Polymerizations in DCM:

Benzyl alcohol (10.8 mg, 0.10 mmol, 1 eq), ε-caprolactone (1.150 g, 10.0 mmol, 100 eq), photoacid (3.9 mg **PAH-1** or 5.0 mg **PAH-2**, 0.01 mmol, 0.1 eq) and deuterated DCM (1.150 g) were placed in a 4 mL glass vial. From this solution, 1.0 mL was transferred to another 4 mL glass vial charged with stir bar. The solution was then irradiated under 470 nm blue light (on) for 8 h followed by removal of blue light (off) for 8 h. The on/off process was repeated for a total of three cycles. Aliquots were withdrawn at predetermined time interval for NMR analysis in CD_2Cl_2. The NMR samples were then quenched with triethylamine and then analyzed by GPC.

3.5.2 Characterization

3.5.2.1 NMR

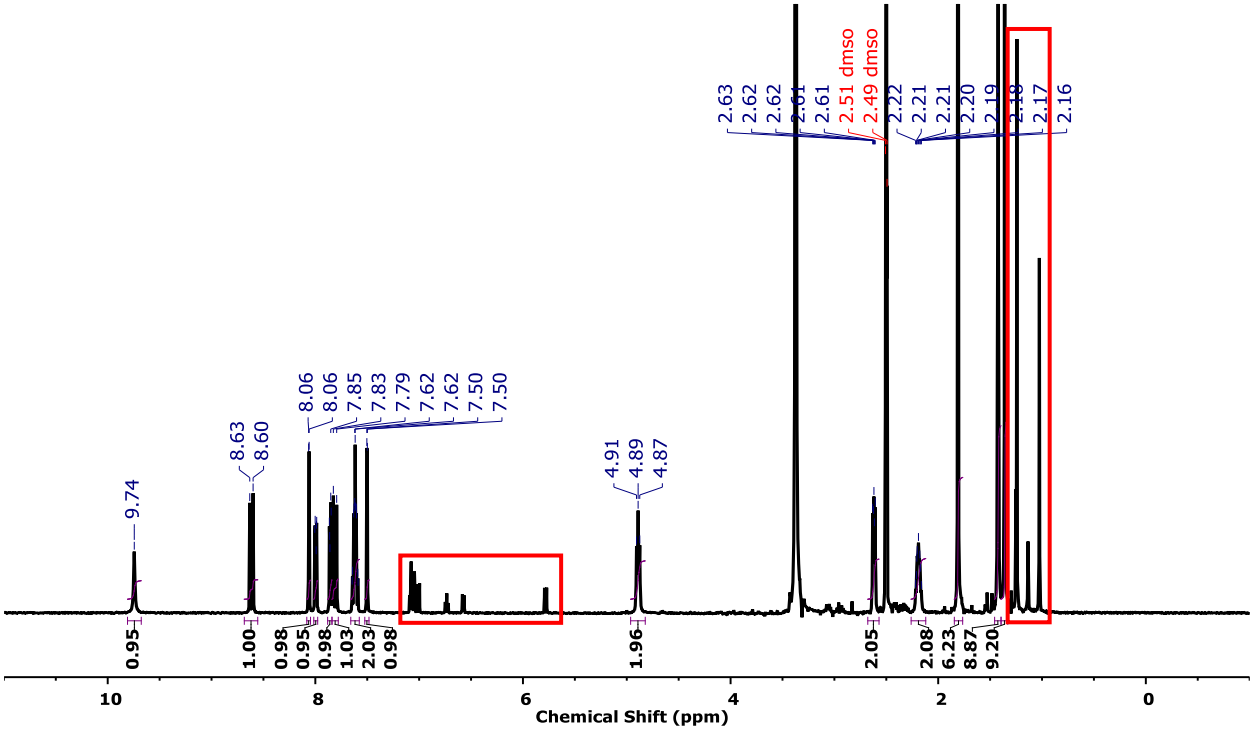

Figure 3.5 ^{1}H NMR (500 MHz, DMSO-d_6) **PAH-2.** Red boxes indicate the peaks that correspond to the **SP** isomer of **PAH-2** (See **Figure 3.6**).

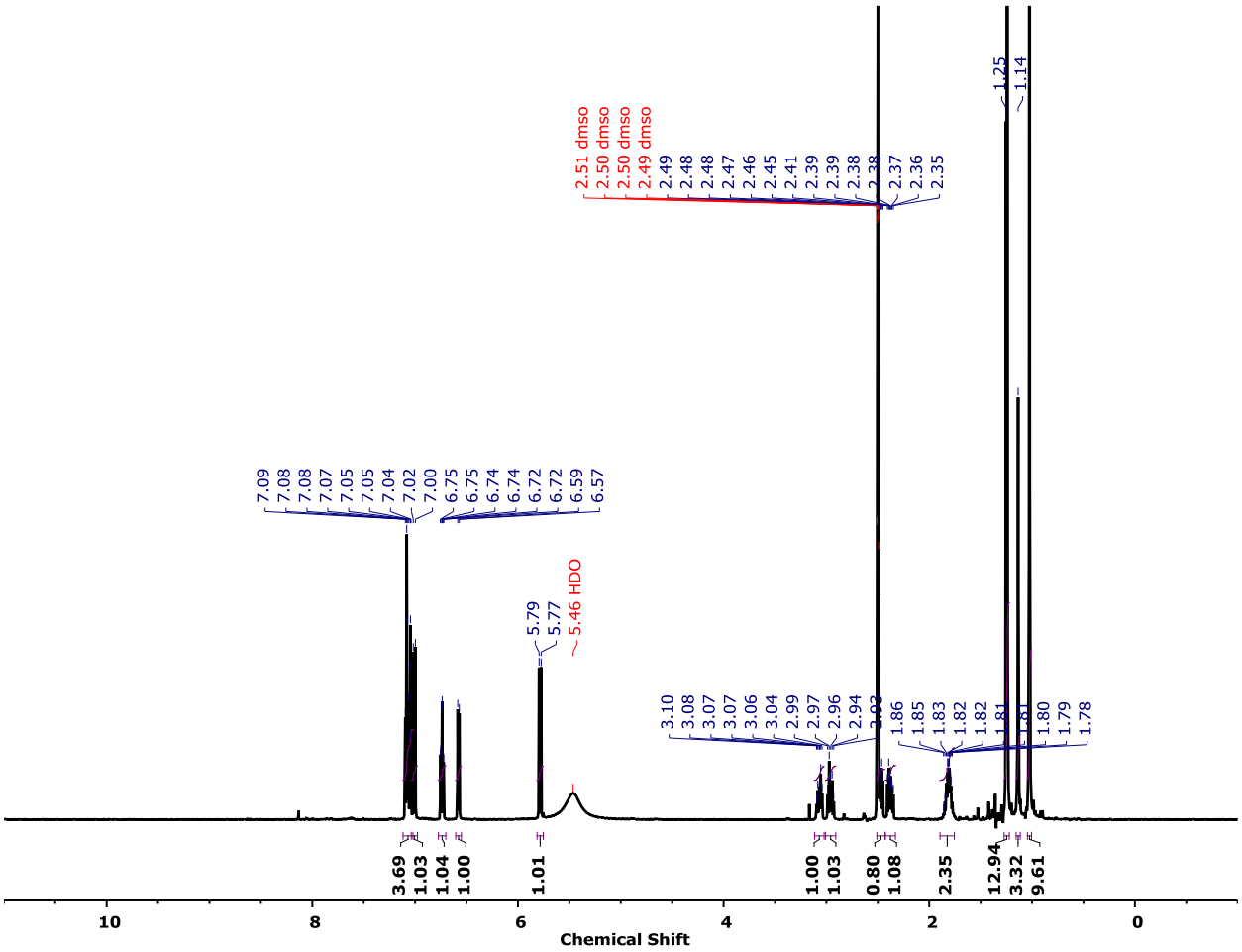

Figure 3.6 ^{1}H NMR (500 MHz, DMSO-d_6) Photoproduct of **PAH-2 (SP isomer)** after irradiation with 470 nm light for 30 min.

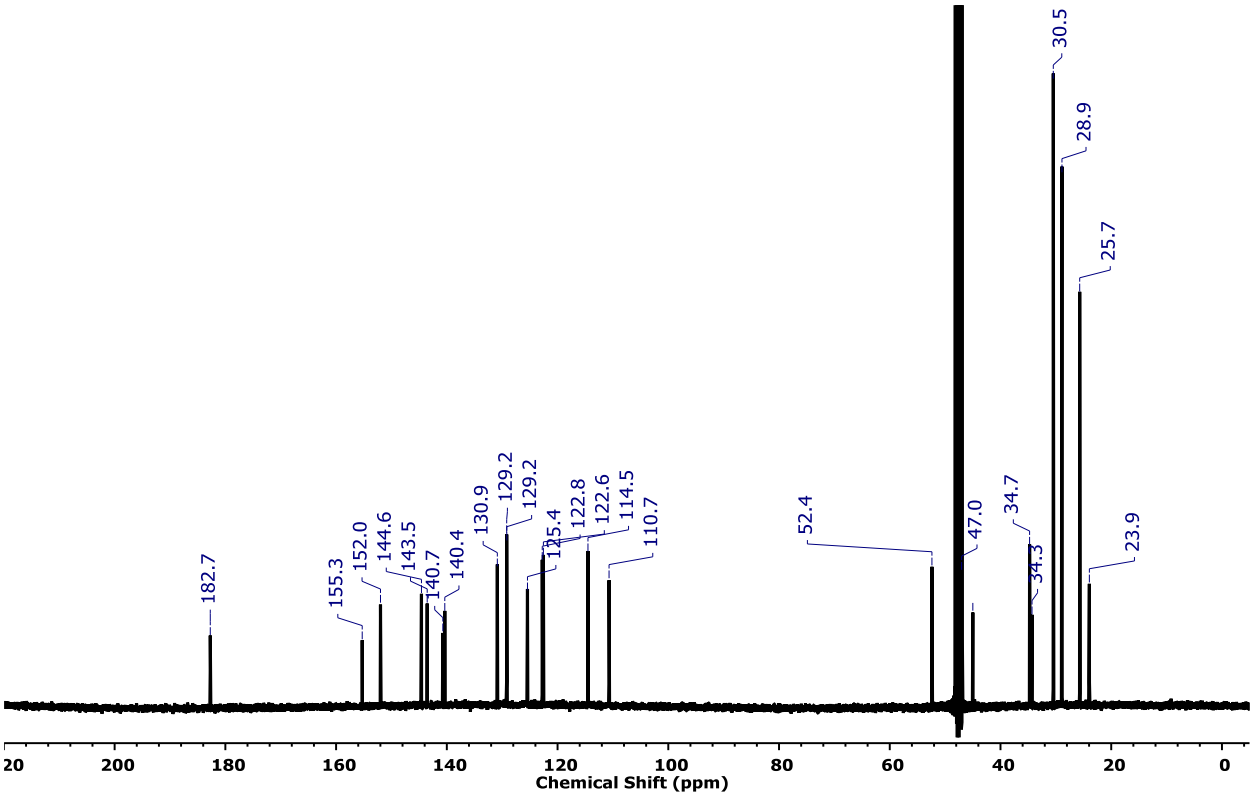

Figure 3.7 ^{13}C NMR (100 MHz, Methanol-d_4) **PAH-2**

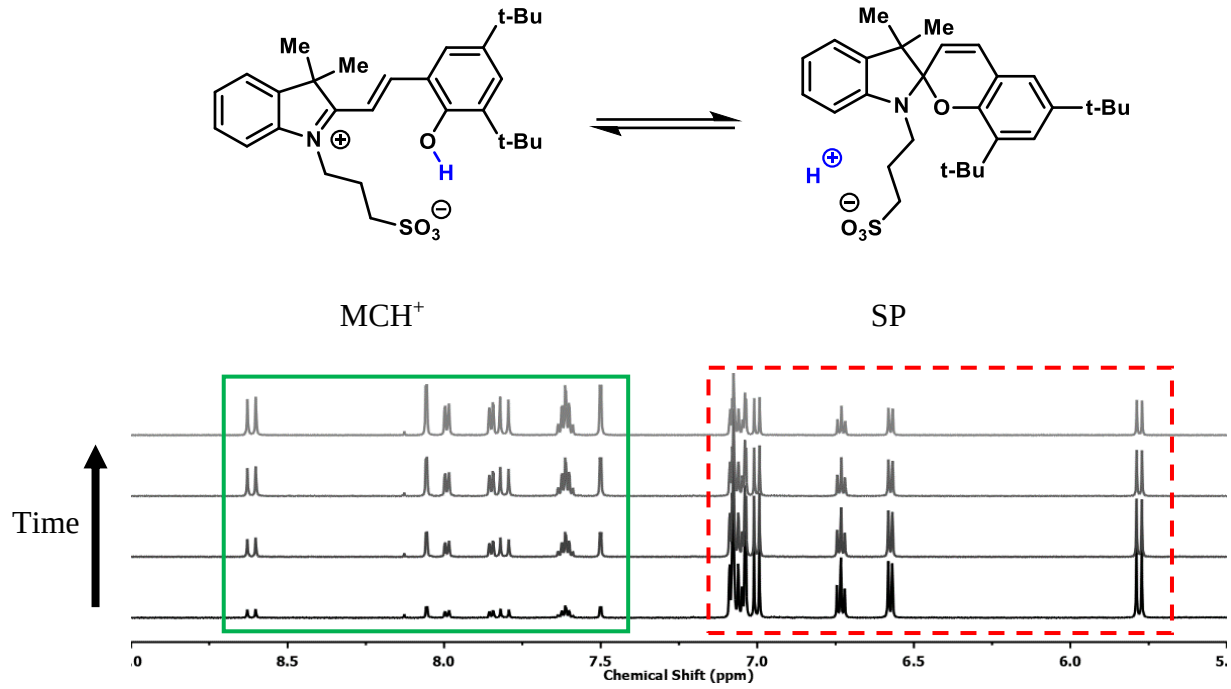

Figure 3.8 NMR spectra of **PAH-2** (9 mM in **DMSO-*d*$_6$**) during thermal relaxation (only aromatic region shown for clarity). Herein, only two species are observed, **MCH$^+$** (shown by green solid box) and the **SP** isomer (shown by red dotted box). The doublet peaks at 8.62 and 7.81 have *J* constants of 16.1 and 16.0, respectively, consistent with a *trans* alkene for the **MCH$^+$** isomer. Whereas the peaks at 7.00 and 5.78 have *J* constants of 10.2 consistent with a *cis* alkene, coupled with the absence of the hydroxy group (not shown in this NMR, see Figure 3.6) suggests that the **SP** isomer is present. Although it is understood that mechanistically, a *cis-trans* isomerization is necessary for the photoacid to switch between states, these findings where only two species are observed is consistent with previous literature of this class of mPAHs.[21]

3.5.2.2 UV-Vis

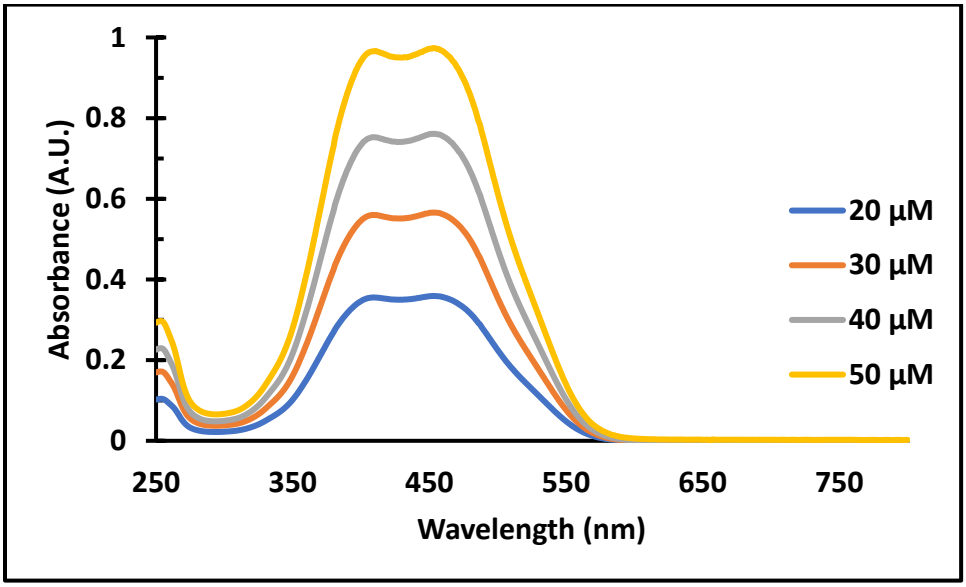

Figure 3.9 Determination of the molar extinction coefficient in **DCM**. Samples ranging from 2.0 x 10^{-5} to 5.0 x 10^{-5} M were freshly prepared and measured. The λ_{max} was determined to be at λ = **453 nm**.

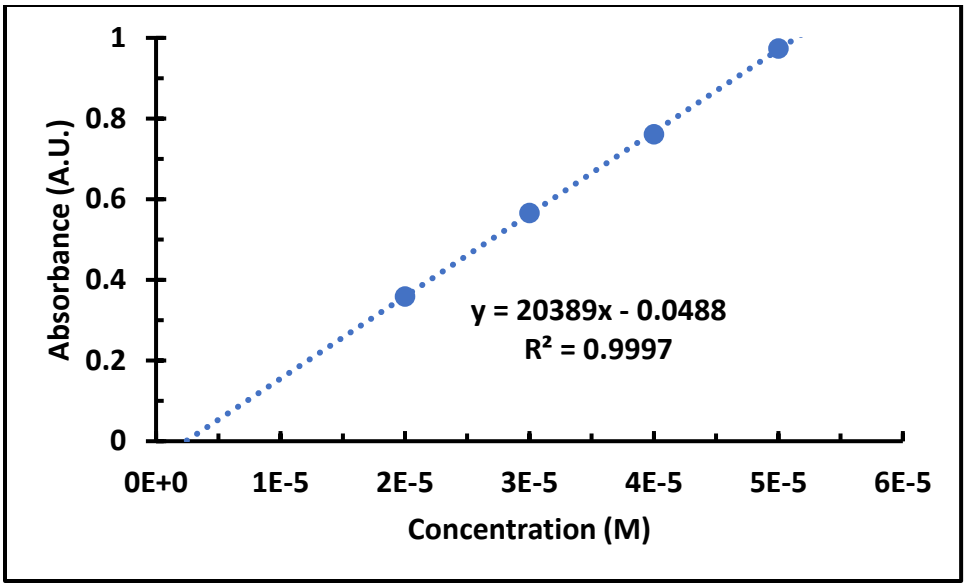

Figure 3.10 The absorbance of the samples from **Figure 3.9** was plotted versus concentration and the molar extinction coefficient was determined to be ≈**20400 L mol^{-1} cm^{-1}.**

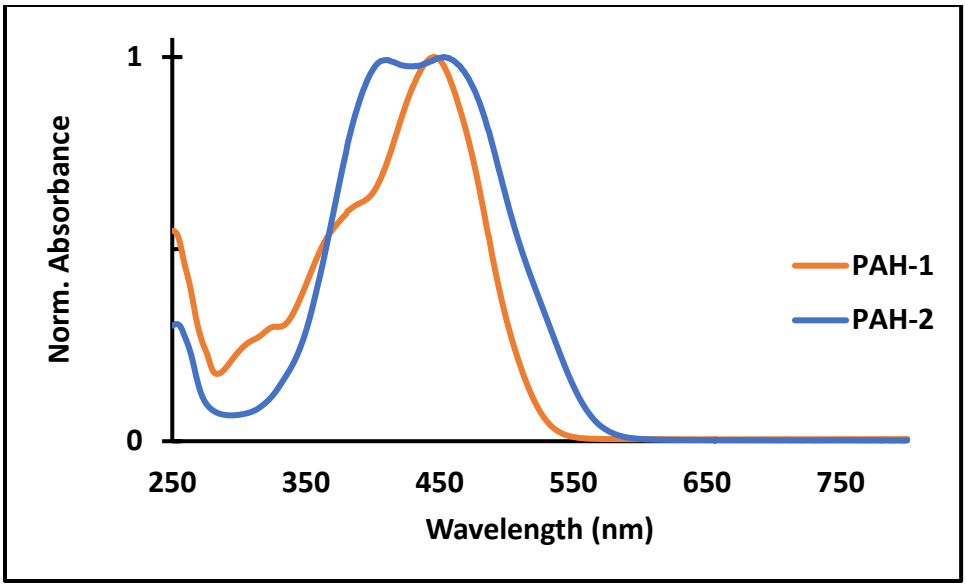

Figure 3.11 Comparison of **PAH-1** and **PAH-2** in **DCM** demonstrating that the structural modifications do not result in a significant shift in the λ_{max}. The solution for **PAH-1** was prepared by mixing a supersaturated solution, irradiating the sample with 470 nm light, and allowing to relax thermally. The dispersion was allowed to settle and a sample of the supernatant was taken and measured via UV-Vis. **PAH-2** was prepared at **5.0×10^{-5} M** in **DCM**.

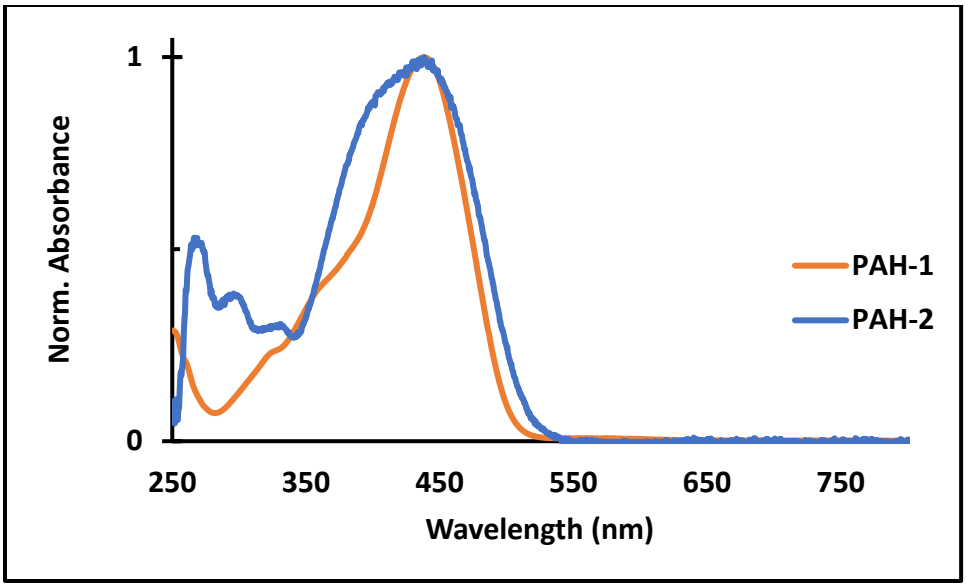

Figure 3.12 Comparison of **PAH-1** and **PAH-2** in **methanol** demonstrating that the structural modifications do not result in a significant shift in the λ_{max}. The solution for **PAH-1** was prepared at **5.0×10^{-5} M** in **methanol**. **PAH-2** was prepared at **1.0×10^{-4} M** in **methanol**.

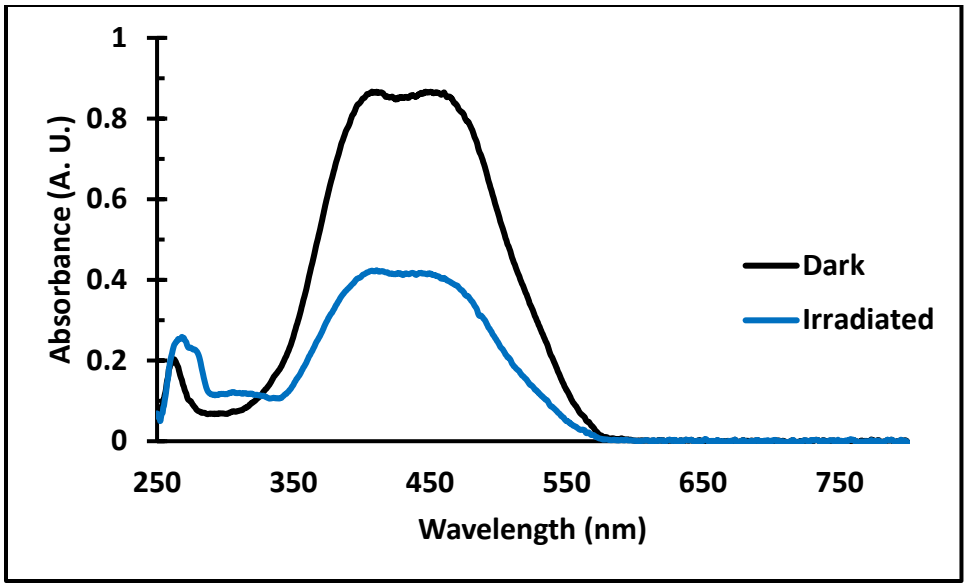

Figure 3.13 UV-Vis spectra of **PAH-2** in **DCM (5.0 x 10^{-5} M)**. The sample was prepared and allowed to equilibrate for 2 h before UV-Vis spectra was collected. The trace labeled 'dark' is from the sample taken at equilibrium, while the 'irradiated' sample was collected after irradiating with 470 nm light for 4 min and the photostationary state achieved at ~46% (**Figure 3.20**).

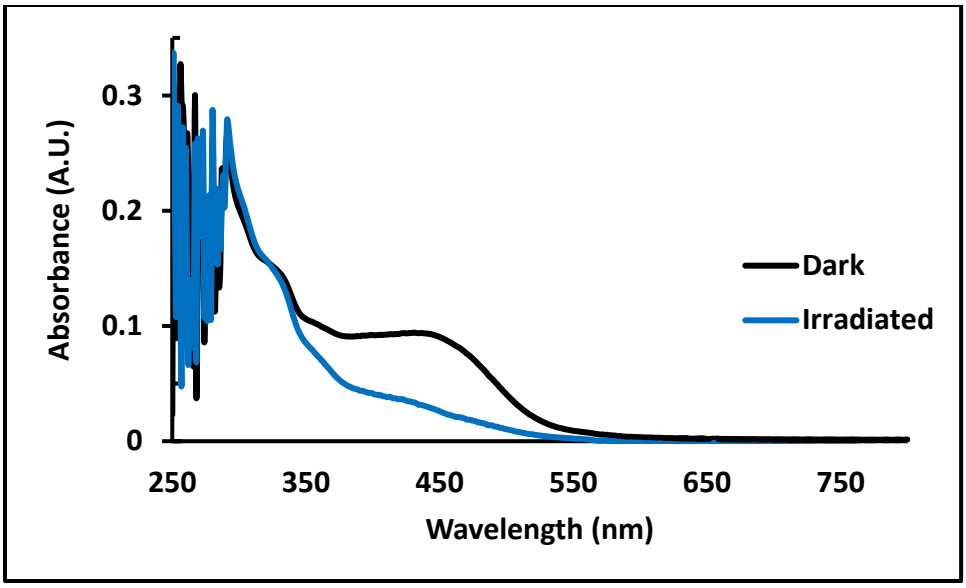

Figure 3.14 UV-Vis spectra of **PAH-2** in ***p*-xylene (saturated)**. The supersaturated sample was prepared and allowed then irradiated for 30 min using 470 nm light. The sample was then allowed to equilibrate for 3 h and a sample of the supernatant was collected, and passed through a 0.45 micron filter before UV-Vis spectra was collected. The trace labeled 'dark' is from the sample taken at equilibrium, while the 'irradiated' sample was collected after irradiating with 470 nm light for 3 min and the photostationary state achieved.

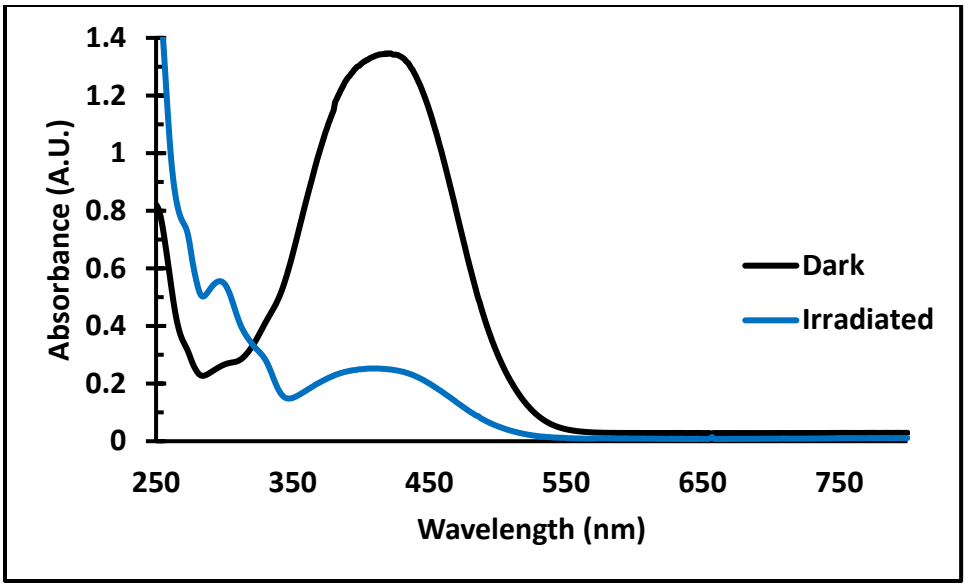

Figure 3.15 UV-Vis spectra of **PAH-2** in **MeCN (1.5 x 10^{-4} M)**. The sample was prepared and allowed to equilibrate for 3 h before UV-Vis spectra was collected. The trace labeled 'dark' is from the sample taken at equilibrium, while the 'irradiated' sample was collected after irradiating with 470 nm light for 3 min and the photostationary state achieved.

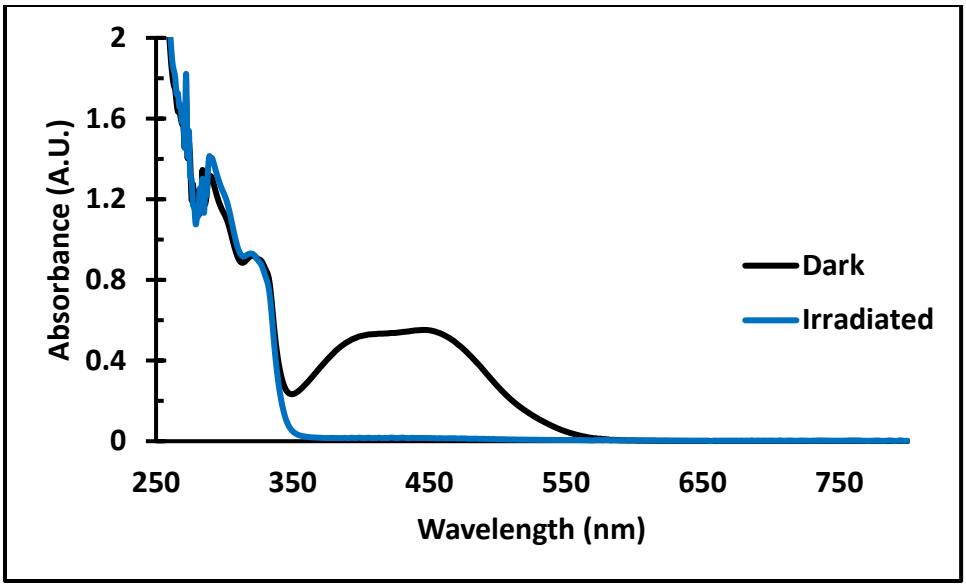

Figure 3.16 UV-Vis spectra of **PAH-2** in **THF (2.0 x 10^{-4} M)**. The sample was prepared and irradiated with 470 nm for 15 min and then allowed to equilibrate for 2 h before UV-Vis spectra was collected. The trace labeled 'dark' is from the sample taken at equilibrium, while the 'irradiated' sample was collected after irradiating with 470 nm light for 3 min and the photostationary state achieved.

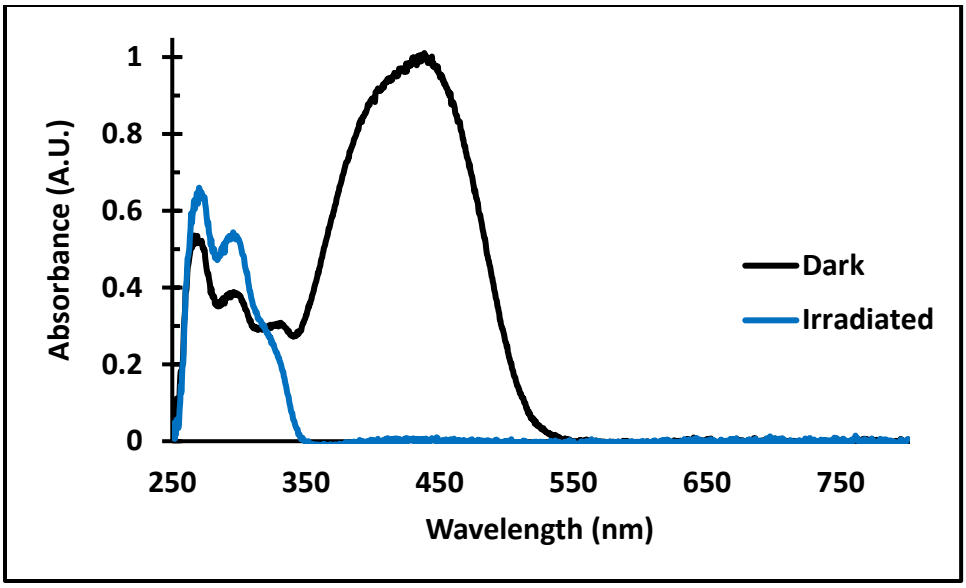

Figure 3.17 UV-Vis spectra of **PAH-2** in **methanol (1.0 x 10^{-4} M)**. The sample was prepared and allowed to equilibrate for 16 h before UV-Vis spectra was collected. The trace labeled 'dark' is from the sample taken at equilibrium, while the 'irradiated' sample was collected after irradiating with 470 nm light for 3 min and the photostationary state achieved.

3.5.2.3 Solubility tests

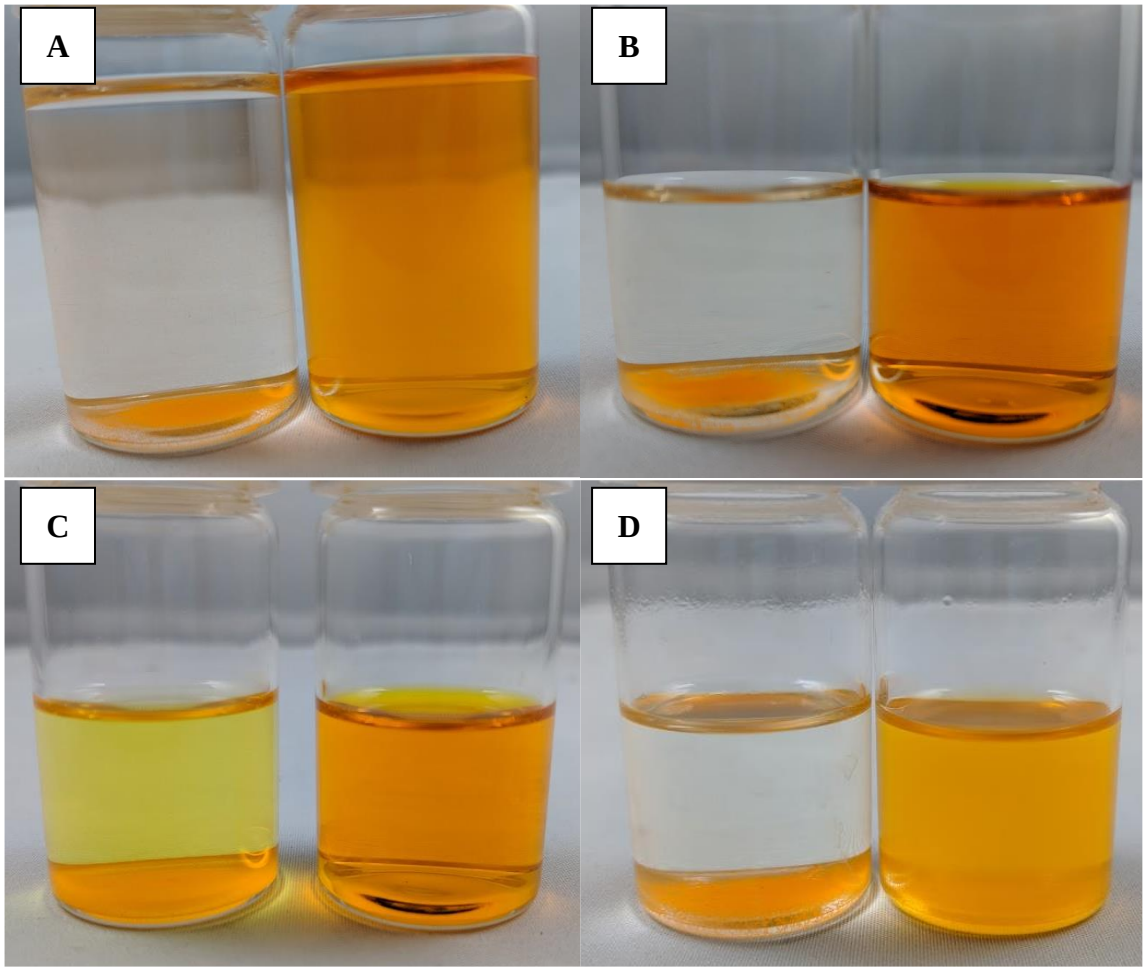

Figure 3.18 A) 3.5 x 10^{-4} M solution of **PAH-1** (left) and **PAH-2** (right) in **THF**. B) 5.2 x 10^{-4} M solution of **PAH-1** (left) and **PAH-2** (right) in **acetone**. C) 5.2 x 10^{-4} M solution of **PAH-1** (left) and **PAH-2** (right) in **acetonitrile**. D) 5.2 x 10^{-4} M solution of **PAH-1** (left) and **PAH-2** (right) in ***p*-xylene**.

3.5.2.4 Kinetics

UV-Vis kinetics: PAH-2 was characterized in a number of different solvents spanning a range of different properties (i.e., polar protic, polar aprotic, aromatic, hydrogen bond donor/acceptor, chlorinated) using a home built UV-Vis pump probe system (**Figure 3.19**). The samples were prepared taking care to avoid direct light exposure. Samples were mixed in the appropriate solvents and equilibrated for at least 2 hours before testing. The *p*-xylene and THF samples were first irradiated for around 10-15 minutes and then allowed to recovery fully before the experiment was performed. The recovery data was fit to a dynamic equilibrium model (**Equation 3.1**) and the half-lives were interpolated from the model fit.

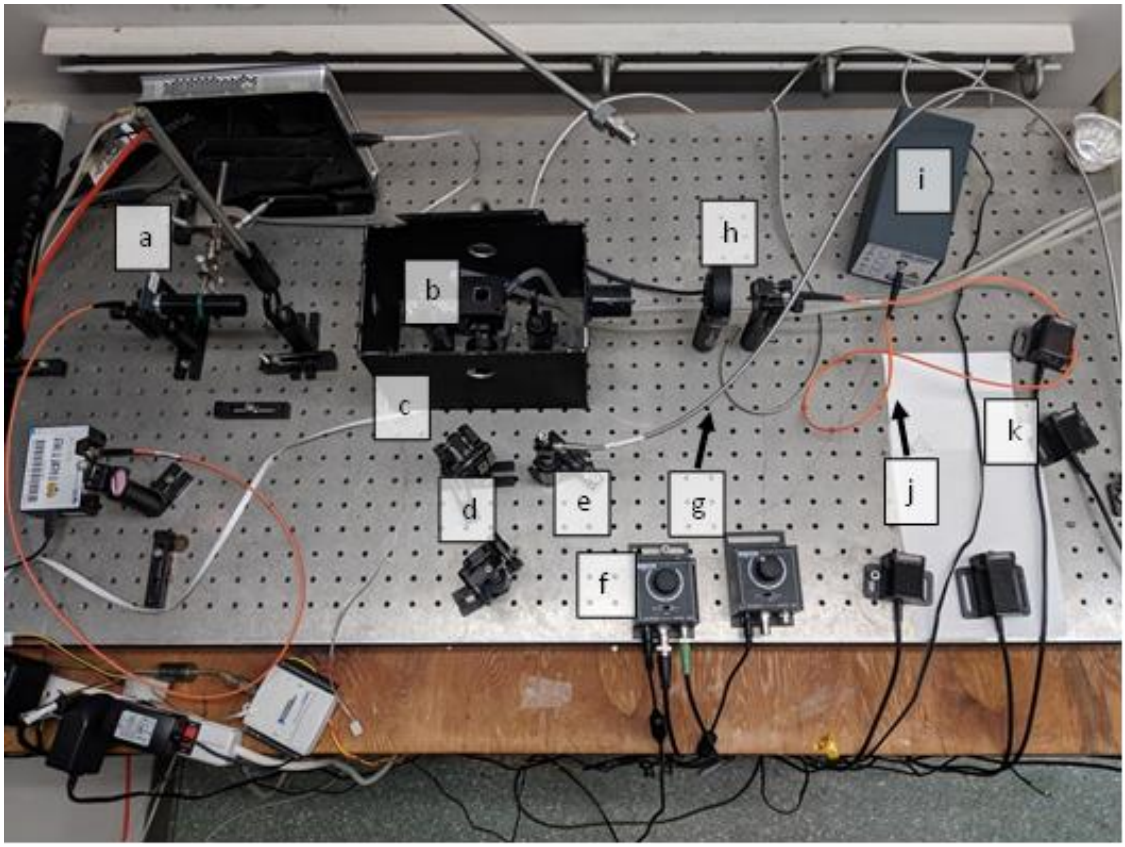

Figure 3.19 Home built UV-Vis pump probe setup.

a: detector	**g:** pump fiber optic (silver metal wire)
b: cuvette holder	**h:** shutter
c: housing (lid not shown)	**i:** probe source (Ocean Optics DH-MINI Deuterium Halogen UV-VIS-NIR Light source)
d: pump light directing mirror	**j:** probe fiber optic (orange wire)
e: output collimator	**k:** pump source - blue LED, 470 nm (Thorlabs M470F3)
f: T-cube LED driver (Thorlabs LEDD1B)	

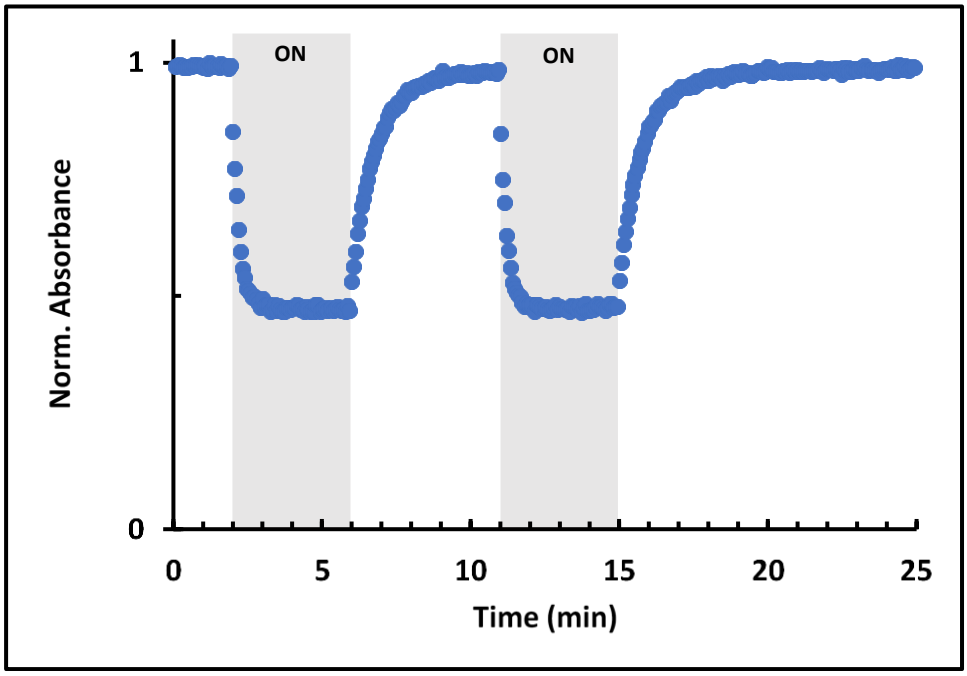

Figure 3.20 PAH-2 in **DCM (5.0 x 10^{-5} M, λ_{max} = 453)** initial 2 min in dark to establish equilibrium state, followed by 4 min of irradiation with 470 nm light with a scan taken every 4 s. The sample was then monitored in the dark with a scan taken every 4 s for 5 min before being irradiated again for 4 min. The final dark recovery cycle was monitored for 10 min. The photoirradiation is denoted by the gray boxes.

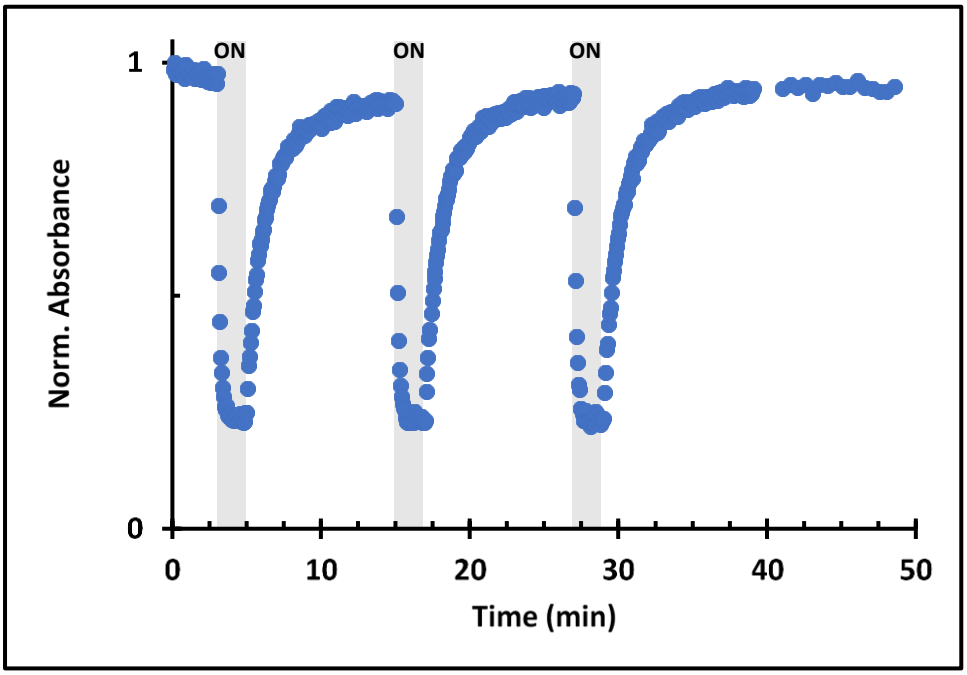

Figure 3.21 PAH-2 in ***p*-xylene (2.2 x 10^{-4} M, λ_{max} = 441)** initial 3 min in dark to establish equilibrium state, followed by 2 min of irradiation with 470 nm light with a scan taken every 4 s. The sample was then monitored in the dark with a scan taken every 4 s for 10 min before being irradiated again for 2 min. This cycle was repeated three times. The final dark recovery cycle was monitored for an additional 10 min. The photoirradiation is denoted by the gray boxes.

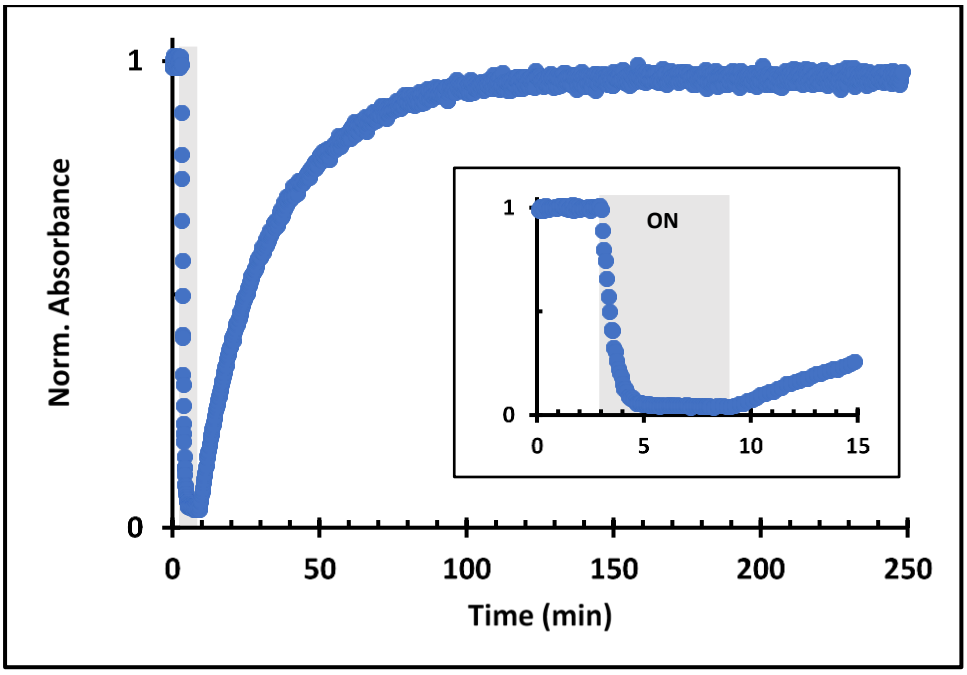

Figure 3.22 PAH-2 in **MeCN (8.0 x 10^{-5} M, λ_{max} = 419)** initial 3 min in dark to establish equilibrium state, followed by 6 min of irradiation with 470 nm light with a scan taken every 4 s. The sample was then monitored in the dark with a scan taken every 12 s. Zoom in on first 15 min of sample (insert) to highlight the initial equilibrated state and photoirradiation (gray box).

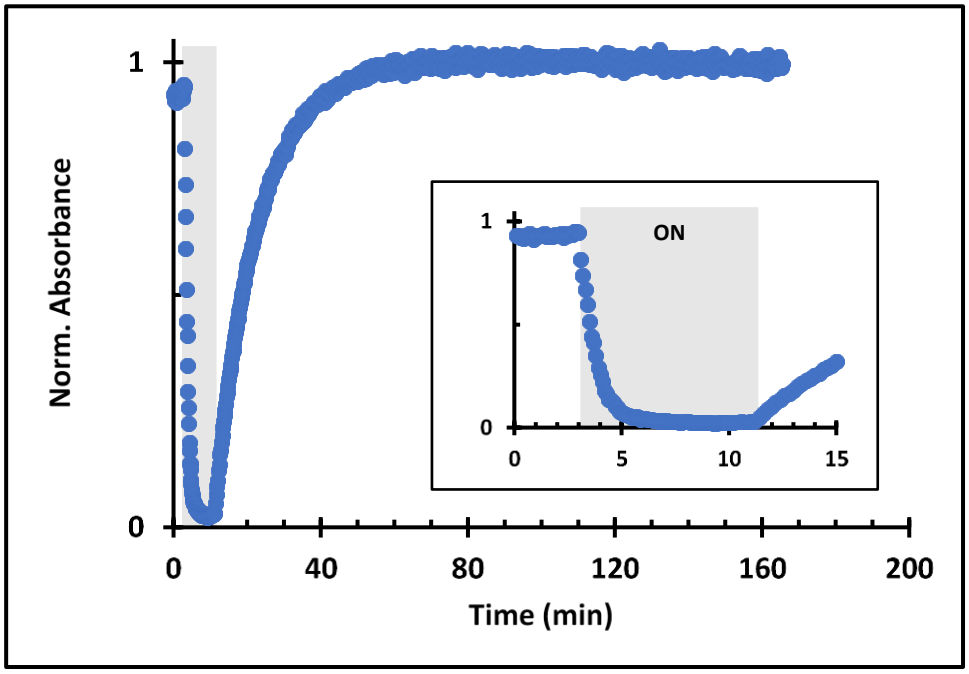

Figure 3.23 PAH-2 in **THF (3.9 x 10^{-4} M, λ_{max} = 440)** initial 3 min in dark to establish equilibrium state, followed by 8 min of irradiation with 470 nm light with a scan taken every 6 s. The sample was then monitored in the dark with a scan taken every 12 s. Zoom in on first 15 min of sample (insert) to highlight the initial equilibrated state and photoirradiation (gray box).

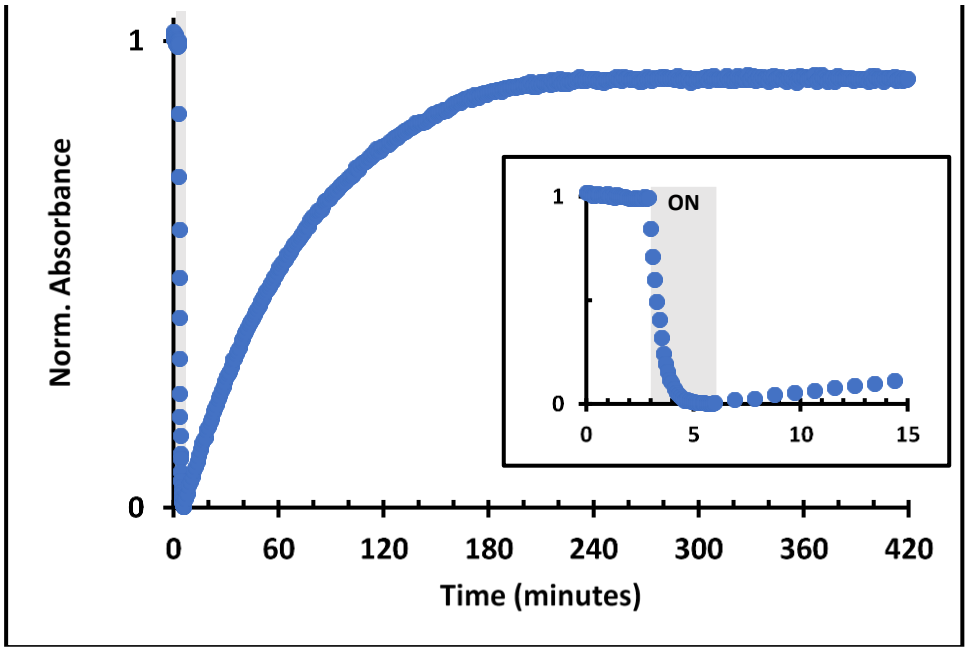

Figure 3.24 PAH-2 in **MeOH (1.0 x 10^{-4} M, λ_{max} = 439)** initial 3 min in dark to establish equilibrium state, followed by 3 min of irradiation with 470 nm light with a scan taken every 6 s. The sample was then monitored in the dark with a scan taken every 60 s. Zoom in on first 15 min of sample (insert) to highlight the initial equilibrated state and photoirradiation (gray box).

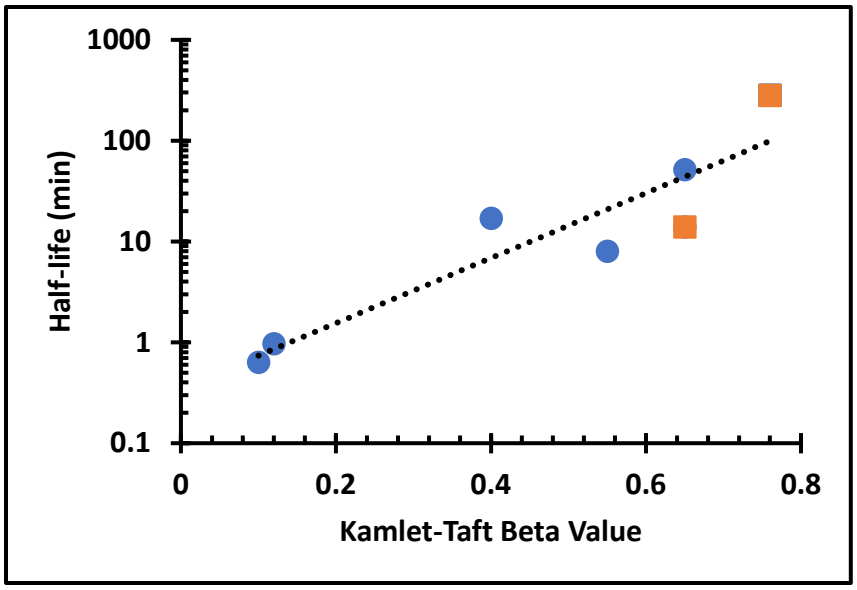

Solvent	Beta[26]	$t_{1/2}$ (min)
DCM	0.10	0.64
Xylene	0.12	0.97
MeCN	0.40	17.09
THF	0.55	8.01
MeOH	0.66	51.73
MeOH	0.66	14
DMSO	0.76	282

Figure 3.25 Correlating half-life of the dark recovery of **PAH-2** with the Taft-Kamlet β values of different solvents. The blue circles correspond to the half-lives interpolated from the model fitted to the data collected *via* UV-Vis spectroscopy presented above. The orange squares correspond to half-lives extrapolated to 22 °C from NMR data presented in the next section.

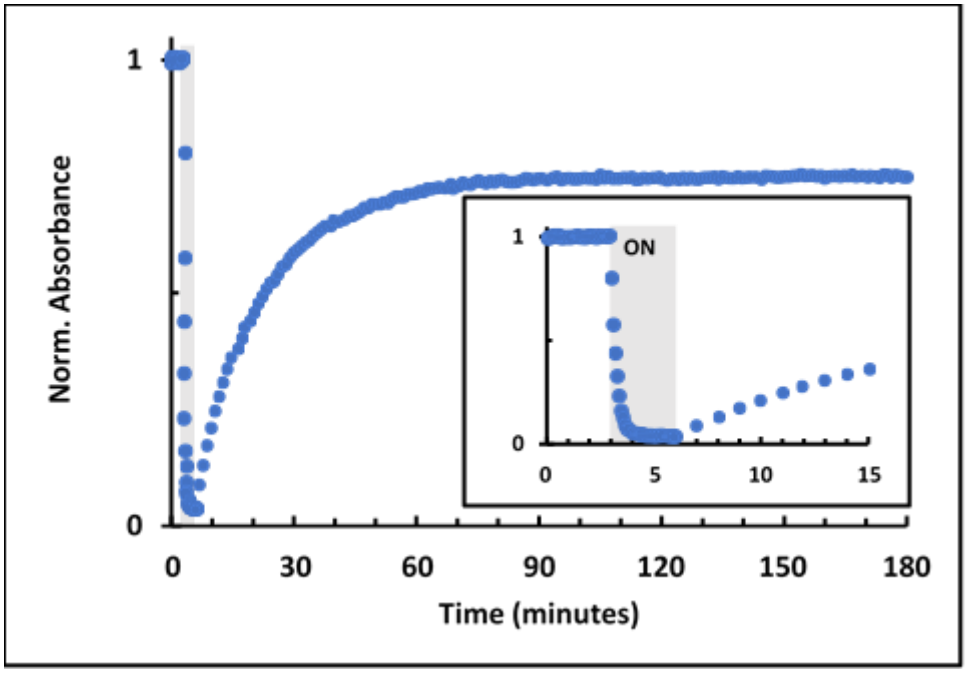

Figure 3.26 PAH-2 in **50 wt% ε-caprolactone/DCM (1.5 x 10^{-4} M, λ_{max} = 442)** initial 3 min in dark to establish equilibrium state, followed by 3 min of irradiation with 470 nm light with a scan taken every 6 s. The sample was then monitored in the dark with a scan taken every 60 s. Zoom in on first 15 min of sample (insert) to highlight the initial equilibrated state and photoirradiation (gray box). The equilibrium state after irradiation lies at 75% of the MCH^+ isomer.

NMR Kinetics: 9 mM solutions of **PAH-1** in DMSO-d_6 (**Figure 3.29**) and **PAH-2** in DMSO-d_6 (**Figure 3.31**) and methanol-d_4 (Figure 3.3b) were prepared and then irradiated while constant stirring under 470 nm light for at least 30 minutes. The samples were then placed in an NMR spectrometer and equilibrated at the given temperature for about 3-5 minutes before collecting the data. The appearance of the MCH^+ isomer was tracked over time, as such, the "forward" reaction for the NMR kinetic studies only is considered the thermal isomerization from the SP photoproduct to the MCH^+ isomer. The "reverse" reaction is the equilibration from the MCH^+ isomer to the SP isomer. The data was collected as an array collecting 300 scans on the Varian Unity Inova AS600 600MHz spectrometer. This data was then processed in MestRevNova software. A spectrum that was roughly in the middle of the overall transformation was chosen to phase and baseline the entire data set. In DMSO, the peak with δ = 8.62 ppm was integrated as the **MCH^+** and the peak with δ = 5.78 ppm was integrated as the **SP** isomer. These integrations were then exported as a Script: 1D Integral series. The ratio of the open form was determined by the following equation:

$$ratio\ open\ form = \frac{\int MCH^+}{\int MCH^+ + \int SP}$$

Equation 3.2

The data was then fit to the dynamic equilibrium model (**Equation 3.1**) and forward (from SP to MCH^+) and reverse (MCH^+ to SP) rate constants in the dark were calculated. A t_{lag} value was added to the model to extrapolate all the data points to 0% of the MCH^+ isomer for each sample. By plotting the rate constants relative to 1/T, we could use the Arrhenius expression to extract activation energies (E_{open} and E_{close}) (Figure 3.3b Insert, Figure 3.3c, **Figure 3.30**, and **Figure 3.32**). Each sample was utilized only once, to avoid potential photobleaching effects.

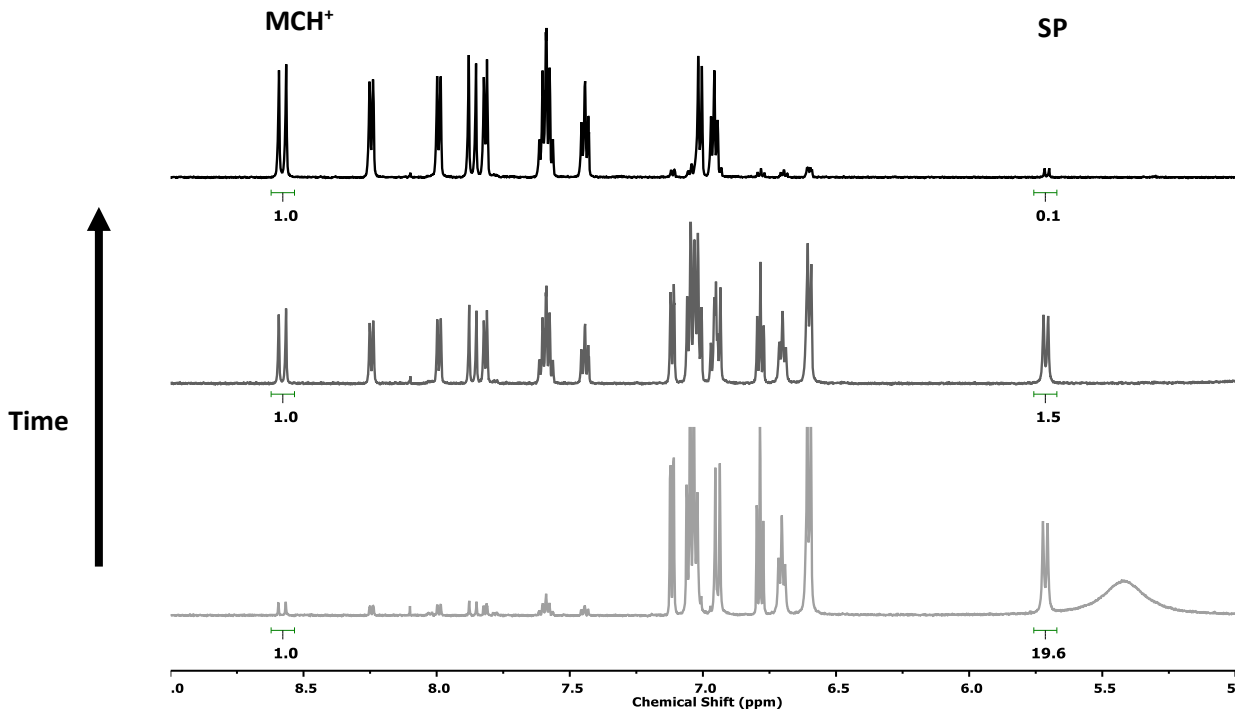

Figure 3.27 Stack of ^{1}H-NMR spectra showing various stages of switching from the open to the closed form of **PAH-1** in **DMSO** at 45 °C. Peaks labeled **MCH**$^{+}$ and **SP**, respectively, were used for calculations according to **Equation 3.2**.

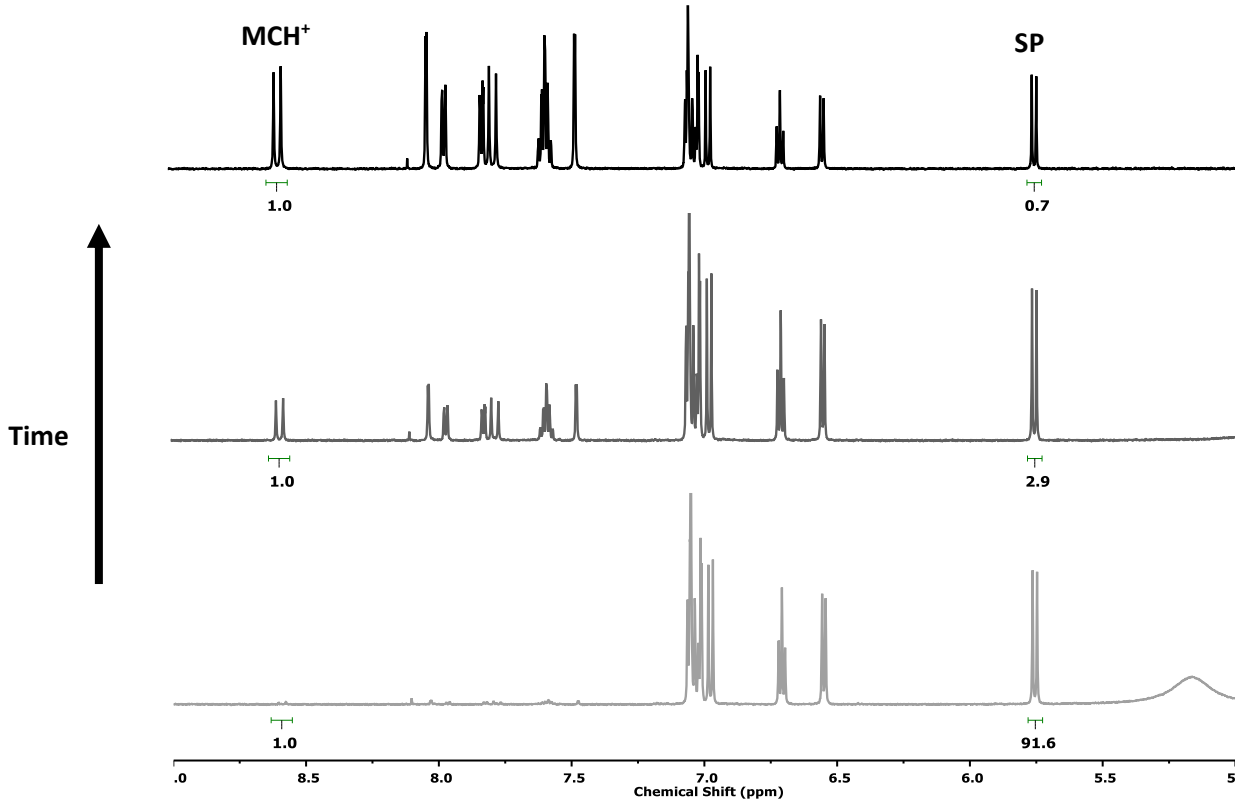

Figure 3.28 Stack of ^{1}H-NMR spectra showing various stages of switching from the open to the closed form of **PAH-2** in **DMSO** at 30 °C. Peaks labeled **MCH**$^{+}$ and **SP**, respectively, were used for calculations according to **Equation 3.2**.

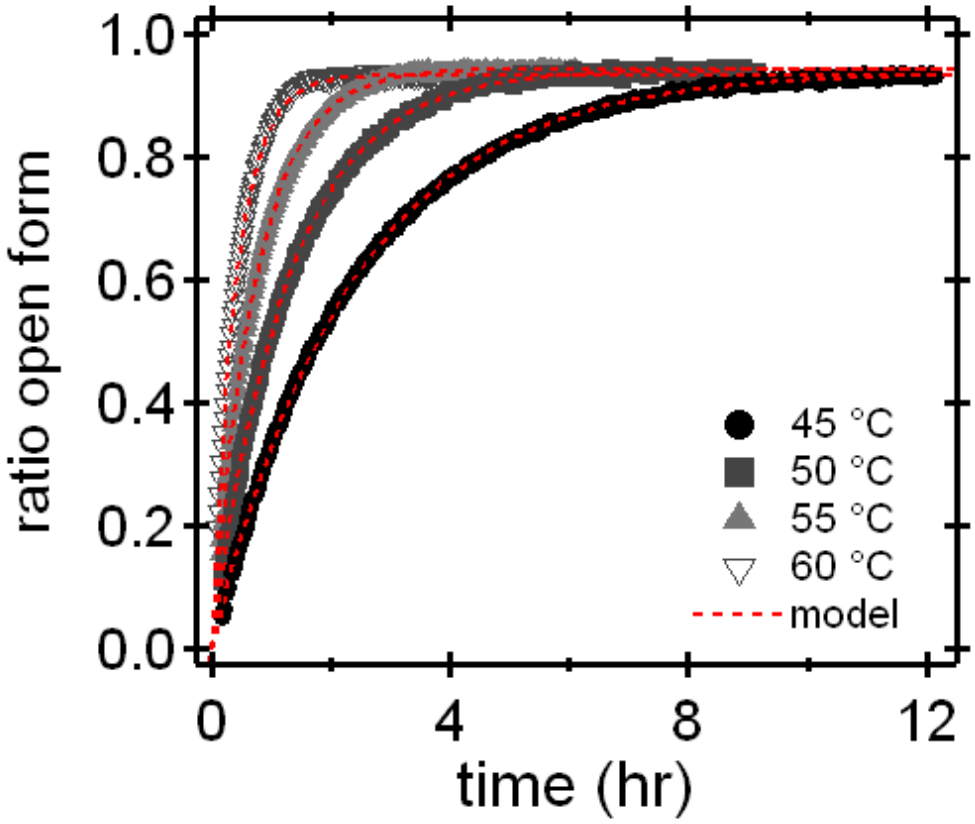

Figure 3.29 9mM solutions of **PAH-1** in **DMSO-d_6** monitoring the recovery of the MCH^+ isomer over time at varying temperatures in the NMR. The red dotted line is the model fit using the dynamic equilibrium model **Equation 3.1**.

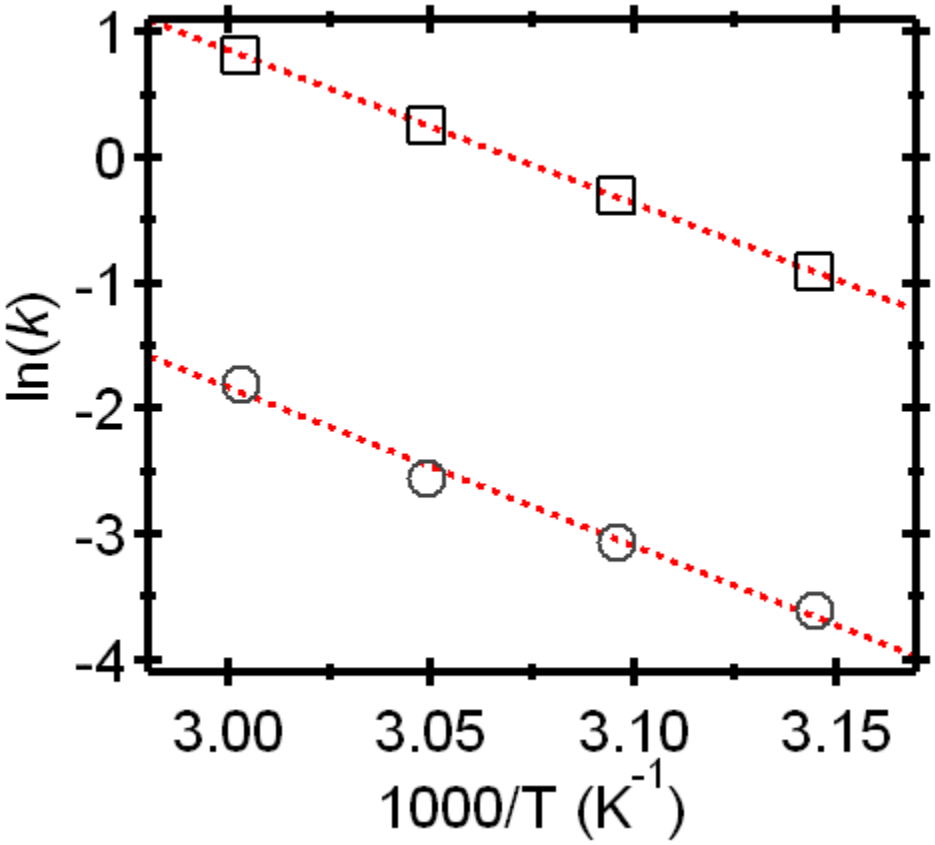

Figure 3.30 Arrhenius plot of the rate constants of **PAH-1** in **DMSO-*d*$_6$**. The square data points are the $k_{forward}$ values and the circle data points are the $k_{reverse}$ values.

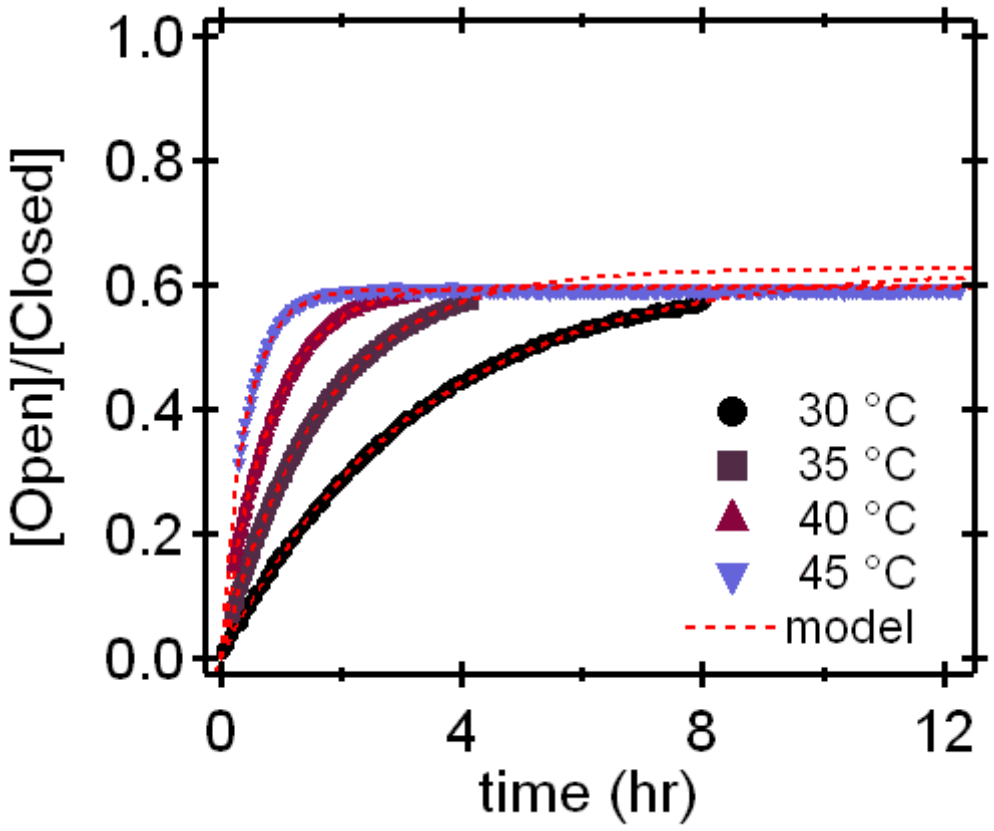

Figure 3.31 9mM solutions of **PAH-2** in **DMSO-*d*$_6$** monitoring the recovery of the MCH+ isomer over time at varying temperatures in the NMR. The red dotted line is the model fit using the dynamic equilibrium model (**Equation 3.1**).

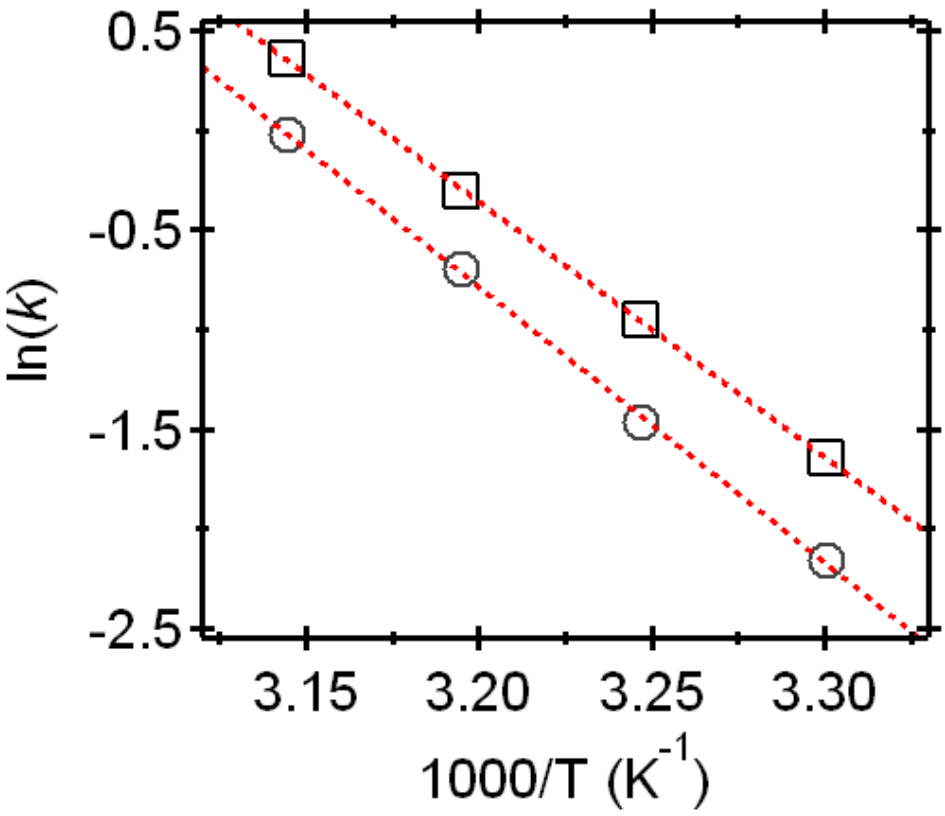

Figure 3.32 Arrhenius plot of the rate constants of **PAH-2** in **DMSO-*d*$_6$**. The square data points are the $k_{forward}$ values and the circle data points are the $k_{reverse}$ values.

3.5.2.5 Photo-ring opening polymerization GPCs

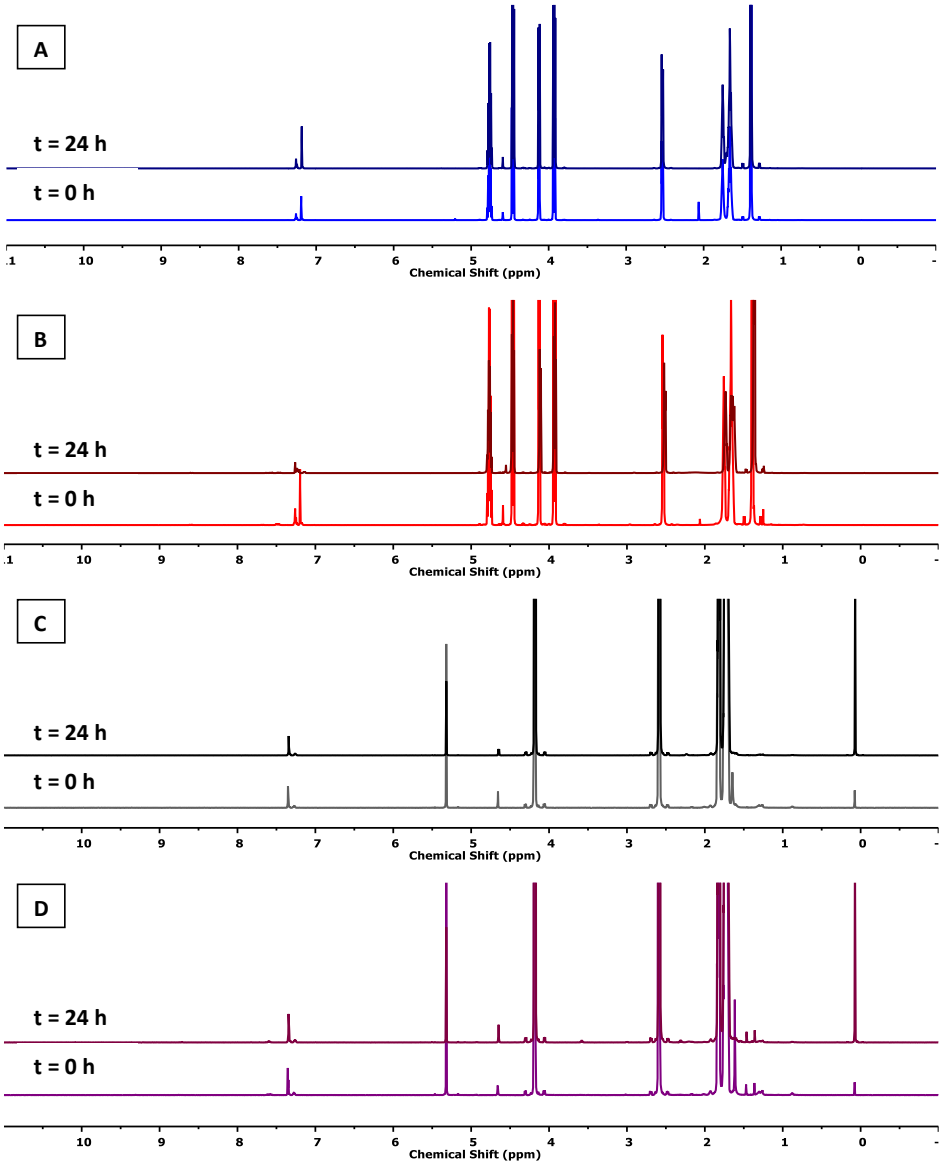

Figure 3.33 Control experiment demonstrating that photoirradiation is necessary for polymerization to occur. Each sample was prepared according to the procedure described on page S5. An NMR was taken immediately after sample was prepared and then 24 h later with the sample kept in the dark. No NMR changes can be observed in any of the samples. A) PAH-1 in propylene carbonate, B) PAH-2 in propylene carbonate, C) PAH-1 in DCM, D) PAH-2 in DCM.

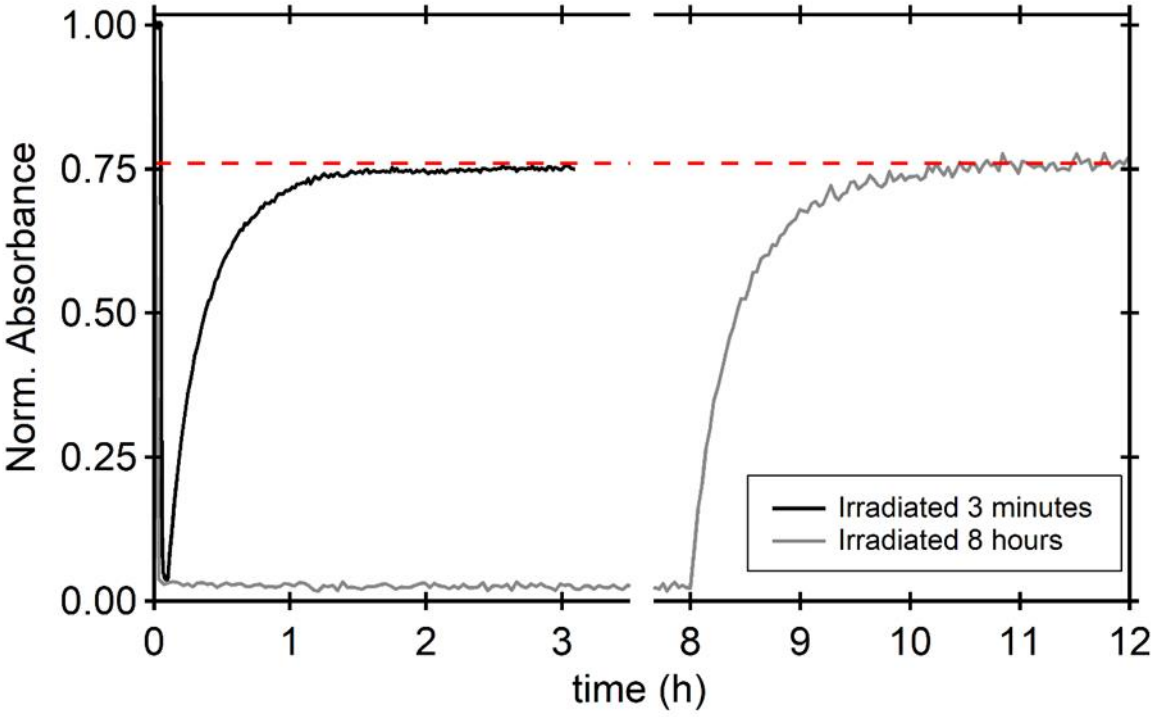

Figure 3.34 UV-Vis sample of **PAH-2** in polymer mixture of 50 wt% ε-caprolactone in DCM. First sample (black tracing) was irradiated for 3 minutes and then monitored as the sample thermally equilibrated at room temperature. An equivalent sample was irradiated for 8 hours (gray tracing) and similarly monitored as it thermally equilibrated at room temperature as well. As observed here, both sample equilibrate to the same state regardless of irradiation time suggesting there is no photodegradation to the mPAH in solution during the long irradiative periods.

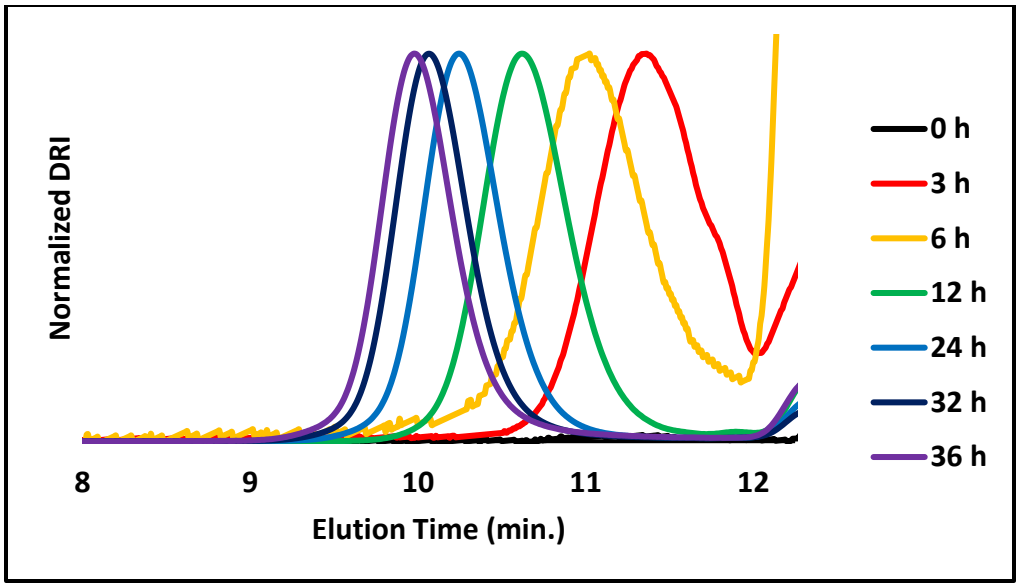

Figure 3.35 GPC tracings (in THF) of polycaprolactone over time of ROP using **PAH-2** in **DCM** under constant irradiation.

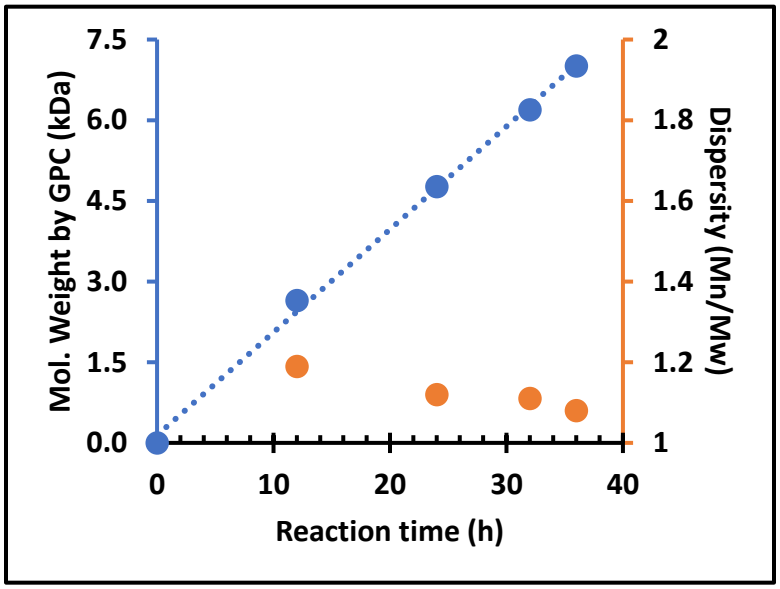

Time (h)	MW (kDa) (GPC)	*Đ*
0	0	-
3	N/A	N/A
6	N/A	N/A
12	2.6	1.19
24	4.8	1.12
32	6.2	1.11
36	7.0	1.08

Figure 3.36 Plot of molecular weight and dispersity (by GPC in THF) versus time of ROP of caprolactone using **PAH-2** in **DCM** under constant irradiation.

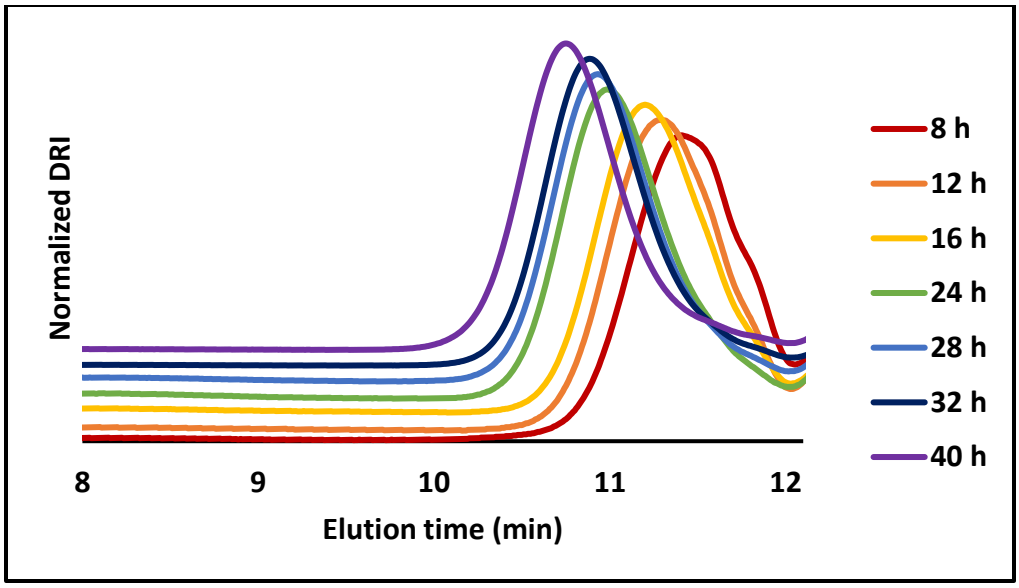

Figure 3.37 GPC tracings (in THF) of polycaprolactone over time of ROP using **PAH-1** in **propylene carbonate** under cycles of irradiation and dark 8 h periods.

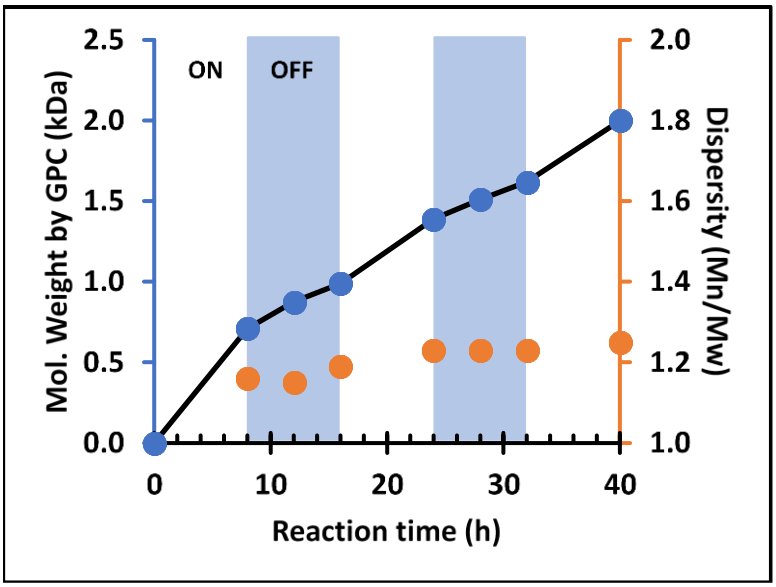

Time (h)	MW GPC (kDa)	*Đ*
0	0	-
8	0.7	1.16
12	0.9	1.15
16	1.0	1.19
24	1.4	1.23
28	1.5	1.23
32	1.6	1.23
40	2.0	1.25

Figure 3.38 Plot of molecular weight and dispersity (by GPC in THF) versus time of ROP of caprolactone using **PAH-1** in **propylene carbonate** under 8 h cycles of irradiation and dark periods. Condition: [BnOH]:[PAH]:[ε-CL] = 1:0.25:50.

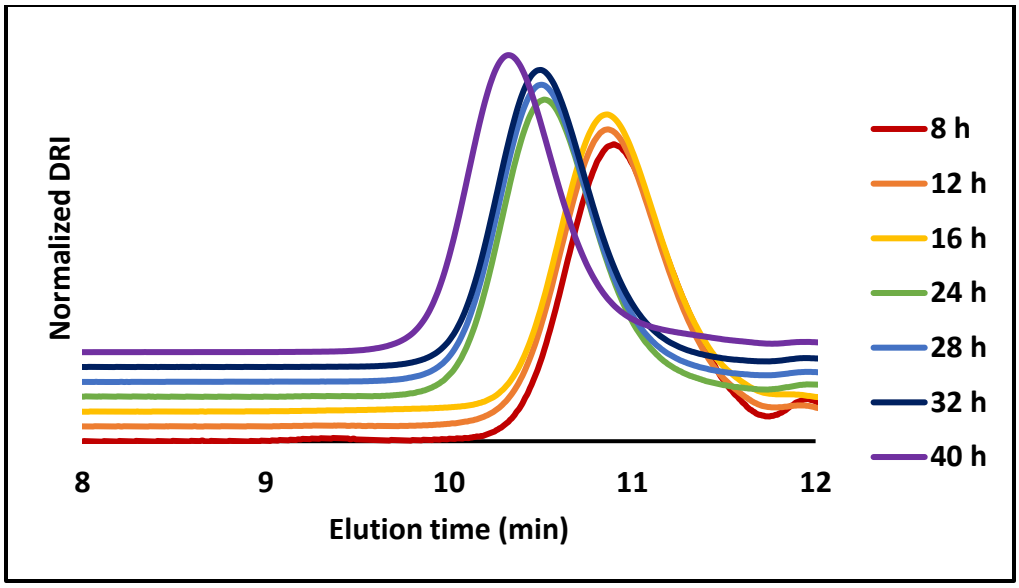

Figure 3.39 GPC tracings (in THF) of polycaprolactone over time of ROP using **PAH-2** in **propylene carbonate** under cycles of irradiation and dark 8 h periods. Condition: [BnOH]:[PAH]:[ε-CL] = 1:0.25:50.

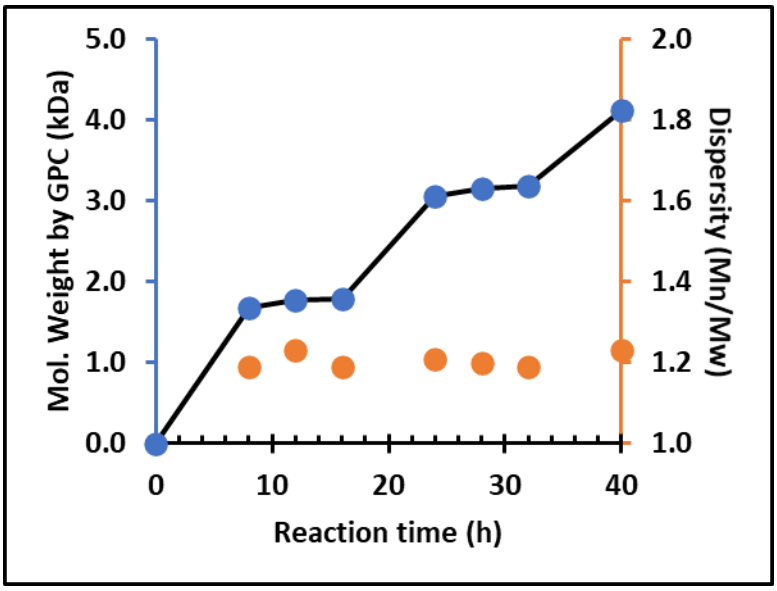

Time (h)	M.W. GPC (kDa)	*Đ*
0	0	-
8	1.7	1.19
12	1.8	1.23
16	1.8	1.19
24	3.1	1.21
28	3.1	1.20
32	3.2	1.19
40	4.1	1.23

Figure 3.40 Plot of molecular weight and dispersity (by GPC in THF) versus time of ROP of caprolactone using **PAH-2** in **propylene carbonate** under 8 h cycles of irradiation and dark periods. Condition: [BnOH]:[PAH]:[ε-CL] = 1:0.25:50.

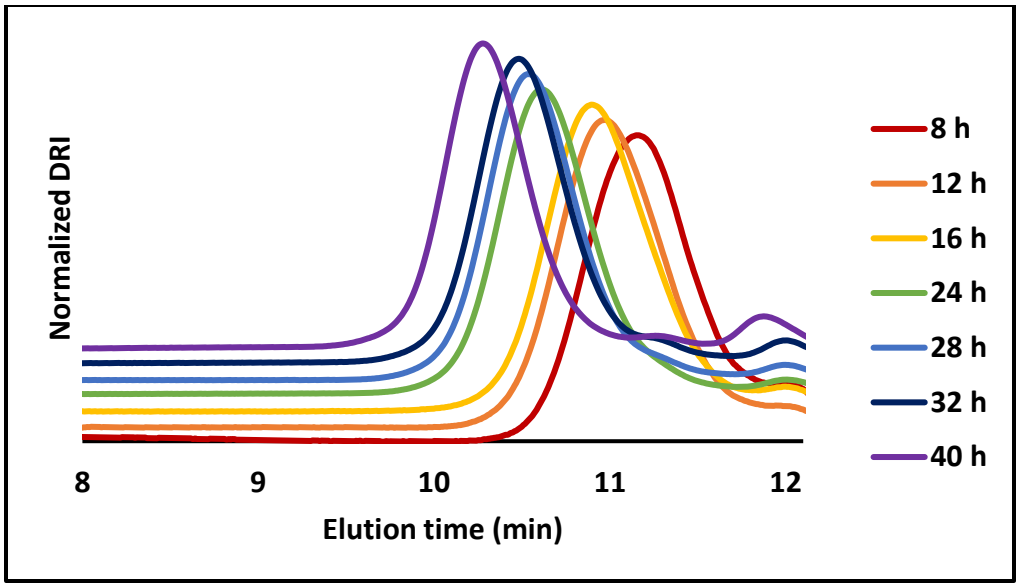

Figure 3.41 GPC tracings (in THF) of polycaprolactone over time of ROP using **PAH-1** in **DCM** under cycles of irradiation and dark 8 h periods. Condition: [BnOH]:[PAH]:[ε-CL] = 1:0.1:100.

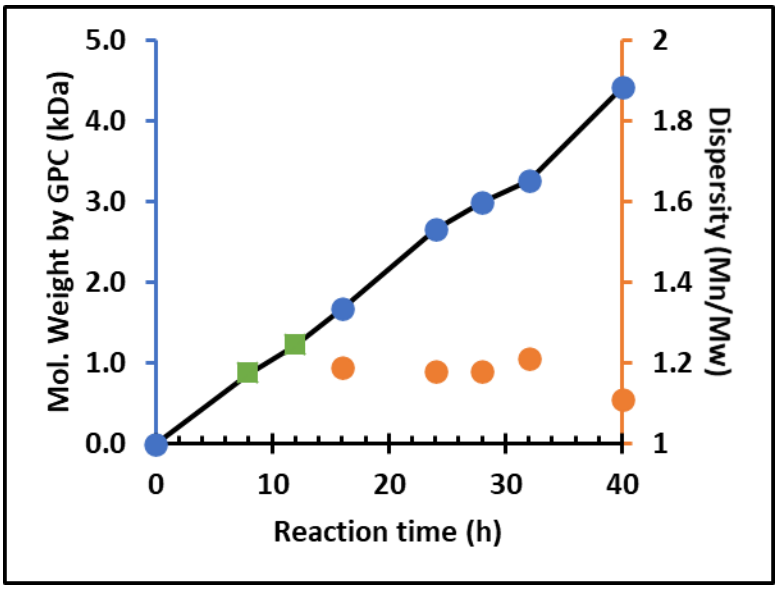

Time (h)	M.W. GPC (kDa)	*Đ*
0	0	-
8	0.9[a]	N/A
12	1.2[a]	N/A
16	1.7	1.19
24	2.7	1.18
28	3.0	1.18
32	3.3	1.21
40	4.4	1.11

Figure 3.42 Plot of molecular weight and dispersity (by GPC in THF) versus time of ROP of caprolactone using **PAH-1** in **DCM** under 8 h cycles of irradiation and dark periods. Condition: [BnOH]:[PAH]:[ε-CL] = 1:0.1:100. [a]Molecular weight of 8 and 12 h conversion were undeterminable by GPC, given molecular weight is estimated by NMR conversion, 8% and 11% respectively (denoted by green squares).

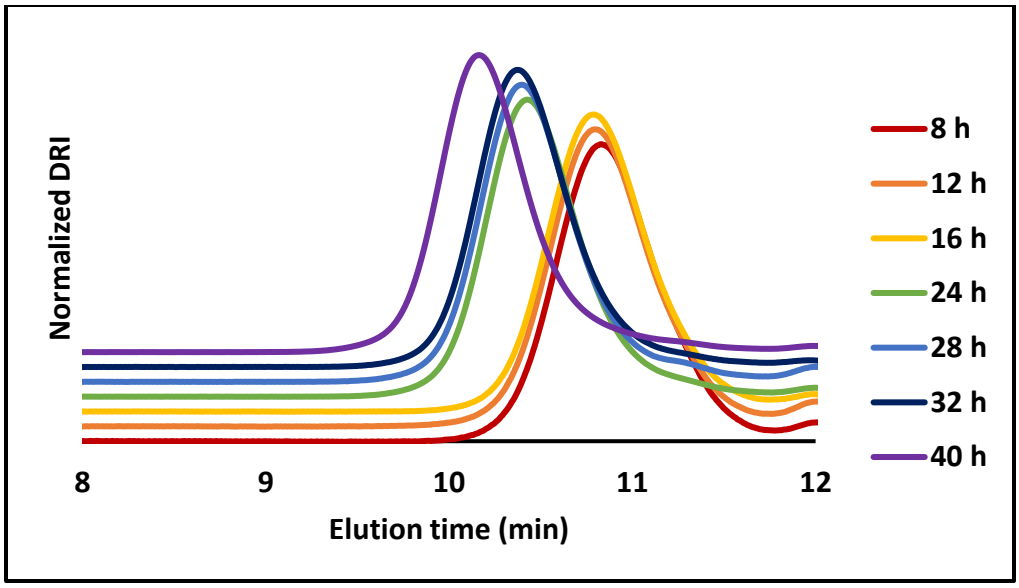

Figure 3.43 GPC tracings (in THF) of polycaprolactone over time of ROP using **PAH-2** in **DCM** under cycles of irradiation and dark 8 h periods. Condition: [BnOH]:[PAH]:[ε-CL] = 1:0.1:100.

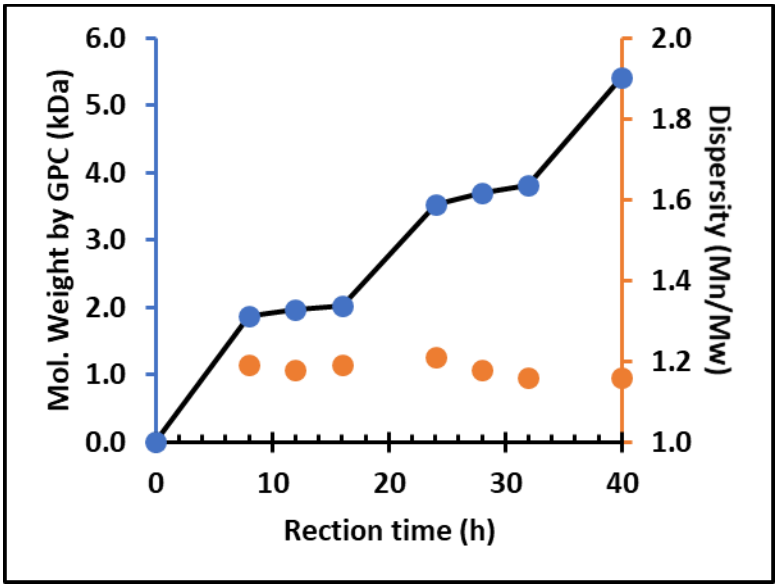

Time (h)	M.W. GPC (kDa)	*Đ*
0	0	-
8	1.9	1.19
12	2.0	1.18
16	2.0	1.19
24	3.5	1.21
28	3.7	1.18
32	3.8	1.16
40	5.4	1.16

Figure 3.44 Plot of molecular weight and dispersity (by GPC in THF) versus time of ROP of caprolactone using **PAH-2** in **DCM** under 8 h cycles of irradiation and dark periods. Condition: [BnOH]:[PAH]:[ε-CL] = 1:0.1:100.

3.6 References – Chapter 3

(1) Kocak, G.; Tuncer, C.; Bütün, V. *Polym. Chem.* **2017**, *8*, 144–176.

(2) Bruns, C. J.; Stoddart, J. F. *Acc. Chem. Res.* **2014**, *47*, 2186–2199.

(3) Vallet, J.; Micheau, J. C.; Coudret, C. *Dye. Pigment.* **2016**, *125*, 179–184.

(4) Kusumoto, S.; Nakagawa, T.; Yokoyama, Y. *Adv. Opt. Mater.* **2016**, *4*, 1350–1353.

(5) Balamuralidhara, V.; Pramodkumar, T. M.; Srujana, N.; Venkatesh, M. P.; Gupta, N. V.; Krishna, K. L.; Gangadharappa, H. V. *Am. J. Drug Discov. Dev.* **2011**, *1*, 24–48.

(6) Neumann, K.; Lilienkampf, A.; Bradley, M. *Polym. Int.* **2017**, *66*, 1756–1764.

(7) Zhu, Y. J.; Chen, F. *Chem. - An Asian J.* **2015**, *10*, 284–305.

(8) Liao, Y. *Acc. Chem. Res.* **2017**, *50*, 1956–1964.

(9) Shi, Z.; Peng, P.; Strohecker, D.; Liao, Y. *J. Am. Chem. Soc.* **2011**, *133*, 14699–14703.

(10) Abeyrathna, N.; Liao, Y. *J. Am. Chem. Soc.* **2015**, *137*, 11282–11284.

(11) Wang, Z.; Johns, V. K.; Liao, Y. *Chem. - A Eur. J.* **2014**, *20*, 14637–14640.

(12) Yang, C.; Khalil, T.; Liao, Y. *RSC Adv.* **2016**, *6*, 85420–85426.

(13) Tatum, L. A.; Foy, J. T.; Aprahamian, I. *J. Am. Chem. Soc.* **2014**, *136*, 17438–17441.

(14) Klajn, R. *Chem. Soc. Rev.* **2014**, *43*, 148–184.

(15) Fu, C.; Xu, J.; Boyer, C. *Chem. Commun.* **2016**, *52*, 7126–7129.

(16) Neilson, B. M.; Bielawski, C. W. *Chem. Commun.* **2013**, *49*, 5453–5455.

(17) Abeyrathna, N.; Liao, Y. *J. Photochem. Photobiol. A Chem.* **2017**, *332*, 196–199.

(18) Satoh, T.; Sumaru, K.; Takagi, T.; Takai, K.; Kanamori, T. *Phys. Chem. Chem. Phys.* **2011**, *13*, 7322–7329.

(19) Feeney, M. J.; Thomas, S. W. *Macromolecules* **2018**, *51*, 8027–8037.

(20) Khalil, T.; Alharbi, A.; Baum, C.; Liao, Y. *Macromol. Rapid Commun.* **2018**, *39*, 1800319.

(21) Johns, V. K.; Wang, Z.; Li, X.; Liao, Y. *J. Phys. Chem. A* **2013**, *117*, 13101–13104.

(22) Wojtyk, J. T. C.; Wasey, A.; Xiao, N. N.; Kazmaier, P. M.; Hoz, S.; Yu, C.; Lemieux, R. P.; Buncel, E. *J. Phys. Chem. A* **2007**, *111*, 2511–2516.

(23) Piard, J. *J. Chem. Educ.* **2014**, *91*, 2105–2111.

(24) Balmond, E. I.; Tautges, B. K.; Faulkner, A. L.; Or, V. W.; Hodur, B. M.; Shaw, J. T.; Louie, A. Y. *J. Org. Chem.* **2016**, *81*, 8744–8758.

(25) Kamlet, M. J.; Taft, R. W. *J. Am. Chem. Soc.* **1976**, *98*, 377–383.

(26) Marcus, Y. *J. Solution Chem.* **1991**, *20*, 929–944.

(27) Hemmer, J. R.; Poelma, S. O.; Treat, N.; Page, Z. A.; Dolinski, N. D.; Diaz, Y. J.; Tomlinson, W.; Clark, K. D.; Hooper, J. P.; Hawker, C.; D, Read de Alaniz, J. *J. Am. Chem. Soc.* **2016**, *138*, 13960–13966.

(28) Hemmer, J. R.; Page, Z. A.; Clark, K. D.; Stricker, F.; Dolinski, N. D.; Hawker, C. J.; Read de Alaniz, J. *J. Am. Chem. Soc.* **2018**, *140*, 10425–10429.

(29) Ulrich, S.; Hemmer, J. R.; Page, Z. A.; Dolinski, N. D.; Rifaie-graham, O.; Bruns, N.; Hawker, C. J.; Boesel, L. F.; Alaniz, J. R. De. *ACS Macro Lett.* **2017**, *6*, 738–742.

4 Triblock polyester vitrimers from commercial polymers

4.1 Abstract

Dynamic covalent chemistry has enabled the advancement of many technologies, but often requires specialty polymers and involved synthesis. However, the ability to convert commodity polymers into high value dynamic networks is limited to only a few chemistries. Herein, a novel triblock polyester system is prepared from the chain extension of readily available commercial polymers, namely hydroxy-terminated polybutadiene (HTPB) and its hydrogenated analogue (Krasol). The chain extension was accomplished via ring-opening polymerization initiated by the terminal hydroxy groups of a commercial polymer and resulted in well-controlled synthesis of several triblock copolymers in a single step. The chemistry is compatible with both Brønsted acids and Brønsted bases as demonstrated by successful chain-extension at mild conditions and further confirmed by diffusion order spectroscopy (DOSY) NMR experiments. With a newly reported bis-lactone crosslinker and a previously reported merocyanine photoacid, a photo-curable resin is demonstrated, highlighting the potential for various applications including photo-patterning and additive manufacturing. We anticipate these findings can be generalized to various monomer types, resulting in a library of copolymers, catalyzed by a variety of catalyst. Future studies aim to elucidate the ability of these systems to behave as dynamic polymer networks.

4.2 Introduction

Dynamic polymer networks have become of increasing interest in recent years, with an expansive scope of compatible chemistries and catalysts having now been demonstrated, including the bond exchange of esters,[1–3] urethanes,[4] siloxanes,[5] boronic esters,[6–9] alkenes,[10,11] thiourethanes,[12–14] and more.[15–18] These materials are distinguished by their ability to internally exchange bonds in response to a range of stimuli—most commonly heat, but also light, pH,

chemical triggers, and others. While dynamic networks and conventional thermosets are both crosslinked networks comprised of covalent bonds, only dynamic networks exhibit self-healing and reconfigurability due to in situ bond exchange.[19–21] Conversely, thermoplastics can be reprocessed quite easily (due to not being crosslinked and only held together by intermolecular forces), but have poor mechanical robustness and chemical resistance due to their lack of covalent crosslinking bonds. For these reasons, dynamic bonds are uniquely situated to provide advantages to various applications, including reprocessable polymer networks,[22–26] additive manufacturing,[27–30] and polymer network composites.[31–33]

Hydroxy-terminated polybutadiene (HTPB) and its hydrogenated analogue (Krasol) are staple polymer precursors for various applications owing to their low cost, favorable mechanical properties (i.e. low glass transition temperatures and lack of crystallinity), as well as their readily accessible terminal hydroxy groups. For these reasons, these polymers have been commonly used as polymer binders for highly filled composite system. Traditionally, the curing of these materials is achieved via chain-extension with di-isocyanates to generate blocks of soft polymer segments with small urethane-rich segments, presumably providing enough H-bonding and restricting segmental motion sufficiently to generate a soft, soluble solid. Others have investigated the chain-extension of these polymers via ring-opening polymerization (ROP) of lactones and lactides, resulting in triblock polymers (resembling traditional thermoplastic elastomers). In these cases, additional hydrogen-bonding units are often necessary to achieve adequate mechanical properties and the compatible temperature window is limited by the T_g of the hard block. A synthetic approach that takes advantage of the readily accessible chain-extension ROP while also incorporating covalent crosslinks could greatly benefit the mechanical and thermomechanical properties of the resulting polymeric solid and potentially introduce advanced functionality such

as reprocessability and self-healing. We hypothesize this can be achieved by wedding the previously demonstrated chain-extension with more recently demonstrated bis-lactone crosslinkers.[2,34]

Previously, it has been demonstrated that transesterification is catalyzed by a wide range of catalyst types (including: Brønsted acids, Brønsted bases, Lewis acids, Lewis bases, and frustrated acid-base pairs) and that the activation energy and compatible temperatures are very catalyst dependent. For example, a polyester network with Bronsted acid catalysts exhibited rapid bond exchange even at mild conditions (25 to 75 °C),[2] whereas Lewis acids typically require much higher temperatures to achieve similar rates of bond exchange (>120 °C).[34] Polymer-based binders are used extensively in systems with strict temperature limits, therefore they would benefit from the implementation of a low temperature dynamic bond motif.

4.3 Results and Discussion

To investigate the viability of this approach, a series of chain-extension experiments were run at various temperatures and catalyst loadings. Of the two polymers, HTPB and Krasol, only the latter showed a well-defined molecular weight distribution as evidenced by SEC (**Figure 4.6**). For this reason, our initial studies focused on developing a system with Krasol. Previous reports have highlighted the viability of poly(4-methylcaprolactone) (p4mCL) as an ester-rich precursor for dynamic polymer networks, thus 4mCL monomer was chosen for the chain-extension of Krasol. The generalized reaction scheme is given below in **Scheme 4.1**.

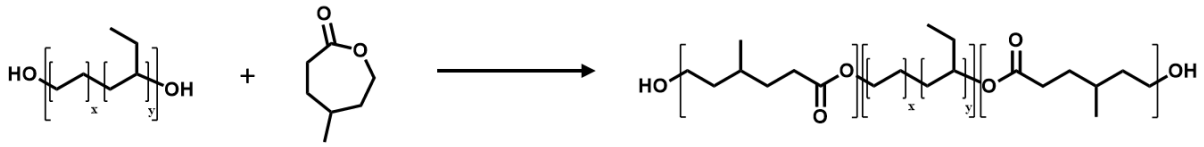

Scheme 4.1 Reaction scheme for the single-step synthesis of a triblock copolymer from commercially available Krasol polymer precursor.

To probe the polymerization rate and demonstrate the viability of the terminal hydroxy group as an initiating ROP site, a kinetics experiment was carried out and monitored by both HNMR and size-exclusion chromatography (SEC) as shown in **Figure 4.1**. The ^{1}H-NMR studies were made feasible by the presence of non-overlapping characteristic peaks (as shown and labelled in **Figure 4.7**) that allowed for identification of each distinct species. Encouraged by previous studies using Bronsted acid catalysts, a strong sulfonic acid (camphorosulfonic acid, "CSA") was used to catalyze the polymerization. Initial studies were carried out in the bulk (approximately 48wt% monomer/51wt% polymer/1wt% catalyst) at 50 °C, but DOSY NMR characterization revealed that although the 4mCL monomer was converted to p4mCL, there was no evident connectivity to the polymer precursor (**Figure 4.8**) as shown by the discrepant diffusivities. This finding indicates that the initiation from Krasol (or HTPB) is difficult in bulk polymerization and low temperature conditions and therefore the chain-extension is unlikely to succeed at very high concentrations. To address this, the reaction solution was diluted to 50 wt% with dry toluene. To ensure fast polymerization rates at the newly diluted condition, the reaction temperature was increased to 100 °C. The ^{1}H-NMR spectra were used to calculate conversion at various time points during the polymerization (**Figure 4.1a**) while the successful chain-extension is confirmed by size-exclusion chromatography (SEC) of select time points (**Figure 4.1b**).

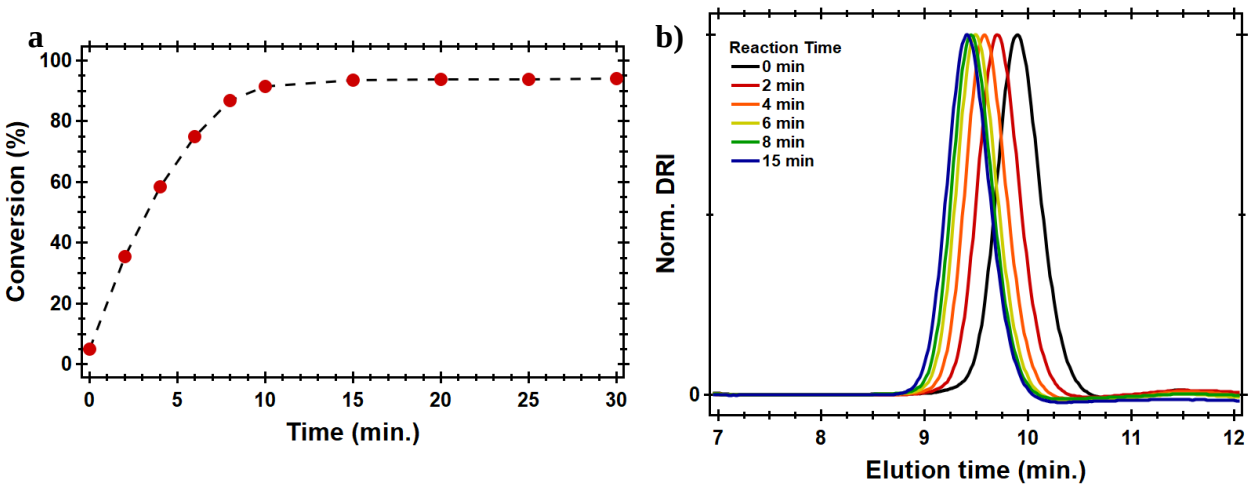

Figure 4.1 Polymerization kinetics study of Krasol-initiated ring-opening polymerized, catalyzed by camphorsulfonic acid. (a) Monomer conversion is monitored via NMR and (b) SEC traces highlight the formation of the triblock by a monotonic increase in Mn.

Although the chain-extension was apparently successful from the SEC results, recent investigation by Philipps and coworkers have highlighted the shortcomings of this technique for the characterization of discrepant block copolymer species.[35] To put these concerns to rest and further confirm the successful initiation from the commercial polymer precursors, DOSY NMR spectra were collected for the final time point of the polymerization (when conversion was >95%). The results of this study are given below in **Figure 4.2**. An analogous study was conducted using a Brønsted base catalyst (triazabicyclodecene, "TBD"). The conversion data for that experiment is determined by ^{1}H-NMR and the corresponding DOSY NMR spectra is plotted in **Figure 4.9**.

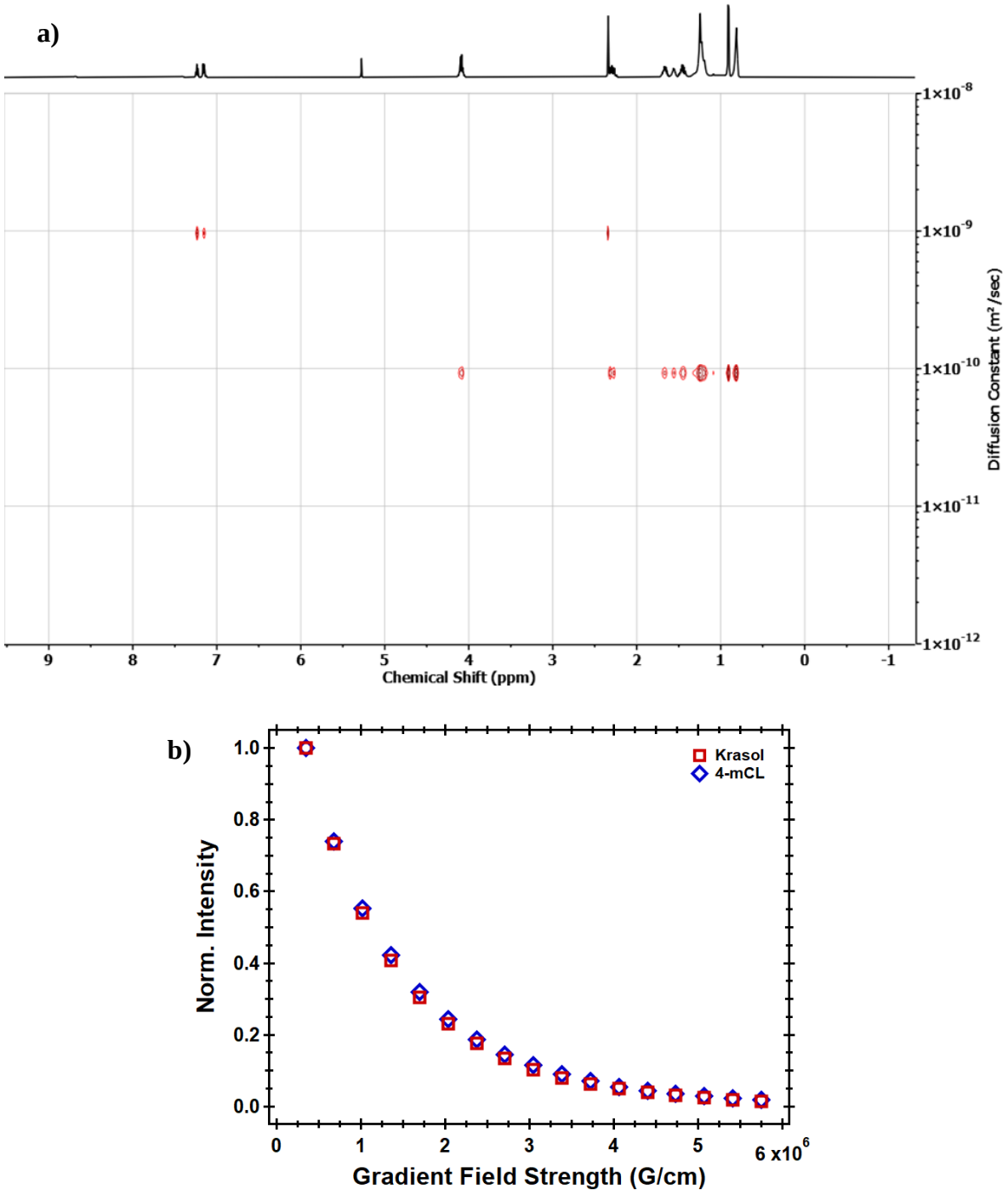

Figure 4.2 CSA initiated chain extenstion. a) DOSY NMR spectra showing great agreement in diffusivity between a characteristic p4mCL peak and a characteristic Krasol peak. b) Intensity normalized gradient-strength resolved decay of both signals demonstrating the agreement in diffusion.

Having demonstrated successful ROP initiation and chain-extension from the Krasol precursor, a route to generate crosslinked polymer networks was then developed. The previously demonstrated bis-lactone was a crystalline solid at room temperature and had limited organic solubility, so a suitable alternative was synthesized. The new crosslinker was generated in a single step via reaction of a α,β-unsaturated lactone (5,6-dihydro-2*H*-pyran-2-one) with a PEG-based dithiol. The reaction and conditions are given below in **Scheme 4.2** and in more detail in Section 4.6. The resulting product was isolated as a viscous oil with good solubility in a variety of organic solvents as well as 4mCL monomer. The synthesis was confirmed by high resolution MS as well as ^{1}H (**Figure 4.10**) and ^{13}C NMR studies (**Figure 4.11**).

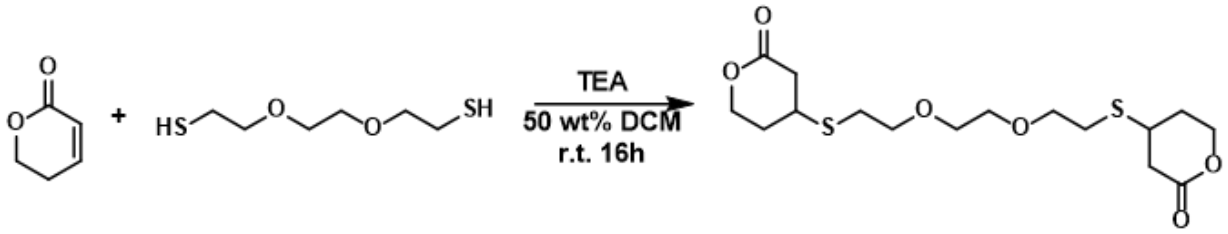

Scheme 4.2 Synthetic route to novel bis-lactone crosslinker

With the newly developed crosslinker, several curing conditions were investigated for the generation of Krasol/polyester networks. Utilizing the tri-blocks previously made, the crosslinker loading was varied between 3 – 15 equivalents of the bis-lactone per triblock chain, and the mixture is diluted with toluene until approximately 50 wt%. The resulting cloudy solution is then brought to 100 °C. The CSA catalyst was then dissolved in a minimal amount of DCM and added to the preheated solution, causing it to rapidly go clear after the addition. Within a few hours, the triblock is visibly crosslinked by the bis-lactone, generating a clear and elastic solid (**Figure 4.3**). The network was then held under high vacuum overnight to remove any remaining toluene. The sol-gel fraction was then tested, and the results are summarized in **Table 4.1**.

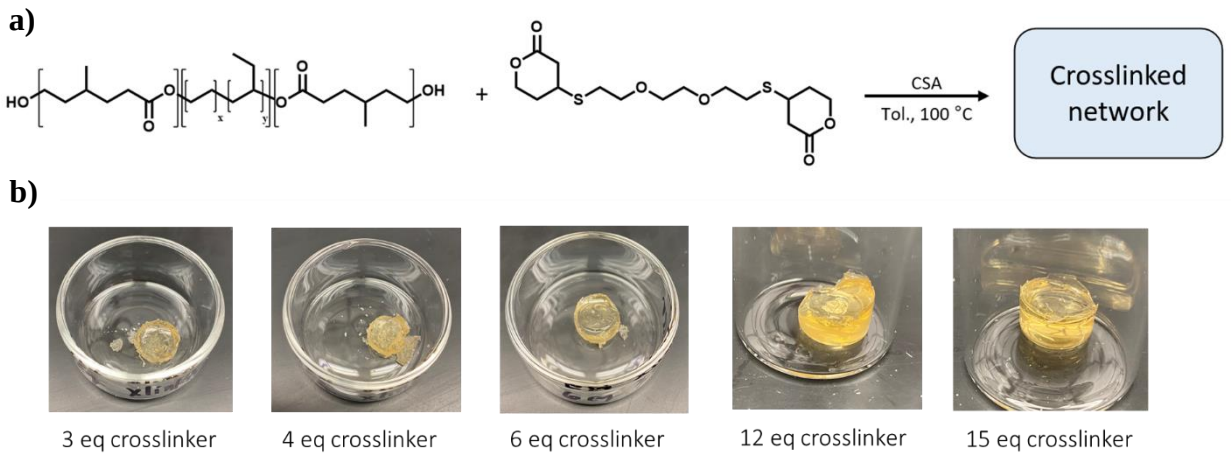

Figure 4.3 a) Reaction scheme depicting the crosslinking of the preformed tri-block with varying amounts of crosslinker. b) Freestanding, elastic solids of the crosslinked triblock with increasing amounts of the bis-lactone crosslinker.

Crosslinking eq	Solvent	Soak time (h)	Mass Recovery Percentage
3	Dry THF/Hexane	24	63.3
4	Dry THF/Hexane	24	70.5
6	Dry THF/Hexane	24	77.7
12	Dry THF/Hexane	24	81.1
15	Dry THF/Hexane	24	78.6

Table 4.1 Sol-gel results for crosslinked tri-block solids referred to in **Figure 4.3**.

As a final demonstration of the utility of this new method towards crosslinked polymer networks from bi-functional commercial polymers, a photocatalyst was used to generate a photo-curable formulation. Because this ring-opening polymerization chemistry is compatible with both acids and bases, there are a variety of viable photocatalysts. To highlight the utility of this approach, a previously demonstrated visible-light-responsive merocyanine photoacid was used. The synthesis and structure of the merocyanine photocatalyst is shown in **Scheme 3.1a**. The formulation was comprised of 52 wt% HTPB polymer, 29 wt% 4mCL, 18 wt% crosslinker, 1 wt% catalyst. This

mixture was then diluted into equal weight equivalent of solvent (dichloromethane was used to promote complete dissolution of the photocatalyst). The solution was heated to 50 °C and irradiated with 470 nm light for 8 hours with the use of a photomask. The setup and the resulting patterned polymer network are shown below in **Figure 4.4**.

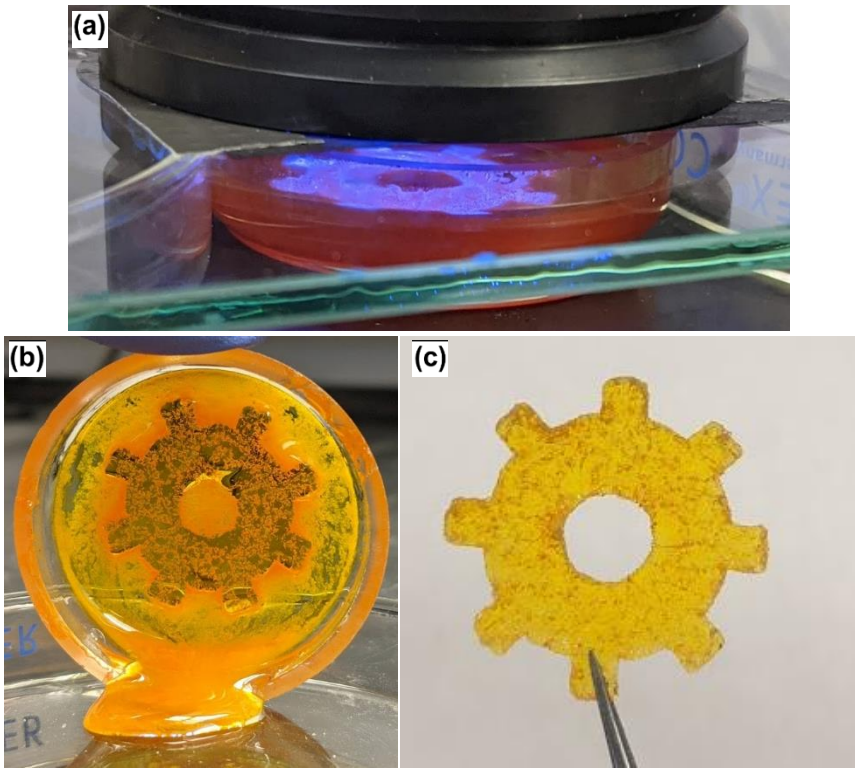

Figure 4.4 a) HTPB, caprolactone monomer, and di-lactone crosslinker (1:12:2.5 molar equivalents respectively) mixture containing mPAH (1wt%) as catalyst under 470 nm irradiation at 50 °C. b) Post irradiation; un-irradiated sections are not crosslinked and are able to flow readily, leaving behind fully crosslinked photopatterned section. c) Freestanding photopatterned sample.

4.4 Conclusion

In this chapter, the development of a new approach to generating block copolymer polyester from commercial polymers (HTPB and Krasol) was presented. The results indicate that the successful chain-extension of these materials requires both elevated temperature and dilution in an appropriate solvent, but the resulting materials are well-defined block copolymers as confirmed by both SEC and DOSY NMR studies. Further, an improved bis-lactone crosslinker was designed and synthesized so that these conditions could be leveraged to generate crosslinked networks. As a demonstration of the utility of the method, a photo-catalyst was incorporated into a resin formulation to allow for photo-patterning. We anticipate these results will be of interest to the polymer community as they expand the scope and utility of commercially available polymer precursors to generate high value materials with advanced functionalities.

4.5 Future Work

Having successfully demonstrated the generation of crosslinked polymer networks from the Krasol-polyester triblock copolymers, future studies will work to understand the ability of the networks to undergo dynamic bond exchange. Block copolymer dynamic networks have been shown in the literature,[36,37] but typically require involved synthetic methods and have limited substrate scope. With the methods reported in this chapter, similar materials can be readily synthesized from commercially available polymers. However, to confirm that these materials are capable of dynamic exchange requires further characterization. Thermomechanical analysis via an AR-G2 TA instruments rheometer will be conducted to i) characterize the mechanical properties of these networks and determine their formulation dependence such that materials can be generated with mechanical performance on par with current working polymer binders, and ii) characterize the ability of the networks to relax stress through oscillatory stress relaxation experiments. That

should allow for the quantification of the stress relaxation rates necessary to design self-healing demonstrations via macroscopically damaging and repairing samples. A preliminary example of this demonstration is shown below in **Figure 4.5**. There is also a lot of interest in developing a system to allow for the 3D printing of these materials. To that end, two future studies will be conducted. First, the Krasol-polyester triblock copolymer empirical shows shear-thinning behavior. This behavior will be further characterized via rheology to determine if these materials would be suitable for extrusion based additive manufacturing processes (i.e. fused deposition manufacturing, FDM). Similarly, the compatibility of this method with various photocatalysts suggests these materials could be translated to light-based 3D printing processes (i.e. stereolithography). Future studies will investigate the use of more aggressive and irreversible photocatalysts to photo-pattern these materials more rapidly and determine if the timescale of curing is compatible with printing processes.

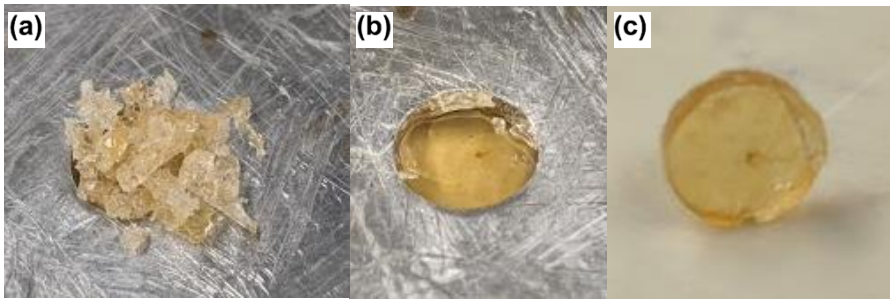

Figure 4.5 Preliminary experiments demonstrating the ability of the network to reform after being damaged via simple molding at elevated temperatures. a) Sample was cut into pieces using a razor blade post crosslinking and drying. b) Using a Carver Press, sample was annealed for 1 h at 100 °C and 4 metric tons of pressure. c) After being reprocessed, sample is a homogenous, free standing sample with no noticeable macroscopic defects.

4.6 Experimental Details

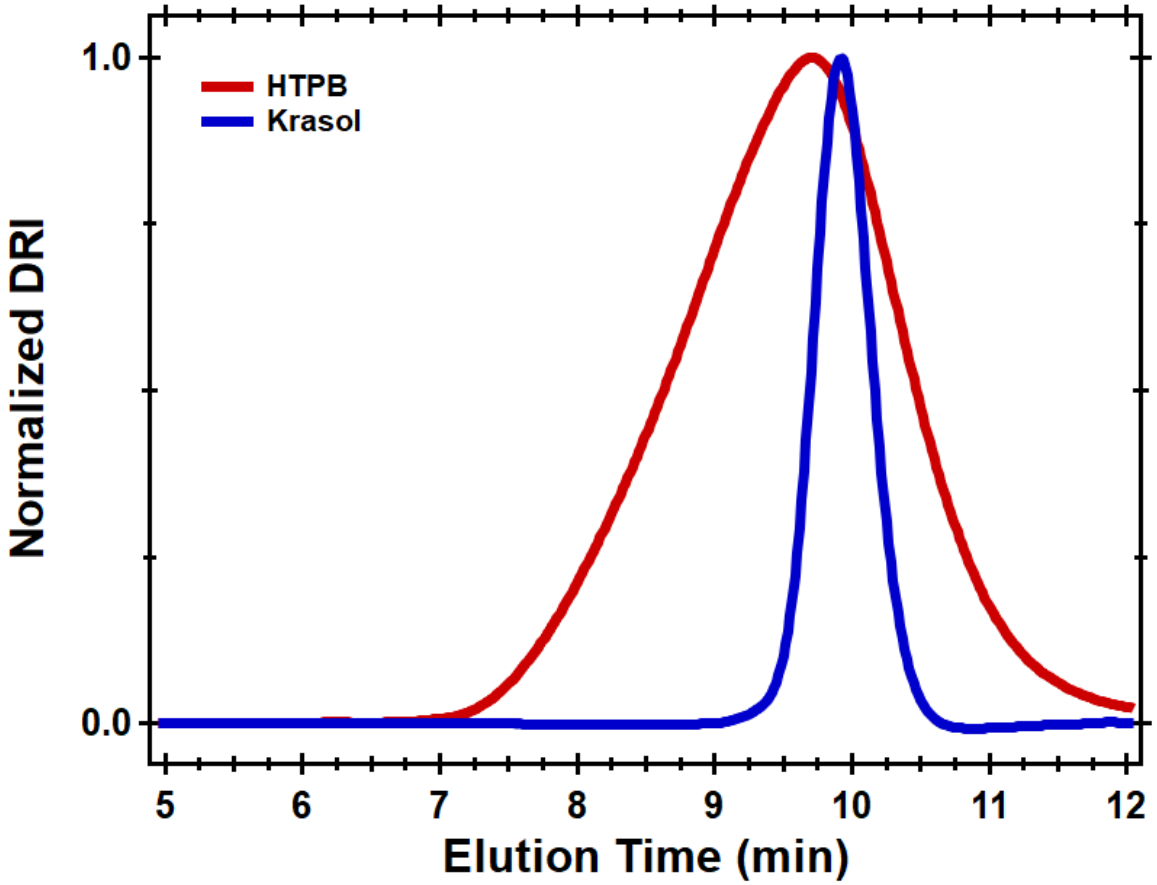

Figure 4.6 Superimposed size-exclusion chromatography (SEC) traces of commercially available HTPB and Krasol.

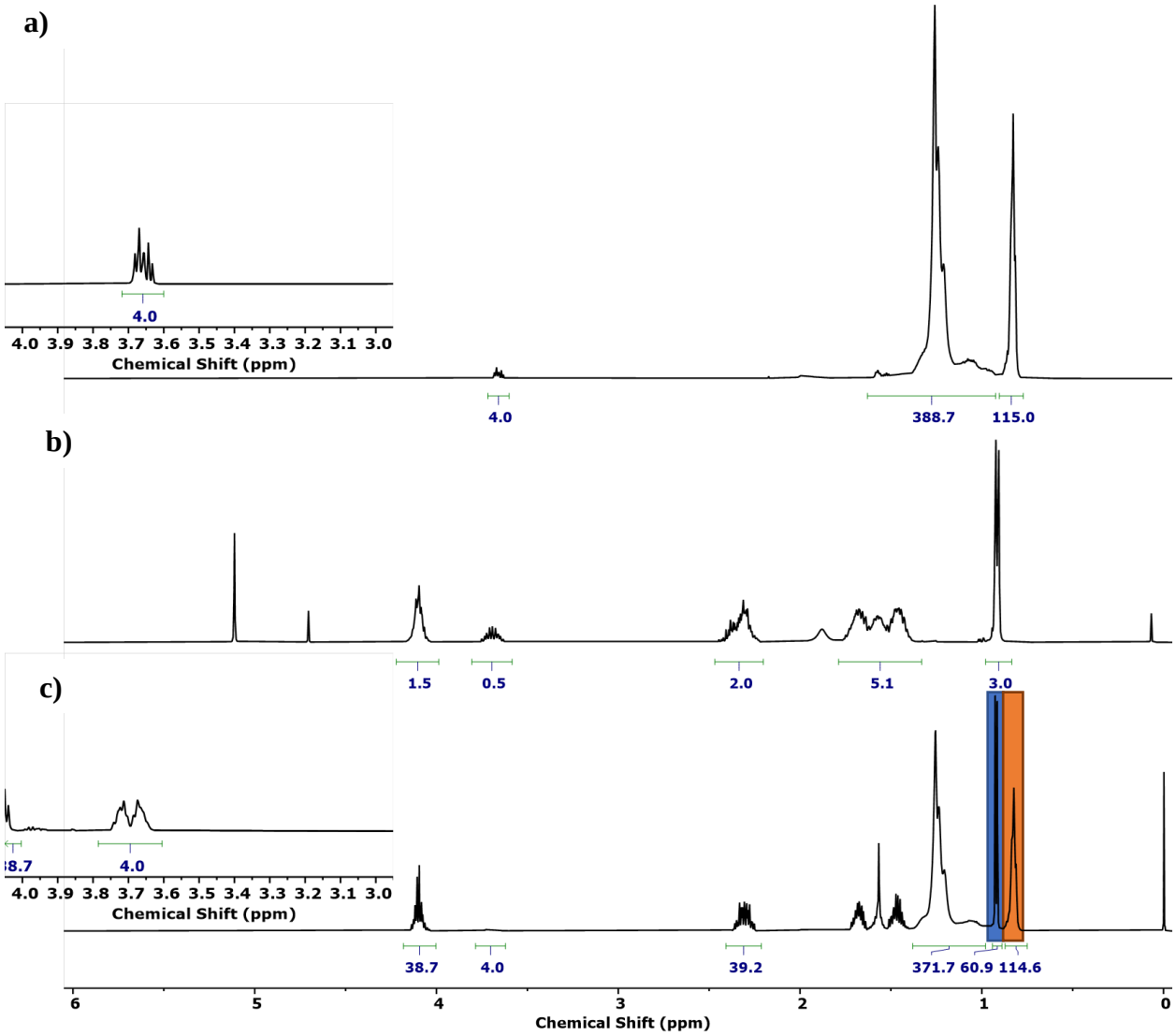

Figure 4.7 Stacked NMR spectra corresponding to a) homopolymer Krasol, b) homopolymer p4mCL, and c) a reaction between Krasol and 4mCL monomer. The two peaks used for independent calculation of diffusivities, Krasol in orange and 4mCL in blue, (via DOSY NMR) and highlighted above in **Figure 4.2**. Insets on (a) and (c) demonstrate the hydrogen peaks alpha to the hydroxy end groups that allow for facile characterization.

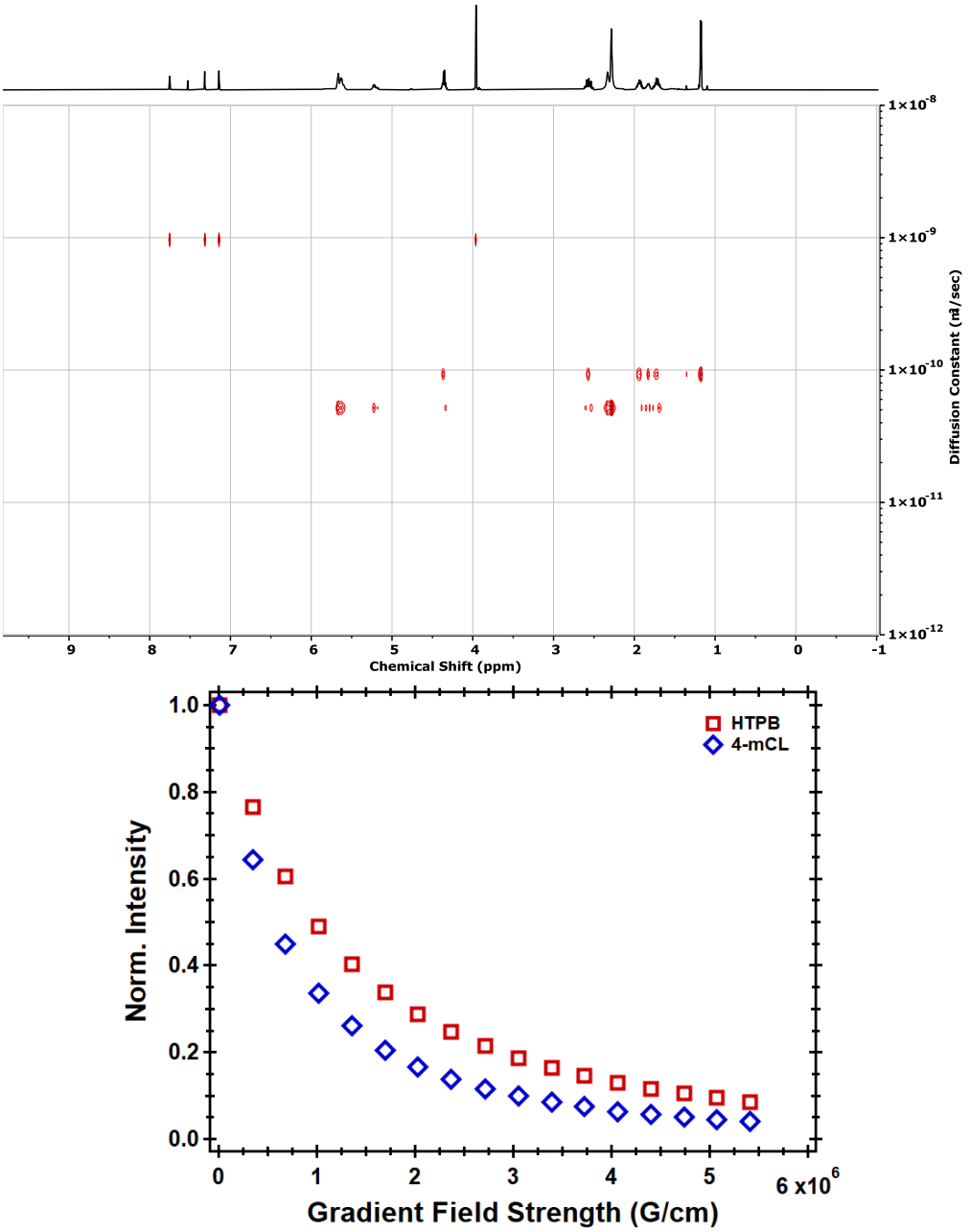

Figure 4.8 DOSY NMR spectra showing peak signals for p4MCL and HTBP corresponding to different diffusivities with an inset highlighting the gradient-strength resolved decay of signal from two peaks (corresponding to p4MCL and HTPB) showing distinctly different diffusivities.

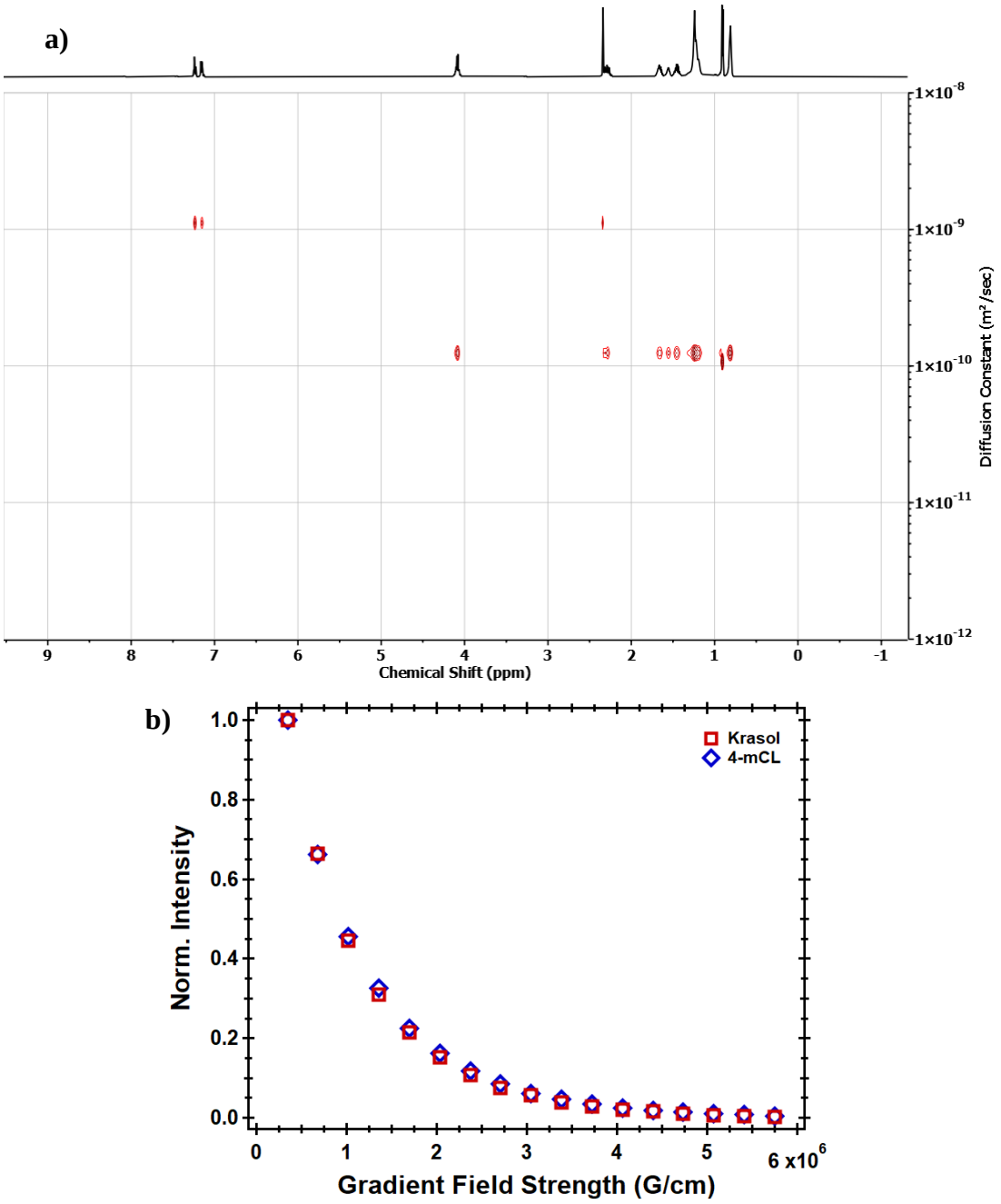

Figure 4.9 TBD initiated chain extenstion. a) DOSY NMR spectra showing great agreement in diffusivity between a characteristic p4mCL peak and a characteristic Krasol peak. b) Intensity normalized gradient-strength resolved decay of both signals demonstrating the agreement in diffusion.

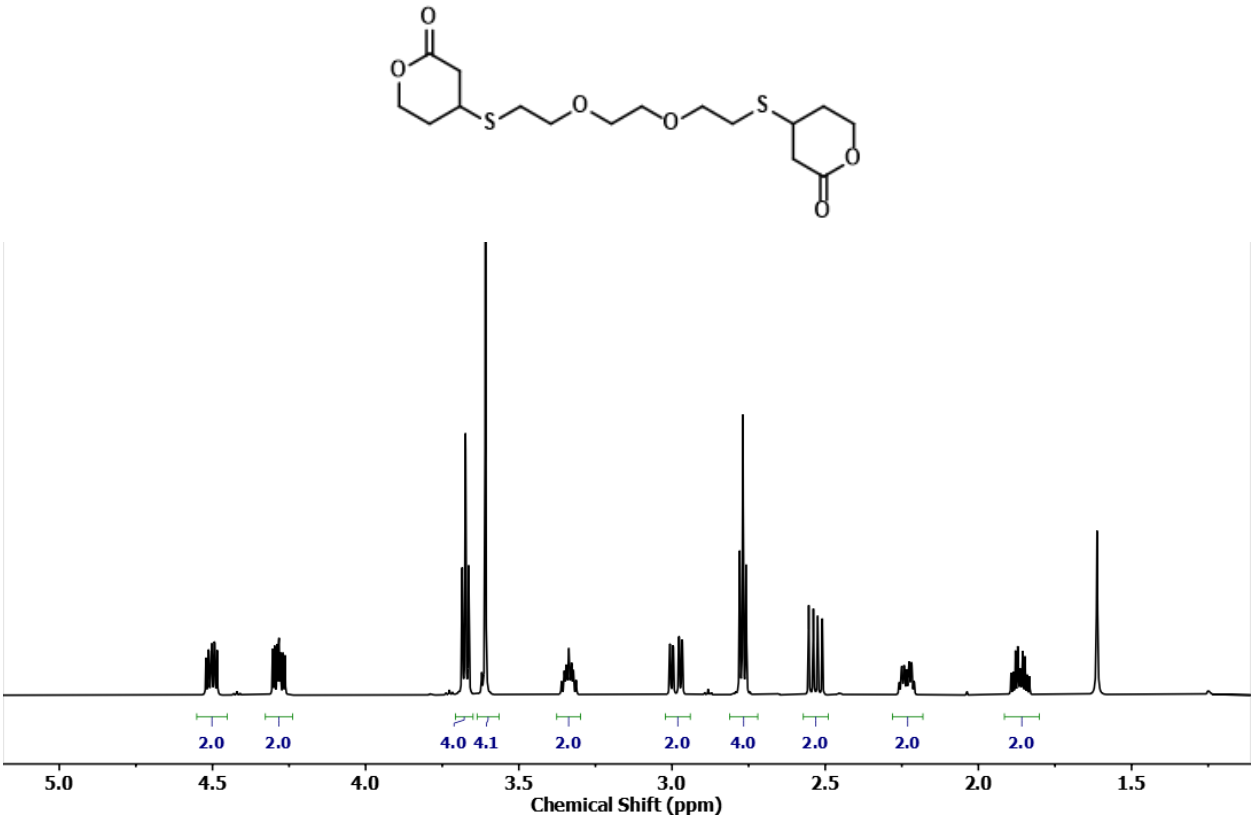

Figure 4.10 ^{1}H-NMR of newly designed bis-lactone crosslinker with corresponding structure.

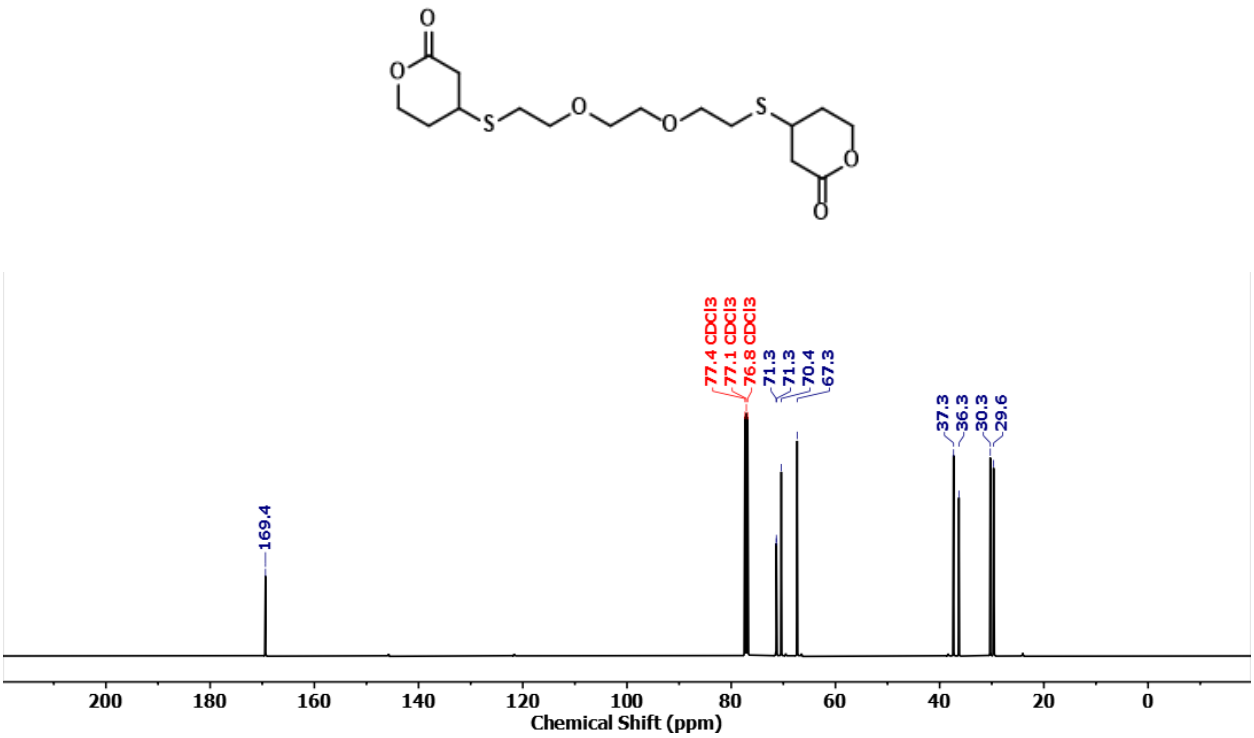

Figure 4.11 ^{13}C-NMR of newly designed bis-lactone crosslinker with corresponding structure.

4.7 References – Chapter 4

(1) Hayashi, M.; Yano, R.; Takasu, A. *Polym. Chem.* **2019**, *10*, 2047–2056.

(2) Self, J. L.; Dolinski, N. D.; Zayas, M. S.; Read De Alaniz, J.; Bates, C. M. *ACS Macro Lett.* **2018**, *7*, 817–821.

(3) Montarnal, D.; Capelot, M.; Tournilhac, F.; Leibler, L. *Science* **2011**, *334*, 965–968.

(4) Fortman, D. J.; Brutman, J. P.; Cramer, C. J.; Hillmyer, M. A.; Dichtel, W. R. *J. Am. Chem. Soc.* **2015**, *137*, 14019–14022.

(5) Saed, M. O.; Terentjev, E. M. *Sci. Rep.* **2020**, *10*, 1–10.

(6) Porath, L. E.; Evans, C. M. *Macromolecules* **2021**, *16*, acs.macromol.0c02800.

(7) Cash, J. J.; Kubo, T.; Bapat, A. P.; Sumerlin, B. S. *Macromolecules* **2015**, *48*, 2098–2106.

(8) Brooks, W. L. A.; Sumerlin, B. S. *Chem. Rev.* **2016**, *116*, 1375–1397.

(9) Smithmyer, M. E.; Deng, C. C.; Cassel, S. E.; LeValley, P. J.; Sumerlin, B. S.; Kloxin, A. M. *ACS Macro Lett.* **2018**, *7*, 1105–1110.

(10) Cromwell, O. R.; Chung, J.; Guan, Z. *J. Am. Chem. Soc.* **2015**, *137*, 6492–6495.

(11) Lu, Y. X.; Guan, Z. *J. Am. Chem. Soc.* **2012**, *134*, 14226–14231.

(12) Wen, Z.; Han, X.; Fairbanks, B. D.; Yang, K.; Bowman, C. N. *Polymer* **2020**, *202*, 122715.

(13) Huang, S.; Podgórski, M.; Han, X.; Bowman, C. N. *Polym. Chem.* **2020**, *11*, 6879–6883.

(14) Li, L.; Chen, X.; Torkelson, J. M. *Macromolecules* **2019**, *52*, 8207–8216.

(15) He, C.; Shi, S.; Wang, D.; Helms, B. A.; Russell, T. P. *J. Am. Chem. Soc.* **2019**, *141*, 13753–13757.

(16) Xu, X.; Ma, S.; Wang, S.; Wu, J.; Li, Q.; Lu, N.; Liu, Y.; Yang, J.; Feng, J.; Zhu, J. *J. Mater. Chem. A* **2020**, *8*, 11261–11274.

(17) Lascano, S.; Zhang, K. Da; Wehlauch, R.; Gademann, K.; Sakai, N.; Matile, S. *Chem. Sci.*

2016, *7*, 4720–4724.

(18) Ishibashi, J. S. A.; Kalow, J. A. *ACS Macro Lett.* **2018**, *7*, 482–486.

(19) Kloxin, C. J.; Bowman, C. N. *Chem. Soc. Rev.* **2013**, *42*, 7161–7173.

(20) Jin, Y.; Yu, C.; Denman, R. J.; Zhang, W. *Chem. Soc. Rev.* **2013**, *42*, 6634–6654.

(21) Denissen, W.; Winne, J. M.; Du Prez, F. E. *Chem. Sci.* **2016**, *7*, 30–38.

(22) Zhao, S.; Abu-Omar, M. M. *Macromolecules* **2018**, *51*, 9816–9824.

(23) Snyder, R. L.; Fortman, D. J.; De Hoe, G. X.; Hillmyer, M. A.; Dichtel, W. R. *Macromolecules* **2018**, *51*, 389–397.

(24) Chen, X.; Li, L.; Jin, K.; Torkelson, J. M. *Polym. Chem.* **2017**, *8*, 6349–6355.

(25) Tellers, J.; Pinalli, R.; Soliman, M.; Vachon, J.; Dalcanale, E. *Polym. Chem.* **2019**, *10*, 5534–5542.

(26) Shi, J.; Zheng, T.; Zhang, Y.; Guo, B.; Xu, J. *ACS Sustain. Chem. Eng.* **2020**, *8*, 1207–1218.

(27) Podgórski, M.; Huang, S.; Bowman, C. N. *ACS Appl. Mater. Interfaces* **2021**, *13*, 12789–12796.

(28) Robinson, L. L.; Self, J. L.; Fusi, A. D.; Bates, M. W.; Alaniz, J. R. de; Hawker, C. J.; Bates, C. M.; Sample, C. S. *ACS Macro Lett.* **2021**, 857–863.

(29) Jiang, Z. C.; Xiao, Y. Y.; Yin, L.; Han, L.; Zhao, Y. *Angew. Chemie - Int. Ed.* **2020**, *59*, 4925–4931.

(30) Heidarian, P.; Kouzani, A. Z.; Kaynak, A.; Paulino, M.; Nasri-Nasrabadi, B. *ACS Biomater. Sci. Eng.* **2019**.

(31) Bai, L.; Zheng, J. *Compos. Sci. Technol.* **2020**, *190*, 108062.

(32) Ji, F.; Liu, X.; Sheng, D.; Yang, Y. *Polymer* **2020**, *197*, 122514.

(33) Wang, H.; Yang, Y.; Zhang, M.; Wang, Q.; Xia, K.; Yin, Z.; Wei, Y.; Ji, Y.; Zhang, Y. *ACS*

Appl. Mater. Interfaces **2020**, *12*, 14315–14322.

(34) Self, J. L.; Sample, C. S.; Levi, A. E.; Li, K.; Xie, R.; de Alaniz, J. R.; Bates, C. M. *J. Am. Chem. Soc.* **2020**, *142*, 7567–7573.

(35) Philipps, K.; Junkers, T.; Michels, J. J. *Polym. Chem.* **2021**, *12*, 2522–2531.

(36) Lessard, J. J.; Scheutz, G. M.; Sung, S. H.; Lantz, K. A.; Epps, T. H.; Sumerlin, B. S. *J. Am. Chem. Soc.* **2020**, *142*, 283–289.

(37) Ishibashi, J. S. A.; Fang, Y.; Kalow, J. A. *ChemRxiv*. ChemRxiv December 2019.